Technische Universität München
Fakultät für Physik
Physics of Energy Conversion and Storage

# Temperature effects in automotive polymer electrolyte membrane fuel cells

Jarek Peter Sabawa

Vollständiger Abdruck der von der Fakultät für Physik der Technischen Universität München zur Erlangung des akademischen Grades eines

Doktor der Naturwissenschaften

genehmigten Dissertation.

**Vorsitzende(r):**

Prof. Dr. Alejandro Ibarra

**Prüfer der Dissertation:**

1. Prof. Dr. Aliaksandr S. Bandarenka
2. Prof. Dr. Andre C. van Veen

Die Dissertation wurde am 25.05.2021 bei der Technischen Universität München eingereicht und durch die Fakultät für Physik am 09.08.2021 angenommen.

This thesis is based on the following publications:

**J.P. Sabawa**, A.S. Bandarenka. Investigation of degradation mechanisms in PEM fuel cells caused by low-temperature cycles // International Journal of Hydrogen Energy (2021) 15951-15964.

T. Lochner, M. Perchthaler, F. Hnyk, D. Sick, **J.P. Sabawa**, A.S. Bandarenka. Analysis of the capacitive behavior of polymer electrolyte membrane fuel cells during operation // ChemElectroChem 8 (2021) 96-102.

**J.P. Sabawa**, F. Haimerl, F. Riedmann, T. Lochner, A.S. Bandarenka. Dynamic and precise temperature control unit for PEMFC single-cell testing // Engineering Reports 3 (2021) accepted (https://doi.org/10.1002/eng2.12345).

**J.P. Sabawa**, A.S. Bandarenka. Applicability of double layer capacitance measurements to monitor local temperature changes at polymer electrolyte membrane fuel cell cathodes // Results in Chemistry 2 (2020) 100078.

T. Lochner, M. Perchthaler, J.T. Binder, **J.P. Sabawa**, T.A. Dao, A.S. Bandarenka. Real-time impedance analysis for the on-road monitoring of automotive fuel cells // ChemElectroChem 7 (2020) 2784-2791.

T. Lochner, L. Hallitzky, M. Perchthaler, M. Obermaier, **J. Sabawa**, S. Enz, A.S. Bandarenka. Local degradation effects in automotive size membrane electrode assemblies under realistic operating conditions // Applied Energy 260 (2020) 114291.

**J. Sabawa**, A.S. Bandarenka. Degradation mechanisms in polymer electrolyte membrane fuel cells caused by freeze-cycles: investigation using electrochemical impedance spectroscopy // Electrochimica Acta 311 (2019) 21-29.

# Abstract

The operating temperature plays a critical role in the performance and lifetime of polymer electrolyte membrane fuel cells (PEMFC). Temperatures outside the normal operating window, such as below freezing or above the boiling point of water, can damage the components of a PEMFC. To optimize the operating strategy and thus the lifetime of PEMFC, it is essential to perform various stress tests over wide temperature ranges. However, not all types of stress tests can be performed on a standard test bench configuration. For the low-temperature tests, an additional cooling device is required, which is associated with high costs and long testing times. At the other end of the temperature range, at high temperatures, a different heating strategy and a modified test bench setup is often required. If the tests are performed on a single cell level, it is additionally questionable whether there is any comparability with real applications at all. A critical point here is the uneven temperature distribution on the PEMFC surface, which can occur both during start-up at low temperatures and during regular operation. In addition, the rates of temperature change occurring in a fuel cell system cannot be readily achieved with a single cell and ordinary temperature control methods. All of the above points could not be represented with the same measurement setup so far.

This work deals with two main topics. In the first part, a new methodology for temperature control of PEMFC single cells is presented. With the two novel highly dynamic single-cell designs (small-size of 50 $cm^2$ and automotive-size of 285 $cm^2$), where high power Peltier elements adjust the cell temperature, the scope of single-cell testing can be significantly extended compared to conventional measurement setups. As a result, the new designs achieve temperatures from -30 °C to over 125 °C, temperature change rates of up to 80 $Kmin^{-1}$, and temperature control accuracy of less than ±0.3 °C. Besides improved dynamics and accuracy, the automotive-size enables temperature gradients in the longitudinal direction of up to 70 °C. With the novel cell designs, it was possible to perform all the fundamental measurements presented in this thesis. The second part of the thesis deals, on the one hand, with the possibility of temperature determination using the cell impedance and, on the other hand, with the degradation mechanisms of PEMFC single cells at low temperatures. With the precise temperature control of the small-size single cell design, the cell impedance could be accurately determined at temperatures between -5 °C and 60 °C. All calculated electrical equivalent circuit (EEC) values were sensitive to the temperature

changes, and a quasi-linear dependence of the double layer capacitance on temperature could be observed. Based on this finding, this method can provide an alternative to commercially available resistive temperature sensors and can be used to estimate the PEMFC cell temperature quantitatively. Furthermore, a total of three types of low-temperature stress tests were performed in this thesis. The first low-temperature stress test was a concept test for the new temperature control method and the newly established test procedure. It was shown that the novel "tempering design" could be used to perform a complete low-temperature stress test on a small-size PEMFC single-cell quickly and affordably without the aid of a climatic chamber. Furthermore, it was shown that electrochemical impedance spectroscopy can be used to determine the degradation state and that the degradation mechanisms are directly related to the test procedure used. Building on the first low-temperature stress test, the influence of different cathode ionomer-carbon weight ratios (0.5/1.0/1.5) on long-term stability was investigated in the second run on small-size PEMFC single cells. The test procedure for this low-temperature stress test was derived mainly from the automotive application. The generated *in-situ* measurement data clearly demonstrate that the performance of each PEMFC single cell changes individually as a function of the cathode I/C-ratio. In addition, postmortem *ex-situ* analysis revealed the exact damage pattern of every single cell, allowing conclusions to be drawn about the exact degradation mechanisms. In the last stress test performed, the automotive-size cell design was used, which in addition to low temperatures, can also map temperature gradients on the PEMFC surface. With this added feature, as well as the ability to measure local current density and impedance, a novel experiment was conducted in which the shutdown temperature exhibited a gradient on the PEMFC surface from +2 °C to -8 °C. It could be clearly shown how the locally calculated EEC elements, as well as the current density, changed during the 132 temperature cycles performed and that the test procedure and especially the temperature gradient had a significant influence on the local degradation.

# Content

**ABSTRACT** ..... **2**

**ACKNOWLEDGMENT** ..... **6**

**1 INTRODUCTION** ..... **8**

**1.1. Energy policy** ..... **8**

**1.2. Energy storage** ..... **8**

**1.3. Hydrogen – energy source for the transport sector** ..... **10**

**1.4. Methodological challenges** ..... **11**

**1.5. Aim of the work** ..... **13**

**2 THEORY** ..... **15**

**2.1. The history of catalysis** ..... **15**

**2.2. PEM fuel cells** ..... **17**
2.2.1. Structure of a PEM fuel cell ..... 18
2.2.2. Theoretical cell potential ..... 21
2.2.3. Reaction kinetics ..... 22

**2.3. Thermoelectric effect** ..... **24**

**3 EXPERIMENTAL** ..... **27**

**3.1. Measurement setup** ..... **27**
3.1.1. Test bench setup ..... 27
3.1.2. Electrical setup for the cell characterization ..... 32
3.1.3. Software ..... 39
3.1.4. Tandem Technologies TP cell hardware ..... 41

**3.2. Experimental techniques** ..... **46**
3.2.1. U-I-curves ..... 46
3.2.2. Cyclic Voltammetry (CV) ..... 48
3.2.3. Electrochemical Impedance Spectroscopy (EIS) ..... 50
3.2.4. Ex-situ (post mortem analysis) ..... 54

**4 DEVELOPMENT OF A DYNAMIC TEMPERATURE CONTROL UNIT** ..... **57**

**4.1 PET TP50 single cell** ..... **57**
4.1.1. State-of-the-art ..... 57
4.1.2. Characteristics ..... 58
4.1.3. Design ..... 62
4.1.4. Control unit ..... 71
4.1.5. New opportunities with PET SC TP50 ..... 74

**4.2 PET TP285 single cell ..... 76**
4.2.1. State-of-the-art ..... 76
4.2.2. Characteristics ..... 76
4.2.3. Design ..... 79
4.2.4. Control cabinet ..... 96
4.2.5. New opportunities with PET SC TP285 ..... 103

**5 RESULTS AND DISCUSSION ..... 106**

**5.1. Determination of the local temperature using the cell impedance ..... 106**
5.1.1. Introduction ..... 106
5.1.2. Test methodology ..... 107
5.1.3. Measurement results ..... 109

**5.2. Investigation of degradation mechanisms caused by freeze-cycles ..... 113**
5.2.1. Introduction ..... 113
5.2.2. Test methodology ..... 114
5.2.3. In-situ measurement results ..... 117
5.2.4. Ex-situ measurement results ..... 126

**5.3. Effect of different ionomer to carbon weight ratios on the degradation ..... 128**
5.3.1. Introduction ..... 128
5.3.2. Test methodology ..... 129
5.3.3. In-situ measurement results ..... 131
5.3.4. Ex-situ measurement results ..... 139

**5.4. Investigation of local degradation caused by temperature gradients ..... 144**
5.4.1. Introduction ..... 144
5.4.2. Test methodology ..... 145
5.4.3. In-situ measurement results ..... 147

**6 CONCLUSION AND OUTLOOK ..... 158**

**SYMBOLS AND ABBREVIATIONS ..... 160**

**FIGURES AND TABLES ..... 162**

**REFERENCES ..... 172**

# Acknowledgment

The preparation of the thesis would not have been possible without the support of many people. Therefore, I want to thank all the people who supported me during the 4 years.

First and foremost, I would like to thank my whole family for their support. Especially to my beloved wife **Tatjana Sabawa**, who put up with my bad moods and always motivated and supported me. My daughter and son, **Lina A. Sabawa** and **Damian D. Sabawa**, who often didn't see their dad for hours or even days.

My supervisor **Prof. Dr. Aliaksandr S. Bandarenka**, who gave me the opportunity to write the thesis in his team. Additionally, I would like to thank him very much for the good supervision and for the open and instructive discussions.

My team leader **Dr. Florian Fergg**, who made it possible for me to write my doctoral thesis at BMW AG in combination with my full-time job and always supported me actively.

**Dr. Olav Finkenwirth**, who released the financial budget and thus made the development of the PET SC TP285 possible in the first place.

**Arno Kipper**, who helped me a lot with the programming and implementation of the scripts as well as with various software topics on the test bench.

**Nico März**, who co-developed the first Peltier element-tempered (PET) single-cell prototype TP288.

**Felix Riedmann**, who co-developed the PET single cell TP285. The development of the PET SC TP285 took us many evenings, but it resulted in a unique product.

**Philliph Erdtmann**, who was involved in the further development of the control cabinet and software of the PET SC TP285.

**Felix Haimerl**, who was involved in the further development of the PET SC TP285 software and supervised the last low-temperature stress test.

**Bogdan Kaczmarczyk**, who always had an open ear and always advised me well.

**Tuan Anh Dao**, who assisted me in selecting the right measurement equipment and data analysis.

To the ET single cell team, especially **Sarah Gelder** and **Jakob Mühldorfer**, who took care of the test bench and measurement setup in my absence.

The FuelCon resident team, **Matthias Rommel** and **David Hubertus**, who helped me upgrade the dyno and were always there when components of the test bench broke.

The TWA team, **Dr. Andreas Bauer** and **Krzysztof Jozwiak**, who performed the ex-situ analyses and had interesting discussions with me.

Thanks again to everyone for the strong support! I could not have done the thesis without all of you.

# 1 Introduction

## 1.1. Energy policy

Global warming, resulting from the accumulation of the greenhouse gas $CO_2$ in the atmosphere, as well as the scarcity of fossil fuel resources, are two of the major problems of the 21st century [1, 2]. There are many sectors, which use fossil fuels to produce energy. One of them is the transport sector. Worldwide, there are approximately about $1.3 \cdot 10^9$ vehicles, and most of them use combustion-powered engines [3]. To gain energy, a commercial gasoline engine consumes fossil fuel and produces rather unacceptable amount of pollutants (solid particles, $CO_2$, $NO_x$, CO, $SO_2$, etc.) as a result of combustion. With the turnaround in energy policy, electrically powered vehicles appear to be more and more attractive. This means that for the automotive sector, the $CO_2$ emissions of the average sold new cars should not exceed 95 g/km after 2021 [4]. Such low emissions are only possible with fossil fuel vehicles powered by an advanced downsized combustion engine, hybrid electric vehicles (PHEV) and battery electric vehicles (BEV). The benefits of electric vehicles are quite obvious: Local low emissions, low-noise and high energy-efficiency compared to vehicles with standard combustion engines. Nevertheless, one considerable disadvantage is the short range of pure battery vehicles. Due to the low energy density of batteries, it seems obvious that the battery takes up a lot of space, and therefore the vehicles are extremely heavy [5]. Another technology that becomes more and more popular is based on the so-called cold combustion of hydrogen. The hydrogen, which is stored in a high-pressure tank, is converted into electricity by a fuel cell stack (more on this in chapter 2.2). The produced energy is used to charge the battery (range extender) or to directly drive the electric motor. This type of vehicle is called a fuel cell electric vehicle (FCEV).

## 1.2. Energy storage

Energy storage describes the possibility of storing various forms of energy that can be used for different physical applications time-independent. Storage and energy generation from fossil fuels has long been considered as the best and most efficient way in the transport sector. With the turnaround in energy policy and the increased popularity of electrically powered vehicles, another way of high density and efficient energy storage is required. Some well-known forms of energy storage for automotive application are:

- **Rechargeable batteries.** A rechargeable battery is a galvanic cell, which converts chemically stored energy into electrical energy through the redox reaction. Depending on the battery type, different electrode materials and electrolytes are used. Accordingly, cell voltages from 1.2 V (nickel-cadmium battery) to 3.7 V (lithium polymer battery) are possible. With the connection of more cells in series, the voltage can be increased. Therefore, rechargeable batteries are suitable for many mobile applications and nowadays one of the most popular forms of energy storage [6, 7].

- **Supercapacitors.** Similar to conventional solid dielectrics capacitors, a supercapacitor belongs to the family of electric double-layer capacitors (EDLC) [8, 9]. The essential difference between a conventional capacitor and a supercapacitor is the liquid electrolyte, which supports up to 10.000 farads/1.5 V and enables a power density that is 10 to 100 times higher than that of rechargeable batteries [10]. Another advantages are the shorter charging/discharging cycles and the higher number of charge/discharge cycles compared to batteries. Probably the biggest disadvantage of supercapacitors is the high production costs and thus the high price compared to rechargeable batteries [11].

- **Hydrogen.** Hydrogen, with the atomic mass of 1.008 u, is the lightest element and the most abundant chemical substance in the universe [12]. Besides the natural occurrence, hydrogen can be produced by different reforming processes, water electrolysis and other methods [13]. Due to the high reactivity and the high calorific value of 141.8 MJ/kg, hydrogen is particularly suitable as an energy source [14]. For this purpose, hydrogen can be stored in different ways: Liquid in vacuum tanks at temperatures under 259.16 °C, in solid storage, where the hydrogen is absorbed by different absorbing alloys or gaseous in special pressurized tanks [15, 16]. The latter is currently particularly suitable for automotive applications, and with a polymer electrolyte membrane fuel cell (PEMFC) the stored hydrogen can be converted into electrical energy.

## 1.3. Hydrogen – energy source for the transport sector

With the turnaround in energy policy and the launch of a new hydrogen strategy to reach the climate targets until 2050, alternative energy sources for the transport sector, such as hydrogen, seems to be becoming more and more attractive [17, 18]. Globally, the transport sector is responsible for 17 % of the greenhouse gas emissions every year [19]. Therefore, the energy conversion with a PEMFC has the potential to reduce pollutant emissions and to solve the dependency on gasoline engines, and ultimately on fossil fuels [20]. However, there are many hurdles to a final solution to cover the entire transportation sector with PEMFC technology. Two main reasons for the slow development and the low number of PEMFC powered vehicles are, in particular, the poor network of hydrogen filling stations (currently 87 $H_2$ filling stations in Germany [21]) and the relatively high costs. The high costs arise from the use of noble metals, special materials and new processing technologies [22, 23]. Therefore, a PEMFC stack represents a major proportion of ~90 % of the total system costs at >500.000 systems per year (as shown in **Figure 1**) [24]. The remaining ~10 % are covered by the balance of the stack. The balance of the stack describes the mechanical peripherals such as air compressor, humidifier and other components that are necessary for the operation of the fuel cell.

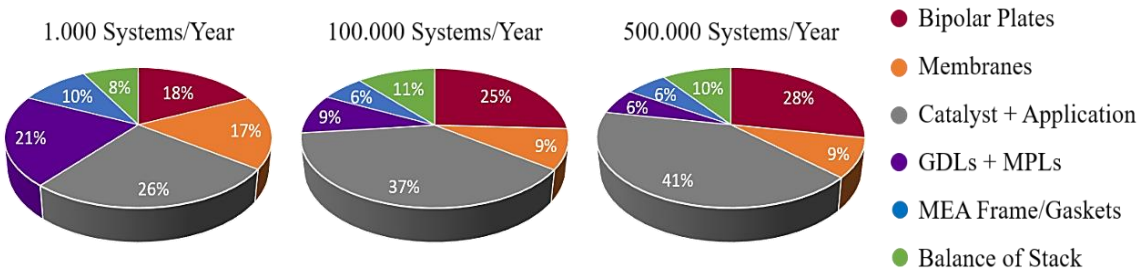


**Figure 1:** Break down of the total costs of a PEM fuel cell system depending on the production figure [24].

Nevertheless, the PEMFC technology in the transport sector offers many noticeable advantages, such as: The high energy conversion efficiency of more than 50 %, short refueling time and the higher range compared to BEV's [20]. Here the limiting factor for the range is not the fuel cell but only the size of the hydrogen fuel tank. For this reason, PEMFC technology is particularly suitable for larger vehicles, where the space for a fuel tank is not the main limiting factor.

Regardless of whether the electrical energy comes from a battery or is generated by a fuel cell system, the thermal management of both applications is a critical point [25, 26, 27, 28]. Temperatures outside the normal operating range can damage components of the fuel cell systems and lead to a reduction in performance and lifetime [29, 30, 31, 32]. It is, therefore, necessary to investigate the degradation behavior of fuel cell components, like e.g. bipolar plates, membrane materials and the catalyst layer (CL) composite, under special boundary conditions such as high (>100 °C) or low temperatures (<0 °C). Through a better understanding of the degradation mechanisms, components can be improved, lifetime increased and thus costs reduced.

## 1.4. Methodological challenges

The field of application of fuel cells range from stationary use, such as use as a combined heat and power unit, to mobile applications. The supreme discipline is the mobile application in the transport sector. In addition to the high power output (>100 kW [33]), the fuel cell system must also operate at a wide range of environmental temperatures and exhibit low degradation at different driving profiles. Depending on the temperatures and the driving profile, the lifetime of each cell can change significantly [34, 35]. Therefore it is essential to know the properties of the individual cell components, optimize the weak points and introduce new and simple measuring methods on single cells for the analysis of degradation mechanisms.

Since real driving tests in vehicles are associated with high costs, most tests are carried out on test benches. Depending on the degree of maturity of the cells or cell components, the tests are performed on different cell sizes. If, for example, only the electrochemical reaction kinetics or simple investigation of the stability of the catalyst needs to be carried out, these can be done experimentally by electrochemical measurements such as the rotating disk electrode (RDE) [36]. Since these measurements are carried out under typical laboratory conditions such as fluctuating room temperatures, liquid electrolytes with often different concentrations and low current densities (mA/cm²), comparability with real applications is often not possible.

Significantly better comparability to real applications is achieved with small size (~50 cm²) and the automotive size single cell (285 cm²). Here not only the performance or durability

of the catalyst can be characterized, but also the composite of catalyst layers, polymer electrolyte membrane and gas diffusion layers (more on this in chapter 2.2). In this way, thermodynamic, hydrodynamic and reactant flow effects can be considered. This, in turn, extends the possibility of characterization and reveals new degradation mechanisms that cannot be determined *ex-situ*, *e.g.* by RDE measurements. But here, too, the comparability strongly depends on the measurement setup and the operating parameters. In the direction of the operating parameters, the cell temperature plays an important role. Not only electrochemical processes, such as charge transfer resistance ($R_{ct}$), are temperature dependent, but also thermodynamic processes inside and outside of the CL [37, 38]. A further point with the automotive size single cell is that depending on which cell (edge cells or inner cells) is considered, different temperature gradients and effects occur in a fuel cell stack, which can only be simulated to a limited extent on an ordinary single-cell setup. Therefore the accuracy and distribution of the temperature over the active surface area of a single cell, regardless of size, play a major role [31, 39].

If the fuel cell is operated outside the normal operating temperatures, increased degradation will occur under certain circumstances. Excessively high operating temperatures can be avoided by means of sophisticated thermal and operational management of the fuel cell system [40]. In contrast, low or subzero temperatures can be caused by the influence of the environment and, therefore, cannot be avoided. Since low-temperature stress tests in real applications are not reproducible and too costly, they are often performed in the test bench environment. For this type of experiment, special measurement setups, such as a cooling unit or cooling chamber, are required. Here, however, it is questionable whether the comparability to the real application is given. Due to the thermal mass of the cell hardware and the heat produced at low temperatures start-up of a fuel cell system (with approx. 400 cells), temperature change rate as well as temperature distribution across the cell significantly distinguish in a stack from that of a single cell [41, 42]. This, in turn, influences the degradation behavior and thus also the test procedure derived from the automotive application. Therefore, comparability between a fuel cell stack and a typical single cell in such a stress test is not given.

Another topic besides the measurement setup is the determination of the changes in the fuel cell during a stress test. Measuring methods such as cyclic voltammetry, polarization curves and electrochemical impedance spectroscopy (EIS) are especially suitable for determining

the degradation behavior *in-situ*. In particular, the EIS is a powerful tool that can show not only changes in the fuel cell during a stress test run, but also temperature-sensitive electrochemical processes. However, choosing the right physical impedance model and understanding it is often a hurdle. Although many models fit the recorded impedance spectrum, but they do not have a physical meaning and the relationship between the changes in the cell components, such as the catalyst layer, and the calculated electrical equivalent circuit values is often not given. Furthermore, a subsequent post-mortem *ex-situ* analysis is often missing for a complete understanding of the generated measurement results. Therefore many degradation mechanisms remain undiscovered or unexplained, and subsequent optimization of the cell components is often not possible.

## 1.5. Aim of the work

As described in the previous chapter, the operating temperature of a PEMFC plays a significant role. This is precisely the direction in which the aims of this thesis are directed.

A major aim of this work was to develop a new “tempering” method for PEMFC single cells. The new development is designed to eliminate all known disadvantages of the previous techniques and provide an all-in-one solution for temperature control. The new “tempering” concept should make it possible to approach cell temperatures between -20 °C and 120 °C, heating or cooling rates of more than 0.5 °C/s and to temperature stability of <±0.5 °C over the entire temperature control range. Furthermore, the new concept should be cost-effective, both in terms of acquisition and maintenance. In the course of the new development of the tempering units, several design stages took place, reaching their final state after more than three years of development. With the two final tempering designs, the remaining aims of the work could be fulfilled.

Since the cell temperature of a PEMFC single cell is one of the most important operating parameters and in a fuel cell stack, the individual cell temperatures cannot be monitored, the next objective of this work was to determine the cell temperature of PEMFC single cells without using a resistive temperature sensor. For this purpose, a novel method had to be developed to fully automatically and reproducibly precondition the PEMFC and then determine the cell impedance at different temperatures. Using this method, it was possible to

accurately determine the cell temperature in the temperature range between -5 °C and 60 °C without a commercially available resistive temperature sensor.

The next aim of this work was also to determine whether the newly developed tempering method can be used to perform a complete low-temperature stress test on a PEMFC single cell with a size of ca 43.56 cm² inexpensively and quickly, without the aid of an additional cooling device. Furthermore, it should be examined whether the degradation mechanisms could be determined using the cell impedance. For this purpose, the first low-temperature stress test was carried out with 100 temperature cycles between -5 °C and 60 °C, and the performance change as well as the degradation mechanisms were evaluated *in-* and *ex-situ*.

Building on the first low-temperature stress test, the aim of the second run was to investigate the effect of different cathode ionomer to carbon weight ratios (I/C-ratio) (0.5/1.0/1.5) on long-term stability during 120 low-temperature cycles between -10 °C and 80 °C. For this purpose, a method almost completely derived from the automotive sector was adapted to a single-cell test bench, and the degradation mechanisms of the individual 43.56 cm² membrane electrode assemblies (MEA) were analyzed *in-situ* during the stress test. To better determine the degradation mechanisms, additional detailed post-mortem *ex-situ* analyses were performed.

The final aim of this experiment was to perform a stress test simulating a parked vehicle in which the fuel cell stack is not completely cooled down. For this purpose, the automotive-sized tempering design with an active area of 285 cm² was used to approach a temperature gradient on the PEMFC surface from -8 °C to +2 °C in the shutdown part. During this stress test, a total of 132 temperature cycles were performed between 80 °C and the temperature gradient. Since a major objective of this test is to amplify local degradation mechanisms, a novel measurement setup was built that can measure *in-situ* both locally resolved impedances and current densities.

# 2 Theory

Since the thesis covers a broad field of research, this chapter deals with the fundamental knowledge and the historical aspects of electrocatalysis, the PEM fuel cells and the thermoelectric effect. The derivations to the fundamental equations are not discussed but can be found in various electrochemistry books dealing with this topic.

## 2.1. The history of catalysis

The first known use of an inorganic catalyst can be traced back to 1552 when V. Cordus used sulfuric acid to convert alcohol into ether [43]. It was not until many centuries later, in 1835, when the chemist J.J. Berzelius described the property of a substance that influences the chemical reaction but is not consumed even in the reaction [44]. J.J. Berzelius was thus the first natural scientist to describe the decomposition of bodies by a new force, which he named the "catalytic force". This was the first recognition of catalysis as a driving force [45]. However, the term catalyst was first introduced in 1895 by another chemist W. Ostwald and defined as follows: “A catalyst is a substance that accelerates the rate of a chemical reaction without being part of its final products”. W. Ostwald was awarded the Nobel Prize for Chemistry in 1909 for his excellent work on catalysis and its influence on the dynamics of chemical reactions [46].

In summary, it can be said that the catalyst accelerates the reaction path of often two molecules or species through the formation of intermediate compounds and thus offers a faster route to the reaction products [47]. In the field of chemistry, catalysis is divided into two main areas. Homogeneous catalysis, where the catalyst is in the same phase as the reactants, such as in biological processes, where biocatalysts such as enzymes reduce the activation energy and accelerate chemical reactions within an organism [48]. Heterogeneous catalysis, where the catalyst is in a different phase than the reactants [49]. The latter plays a decisive role in the direction of the automotive industry. A well-known example would be the catalytic converter of combustion engines, which lowers the reaction energy barrier, catalyzes a redox reaction, and largely neutralizes toxic gases and pollutant emissions [50]. The catalytic converter is one of many examples of surface catalysis, in which the molecules of the reactants are adsorbed on the surface of the catalyst before they reach their final form via a modified reaction path.

The adsorption of atoms, molecules and other species on the catalyst surface plays a decisive role in catalysis. The bond formed by adsorption must be just right, i.e. it must be neither too strong nor too weak [51]. If the bond is too strong, the surface may be blocked, and desorption may be hindered. This qualitative concept was defined in 1902 by the French chemist P. Sabatier and is a basic characteristic of heterogeneous catalysis [52]. Since this principle represents only a concept of ideal binding, no statement could be made about the binding energy or the maximum activity of the catalyst [53]. In 1916 the chemist I. Langmuir dealt with this problem and created a simple model for the adsorption of species on simple surfaces. I. Langmuir also believed that only a certain part of the catalyst surface can be responsible for the adsorption of atoms or molecules and that the activity of the surface is related to the arrangement and spacing of the atoms in the surface layer [54]. This assumption was further advanced in 1925 by H. S. Taylor, who described that a catalytic chemical reaction does not occur on the entire surface, but only on active sites of the catalyst. He also went further and described that the active sites would contain terraces, ledges, kinks, and empty spaces with different coordination numbers and contribute to a large extent to the catalytic activity [55].

Based on the Sabatier principle, A. A. Balandin introduced in 1969 for the first time a graphical representation for the catalytic activity, which he defined as so-called volcano plots [56]. With the volcano plots, the catalytic activity of different catalysts, especially the correlation between reaction energy and adsorption heat, can be displayed graphically in the simplified form [57]. The advantage of volcano plots was also recognized by the electrochemist S. Trasatti, who three years later presented the first volcano plot for the hydrogen evolution in acid solutions based on collected experimental data [58]. Trasatti's volcano plot continues to form the basis for the development and classification of novel heterogeneous catalysts for use in electrochemistry, such as PEM fuel cells.

## 2.2. PEM fuel cells

Due to the fact that the PEM fuel cell is an energy converter and the range ultimately depends only on the size of the hydrogen pressure storage, interest in the automotive sector is growing steadily. **Figure 2** shows a PEMFC system with peripherals and the hydrogen pressure storage tanks. The periphery supplies the fuel cell stack with preconditioned reactants, where hydrogen is injected from the pressure tank into the anode side, and the air is compressed from the environment by a compressor and directed to the cathode side of the cells. In contrast to the anode, which forms a closed volume, in the cathode, the unused air with the excess product water is fed directly into the exhaust gas. Since in practice an MEA only achieves an OCV voltage ofca 1 V and under load significantly less, several MEAs must be connected in series to form a stack. The enlarged section (**Figure 2**) shows in simplified form the series connection of several cells as it exists in a fuel cell system. Due to the series connection, system voltages of up to ~400 V can be easily achieved. The subsequent DC/DC or DC/AC converters then supply the vehicle electrical system as well as the battery and the power electronics of the e-machines.

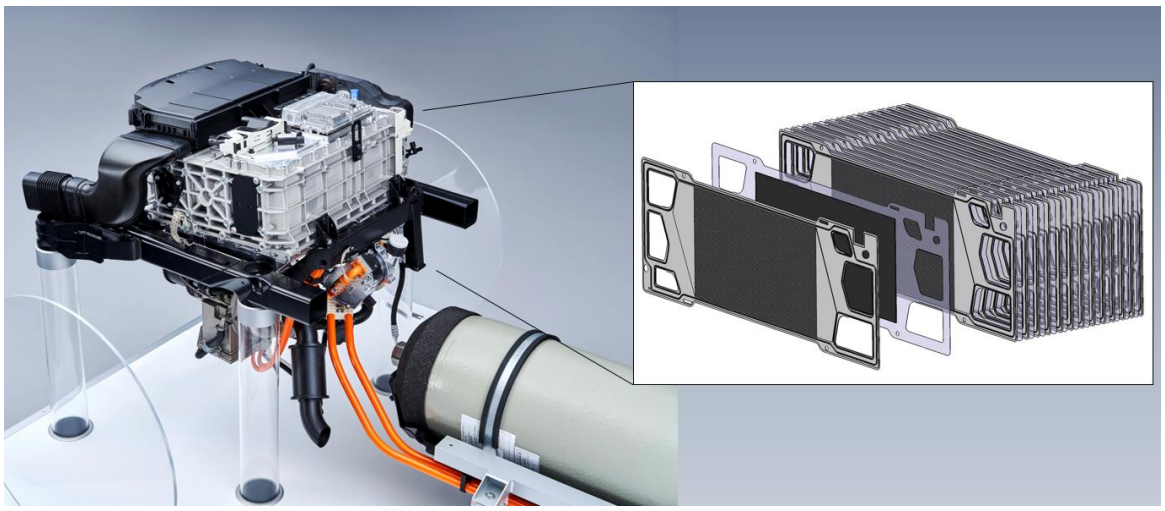

**Figure 2:** PEM fuel cell system with the simplified representation of the cells connected in series to achieve the required operating voltage.

### 2.2.1. Structure of a PEM fuel cell

The expression PEM fuel cell is the generic term for the type of fuel cell in which the polymer electrolyte membrane (PEM) is the proton-conducting Nafion® membrane separating the two electrodes as well as the reactants from each other. When considering a PEMFC single cell, the active region involved in the reaction is called the membrane electrode assembly (MEA). As the name implies, an MEA consists of the PEM and the anode and cathode catalyst layers (CL). Whereby the gas diffusion layers (GDL) as well as the gasket, which forms the outer frame, are often also an integral part of the MEA and are included in the definition. The MEA can be prepared either by hot pressing the individual layers (decal transfer method) or by direct application, e.g. by spraying the CL onto the membrane [59]. **Figure 3** shows a simplified cross-section through an MEA with the reactants $H_2$ and air, the protons $H^+$ and the output product water $H_2O$. The generated electrons flow via the flow fields (not shown here, for further details, see chapter 3.1.4) to the current collectors and to the electrical load. This principle allows the voltage and thus the output power to be increased as required.

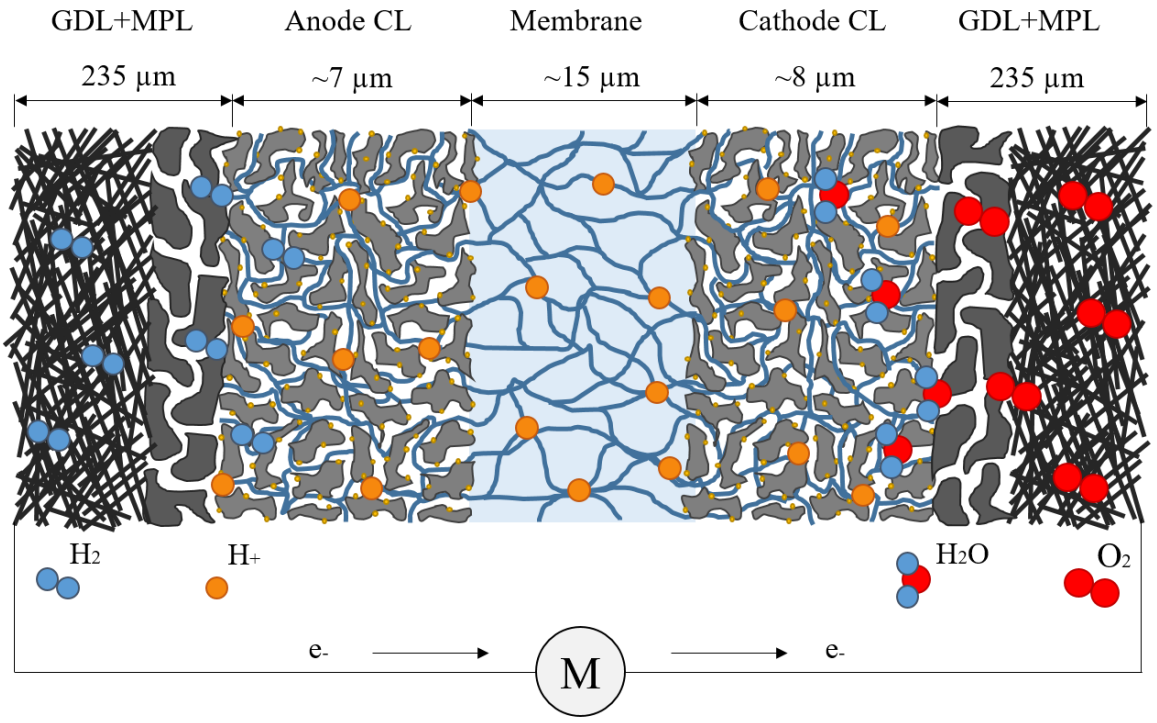


**Figure 3:** A simplified cross-section through an MEA showing the individual layers, as well as the reactants $H_2$ and air, the protons $H^+$ and the output product water $H_2O$.

If we now go through the individual layers from the outside to the inside, they can be divided as follows:

**Gas diffusion layer (GDL) + Microporous layer (MPL)**

The gas diffusion layer (GDL) forms the end of the MEA and is in direct contact with the flow field. Although the GDL is not involved in the electrochemical reaction, it serves several important functions. On the one hand, the GDL must distribute the reactants arriving via the flow fields as uniformly as possible over the active CL, whether in the flow field channel or below the bars. On the other hand, the GDL must provide sufficient flow paths for the removal of the product water, especially at the cathode, and ensure the electrical connection between the microporous layer (MPL) and the flow field. In order to achieve all these properties and also ensure sufficient mechanical stability, the GDL is made of highly porous carbon papers or structural fabrics. Here it should also be mentioned that depending on the GDL compression, the listed properties change. The MPL is usually an integral part of the GDL and is therefore often not mentioned. Due to the highly porous and strongly hydrophobic layer, the MPL supports the back transport of the product water, especially at higher current densities from the CL to the GDL [60]. In addition, similar to the GDL, the MPL supplies reactants to the CL and provides electrical conduction between the CL and the GDL.

**Catalyst layer (CL)**

The anode or cathode CL forms the reaction center where the reduction or oxidation of the reactants occurs. In simple terms, the catalyst lowers the activation energy and thus increases the speed of the electrochemical reaction. Here, it is not the quantity of the catalyst that is decisive, but much more its active surface and its catalytic activity. Other factors also influence the speed of the reaction. The electrochemical reactions themselves can only take place in the 3-phase boundary, where the catalyst, proton conduction, and reactants are all present at the same time. In this process, the $H^+$ protons can only flow through the ionomer proton conductors. The electrons $e^-$ can only flow through the electrically conductive materials, such as carbon and platinum, and the gases can only flow through the cavities in the porous carbon support material. Depending on the structure of the carbon support material and the ionomer loading in the CL, the gas pathways can be blocked by the product

water at high current densities, leading to a reduction in the conversion efficiency of the CL.

The most commonly used catalyst material in the PEM fuel cell is pure or alloyed platinum. With alloyed platinum, core-shell structures can be used to reduce the loading of the platinum or increase efficiency. One of the most common strategies is to put one or more layers of platinum on top of another material such as palladium, ruthenium or gold [61]. Typically, the catalyst particles have a size of less than 5 nm and are finely dispersed on a highly porous carbon support material, such as Vulcan XC-72, with a size of about 40 nm [59, 62]. However, metal-organic frameworks (MOF) are also becoming increasingly interesting due to their long-term stability and insensitivity to higher potentials [63]. Regardless of the support material, ionomer (usually Nafion®) must be incorporated into the catalyst composition during catalyst preparation or premixing. This is necessary to increase the active catalyst surface area and to ensure proton conduction throughout the CL. During production, the catalyst suspension is applied either to the decal substrate or directly to the membrane, e.g. by spraying [64]. In this process, the catalytically active layers should be as thin as possible and as thick as necessary. Typically, layer thicknesses of approx. 5-8 µm and platinum loadings of 0.2-1.0 mg/cm² are used.

**Polymer electrolyte membrane (PEM)**

The PEM at the center of each MEA forms the barrier between the anode and cathode. This means that the PEM must separate the reactants from each other and be electrically insulating while at the same time having a high proton conductivity. As with the ionomer introduced into the CL, the same proton transport mechanism occurs with the Nafion® PEM. The best-known approach to proton conductivity is the so-called cluster network model [65]. According to this model, proton transport occurs along with the sulfonic acid anions ($SO_3^-$). Due to the free volume in the polymer, the sulfonic acid anions form clusters and channel structures in which an interaction between $SO_3^-$ groups and the $H_2O$ dipoles takes place. This results in all the wetting water being in the hydrophilic clusters. The $H^+$ form hydronium complexes ($H_3O^+$) with the water present in the clusters, which can then be transported in the aqueous solution [66, 67]. Here it is clear that the proton conductivity is directly related to the stored water and that drying out the membrane leads to an increase in membrane resistance and thus to a decrease in reactant conversion and efficiency [65, 68]. Furthermore, the membrane resistance is directly related to the membrane thickness.

Nevertheless, to ensure sufficient mechanical stability, the membrane should be as thin as possible and as thick as necessary. Usually, PEMs with a thickness between 10-200 µm are used.

### 2.2.2. Theoretical cell potential

Considering the direct combustion of hydrogen, this energy is released in the form of heat. The reason for the exothermic reaction is the different energy levels, more precisely the enthalpy of reaction $\partial H$ between the two reactants $H_2$ and $O_2$ and the end product $H_2O$ [69]. The reaction can be simplified described as follows:

$$H_2 + \tfrac{1}{2}O_2 \rightarrow H_2O + \partial H \tag{2.2.1}$$

Since an ideal combustion process is described here and the higher heating value of hydrogen can be assumed, the enthalpy of reaction is $\partial H$ = -286 kJmol$^{-1}$ at 25 °C. In the PEMFC, the reaction takes place by means of silent combustion, and therefore, not the entire enthalpy can be converted into usable energy (e.g. electricity). The energy conversion leads to an increase in entropy $\partial S$ and thus to irreversible losses [69]. The amount of energy that can be used is equal to Gibbs' free energy and can be described by the following equation:

$$\partial G = \partial H - T \cdot \partial S \tag{2.2.2}$$

With an entropy $\partial S$ of -0.1633 kJmol$^{-1}$K$^{-1}$ and the assumption that the final product is in the liquid phase, a Gibbs' free energy of $\partial G$ = -237.34 kJmol$^{-1}$ can finally be used [69]. The Gibbs' free energy $\partial G$ corresponds to the molar electrical energy $-W_{m,elec}$ and can therefore be calculated with the number of electrons $n$, the Faraday's constant $F$ and the potential difference $E$:

$$\partial G = -W_{m,elec} = -n \cdot F \cdot E \tag{2.2.3}$$

With the number of electrons released by the oxidation reaction at the anode per hydrogen molecule $n$ = 2 and the constants $\partial G$ and $F$, the theoretically achievable cell voltage $E_0$ can be calculated:

$$E_0 = \frac{|\partial G|}{n \cdot F} = \frac{237.34\ kJ}{2 \cdot 96.485\ Asmol^{-1}} = 1.23\ V \tag{2.2.4}$$

### 2.2.3. Reaction kinetics

Since this work deals solely with PEM fuel cells, only the basic electrochemical reactions that are crucial at the anode and cathode (two-electrode arrangement) are explained in more detail here. The PEMFC works as an electrochemical converter so that the overall reaction, i.e., the redox reaction, can be divided between the anode and cathode reactions. The oxidation of hydrogen takes place at the anode, where 2 electrons are delivered to the consumer and protons are passed through the Nafion® electrolyte membrane to the cathode [59]:

$$H_2 \rightarrow 2H^+ + 2e^- \tag{2.2.5}$$

Simultaneously, the reduction of oxygen $O_2$, electrons $e^-$, and $H^+$ protons takes place at the cathode, as a product of which water $H_2O$ is formed:

$$\frac{1}{2}O_2 + 2H^+ + 2e^- \rightarrow H_2O \tag{2.2.6}$$

In this redox reaction, the reaction rate depends on the cathode because the oxygen reduction reaction (ORR) involves sequential and parallel steps and is much more sluggish than the hydrogen oxidation reaction (HOR).

Simplified, the redox reaction described above, in which the reaction rate depends on the Faradaic process, can be represented as follows [70]:

$$O_x + ne^- \underset{k_b}{\overset{k_f}{\leftrightarrows}} R_d \tag{2.2.7}$$

Where $O_x$ describes the oxidized form and $R_d$ the reduced form. The reaction rate depend on the forward and reverse oxidation reaction rates $k_f$ and $k_b$, which can be described as follows:

$$k_f = k_{0,f}\exp[\frac{-\alpha_{Rd}nFE}{RT}] \tag{2.2.8}$$

$$k_b = k_{0,b}\exp[\frac{\alpha_{O_x}nFE}{RT}] \tag{2.2.9}$$

Where $k_{0,f}$ and $k_{0,b}$ are the standard rate constants, $\alpha$ the transfer coefficient, $F$ the Faraday constant, and $E$ the potential. From the forward and reverse oxidation reaction rates, the net current can be calculated, which is the difference between the electrons released and consumed:

$$i = nF(k_f C_{O_x} - k_b C_{Rd}) \tag{2.2.10}$$

By substituting equations (2.2.8) and (2.2.9) into equation (2.2.10), the net current density is obtained:

$$i = nF\left\{k_{0,f}\, C_{O_x}\exp\left[\frac{-\alpha_{Rd}FE}{RT}\right] - k_{0,b}C_{Rd}\exp\left[\frac{\alpha_{O_x}FE}{RT}\right]\right\} \tag{2.2.11}$$

At the equilibrium potential $E_{rev}$, the reaction proceeds simultaneously in both directions, and the net current density here is zero. The rate of the reaction occurring at equilibrium is called the exchange current density $i_0$ and can be calculated as follows [70]:

$$i_0 = nFk_{0,f}C_{O_x}\exp\left[\frac{-\alpha_{Rd}FE_{eq}}{RT}\right] = nFk_{0,b}C_{Rd}\exp\left[\frac{\alpha_{O_x}FE_{eq}}{RT}\right] \tag{2.2.12}$$

Combining the two equations from 2.2.11 and 2.2.12 yields the Butler-Volmer equation, which is the cornerstone of electrochemical kinetics:

$$i = i_0 \left\{ \exp\left[\frac{-\alpha_{Rd} F(E - E_{eq})}{RT}\right] - \exp\left[\frac{\alpha_{O_x} F(E - E_{eq})}{RT}\right] \right\} \qquad (2.2.13)$$

The Butler-Volmer equation describes that the exchange current *i* generated by the electrochemical reaction increases exponentially with the activation overvoltage and depends directly on the potential difference $E$-$E_{eq}$.

## 2.3. Thermoelectric effect

The thermoelectric effect, also called the Peltier effect, refers to the reversible interaction between electricity and temperature. This interaction was first discovered by the French watchmaker Jean Peltier (1785-1845), who observed that when current flows through an existing conductor circuit made of two different metals, heat or cold is generated at the solder joints [71]. This effect occurs in electrothermal transducers, such as Peltier elements. When a current flow is applied, a temperature difference occurs on both sides of the Peltier element. The direction of the current flow determines which side of the Peltier element heats and which side cools. **Figure 4 (a)** shows a high-performance Peltier element that was used in the PET single cells (for more details, see chapter 4). The advantages of Peltier elements are obvious. The compact design, combined with the simultaneous ability to heat and cool, create new ways to control the temperature. The basic operating principle and internal structure of a Peltier element are shown in simplified form in **Figure 4 (b)**. If a voltage source is now applied to the two leads of the Peltier element, electrons flow from the conductive undoped material into the n- or p-doped material. Since the transfer of electrons is not readily possible due to the different energy levels between the doped and undoped materials, heat or cold is generated at the boundary of the two materials. In summary, the flowing electrons must assume a higher energy level as they enter the n-doped material and a lower energy level as they exit, resulting in cooling and heating, respectively. The same applies to the p-doped material only in the opposite direction [72]. Depending on the size of the Peltier element and the operating voltage, different numbers of semiconductors are connected in parallel or in series.

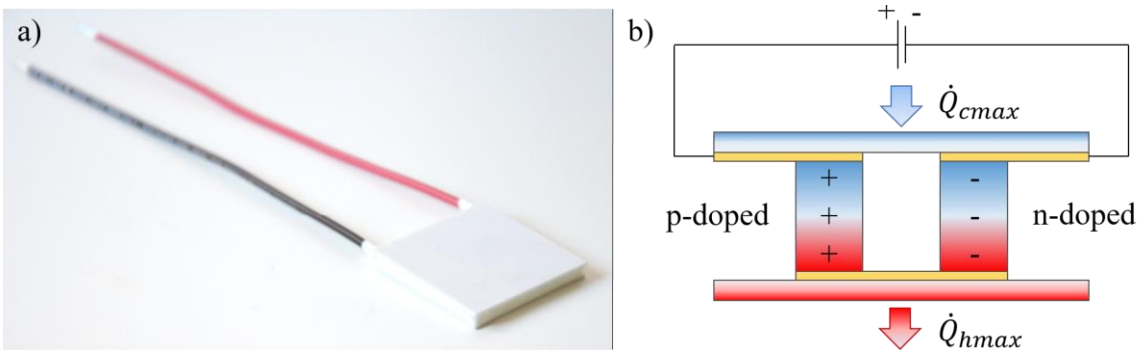


**Figure 4: (a)** High-performance Peltier element used in the PET single cell, and **(b)** its basic operating principle with a simplified representation of the internal structure.

The total electrical power $\dot{P}_{El}$ of a Peltier element can be calculated as follows [73]:

$$\dot{P}_{El} = \dot{Q}_{hmax} - \dot{Q}_{cmax} \tag{2.3.1}$$

With the total heating power $\dot{Q}_{hmax}$ and the maximum cooling capacity $\dot{Q}_{cmax}$, which in the optimum case can be described without losses by the heat transfer $\dot{Q}_{Peltier}$ caused by the Peltier effect:

$$\dot{Q}_{cmax} = \dot{Q}_{Peltier} = I \cdot \alpha_t \cdot T_c \tag{2.3.2}$$

With the temperature of the cold side $T_c$, the material-dependent thermal force $\alpha_t$ and the current $I$. Due to the ohmic resistance $R$ of the current-carrying materials, a Joule heating $\dot{Q}_J$ occurs on both sides of the Peltier element as a function of the current flow:

$$\dot{Q}_J = \frac{1}{2} \cdot I^2 \cdot R \tag{2.3.3}$$

In addition to Joule heating $\dot{Q}_J$, the heat transfer and thus the maximum cooling capacity $\dot{Q}_{Tc}$ is additionally reduced by the specific heat capacity $c$ of the Peltier element:

$$\dot{Q}_{\partial T} = c \cdot \partial T \tag{2.3.4}$$

If now all occurring losses are added, the real cooling capacity of a Peltier element can be calculated as follows:

$$\dot{Q}_{Tc} = \dot{Q}_{Peltier} - \dot{Q}_J - \dot{Q}_{\partial T} \tag{2.3.5}$$

Since the Joule heating $\dot{Q}_J$ increases quadratically and thus much faster than the heat transfer $\dot{Q}_{Peltier}$ with the current flow *I*, it can be seen here that the efficiency and thus the maximum cooling power $\dot{Q}_{Tc}$ depends mainly on the current flow. If the Peltier element is also used for heating, the losses $\dot{Q}_J$ and $\dot{Q}_{\partial T}$ add up, which in practice results in a heating capacity that is about 50 % higher than the cooling capacity.

# 3 Experimental

This chapter deals with the experimental part of the work. The first chapter describes the measurement hardware, such as the commercially available test bench, the cell hardware and the electrical measurement setup. In the second part, the measurement techniques for *in-* and *ex-situ* characterization are described. These techniques played an important role in determining performance changes during the stress test run and in determining degradation mechanisms after that.

## 3.1. Measurement setup

### 3.1.1. Test bench setup

The performance of a PEMFC depends primarily on the operating parameters. In this context, general parameters such as temperatures, pressures, stoichiometries or humidity of the reactants play a decisive role. Characterization of the PEMFC independent of the number of cells is therefore only possible with the help of a test bench. The test bench provides a precisely defined test environment and ensures that the reproducibility and comparability of different test cases are given. It is evident that besides the quality of the PEMFC, the control and measurement accuracy of the operating parameters is particularly important for the quality of the final measurement results. However, even if the measurement system is of a high standard, errors can often occur in the configuration of the cell hardware. A typical error that should not be underestimated is, for example, insufficient insulation of the gas supply lines. The so-called cold bridges cause water condensation, deviating operating parameters, and last but not least deterioration of performance. This is one of many examples of why the test setup, especially the interfaces between the test object and the test bench, is crucial for the generation of reproducible measurement data.

All measurements presented in this thesis were performed on a commercially available Horiba FuelCon test bench type C1000-LT (shown in **Figure 5**). Depending on the cell surface and thus the size of the test sample (TP50 or TP285, for more details, see chapter 3.1.4), there are different configuration levels of the same type of test bench. The various configuration levels differ mainly in the limiting characteristics of the test bench, such as the maximum possible reactant flows or the maximum possible load current. Since the work

deals with two cell sizes, the measurements were performed on two different configuration levels of the C1000-LT test benches.


**Figure 5:** Two Horiba FuelCon test benches of the type Evaluator C1000-LT.

The C1000-LT type test benches consist of a front and a rear part. The front part contains the test chamber and, below that, the electrical components, such as the load, the power supply and the power contactor. The test chamber forms a closed unit in which a permanent air exchange takes place. The air is systematically extracted in the test chamber and guided past the safety $H_2$- and CO-sensor. This is necessary in order to be able to react quickly in the event of a fault, such as an unintentional hydrogen leakage, and to shut down the test item in time. In the rear part, the whole periphery is installed, like the components for the conditioning of the gases, the control electronics and the fuse box of the test bench. All components that are in contact with gases or liquids, such as the humidifiers, gas lines or valves, are made of v4a stainless steel. **Figure 6** shows a simplified technical representation of the C1000-LT test bench. For a better overview, some valves, pipelines or other peripherals are not shown or are very simplified in this representation. The test chamber with the

connected fuel cell test item is shown in the middle. For easier identification of the components, all kinds of valves are shown in green, components that work with water in blue and different electric heaters in red. The detailed description of the numbered elements in **Figure 6** is given in **Table 1**.

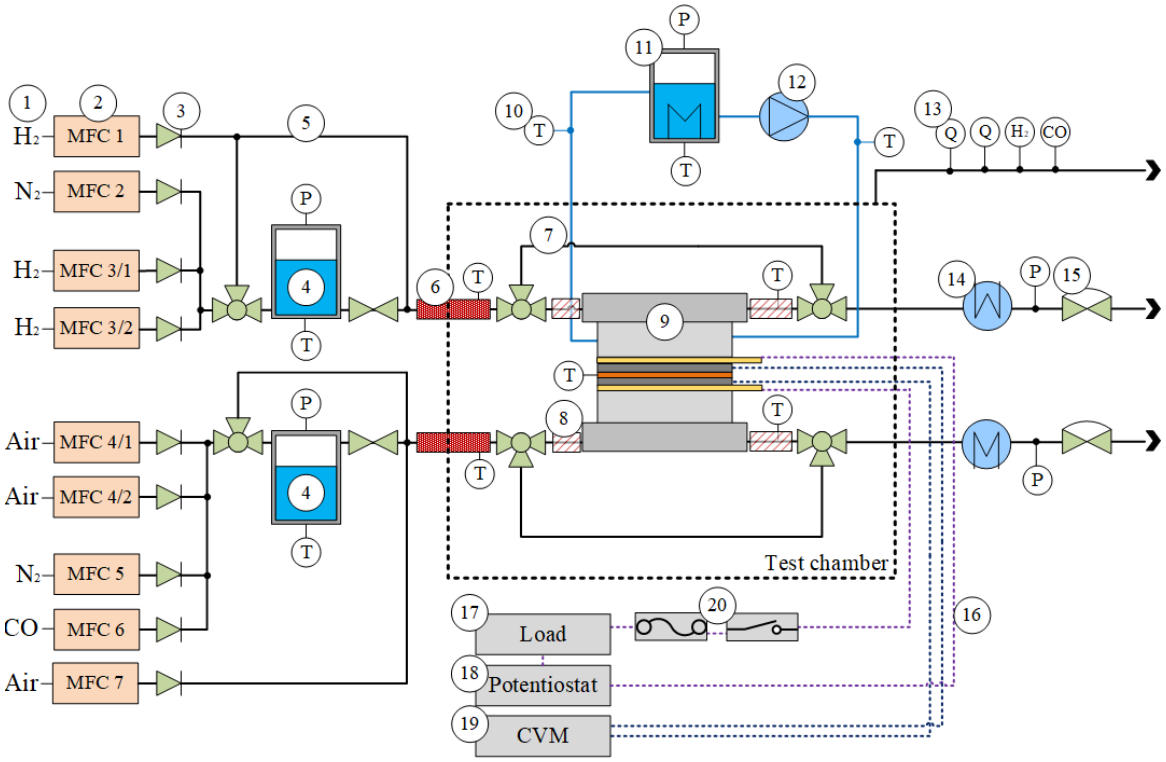


**Figure 6:** Simplified technical drawing of test bench type C1000-LT.

**Table 1:** Detailed description of the numbered components in **Figure 6**. Please note that the working ranges of the individual components, as well as the tolerance specifications, are provided by the test bench manufacturer.

| Nr. | Description of the corresponding component |
|---|---|
| **1** | Supply lines of the respective gases to the test bench. The gases are provided by the infrastructure of the test facility and are supplied, with the exception of air, from a pressure tank. All gases with the exception of the air have a purity of at least 5.0, which means that the gases used here contain a minimum content of 99.999 % pure gas. The air is compressed by an oil-free compressor and cleaned in several stages. All gases are provided at a pressure level between 500-700 kPa. |

| Nr. | Description of the corresponding component |
|---|---|
| **2** | The mass flow controllers (MFC) measure and control the flow of the gases. The extension of the control range of the $H_2$ and airflow is achieved by a twin-flow cascading (marked as MFC 3/1 or 3/2). Using this principle, the flow control range can be extended from 50 to 2500. This allows setting both very low and very high flows. Depending on the configuration level of the test bench, flows of 0-83.3 or 0-333.3 $cm^3/s$ $H_2$ on the anode and 0-333.3 $cm^3/s$ or 0-1666.6 $cm^3/s$ air on the cathode can be set with an accuracy of ±0.2 % (related to the working range of the respective MFC)[i]. |
| **3** | Since the MFC is sensitive to moisture, a non-return valve is installed after each MFC to prevent the gases from flowing back in case of a fault. |
| **4** | The gases are humidified to the desired dew point by a bubbler-humidifier. This humidification system regulates the dew point of the gas via the water temperature and is therefore very accurate within a working range of 35-90 °C with a control accuracy of ±1 K[i]. However, the water temperature can only be actively increased by means of the jacket heating. To increase the dynamics of the humidifier, this system is therefore often combined with a dry gas bypass (see point 5). |
| **5** | Dry gas bypass with which the gas flow of the three $H_2$ MFCs (3/1, 3/2 and 1) can be mixed on the anode side. This allows a dew point range of <10-90 °C to be covered dynamically. |
| **6** | The gases can be heatedvia the inlet heating hoses, to a temperature of 40-180 °C. Since the heating hoses are very sluggish, the temperature is usually set once before the test run begins. |
| **7** | The test item bypass is used for the defined isolation of the test item from the test bench environment. |
| **8** | Transition heating to avoid cold bridges and the condensation of water. As with the heating hoses, the temperature can be set variably between 40-120 °C. |

| Nr. | Description of the corresponding component |
|---|---|
| **9** | Fuel cell test item (more details in chapter 3.1.4) with one or more stacked cells. |
| **10** | A temperature measuring point which measures the temperature by means of a resistive sensor (usually a Pt100 sensor). Other measuring points have the following abbreviation:<br>• P for pressure measurement.<br>• Q for measuring the flow velocity of the exhaust air.<br>• $H_2$ or CO for the measurement of the hydrogen or carbon monoxide concentration in the circulating air. |
| **11** | Temperature control and balancing tank of the cooling circuit. This can be both actively heated and cooled in a temperature range between 35-105 °C. Water temperatures above the boiling point can only be reached by applying additional pressure in the cooling circuit. |
| **12** | Water pump to control the coolant flow. On the C1000-LT series test benches, a coolant flow between 25-166.7 $cm^3/s$ can be set with an accuracy of 2 %[i]. |
| **13** | Safety sensors for monitoring the test chamber exhaust air. Since all sensors have to switch off the test bench as well as the fuel cell test item in the case of failure, they are designed according to SIL Level 2 (probability of dangerous failure per hour ($\geq 10^{-7}$ to $<10^{-6}$) [74]. |
| **14** | To dehumidify and cool down the residual gases, heat exchangers and condensers are connected in series in both exhaust lines. |
| **15** | Pneumatically controlled membrane pressure control valve for setting a working pressure between 110-300 kPa with control stability of ±5 kPa[i]. |
| **16** | Load cable and sense cable for the electrical connection between test bench load and fuel cell test item. |

| Nr. | Description of the corresponding component |
|---|---|
| **17** | Water-cooled electronic load for adjusting the working current. Depending on the number of load modules, up to 1000 A current or 3 kW electrical power can be drawn from the fuel cell test item. With the integrated zero-volt option, the voltage drop caused by the fuse or relay (see point 20) can be compensated, and voltages around 0 V can be adjusted for a single cell. Depending on the working range, which is automatically adjusted by the load (0-22 A or 0-≤1000 A) a maximum accuracy of ±0.1 % can be achieved[i]. |
| **18** | Potentiostat for applying a defined voltage or current to the fuel cell test item. |
| **19** | Cell Voltage Monitoring (CVM) for monitoring and measuring the single-cell voltage with an accuracy of ±0.08 % (referred to as the measured value). |
| **20** | Load contactor and fuse to unload the fuel cell test item in the case of a failure. |

To guarantee a constant measuring quality, all sensors installed in the test bench are maintained and adjusted yearly. This yearly maintenance is especially important to detect any drift of the sensors at an early stage.

### 3.1.2. Electrical setup for the cell characterization

Analogous to the standard test bench setup described in chapter 3.1.1, the test bench used in this work with the TP50 cell hardware was equipped with an EIS capable measuring device. **Figure 7** shows a simplified technical representation of the electrical measurement setup with the TP50 cell hardware, the TrueData-EIS impedance spectrum analyzer (ISA) (**Figure 7 (a)**) and the potentiostat (**Figure 7 (b)**). The TrueData-EIS ISA works here simultaneously as a load module and impedance measuring device and is directly connected in series with the internal potentiostat. The advantages of such a system built into the test bench are obvious: On the one hand, the measuring system is matched to the individual components, i.e. all internal resistances or capacitances are taken into account when calculating the impedance. Furthermore, the measuring system can be controlled by FuelCon software and automated by script without additional effort. However, this system also has

[i] The technical specifications are provided by test rig manufacturer Horiba FuelCon.

disadvantages. A major one is that the impedance measurement can only be performed in the galvanostatic mode. This means that only the current can be impressed as a sine wave and measurements in partially inerted mode ($H_2$ - anode/$N_2$ - cathode) are not possible. Therefore, the impedance of a fuel cell can only be measured during "running operation", i.e. only with $H_2$ on the anode and air on the cathode. The load cables with a cable surface of 50 mm² (**Figure 7 (c)**) as well as the sense cables of the TrueData EIS ISA (**Figure 7 (d)**) are twisted up to the PEMFC test item. This significantly reduces the inductive components in the higher frequency range (>2 kHz) and increases the accuracy of the measurement results. The TrueData EIS ISA can imprint frequencies between 200 µHz and 100 kHz with a maximum current amplitude of 2.5 A. This allows an impedance range between 0.1 mΩ and 15 Ω to be covered with an impedance accuracy of ±1 %. The additional potentiostat allows currents and voltages of a maximum 150 A and 10 V to be impressed on the PEMFC test item. This enables CV measurements which are described in detail in chapter 3.2.2.

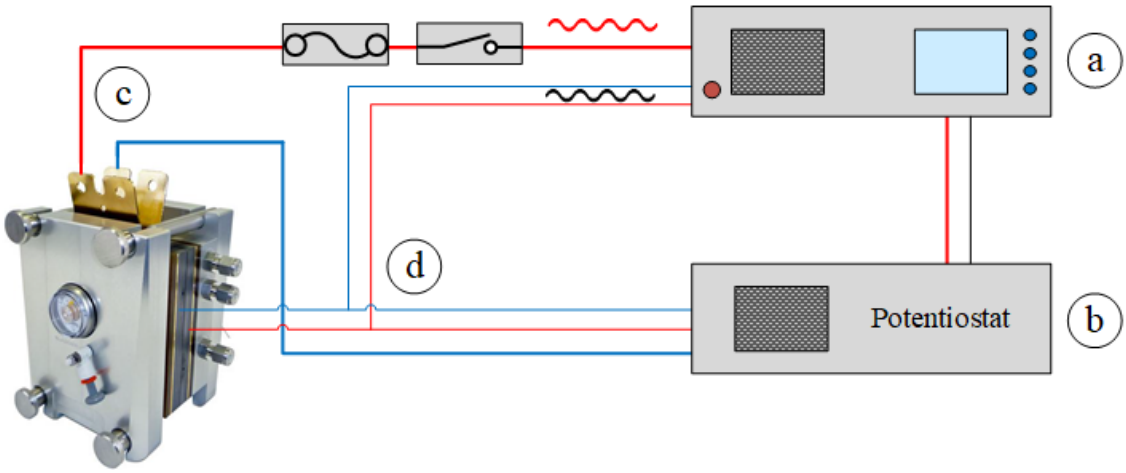


**Figure 7: (a)** Simplified technical representation of the electrical measurement setup used on the TP50 cell with the load cables, **(b)** the sense cables, **(c)** the TrueData-EIS impedance spectrum analyzer and **(d)** the potentiostat.

In contrast to the test bench and TP50 cell configuration, the TP285 cell hardware used a completely different measurement hardware concept for the impedance measurements. While in the TP50 configuration, the impedance response was tapped directly via the sensor cables and evaluated via the TrueData EIS ISA, the TP285 cell hardware used a current scan shunt board from the company S++®, which was directly built into the cell hardware.

The main advantage of this setup with the current scan shunt board is that up to 612 measurement points can be measured over the active area of the MEA. A further advantage is that with this cell configuration, not only the impedance response can be tapped via the individual measuring points, but also the current flow and local temperature can be measured and evaluated independently. This allows a comparison between the current density and the impedance behavior over the active surface of the MEA. **Figure 8 (a)** shows the current scan shunt board with the detailed functional description of one measuring point. To calculate the impedance, the directly measured voltage $U_1$, which corresponds to the local voltage on the monopolar plate, is used (**Figure 8 (b)**). This voltage is tapped with a separate connection at the current scan shunt board and led to the electrochemical workstation (more about this in the further course of the chapter). The current flowing through each measuring point can be calculated relatively easily using the Ohm's law. With the known shunt resistance (**Figure 8 (c)**) and the voltage drop between $U_1$ and $U_2$, the current $I_n$ can be calculated as follows:

$$I_n = \frac{\partial U}{R} \tag{3.1.1}$$

The same applies to the determination of temperature (**Figure 8 (d)**). Here a constant current is used, and the voltage drop across the resistive temperature sensor is determined. In a further step, the measured voltage drop of the shunt resistor and the resistive temperature sensor is digitized via the multiplexer and the analog/digital converter (A/D converter) and transmitted to the measuring computer via USB interface (**Figure 8 (e)**).

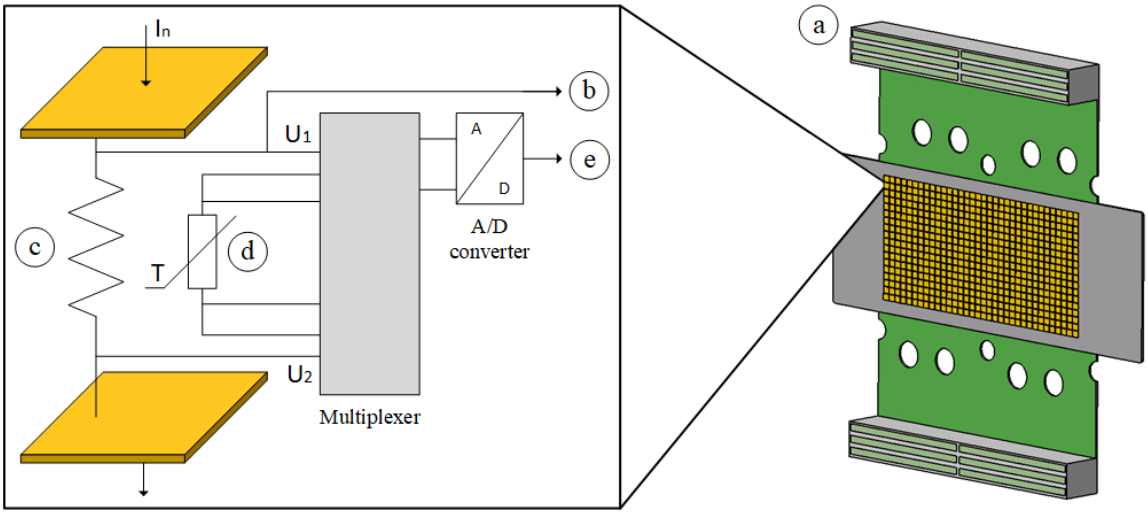


**Figure 8: (a)** Simplified CAD (Computer-Aided Design) representation of the current scan shunt board from the company S++® with the detailed magnification of one measuring point: **(b)** The separately tapped input voltage of each measuring point $U_1$, which also corresponds to the local impedance behavior, **(c)** the shunt resistor and **(d)** the resistive temperature sensor, with which the current and temperature can be read out in digital form via **(e)** the USB interface.

As described above, theoretically, up to 612 voltages $U_{1\text{-}n}$ and impedance responses can be tapped and evaluated. However, the measurement technology required for this would be practically unaffordable, and the number of measurement lines would be unmanageable. Furthermore, since the measuring points are very close to each other and the voltage response is evaluated here, the relative lateral influence would be relatively high if too many measuring points were used, which would lead to a falsification of the measurement result. Therefore, in this thesis, the measurement points were reduced to 46 and distributed evenly over the active surface, which significantly improved the handling of the measuring system. **Figure 9** shows the top view of the current scan shunt board with the red-framed active surface area of the MEA and the measuring points used in this work, displayed in different colors.

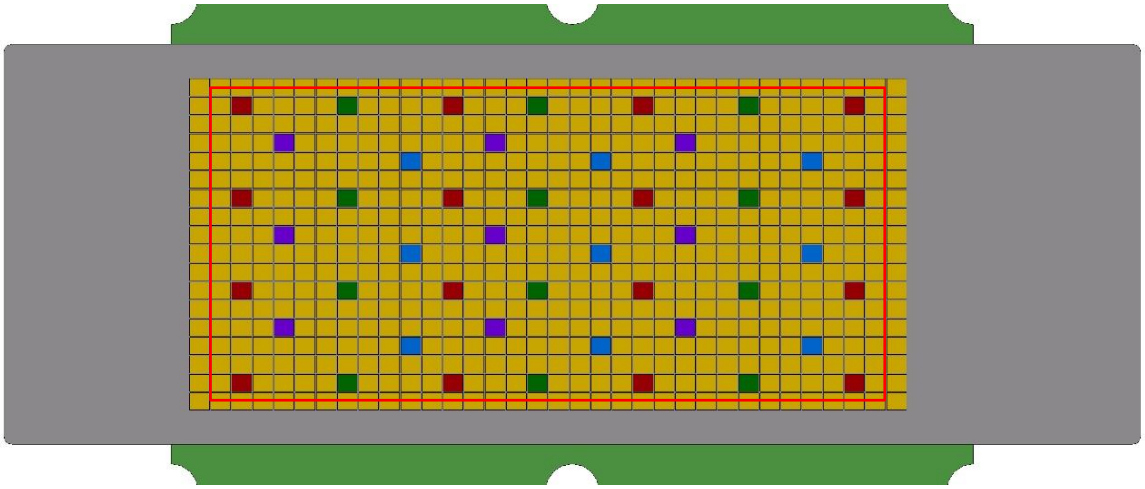

**Figure 9:** The top view of the current scan shunt board from the company S++® with the red-framed active surface of the MEA. The measuring points used in this thesis are colored and divided into 4 measuring groups (red, violet, green and blue), which are individually switched through the multiplexer to the impedance evaluation unit.

Since not all measuring points can be recorded and evaluated at the same time, they are divided into groups. Each color (red, violet, green and blue) represents a measuring group with a maximum of 16 measuring channels, which are individually switched to the impedance evaluation unit by the multiplexer. This means that an impedance measurement must be repeated four times, and the multiplexer automatically switches to a different measurement channel group with each cycle. **Figure 10** shows the complete electrical measurement setup with commercial TP285 cell hardware and the current scan shunt board. The detailed description of the numbered components in **Figure 10** is given in **Table 2**.

As described above, the current scan shunt board is installed directly into the TP285 cell hardware between the cathode monopolar plate and the cathode current collector. The TP285 cell unit is connected in parallel to two loads. The main load, which draws up to 99 % of the current, is the internally installed load of the test bench manufacturer FuelCon (see chapter 3.1.1). The secondary load is used to impress the sinusoidal current and can take a maximum of 10 A from the main current. In other words, if impedance measurements are made at an operating point of 600 A, for example, 590 A are drawn from the main load and 10 A from the secondary load. The secondary current is then modulated with a defined current amplitude and frequency. Since the entire measurement setup harmonizes with each other, the test bench works as the “master” and the rest of the measurement equipment as a “slave”. This means that the test procedure is started directly at the test bench and controls

the additional measuring equipment via software trigger. In parallel to this, another automation script runs on the additional measuring computer, which sets the measuring parameters, such as the secondary current, the current amplitude, the frequency ranges, etc., and names and sorts the measuring data.

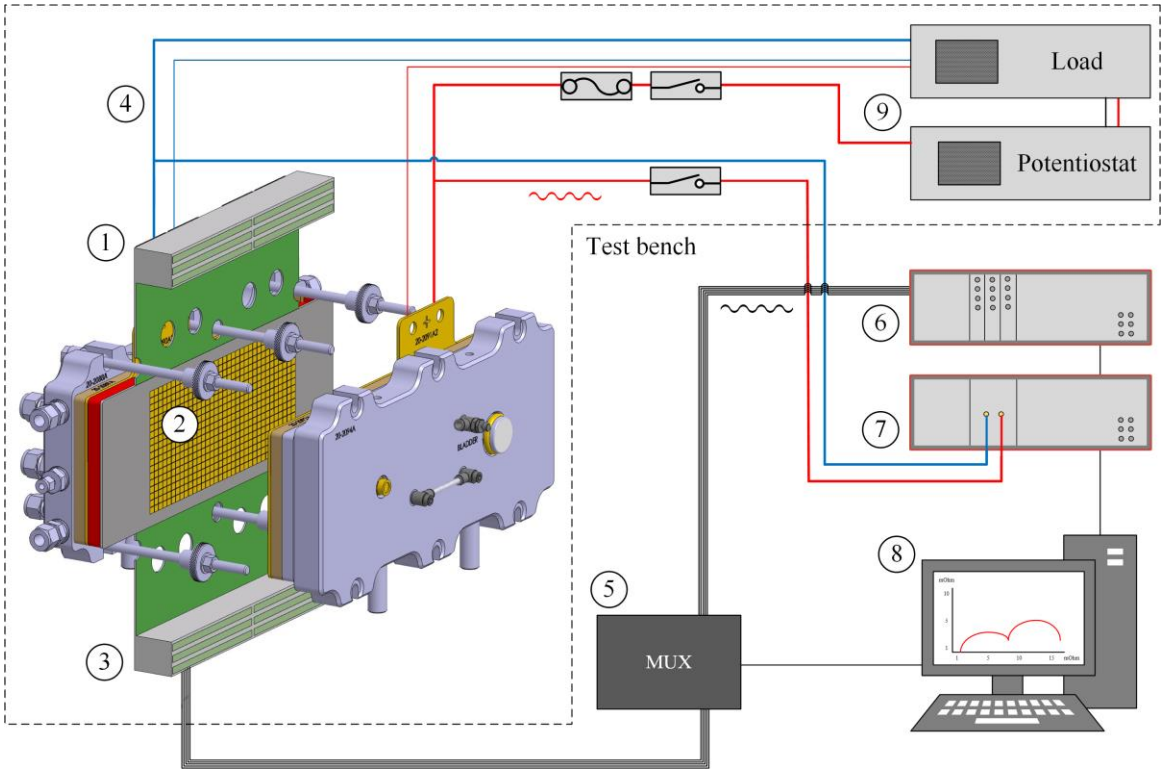


**Figure 10:** Simplified representation of the complete electrical measurement setup with commercial TP285 cell hardware and the built-in current scan shunt board, which can be used to measure the local impedance, current density distribution and temperature distribution over the active area of the MEA.

**Table 2:** Detailed description of the numbered components in **Figure 10**. Please note that the specified measuring tolerances of the individual electrical components were provided by the respective manufacturers.

| No. | Description of the corresponding component |
|---|---|
| **1** | Current scan shunt board of the company S++® with 612 measuring points, which is installed between the cathode monopolar plate (part of the MEA "sandwich structure", more on this in chapter 3.1.4) and the cathode current collector. |
| **2** | USB interface and connectors for measuring the current, temperature and voltage response of the individual measuring points. |
| **3** | 300 mm² load cables, which conduct the main current to the test bench load and the partial current to the secondary load. The current for the impedance measurement is modulated by the secondary load. |
| **4** | Digital multiplexer from the company National Instruments, which automatically switches the measuring groups for the impedance measurement. The multiplexer is controlled by an additional measuring computer. |
| **5** | The 16-channel electrochemical workstation Zahner Zennium X from the company ZAHNER-elektrik GmbH & Co. KG. With this electrochemical station, potentiostatic impedance responses in a frequency range from 10 µHz to 12 MHz can be evaluated with an accuracy <0.0025 %[ii]. |
| **6** | The Zahner PP241 4-quadrant power potentiostat, which was used in this setup as secondary load and potentiostat for the modulation of the current. The potentiostat can tap a maximum of 40 A from the main current and modulate it with a maximum amplitude of up to 10 A. Thus frequencies in the range of 10 µHz up to 200 kHz are possible. The adjustment accuracy of the current is ±0.25 %[ii]. |

[ii] The technical specifications are provided by the measuring equipment manufacturer ZAHNER-elektrik GmbH & Co. KG.

| No. | Description of the corresponding component |
|---|---|
| **7** | Additional measuring computer, which controls the electrochemical workstation, the secondary load and the multiplexer. The computer works as a “slave” and is controlled by the test bench via software trigger. |
| **8** | Test bench main load package to adjust the main current. For further details, see **Table 1**, points 17 and 18. |

### 3.1.3. Software

The test stand is controlled by a software environment called "Testwork", which was specially developed by the test stand manufacturer. The user interface consists of several windows. The main window, which is displayed in the form of a simplified technical piping and instrumentation diagram (P&ID), is called the cockpit (**Figure 11**). The cockpit is separated into color-coordinated areas and can be divided as follows: Under **(a)** the gases can be released, and their flow can be adjusted, under **(b)** the dew points, gas temperatures, and the heat tracing can be set, **(c)** shows the test item, the characteristics and the pressure in the compression plate, under **(d)** the pressures in the two gas paths can be adjusted, **(e)** describes the load and **(f)** the complete cooling circuit where the coolant flow and the test item temperature can be adjusted. The circled abbreviations such as F1040 describe the so-called TAG variables, which are used in the Siemens SIMATIC control system for data processing, calculation and control of the test bench system. The light blue or gray numeric areas, usually in pairs, represent the set point or actual value of the respective parameter. Here the individual operating parameters can be set and monitored.

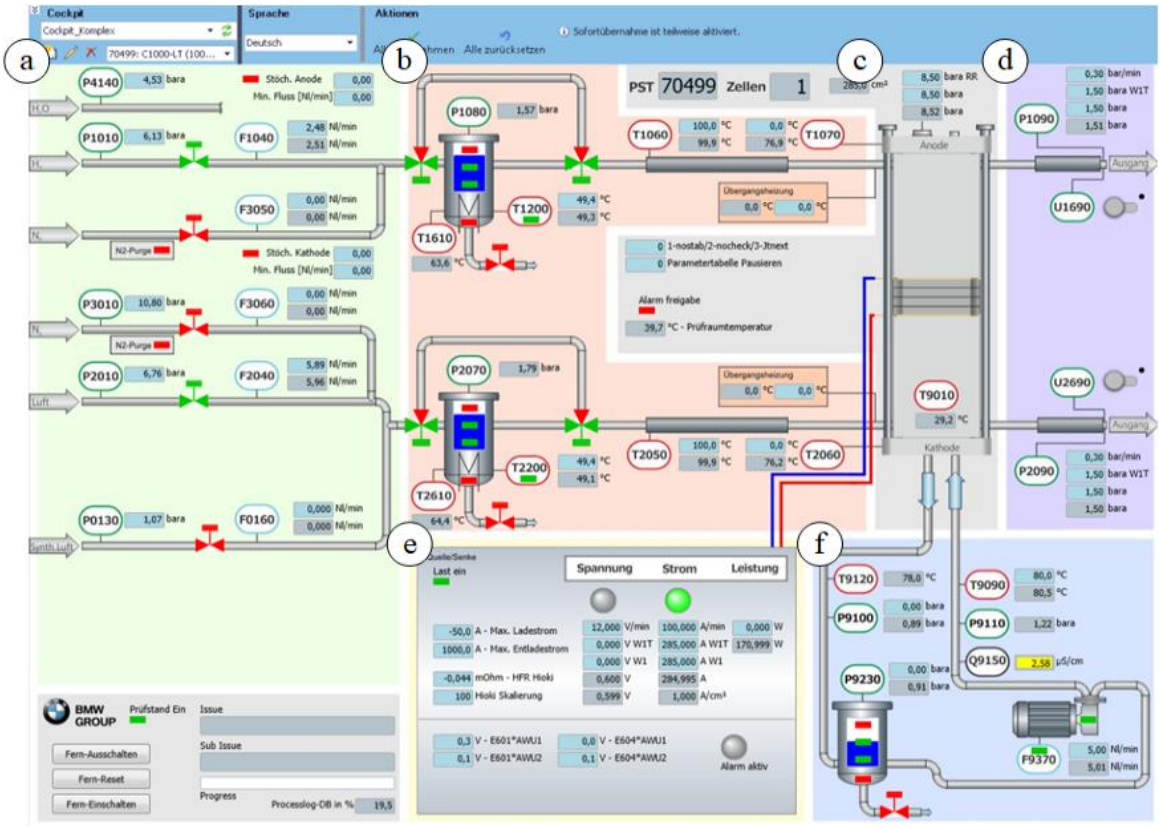


**Figure 11:** Testwork main window for the manual control of the test item's operating parameters, divided into color-coordinated areas.

Since only the essential operating parameters are displayed in the main window, all TAG variables and constants available on the test bench can be searched and changed in the so-called TAG manager (see **Figure 12 (a)**). This includes the set point values of the operating parameters, the alarm values or also the control parameters of the individual controllers. In the trend-viewer window, the operating parameters or other TAG variables can be evaluated live or historically in a variable timeline (see **Figure 12 (b)**). The advantage of this window is obvious. Due to the graphical and historical representation, both test bench and test item anomalies can be evaluated and corrected quickly. All TAG variables that can be changed manually in the user interface or in TAG manager can also be used automatically via script. The scripts are described in the programming language Visual Basic for Applications (VBA) and can be started and stopped in the script manager (see **Figure 12 (c)**). In this way many test procedures can be automated, such as the experiments in this thesis. The state or current action of the running script can be tracked in the script monitor (see **Figure 12 (d)**). This output is often used for error analysis of newly developed scripts or to determine the current script runtime.

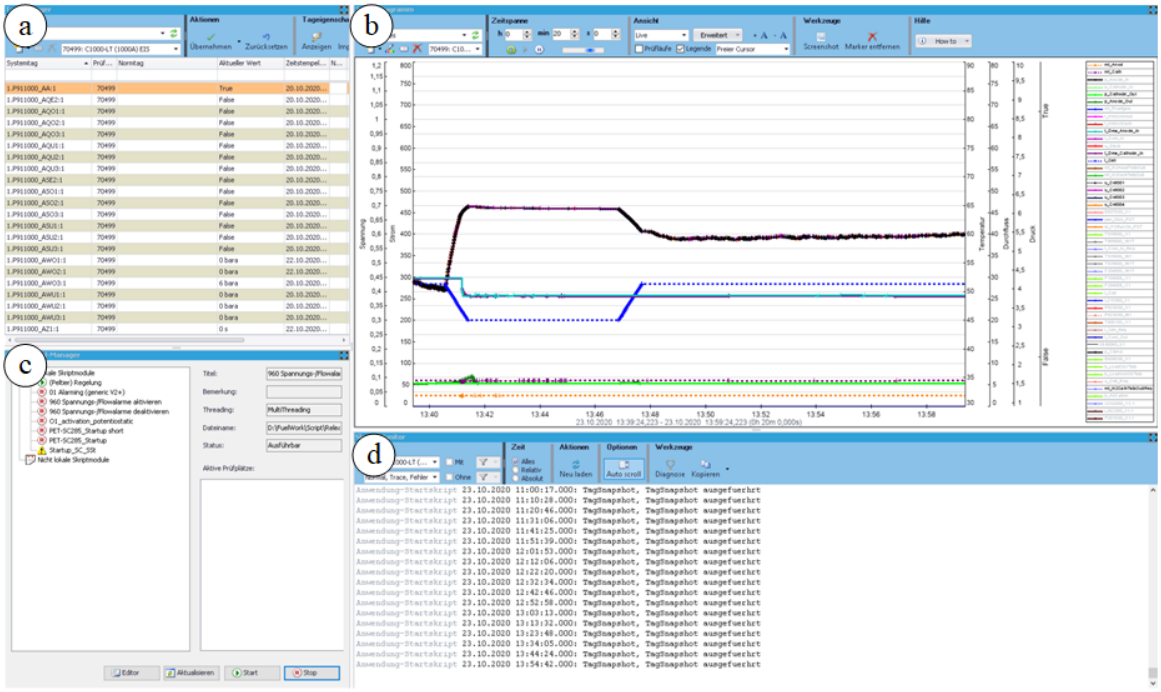


**Figure 12: (a)** Additional Testwork views with the TAG manager, **(b)** the trend-viewer for quick analysis of current and historical measurement data, **(c)** the script manager for starting and stopping automated testing procedures and **(d)** the script monitor.

### 3.1.4. Tandem Technologies TP cell hardware

For the characterization of PEM fuel cells on a C1000-LT test bench, whether single cell or stack (≥2 cells), cell hardware is required. The hardware primarily serves as a stable and sealed housing and forms the interface between the test bench and the PEMFC. In this thesis, two different sizes of cell hardware were used. Both are based on the commercially available TP unit of the company Tandem Technologies Ltd. In the following, the functionality of the two basic hardware TP50 and TP285 is explained.

The small size hardware with the designation TP50 can be used for MEA with a maximum active area size of 50 cm² and is particularly suitable for the characterization of single cells (see **Figure 13 (a)**). Due to their small size (compared to an automotive-sized cell with ~285 cm²), the MEAs are much more cost-effective and the handling correspondingly easier, which in turn leads to a shortened assembly time of the single cell. The larger of the two hardware is designated TP285 and can accommodate an MEA with a size of 285 cm² (see **Figure 13 (b)**). Although the preparation of the cell hardware is more complex, it offers the advantage that the same MEA that is used in the automotive application can also

be characterized on the test bench. As a result, the test bench's measurement results are largely comparable with those in real applications.

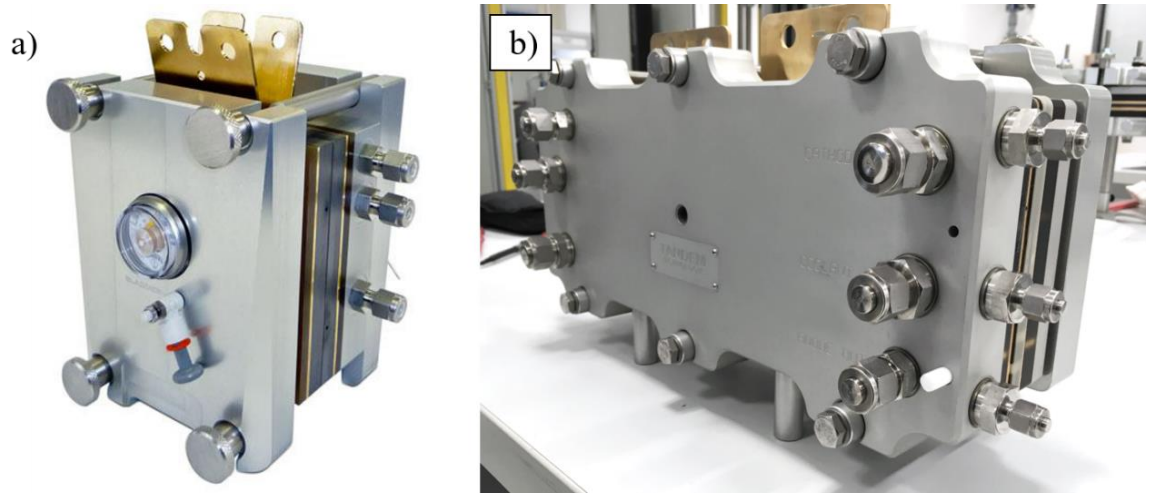


**Figure 13: (a)** Commercially available TP units from the company Tandem Technologies Ltd, including the TP50, which can accommodate MEAs with a maximum active surface area of 50 cm², and **(b)** the TP285, which can accommodate automotive-size MEAs with a size of 285 cm².

Since both cell hardware sizes are similar in terms of technical design, only the exploded view of the CAD (Computer-Aided Design) model of the TP285 is shown in **Figure 14** and subsequently explained in detail in **Table 3**. Here it is immediately apparent that the components of the cell hardware resemble a stacked structure. The advantage of this design is that the components are stacked during assembly and then compressed to a defined pressure using the compression plate. In the compression plate, the air pressure of the pneumatic pressure pads is permanently controlled by the test bench and can be changed flexibly during the test run. In this way a defined and homogeneous compression of the active surface area can be achieved even at fluctuating operating temperatures. A further advantage of this stacked structure is that the individual components and thus the internal structure of the cell hardware can be modified as desired. This allows improving of the cell hardware, as described in the further course of this thesis (see chapter 4.1 and 4.2).

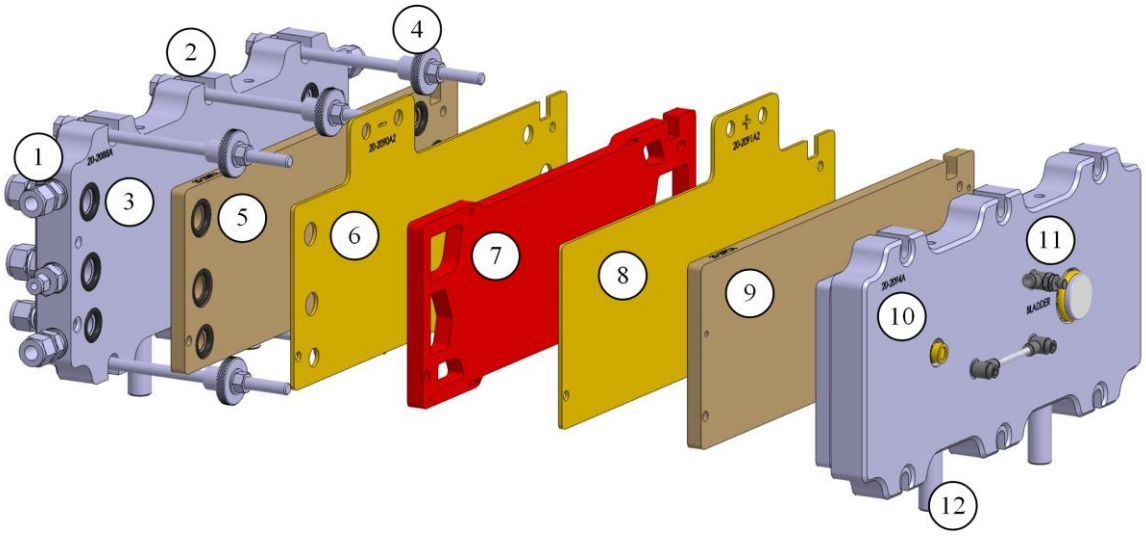


**Figure 14:** Detailed view of the CAD (Computer-Aided Design) model of the TP285 cell hardware. The numbers for the individual cell components are explained in detail in **Table 3**.

**Table 3:** Detailed description of the numbered cell components in **Figure 14**.

| No. | Description of the corresponding component |
|---|---|
| **1** | Screw-in units for gas and cooling water connections from Swagelok®. The screw-in units are made of v4a stainless steel and form the direct interface between the cell hardware and the test bench. Since the screw-in elements represent a cold bridge, they must be insulated or heated to prevent water condensation. |
| **2** | Massive end plate made of aluminum, which primarily ensures the stability and cohesion of the individual components. |
| **3** | O-rings for sealing the gas and water channels made of Viton®. |
| **4** | Tie rods for clamping the cell components and the MEA. |
| **5** | Anode insulation panel made of Ultem™ Resin 1000 with gas passages that ensure electrical and thermal insulation from the end plate. |
| **6** | Anode current collector made of gold-plated copper with gas passages and direct connection for the load cable. |

| No. | Description of the corresponding component |
|---|---|
| **7** | "Sandwich structure" of the MEA and the anode and cathode monopolar plates. In the TP285 cell hardware, MEAs with the A3 design level are characterized. |
| **8** | Cathode current collector made of gold-plated copper with direct connection for the load cable. |
| **9** | Cathode insulation plate, made of Ultem™ Resin 1000. |
| **10** | Compression plate made of aluminum with integrated pneumatic pressure pads. With the gas pressure, the force and thus the compression of the MEA can be adjusted. Maximum pressure of 300 kPa can be set here. |
| **11** | Gas connection and pressure gauge of the compression plate. |
| **12** | Feet for lateral positioning of the cell hardware. |

Apart from the size of the active area, the main difference between the two cell sizes is the "sandwich structure" of the MEA and the anode and monopolar cathode plates described in **Table 3 -** point 7. **Figure 15** shows the "sandwich structure" of the TP50 cell hardware with the two monopolar plates per electrode, the MEA and the brownish gaskets. The flow fields as well as the coolant channels, which regulate the cell temperature with the help of the test bench cooling water, are integrated into the monopolar graphite plates and are considered an essential part of the cell hardware. More precisely, two monopolar plates are stacked per electrode, one of which contains the gas channels for the gas supply of the MEA (see **Figure 15 (b)**) and the other the coolant channels for adjusting the cell temperature using cooling water (see **Figure 15 (a)**). To get as close as possible to the real application, a flow field with low-pressure drop was used in this thesis. The flow field consists of 14 parallel channels with an area of 0.2544 mm² per channel. In contrast to the automotive size cell, the compression of the GDL is adjusted by means of a glass fiber gasket (see **Figure 15 (c)**). In this way, an exact compression of the two GDLs can be achieved, which in this thesis was ~20 % for all tested MEAs.

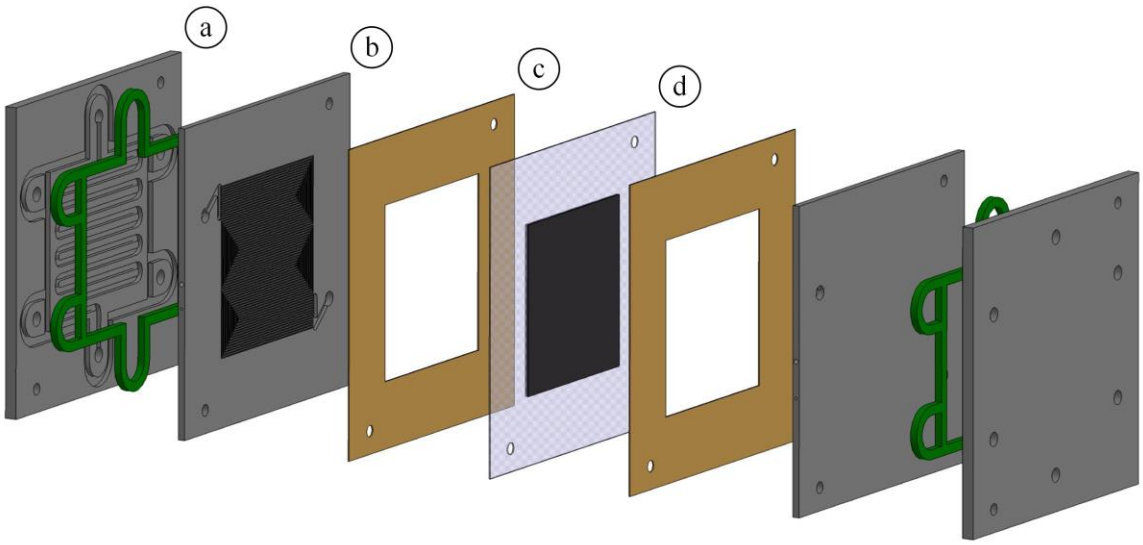


**Figure 15: (a)** Detailed view of the CAD (Computer-Aided Design) model of the "sandwich structure" with the graphite monopolar plates with integrated cooling channels, **(b)** the monopolar graphite plates with integrated gas channels, **(c)** the glass fiber gaskets ensuring a correct compression of the GDLs and **(d)** the membrane electrode assembly (MEA).

In the automotive-sized TP285 cell hardware, the anode and monopolar cathode plates (see **Figure 16 (a, c)**) are made of thin stainless steel. In contrast to the TP50, where the channels are milled into the monopolar graphite plates, the shape and thus the gas and water channels of the automotive-sized monopolar plates are created by a special stamping and welding process. Both the gas channels and the cooling channels are incorporated into the metallic monopolar plate. This means that only one plate is used per electrode side. When the "sandwich structure" of monopolar plates and MEA (see **Figure 16**) is built up, a specific deformation of the monopolar plates occurs during compression. As a consequence, the monopolar plates must be replaced with each new configuration of the cell hardware. The compression of the GDL and the sealing surfaces of the monopolar plates is achieved by the adjusted gas pressure in the pneumatic pressure pads of the previously described cell hardware compression plate. A pressure of ~804 kPa is typically set for this cell design, which corresponds to a vertical force of 32 kN.

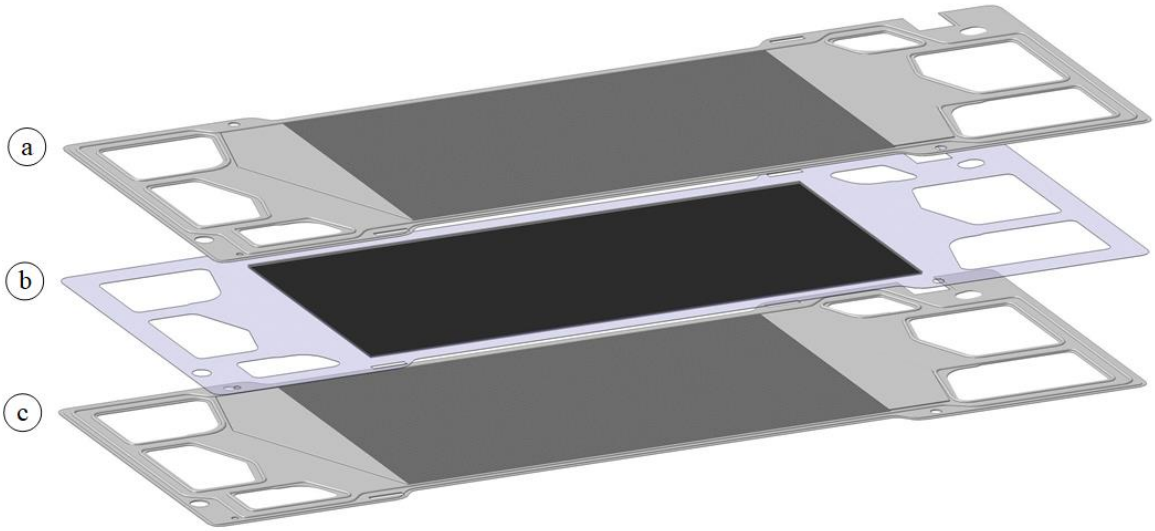


**Figure 16: (a)** Exploded view of the CAD (Computer-Aided Design) model of the "sandwich structure" with the automotive-sized metallic cathode monopole plate, **(b)** the membrane electrode assembly (MEA) with 285 cm² active area and **(c)** the automobile-size metallic anode monopole plate.

## 3.2. Experimental techniques

In the following section, the electrochemical measurement methods used in this thesis are explained.

### 3.2.1. U-I-curves

The easiest way to determine the power output of a fuel cell is to perform a polarization curve (U-I-curve). Two methods have been established for performing U-I-curve measurements: In the potentiostatic method, the potential of the cell is stepwise reduced in potentiostatic mode between the open-circuit voltage (OCV) and a defined full load voltage, e.g. 0.5 V. At each potential point, a working current is established. Since the output current at each potential step is unknown, these U-I-curves can only be performed at very high stoichiometric reactant flows. Therefore the comparability between different MEAs and cell sizes is limited with this method. With the galvanostatic method, the cell is operated in galvanostatic mode, and the current is reduced from 0 A to a full load current. In most cases, however, the cell voltage is taken into account as in the potentiostatic method. As soon as a previously defined lower cell voltage has been reached, the measurement is considered to be completed and a comfortable operating point is approached. The advantage of this method is that the reactant flows can be precisely adjusted on the basis of the load

current, and thus the stoichiometries for each current step are known. In this way, a defined stoichiometry can be determined for each current step, and much better comparability between different cell sizes can be achieved.

U-I-curves are usually displayed in a 2D coordinate system, where the y-axis describes the potential and the x-axis the current. **Figure 17** shows the typical course of the U-I-curve of a hydrogen PEMFC. As previously described in chapter 2.2.1, the theoretically possible cell potential of a hydrogen PEMFC is 1.23 V. However, this potential is never reached in practice due to various mechanisms, such as the formation of mixed potentials at the cathode caused by the crossover of hydrogen through the membrane [75]. In practice, an OCV potential of approx. 1 V is established and decreases steadily with increasing the current density. The further course of the U-I-curve can be divided into 3 main sections. As the current density increases, the cell voltage drops relatively strongly in the first moment. This first section (shown in blue in **Figure 17**) describes the activation area and is significantly influenced by the oxygen reduction at the cathode. By further increasing the current density, a linear voltage drop occurs, which is significantly lower than the voltage loss in the activation area. Due to the linear voltage drop, this section of the characteristic curve is called the ohmic region and is primarily caused by the internal resistances of the fuel cell (shown in red in **Figure 17**). At the end of the linear range comes the so-called full load point, which is usually the last point when recording a U-I-curve. The last section of the characteristic curve is called the transport or diffusion section (shown in green in **Figure 17**). Due to the high reactant flows and a large amount of product water, there is an increased flow resistance and diffusion limitation. This, in turn, results in a lower oxygen concentration at the reactive zones and causes an increased voltage drop up to a complete voltage collapse. The voltage loss between the theoretically possible OCV voltage and the voltage that settles under a defined current density is called overvoltage. Thus at very high current densities, the individual overvoltages, such as $\eta_{cross}$, $\eta_{kinetic,}$ $\eta_{ohmic}$ and $\eta_{diffusion}$ add up to the total voltage loss.

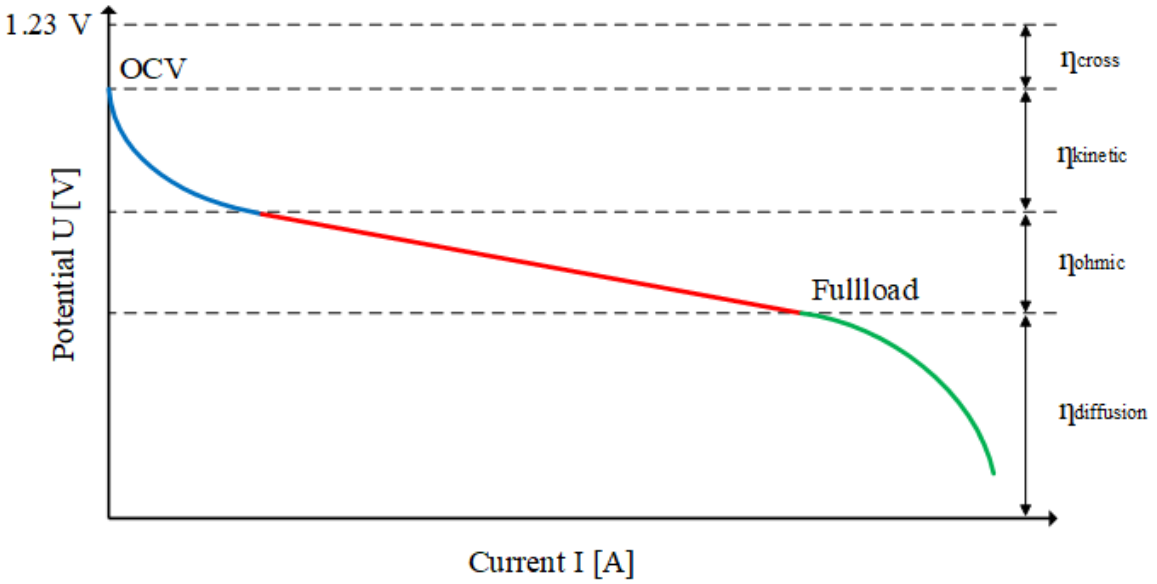


**Figure 17:** Typical course of a polarization curve (U-I curve) of a hydrogen PEMFC, divided into 3 main sections: Blue area describes the activation range; red area describes the ohmic range; green describes the diffusion limiting range.

### 3.2.2. Cyclic Voltammetry (CV)

Besides the catalyst activity, an essential factor for the performance of the PEMFC is the electrochemical catalyst surface area (ECSA) involved in the oxygen reduction reaction (ORR). For the determination of the ECSA, the CV measurement method can be used. This allows detailed information to be obtained about the course of electrochemical reactions on the catalyst surface and absorption processes at the electrode/electrolyte interface. Since the configuration of a PEM fuel cell is a 2-electrode arrangement and the anode is both the counter (CE) and reference electrode (RE), the measurement is performed in a partially inerted state. This means that the cathode, which is the working electrode (WE), is inerted with nitrogen, and the anode is still supplied with hydrogen. For the measurement, the electrode potential is moved in a window between the lower reversal potential $E_L$ and the upper reversal potential $E_U$ at a defined speed:

$$v_E = \frac{\partial E}{\partial t} \tag{3.2.1}$$

In response, a potential-dependent current is measured, which can be displayed in a voltammogram (see **Figure 18**). The current flow can be traced back to two basic electrochemical processes:

**Faraday currents:** These are generated by the electrochemical reaction (oxidation/reduction) taking place on the catalyst surfaces and are connected to the passage of charge at the electrode/electrolyte interface. Depending on the active catalyst surface and the resulting adsorption of the electroactive species, this process becomes visible in a defined current flow.

**Capacitive currents:** If no Faraday reaction occurs, the electrochemical double layer is formed at the electrode/electrolyte interface. Depending on whether the applied potential rises or falls, the double layer is built up or reduced, which in turn becomes visible in a current flow. The electrochemical double layer capacitance ($C_{dl}$) can be compared approximately to a plate capacitor.

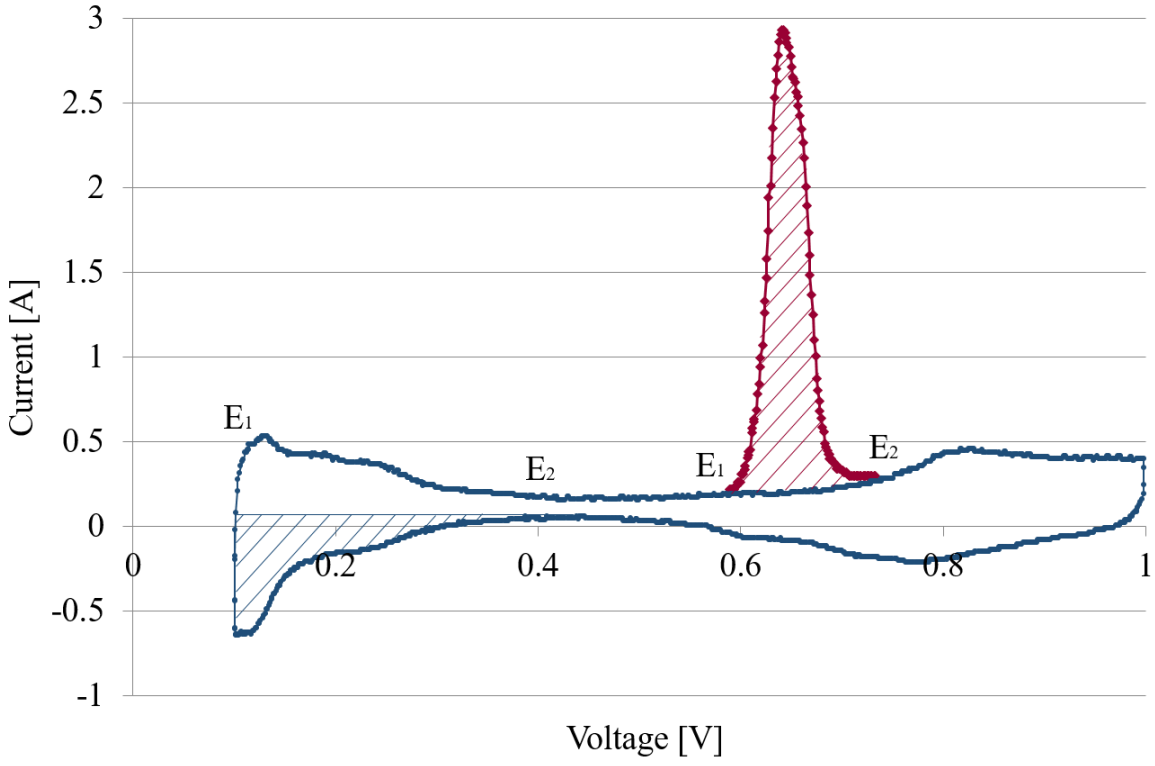


**Figure 18:** Cyclic voltammetry (CV) measurement with the CO-stripping method. Blue hatched area corresponds to the monolayer adsorption of hydrogen, red hatched area corresponds to the carbon monoxide (CO) monolayer oxidation. By integrating the corresponding areas between $E_1$ and $E_2$ (blue or red hatched) the electrochemical catalyst surface area (ECSA) can be calculated.

In the standard method, the hydrogen adsorption area is integrated within the two potential limits $E_1$ and $E_2$ (hatched blue in **Figure 18**), and the result is the charge flowing due to the Faradaic reaction:

$$A_E = \int_{E1}^{E2} I \partial t \tag{3.2.2}$$

In this thesis, the CO-stripping method was also used. Before measuring the active area, nitrogen with 0.1 % carbon monoxide (CO) was applied to the cathode. This forms a stable monolayer of CO on the active catalyst surface, which is retained when the cathode flow is switched to pure nitrogen. If the electrode potential in a window of $E_1$ and $E_2$ (hatched red in **Figure 18**) is moved with a defined speed, an oxidation of the CO monolayer takes place. By integrating the CO-oxidation peak, the electrochemical catalyst surface area ($A_{ECSA}$) can be calculated as follows:

$$A_{ECSA} = [\frac{cm^2}{mg_{Pt}}] = \frac{A_E}{m_{Pt} Q_f v} \tag{3.2.3}$$

Where $A_E$ represents the integrated area between $E_1$ and $E_2$, $mg_{Pt}$ the platinum mass, $Q_f$ corresponds to the monolayer adsorption with $Q_{fh}$ = 210 µC$(cm^2)^{-1}$ for hydrogen and $Q_{fco}$ = 420 µC$(cm^2)^{-1}$ for carbon monoxide and the potential scan rate $v$.

### 3.2.3. Electrochemical Impedance Spectroscopy (EIS)

Electrochemical impedance spectroscopy (EIS) is a useful and powerful tool for obtaining reliable information about electrochemical processes, electrode capacitances or ohmic resistances in the PEMFC. To determine the impedance characteristics and complex resistance of a PEMFC, a sine probing signal is applied, and the response at the output is measured and evaluated. To perform the EIS measurement, there are two possibilities to impress the sine wave: With the potenstiostatic method, the potential $E$ is kept constant, a sinusoidal potential signal $\partial E$ is applied, and the current response $\partial I$ is measured. This method is often used for measurements in partially inerted mode ($H_2$ - anode/$N_2$ - cathode) since no working current flows here, and thus the potential and the potential wave are applied by the potentiostat [76]. With the galvanostatic method, the current $I$ is kept constant,

a sinusoidal current probing signal $\partial I$ is applied, and the potential response $\partial E$ is measured. The main advantage of this method is that even in fuel cell stacks, the individual cell impedance can be determined via the voltage response $\partial E$. Therefore, this is the most common method to determine the cell impedance of a PEMFC in quasi-stationary operation. In contrast to a classical electrical circuit, an electrochemical system response is generally nonlinear. Under certain operating conditions, especially in the "ohmic range" (see chapter 3.2.1) and a sufficiently small perturbation, the system and the response can be considered quasi-linear. In this case, the response has the same frequency $f$, but the phase and amplitude are shifted by $\partial\varphi$ and $\partial A$, respectively. However, since Ohm's law also applies here, as a rule, the selected disturbance should be as large as necessary and as small as possible. If the selected amplitude $A$ is too large compared to the total cell resistance, the voltage response is excessive, and the quasi-linearity of the system is disturbed. Again, if the amplitude $A$ is too small, the noise predominates, and the response is difficult, if not impossible, to evaluate.

The measured impedance data are usually represented in a Cartesian coordinate system, more precisely the so-called Nyquist plot, where the y-axis represents the imaginary part *(-)Im(Z)* and the x-axis - the real part *Re(Z)* (see **Figure 19 (a)**). This simple and understandable form of presentation is probably the most commonly used way to display impedance data. However, this form of representation lacks the possibility to show frequency dependencies. Therefore the Bode representation is used in addition to the Nyquist representation, which shows the absolute impedance $|Z|$ and the phase shift $\partial\varphi$ with respect to the frequency $f$.

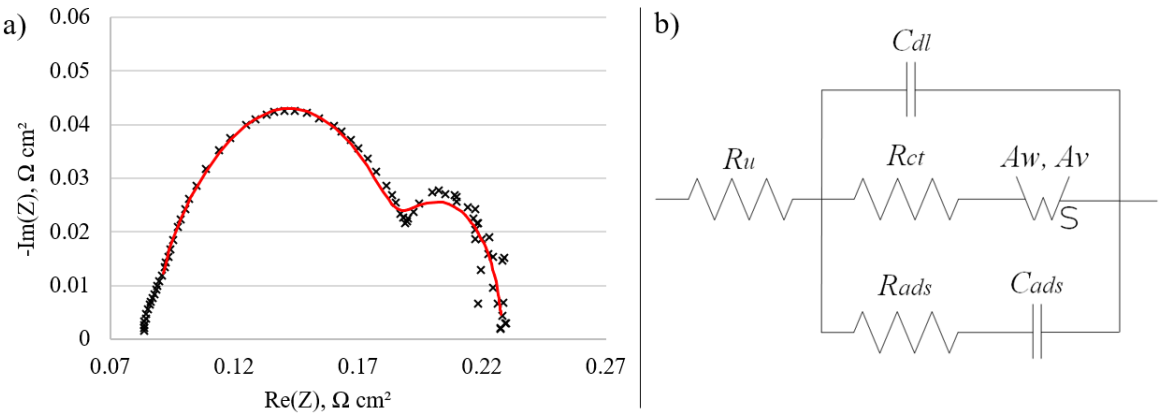


**Figure 19: (a)** Exemplary EIS-data (open symbols), and fitting of these data to **(b)** the equivalent electric circuit (EEC).

The final aim of the EIS characterization is to convert the measured raw data into physical models and their parameters to describe reactions and mechanisms in the PEMFC. There are many approaches to this, whereby the probably simplest form is the so-called structural modeling. With structural modeling, the mathematical impedance model can be represented in the measured frequency range as equivalent electric circuit (EEC) elements (**Figure 19 (b)**) [77]. Each EEC element can describe a single physical object or a processthat takes place in the PEMFC. One should however, note that many EEC elements can often guarantee a good fit, but too many elements can "falsify" the calculated values of each element. After the composition of a suitable physical equivalent circuit, the parameter identification can be made in two ways: The most common method is the approximation with the so-called complex nonlinear least square (CNLS) method [78]. The goal of the least-squares fitting method is to find a set of parameters *P* which are as small as possible in the sum:

$$S(P) = \sum_{i=1}^{n} w_i [y_i - Y_i(P)]^2 \tag{3.2.4}$$

where *S(P)* represents the sum, $w_i$ the weighting of the respective points, $y_i$ the data point to be fitted, and $Y_i$ is the value of the calculated fitting function. With the mathematical function, which corresponds to the physical equivalent circuit (**Figure 19 (b)**), the approximation can be calculated with the graphical CNLS method and thus the values of the individual EEC elements.

$$Z(\omega) = R_u + \left(\frac{1}{\left(\frac{1}{\left(R_{ct} + \frac{W_{SR}}{\sqrt{\omega}}(1-j)tanh\left[W_{SC}\sqrt{j\omega}\right]\right)} + \frac{1}{\left(\frac{1}{j\omega C_{dl}}\right)} + \frac{1}{\left(R_{ads} + \left(\frac{1}{j\omega C}\right)\right)}\right)}\right) \quad (3.2.5)$$

The main disadvantage of this method is the complexity, the many adjustable boundary parameters and the model finding, which requires a more profound knowledge of the meaning of the individual EEC elements. This makes the method particularly well suited for the more precise analysis of individual elements but carries a risk in automation, such as real-time monitoring of impedance in the automotive application.

Since, as a rule, only values such as uncompensated (Nafion® -electrolyte) resistance $R_u$, charge transfer resistance $R_{ct}$ or double layer capacitance $C_{dl}$ are required in automotive applications for monitoring the life parameters of the PEMFC, a much simpler calculation method can be used here. This would be the second method, named Differential Impedance Analysis (DIA) [79]. The core of the DIA is the local scanning analysis, which uses a Local Operation Model (LOM) to determine the frequency dependent parameters ($R_u(\omega)$, $R_{ct}(\omega)$, $C_{dl}(\omega)$) and their derivatives ($\frac{dZ_{Im}}{d\omega}$, $\frac{dZ_{Re}}{d\omega}$) to calculate the $R_u$, $R_{ct}$ and $C_{dl}$ of a Randles circuit. This method's main advantage is the fast calculation and in contrast to the CNLS method, which has a lot of calculation latitude, the fixed calculation path. For an exact determination of the EEC element parameters, the impedance measurement should be performed in the quasi-linear working range of a PEMFC (see chapter 3.2.1). Another positive aspect is the small number of measurement points. While in the CNLS method, the more measurement points, the more accurate the fit, the parameters of the EEC elements ($R_u$, $R_{ct}$ and $C_{dl}$) can be determined quantitatively with at least three measuring points. This makes the DIA method particularly suitable for automated and fast analysis in between, up to the real-time monitoring of a PEMFC [80]. Since the LOM is based on the Randles circuit, the impedance can be described as follows [81]:

$$Z(\omega)_{LOM} = R_u(\omega) + \frac{R_{ct}(\omega)}{1+\omega^2\tau(\omega)^2} - j\frac{\omega R_{ct}(\omega)\tau(\omega)}{1+\omega^2\tau(\omega)^2} \quad (3.2.6)$$

with the uncompensated resistance $R_u$, the charge transfer resistance $R_{ct}$ and the effective time constant τ. Based on the derivative of the effective inductance $dL_{eff}(\omega)$ and the measured impedance data ($Z_{Im}(\omega)$, $Z_{Re}(\omega)$), equation 3.2.6 can be rewritten to determine the effective time constant τ:

$$\tau(\omega) = \frac{\partial L_{eff}(\omega)}{\partial Z_{Re}(\omega)} = \frac{\left(\omega^{-1}\partial Z_{Im}(\omega)\right) \cdot \partial\omega}{\partial\omega \cdot (\partial Z_{Re}(\omega))} \tag{3.2.7}$$

With this, it is then possible to calculate the $R_{ct}$ at a given frequency:

$$R_{ct}(\omega) = -\frac{\partial Z_{Re}(\omega)}{\partial\omega} \cdot \frac{(1+\omega^2\tau(\omega)^2)^2}{2\omega\tau(\omega)^2} \tag{3.2.8}$$

Finally, the calculated $R_{ct}$ can be used to determine the *Ru* and $C_{dl}$ of a PEMFC:

$$R_u(\omega) = Z_{Re}(\omega) - \frac{R_{ct}(\omega)}{1+\omega^2\tau(\omega)^2} \tag{3.2.9}$$

$$C_{dl}(\omega) = \frac{\tau(\omega)}{R_{ct}} \tag{3.2.10}$$

### 3.2.4. Ex-situ (post mortem analysis)

In a durability test, the determination of degradation is important both *in-situ*, i.e. non-destructively during the test run, and *ex-situ* as post-mortem analysis. The latter is particularly important if the cause of the performance loss is unknown, and thus, the degradation mechanisms have to be determined. One part of this thesis deals with the degradation of PEMFC single cells in a temperature stress test with temperature cycles between -10 °C and 80 °C. Using the *in-situ* measurement methods described above, it was possible to observe how the respective performance and test item parameters, such as ECSA or impedance, changed during the temperature stress test. As this was a completely new test method, it was difficult to establish the relationship to the responsible degradation mechanisms. Therefore, in this case, it was imperative to perform *ex-situ* analyses, such as highly magnified images of the object structure or the determination of the object composition, in order

to gain a better understanding of the cause of the loss of performance. The *ex-situ* analysis methods performed in this thesis are described in detail below:

A simple and yet efficient way to detect changes in an object is creating detailed and high-resolution images. If the object magnification of a normal light microscope is not sufficient, the scanning electron microscope (SEM) is usually used. In the SEM, an electron beam generated by an electron source is passed over the object in a certain pattern, and the resulting interaction between the object and the electron is used for a magnified image (see **Figure 20 (a)**). Two types of electron sources can be used to generate an electron beam: The cheaper variant usually uses a hairpin-shaped tungsten wire or a LaB6 crystal. It emits electrons when heated, which are then accelerated onto the object in an electric field with a voltage of ~6 kV to 30 kV. The more complex variant uses the technique of field emission. Here, a very high electric field strength is applied to the field emission cathode, and thus electrons are released. The advantage of this method is the particularly good image quality, even at low acceleration voltage. The electron beam, finely focused by the magnetic coils, hits the object with defined energy and scans its surface step by step. This scanning process usually takes place in a high vacuum to avoid interactions between other atoms and molecules in the air. Depending on the angle of reflection, the interaction between the object and the primary electron beam produces several responses. For object magnification, the secondary electrons (SE) or the backscattered electrons (BSE) are detected and evaluated. The resolution and contrast of the image depend primarily on the beam diameter, the inclination of the surfaces, and the material of the object. Furthermore, the BSE method offers the advantage that the intensity of the signal varies depending on the atomic number of the material. Thus, conclusions about the composition of the material can be drawn from the intensity of the response. However, the topography (surface inclination, shadows, surface charge, etc.) of the object surface also influences the contrast of the image. Therefore, images generated by BSE usually have a lower resolution than the images created by SE [82, 83]. **Figure 20 (b)** shows a typical SEM image which is discussed in detail in chapter 5.3.4.

Therefore, the surface composition is often qualitatively determined by X-ray surface analysis (EDX). The X-ray analysis method is usually an integral part of the SEM and uses the characteristic X-ray radiation of the object. Like the secondary electrons or the backscattered electrons, X-rays are part of the response caused by the primary electrons and the interaction between the object surface. More precisely, the reaction is caused by the ejection

of an electron close to the nucleus from its position by the primary electrons and the immediate replenishment of a more energetic electron from a higher orbital. The resulting energy difference is released in the form of an X-ray quantum and can be directly assigned to the atom or element. Using special semiconductor detectors, the energy generated here can be absorbed and assigned to the scanned object surface [84, 85].

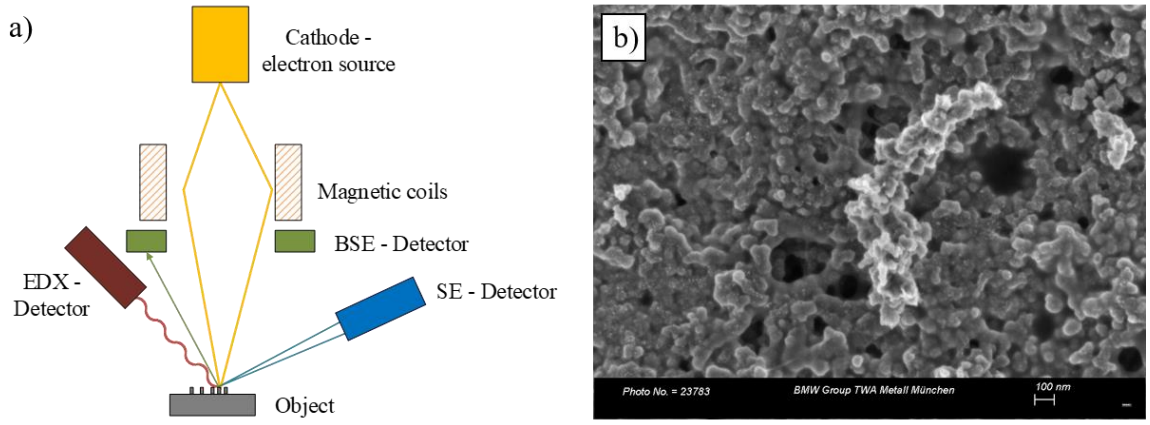


**Figure 20: (a)** Simplified technical description of a scanning electron microscope (SEM) and **(b)** a typical SEM image, which is discussed in detail in chapter 5.3.

Especially with temperature cycles, as they have been carried out in this work, structural surface changes can occur. The laser scanning microscope (LSM) can be used to detect and evaluate such superficial changes. Using an LSM, images can be taken with a magnification of up to ~28800 times, and the surface can be scanned using point-by-point scanning or a scanning line [86]. Here, fluorescence-exciting laser light is continuously passed over the object, and the time-delayed fluorescence response of an image pixel is recorded by means of a photomultiplier. Both the fluorescence lifetime and the fluorescence intensity can be evaluated and used for image generation. Since no complete image is captured during image acquisition and the surface is scanned point by point, the final step is to digitally assemble the complete image, similar to SEM [87].

# 4 Development of a dynamic temperature control unit

This chapter deals with the tempering units for small (50 cm²) and for automotive-size PEMFC single cells (285 cm²). It is mainly based on the following publication: J.P. Sabawa, F. Haimerl, F. Riedmann, T. Lochner, A.S. Bandarenka. Dynamic and precise temperature control unit for PEMFC single-cell testing // Engineering Reports 3 (2021) accepted (https://doi.org/10.1002/eng2.12345).

## 4.1 PET TP50 single cell

### 4.1.1. State-of-the-art

Improving the cost and lifetime of PEMFCs is now an important factor in becoming competitive with conventional internal combustion engines [22, 88]. In terms of durability, the operating temperature of PEMFCs plays a crucial role. PEMFCs must be able to operate over a wide temperature range. At very low temperatures, such as -20 °C, a start-up, in particular, is a challenge for the long-term stability of PEMFCs [89, 90, 91]. At the other end of the temperature range, there is again growing interest in high-temperature PEMFCs. Operating temperatures between 120 °C and 200 °C increase the kinetics and thus also the efficiency [92, 93]. Therefore, single-cell test equipment must be able to reproduce such conditions. As already described in chapter 3.1.4, water-cooled cell hardware is usually used to simulate ambient conditions. However, with this type of temperature control, the only temperature ranges from 0 °C to just above 100 °C are possible. At temperatures below 0 °C, frost-resistant substances such as glycols must be added to the cooling water [94]. This allows the cooling medium to be cooled down to a temperature of -55 °C but creates a new source of contamination for the PEMFC [95]. Therefore, special measurement setups such as environmental chambers [96, 97] or/and additional cooling equipment [41] are usually required for investigations at low temperatures. However, durability tests in environmental chambers are expensive, very time-consuming, and at this cell size, it is questionable whether there is any comparability at all with real applications. In addition, only low temperatures can be achieved with such an experimental setup. High temperatures can generally only be achieved with an electric auxiliary heater, which can act very dynamically in the direction of rising temperatures, but has no active cooling. With this heating method,

high cell temperatures can be covered, but dynamic temperature jumps are still not possible. The lack of possibility to cover all temperature ranges dynamically, without an additional source of contamination or great effort, requires further or new development of the measurement technology.

### 4.1.2. Characteristics

The temperature control of the cell hardware via the cooling water is relatively easy to realize since this method is offered as an option by almost every test bench manufacturers. The cooling water temperature, which later adjusts the temperature of the active surface, is already tempered in the temperature control and balancing tank of the test bench (see 3.1.1) and then pumped to the cell hardware. As adjustable parameters, the tank temperature and the cooling water flow can be adjusted and varied. In the following, all advantages and disadvantages of the tempering method are listed:

**Table 4:** All summarized advantages and disadvantages of the commercial TP50 cell hardware, which is used on a test bench with common water cooling circuit.

| **Advantages** | **Description** |
|---|---|
| Cost and probability of default | Since the water temperature is controlled directly in the temperature control and compensation tank of the test bench, no additional heaters or control electronics are required. This eliminates wear parts, and the cell hardware itself is much more cost-effective. |
| Flexibility | Since the cell is tempered by the cooling water, which is adjusted in the test bench, different types of cell hardware can be used on the same test bench. On the other hand, the same cell hardware can be operated without much effort on another test bench of the same type. |

| Disadvantages | Description |
|---|---|
| Long controlled loop | Usually, the actual temperature is measured directly in or in front of the cell hardware. As a result, the control loop is very long, which makes it extremely difficult to define suitable PID control parameters. Depending on the coolant flow and temperature, temperature jumps of varying intensity can cause overshoots or undershoots and, in the worst case, the cell temperature is not controllable, i.e. it oscillates permanently. |
| Dynamics of temperature control | A further disadvantage of the long controlled loop is the slow dynamics of the method. |
| Temperature range | Since distilled water is generally used as the coolant, cell temperatures between ~35 °C and 105 °C can be set. Temperatures above the boiling point are only possible with additional pressurization of the temperature control and expansion tank, leading to increased wear of the entire cooling circuit. |

The last two disadvantages are often the limiting factors for various stress tests and therefore finally led to the search for a new way to control the temperature of the PEMFC. During the search for a new temperature control option, the following boundary conditions had to be met:

- A cell temperature between **-20 °C-140 °C** should be possible.
- Heating and cooling rates of more than **1 K/s** and **0.5 K/s** should be possible.
- A temperature stability of <**±0.5 °C** (at all temperature points).
- No additional source of contamination.
- Easy handling, i.e., easy set-up with a new PEMFC, should be given.

With the help of electro thermal transducers, the so-called Peltier elements, temperatures outside the normal operating range, such as below freezing point and well above the boiling point of water, can be easily reached [98, 99, 100]. In the case of temperature control of a PEMFC, however, there has never been such a combination between an electrothermal converter and commercial single-cell hardware before, so that the entire cell structure had to be redesigned and developed (more on this in chapter 4.1.3).

The newly developed and patented[iii] Peltier-Element Tempering (PET) single-cell represent a significant step forward compared to conventional temperature control methods and therefore offer many advantages, but also some disadvantages, which are listed below[iv]:

**Table 5:** All summarized advantages and disadvantages with the associated technical data of the newly developed single-cell PET SC TP50.

| **Advantages** | **Description** |
|---|---|
| Extended temperature range | Due to a $\partial T_P$ of a maximum of 79 °C, temperatures between -30 °C and 170 °C are possible in practice. |
| Dynamics of temperature control | Due to the high cooling power of up to 246 W per electrode, heating rates of more than 1 K/s are possible. |
| Short controlled loop | The short control loop allows the temperature to be set within a control window of ±0.3 °C (in the regulated state). In this way, the influence can also be quickly compensated for dynamic disturbance variables (e.g. spontaneous increase in current). |
| No further sources of contamination | The cooling water is needed to remove the waste heat of the Peltier elements but has no direct contact with the monopolar plates or the MEA. |

[iii] Patent was registered on 24.08.2018 with the file number DE 10 2018 214 366.8.

[iv] All the following technical data and statements in this chapter (4.1.2) refer to the final version of the PET SC TP50.

| Advantages | Description |
|---|---|
| Cost effective | Due to the high dynamics and the extended temperature range, e.g. low-temperature tests can be carried out cost-effectively without additional hardware. |

| Disadvantages | Description |
|---|---|
| Additional electrical hardware | For the control of the Peltier elements, an additional power supply, and an additional controller is required. More about this can be found in chapter 4.1.4. |

With the new PET single-cell hardware designs, all experiments were carried out in this thesis, and in parallel, the robustness was tested. Basically, it can be said that the only wear part in the new cell design is the Peltier elements and the O-rings. However, due to the optimized design, they can be replaced in a very short time. After several tests, it can be confirmed that the Peltier elements wear out after approximately 1000 repetitions at dynamic temperature cycles between -10 °C and 80 °C. It should be mentioned at this point that this is the most intensive type of stress for the electrothermal transducers, especially when the target temperatures are approached with the maximum rate of temperature change.

### 4.1.3. Design

As described in chapter 3.1.4, all components of the commercially available TP unit are arranged in “sandwich” construction. This structure should be retained as far as possible in the new development so that components such as endplate, pressure plate and flow fields can be reused. Thus, the tempering units had to have the identical dimensions of the remaining components. The development of the final version of the PET TP50 with the Peltier element tempering units took place in two stages. The first prototype was to be used to verify whether

- Peltier elements are suitable for adjusting the cell temperature;
- long-term stability of the tempering units is given. Especially for wide and fast temperature changes;
- temperatures outside the standard operating temperatures of a PEMFC, in particular below the freezing point of water, can be achieved.

The dynamics and the higher temperature edge points did not have to be achieved in the first prototype. Much more, the cost and the previously listed points were more important. Additionally, the first prototype was used to develop the software algorithm for temperature control, which was also used in the final version of the PET TP50 single cell. The test runs and thus the recording of the measurement data were carried out with the PET TP50 single cell prototype [30, 101]. **Figure 21** shows the PET SC TP50 prototype during commissioning and the CAD model with the exploded view of the anode side. The principle of how the tempering units set the cell temperature is identical to the final version of the PET SC TP50. When the modulated current flows through the Peltier elements (see **Figure 21 (b)**), a temperature difference is formed due to the dissimilar energy levels, with which the MEA is actively tempered on one side, and the waste heat is dissipated via the waste heat transfer plate (WHTP) (see **Figure 21 (d)**) and the test bench cooling water on the other.

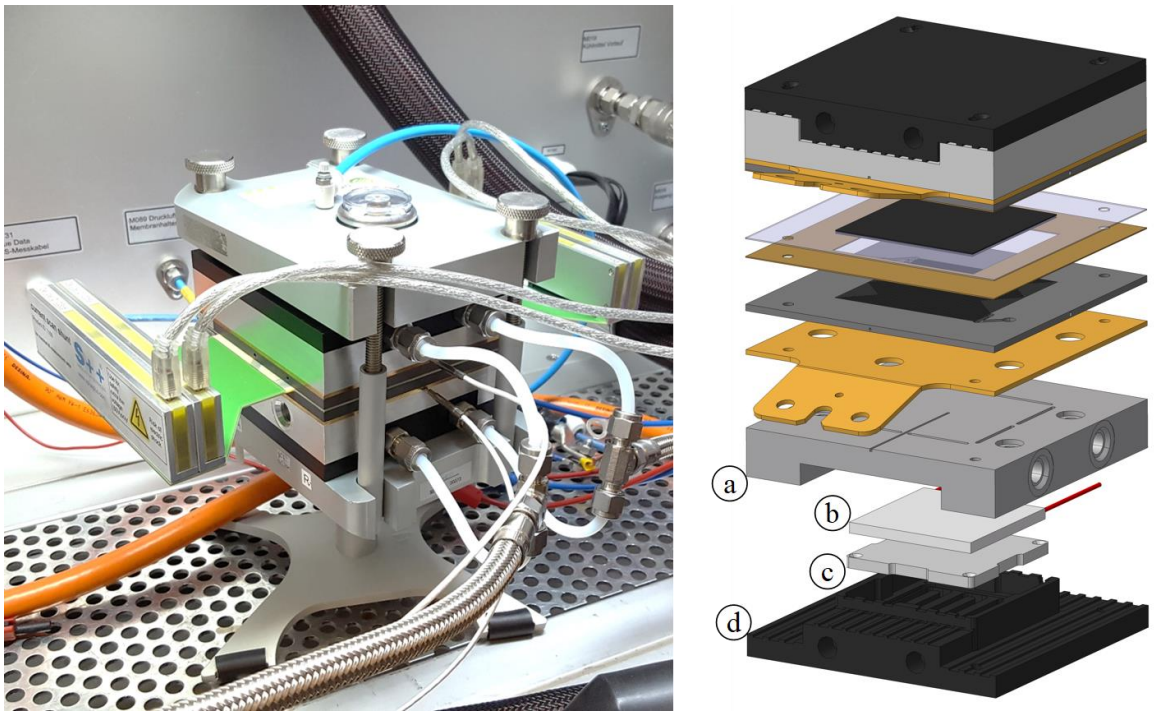


**Figure 21: (a)** The PET SC TP50 prototype during initial commissioning with the CAD model. The anode side is shown in exploded view with the thermal transfer plate (TTP), **(b)** the Peltier element, **(c)** the waste heat transfer plate (WHTP) and **(d)** the polyoxymethylene plastic (POM) base plate (BP).

The prototype was made of aluminum and polyoxymethylene plastic (POM). The main advantage of the plastic used here is its low price, high hardness and good machinability. However, it can only be heated up to ~90 °C permanently and up to ~140 °C for a short time, which unfortunately did not meet the previously defined requirement [102]. Moreover, due to the significantly different coefficient of linear expansion $\alpha$ between aluminum and POM (~$23.5 \cdot 10^{-6}\,K^{-1}$ vs. ~$1.4 \cdot 10^{-6}\,K^{-1}$), components made of different materials could only be built on top of each other and not side by side [103]. Therefore, the thermal transfer plate (TTP) (see **Figure 21 (a)**) and the base plate (BP) (see **Figure 21 (d)**) had to have the same dimensions as the flow fields or other components of the “sandwich structure”. Since the Peltier element "floats" between two layers of thermal paste and the area in the center of the TTP has to absorb most of the force, there was the risk that the TTP would distort during compression. This would result in an inhomogeneous or distorted contact area between the current collector and the TTP. For this reason, the TTP had to be designed relatively massively, which in turn meant that the previously defined target dynamics and the desired temperature ranges could not be achieved. Nevertheless, the first trial with the PET

SC TP50 prototype was a complete success and was subsequently developed further. However, before the new design and construction could be defined, it was necessary to determine which points need to be improved. As previously mentioned, two of the previously defined points could not be achieved, including the desired dynamic range (1 K/s) and the outer working range (-20 °C-140 °C). Therefore, the following points need to be improved in the new version of the PET SC TP50:

- **Reduction of the thermal mass of the TPP.** In the PET SC TP50 prototype, the TPP was designed to be very massive for stability reasons. For higher dynamics and higher power reserves of the Peltier elements, this must be significantly reduced in size and installed in the BP.

- **More resistant material of BP.** To achieve the required limit operating points, new material must be selected for the BP. Besides, the material should have a similar coefficient of expansion to the TPP material.

- **More powerful Peltier elements.** More powerful Peltier elements increase the dynamics and the cooling capacity so that a power reserve remains even at limit operating points.

- **Higher cooling capacity of the WHTP.** More powerful Peltier elements require improved dissipation of the waste heat generated into the test stand cooling water.

**Figure 22** shows the final version of the PET SC TP50 design and the CAD model with the exploded view of the anode side. Similar to the prototype, a tempering unit consists of several main parts, namely the integrated thermal transfer plate (TTP) **(a)**, the Peltier element with the heat-conducting pads **(b)**, the waste heat transfer plate (WHTP) **(c)**, the base plate (BP) **(d)** and the water-conducting plate (WCP) **(e).**

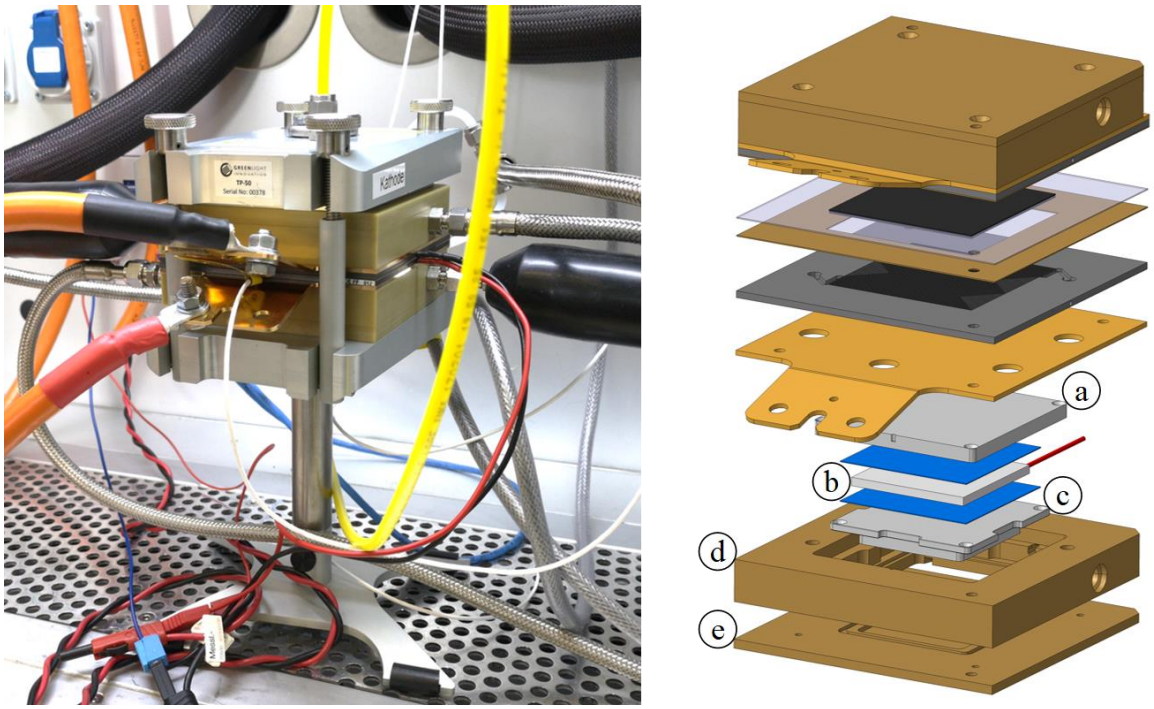


**Figure 22: (a)** The final version of the PET SC TP50 with the CAD model. The anode side is shown in exploded view with the significantly reduced thermal transfer plate (TTP), **(b)** the Peltier element with the 0.5 mm thick heat-conducting pads, **(c)** the waste heat transfer plate (WHTP), **(d)** the base plate (BP) and **(e)** the water-conducting plate (WCP).

The exact function and properties of the individual components are described step by step in the following section.

### Operating principle of the PET SC TP50

**Figure 23** shows a simplified technical representation of the entire PET SC TP50 structure. The letters **(a)-(e)** correspond to those used in **Figure 22**. As described in chapter 3.1.4, the compression plate and the solid end plate (**Figure 23 (f)**) establish the desired contact pressure $F$ and thus the necessary pressure on the glass fiber gasket and the GDL of the stacked structure. For simplified representation, both the reactant channels ($H_2$ and air) and the water channels ($H_2O$) were shown on a cross-sectional axis. Depending on the desired cell temperature, which is tapped via the temperature measuring points $T$, the corresponding heat flow $\dot{Q}_T$ must be dissipated via the WHTP and the cooling water. Thereby the direction of the heat flow as well as the power of the heat flow depends on the flow direction of the current through the Peltier element and the power release of the control unit. Furthermore,

the dissipation of waste heat by the WHTP is crucial here, which depends primarily on the cooling water temperature and the cooling water flow rate.

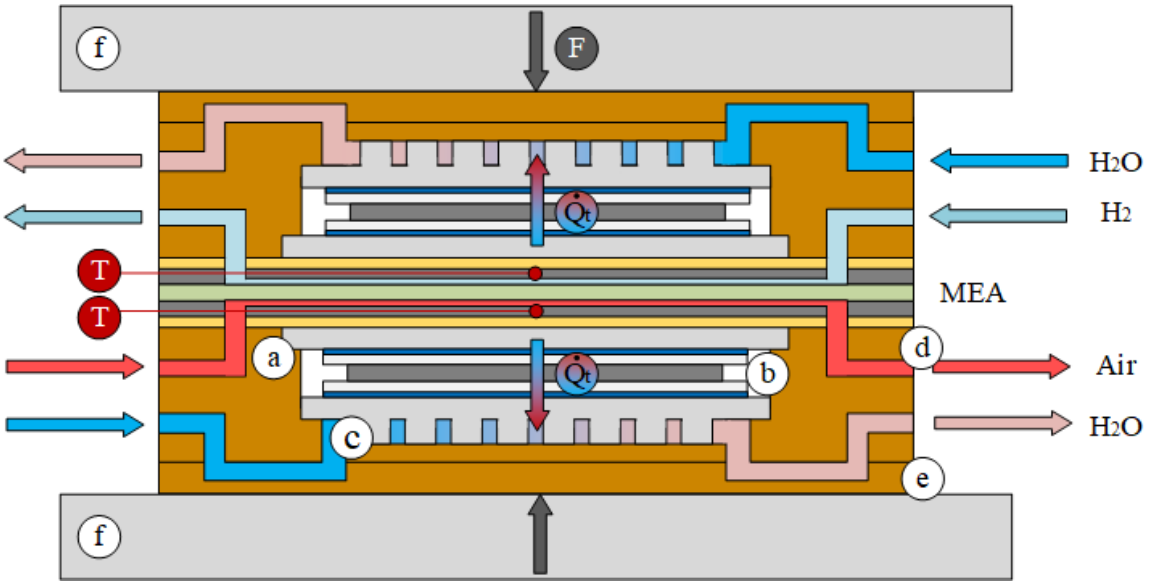


**Figure 23:** Simplified technical representation of the entire PET SC TP50 structure. For better understanding, both the reactant channels ($H_2$ and air) and the water channels ($H_2O$) were shown on a cross-sectional axis. The letters **(a)-(e)** correspond to those used in **Figure 22**.

### Thermal transfer plate (TTP)

Besides the better material, the main difference to the PET SC TP50 prototype is the significantly smaller TPP and its arrangement. The aluminum TTP was incorporated directly into the base plate (BP), resulting in a considerably lower mass of temperature-active parts. In addition, with this design, the TTP no longer has any contact with the surrounding air, which increases the efficiency of the temperature control unit (comparison TTP prototype $16.14 \cdot 10^3$ mm²). Using the direct relationship between the heat quantity for heating $\dot{Q}_{Th}$ and cooling $\dot{Q}_{Tc}$, the mass of the current collector $m_{CG}$ and of the graphite monopolar plate $m_{MP}$, the specific heat quantity of copper $c_{Cu}$ and aluminum $c_{Al}$, and the temperature change rate $\dot{T}$, the permissible material mass of the TTP $m_{TTP}$ can be calculated:

$$\dot{T} = m^{-1} \cdot c^{-1} \cdot Q_T = (m_{TTP} \cdot c_{Al} + m_{CC} \cdot c_{Cu} + m_{MP} \cdot c_{Gr})^{-1} \cdot Q_T \qquad (3.3.1)$$

$$m_{TTP} = \dot{Q}_{Tc} | \dot{Q}_{Th} \cdot -\dot{T}(m_{CC} \cdot c_{Cu} + m_{MP} \cdot c_{Gr}) \cdot (\dot{T} \cdot c_{Al})^{-1} \qquad (3.3.2)$$

$$m_{TTP} = \frac{246|369\,Ws - 0.5|1\,K^{-1}s(0.351\,kg \cdot 385\,JKg^{-1}K^{-1} + 0.085\,Kg \cdot 841\,JKg^{-1}K^{-1})}{0.5|1\,K^{-1}s \cdot 896\,JKg^{-1}K^{-1}} \quad (3.3.3)$$

$$m_{TTP-Cool} = 0.3187\,Kg \qquad m_{TTP-Heat} = 0.1814\,Kg \quad (3.3.4)$$

It follows that a material mass of the TPP $m_{TTP}$ of 0.1814 kg must not be exceeded when redesigning the TPP. Ultimately, the optimized design reduced the TTP mass by 84 % to 0.103 kg.

**Peltier element**

Besides the more compact and optimized cell design, two more powerful Peltier elements with a total cooling power of 492 Watts (PET SC TP50 prototype ~280 Watts) were used, which significantly increase both the dynamics and the operating range. The key data for the selected Peltier elements are shown in **Table 6**.

**Table 6:** The main physical properties of the selected Peltier element used with the PET SC TP50.

| **Property** | **Value**[v] |
|---|---|
| Maximum voltage $U_{max}$ | 33.1 V |
| Maximum current $I_{max}$ | 12.1 A |
| Maximum cooling capacity $Q_{cmax}$ | 246 W |
| Maximum temperature difference $\partial T_{max}$ | 79 °C |
| Maximum working temperature $T_{wmax}$ | 180 °C |
| Dimensions | 55±0.1 mm x 55±0.1 mm x 3.75±0.1 mm |

[v] With a tolerance of ±10 % for thermal and electrical parameters specified by the manufacturer.

Here, the Peltier element works like a heat pump when heating, and thus the heating capacity is about 50 % higher than the cooling capacity.

**Waste heat transfer plate (WHTP)**

Like the TTP, the metallic WHTP was built directly into the BP, which also results in good isolation from the environment. For better heat dissipation, the active cooling surface $A_{CS}$ of the WHTP was increased by ca 37 % to $15 \cdot 10^3$ mm². In addition, the averaged cooling channel diameter of the WHTP was increased to 20 mm². This allows the cooling water pressure rise in the cell to be kept as small as possible and as large as necessary. These dimensions are sufficient to dissipate the waste heat from the Peltier element while ensuring adequate stability. Depending on the desired cell temperature, the cooling water flow is adjusted accordingly. At very low temperatures, such as below the freezing point of water, an increased cooling water flow is required to dissipate the waste heat generated and thus achieve a maximum $\partial T$ between both sides of the Peltier element. Here, a cooling water flow rate of 33.3 cm³/s per tempering unit proved to be optimal. This results in a water supply pressure of ~280 kPa. Higher flow rates are possible but put unnecessary strain on the entire system. Since the Peltier element works like an electrical resistor at higher temperatures (e.g. 80 °C), significantly lower cooling water flows can be set here.

**Base plate (BP) & water-conducting plate (WCP)**

As already described, the TTP was made of aluminum and installed directly in the BP. For this design leap, a material with a coefficient of thermal expansion almost equal to that of aluminum had to be selected for the BP. In addition, the material should be very robust, electrically insulating and insensitive to acids. Only one material was suitable here, namely amorphous polyimide Ultem™ (Type 2300). The main advantage of this material is the low thermal conduction of 0.22 $Wm^{-1}K^{-1}$, the high hardness, and the coefficient of linear expansion $\alpha$, which is comparable to aluminum (~$30.0 \cdot 10^{-6}$ $K^{-1}$ vs. $23.5 \cdot 10^{-6}$ $K^{-1}$) [104, 105]. In addition, the polyimide can be permanently heated to a temperature of ~170 °C and up to ~210 °C for the short term. In contrast to the prototype, the BP now consists of two components, namely the redesigned base plate (BP) and the water-conducting plate (WCP). Like the BP, the WCP was also made of the amorphous polyimide Ultem™. This had to be solved constructively in order to keep the tempering unit as flat as possible.

**Constructive properties**

**Figure 24** shows the CAD model of a tempering unit from different perspectives and the main design features with which the enormous heating and cooling performance is achieved. One of the most essential points of any tempered unit is the flat contact surface to the current collector. Only a flat contact surface can ensure optimum heat transfer to the current collector and thus to the PEMFC. Due to the risk of contamination, no contact pastes or the like may be used here (see chapter 3.1.4). As mentioned before, the expansion coefficient of the TTP and the BP plays an essential role here. $l_{TTP}$ describes the thickness of the TTP and thus the measure that changes at different temperatures. Since the TTP was manufactured at a temperature of approx. 30 °C, this is taken as the zero point at which the TPP is exactly $l_{TTP}$ = 6.15 mm thick (see **Figure 24 (a)**). Thus, the thickness change at the max/min desired temperature can be calculated using the following equation:

$$\partial l_{T140} = \alpha_{Al} \cdot l_{TTP} \cdot \partial T = 23.5 \cdot 10^{-6}\ \mathrm{K}^{-1} * 0.00615\ m \cdot 110\ K = +1.6 \cdot 10^{-5}\ m$$

$$\partial l_{T-20} = \alpha_{Al} \cdot l_{TTP} \cdot \partial T = 23.5 \cdot 10^{-6}\ \mathrm{K}^{-1} \cdot 0.00615\ m \cdot -50\ K = -7.2 \cdot 10^{-6}\ m$$

It should be mentioned here that in operation, the BP does not have exactly the same temperature as the TP. The values $\partial l_{T\text{-}20}$ and $\partial l_{T140}$, therefore, correspond to the maximum step $\partial S$ that can occur between the TP and the BP. After a longer standing time at a required cell temperature of 120 °C, the BP also reaches a temperature of approx 76 °C[vi] despite its low thermal conductivity value. It can therefore be said that the step is minimized at longer constant operating temperatures. Soft thermal pads with a thickness of 0.5 mm and a thermal conductivity value of 6 $Wm^{-1}K^{-1}$ were used to contact the Peltier element with the TPP and the WHTP. With a thickness of the Peltier element of 3.75 mm and an installation height $l_{Pe}$ of 4.55 mm, an optimum compression of 20 % of the two heat-conducting pads is achieved. **Figure 24 (b)** shows a bottom sectional view of the BP together with the WHTP. **Figure 24 (c)** shows the top view of the cathode tempering unit without the TPP. For better illustration, the hidden edges were faded in, and the Peltier element was colored red. While with air, the connections are offset on both sides, the cooling water connections are on one

[vi] Value was determined experimentally in operation at 120 °C and a holding time of 30 minutes.

side. The offset reactant connections are due to the monopole plates and are decisive for the cross-flow configuration.

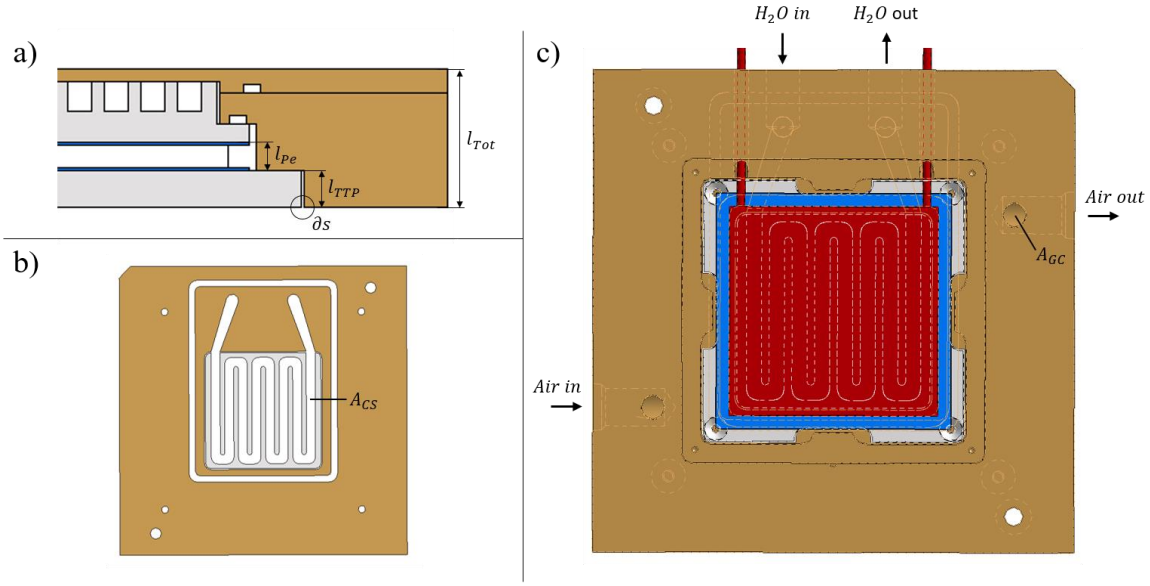


**Figure 24: (a)** The CAD model of a tempering unit from different perspectives with a partial cross-section, **(b)** the bottom sectional view of the BP and the WHTP and **(c)** the top view without the TPP and faded-in hidden edges.

### 4.1.4. Control unit

**Hardware**

In contrast to the commercial TP50 cell hardware, the cell temperature of the PET SC TP50 is set electrically. Therefore, the PET SC TP50 requires an additional control unit that includes a 24 V DC power supply and H-bridge-based power electronics. In contrast to the control cabinet of the PET SC TP285 design (see chapter 4.2.4), the control unit here is only an amplifier, which amplifies the +24 V signal coming from the test bench interface (Siemens SIMATIC interface card) (see **Figure 25**). The amplification per tempering unit is provided by an H-bridge circuit consisting of two BTN8982TA high-current half-bridges. The main advantage of this H-bridge circuit is that the polarity on the Peltier element can be reversed, allowing heating or cooling with the tempering unit. Another advantage is the design of the BTN8982TA high-current half-bridges. In contrast to conventional coupling relays, the current is switched here with the aid of a p-channel high-side MOSFET and an n-channel low-side MOSFET. Thus, very high currents can be switched quasi loss-free, and switching speeds in the kHz range can be easily achieved, which enables pulse width modulation (PWM) [106].

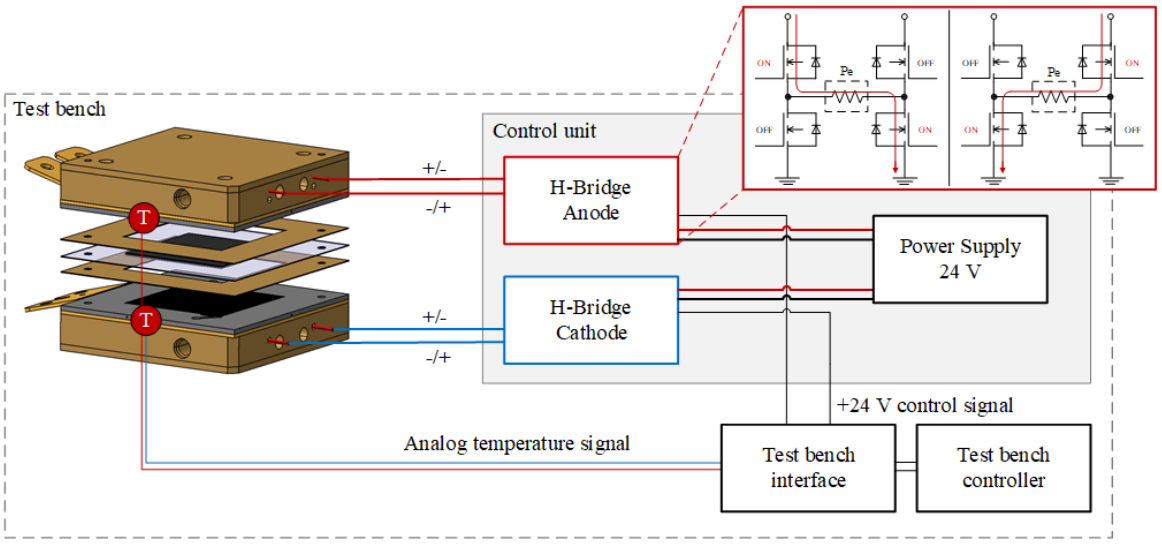


**Figure 25:** Simplified interconnection of the PET SC TP50 with the H-bridge-based control unit, which amplifies the +24 V signal of the test bench interface and the test bench. For a better understanding of the operation of the H-bridges, the switching states of the MOSFETs of the anode side during the heating and cooling modes have been magnified.

## Software

The software and thus the algorithm that processes the temperature data from the resistive PT100 temperature sensors and controls the performance of both tempering units is executed on the test bench controller (Siemens SIMATIC controller). As already described in 3.1.3, the control software is programmed in the VBA programming language and must be started separately before the test run. Since VBA is a very simple programming language, tasks can only be processed serially. Therefore the over-temperature alarms were not stored in the software but directly superordinated in the TAGs of the test bench controller. **Figure 26** shows the simplified sequence of the programmed software for the control of the anode and cathode cell temperature.

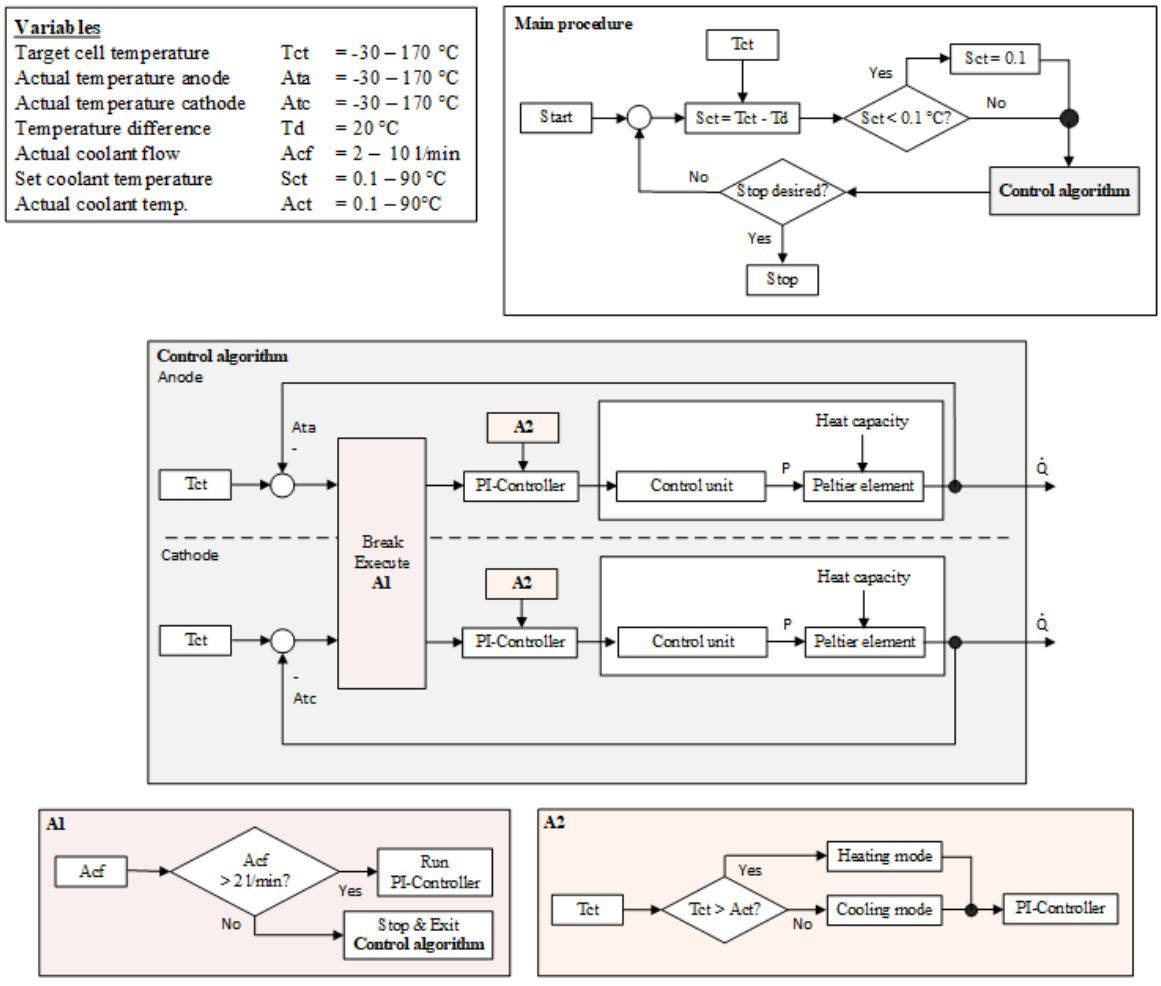


**Figure 26:** Simplified flow of the programmed software for anode and cathode cell temperature control. From the main procedure, the control algorithm is called, and in it, the algorithms A1 and A2 are arranged hierarchically further below.

When starting the software and thus executing the main procedure, the target cell temperature is first adopted, and the required coolant temperature is set. The variable *Td* is freely selectable, but the control of the temperatures was most stable at a temperature difference between coolant and target cell temperature of 20 °C. The limitation at 0.1 °C had to be chosen because of the test bench. Temperatures equal to or below 0 °C stop the coolant flow, and thus the temperature control process of the test stand cooling water.

After setting the coolant temperature, the control algorithm is executed, which describes the actual temperature control algorithm for the anode and cathode. A proportional–integral–derivative (PID) controller was used to control the temperatures. The PID algorithm generally follows the following equation:

$$Y(t) = K_p e(t) + K_i \int_0^t e(\tau)\,\partial\tau + K_d \frac{d}{dt} e(t) \tag{3.3.1}$$

Where *e* is the control deviation, $K_p$ the proportional component, $K_i$ the integral component with τ [0...t], and $K_d$ the differential component with the difference *d*. Since the D component does not react to the duration but to the speed at which the difference between the setpoint and actual value changes, it is only required for extremely dynamic systems. In the case of the PET SC TP50, the D component could be deactivated, and the control of the cell temperature could only be handled with the aid of two PI controllers. The parameters of the two PI controllers were determined heuristically using the Ziegler/Nichols oscillation method [107]. This method could be used without further ado, as the system cannot cause any damage even in a very unstable state. The specification of whether a positive (heating) or negative (cooling) temperature change is necessary is determined based on the coolant temperature *Act* and target cell temperature *Tct* (see **Figure 26 A1**). More precisely, when a target temperature of the cell below the cooling water temperature has to be reached, the Peltier element is triggered for cooling. This principle is derived from the operation of the Peltier element, where it is assumed that when the Peltier element is actuated, there arises a $\partial T$ between the two sides, and the amount of generated waste heat $\dot{Q}_w$ must be dissipated through the cooling water. The same controller parameters were used for both temperature control cases. However, depending on the test protocol, the minimum and maximum possible value of the $K_i$ component is limited. This can avoid excessive overshoot, especially

with significant temperature changes (e.g., -10 °C to 80 °C), where it takes more time to reach the target temperatures. Since the cooling water is essential for achieving low temperatures and its failure would lead to uncontrollable heating of the Peltier element, the flow is verified during each cyclic run of the control algorithm (see **Figure 26 A2**). If the coolant flow falls below the minimum value of 2 l/min, the control algorithm is interrupted, and the power supply to the Peltier elements is switched off. Should the coolant flow be present again during the next run of the control algorithm, the temperature control will be continued. The cycle time, which describes the period duration of a PWM signal, is specified by an internal timer of the test bench controller. For each PI controller, 1000 ms was specified as the PWM cycle time. This means that depending on the calculated and required power, the Peltier element is switched on for 0-1000 ms per cycle. For example, if 50 % of the output power is required, the Peltier element is turned on 500 ms of the cycle time (1000 ms). With this principle, on the one hand, very high outputs and thus fast rates of temperature change can be achieved, but slow and steady ones are also possible.

### 4.1.5. New opportunities with PET SC TP50

The new tempering units offer various advantages that are not available with conventional tempering using test stand cooling water. The cell temperature and thus its stability is crucial for accurate measurement results. **Figure 27 (a)** shows a typical control behavior of the PET SC TP50 anode temperature. At this point, it must be mentioned that the control accuracy of ±0.3 °C depends on the processing performance of the test bench computer and the switching speed of the Siemens SIMATIC interface card. Here, with the aid of an additional microcontroller (similar to the PET SC TP285, see chapter 4.2), which takes over the control, a significantly better control accuracy could be achieved. **Figure 27 (b)** shows a temperature cycle between 80 °C and -10 °C of the anode temperature used for the low-temperature stress test (LTST) in Chapter 5.3.

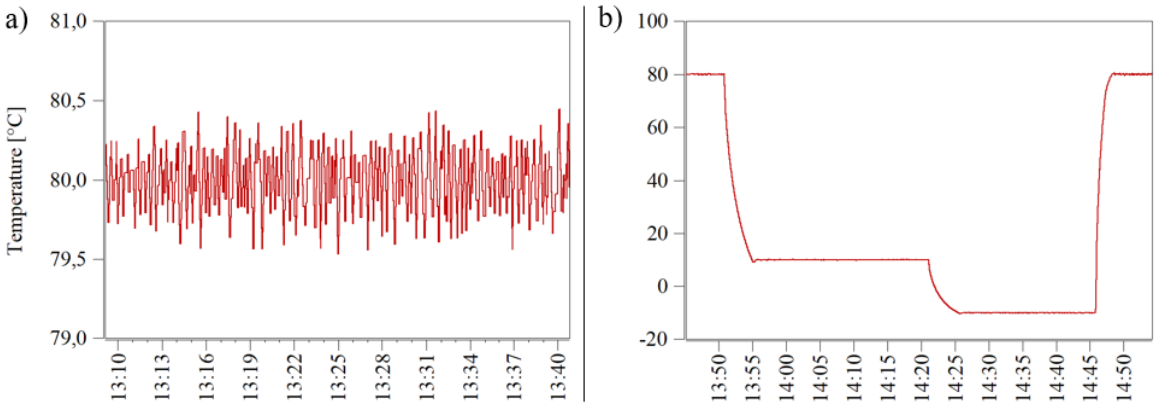


**Figure 27: (a)** The anode temperature control behavior of the PET SC TP50, and **(b)** a temperature cycle between 80 °C and -10 °C as performed in chapter 5.3.

Besides the wide working temperature range, the temperatures can be approached with high dynamics and low overshoots. **Figure 28 (a)** shows the cooling behavior of the PET SC TP50 at a temperature jump from 80 °C to 10 °C. The cooling rates determined are strongly dependent on the outside and the test chamber temperature. Higher dynamics are possible but require colder cooling water to dissipate the waste heat more efficiently and achieve better cooling rates of the tempering units. **Figure 28 (b)** shows the heating behavior during start-up at a temperature of -10 °C. At the first moment, a tremendous heating rate of more than 2 K/s is achieved, decreasing to 0.66 K/s from a temperature of 40 °C onwards. A standard Horiba FuelCon test bench of type C1000-LT achieves an average temperature change rate of 0.02 K/s, which is well below the dynamics of the PET SC TP50 at all times.

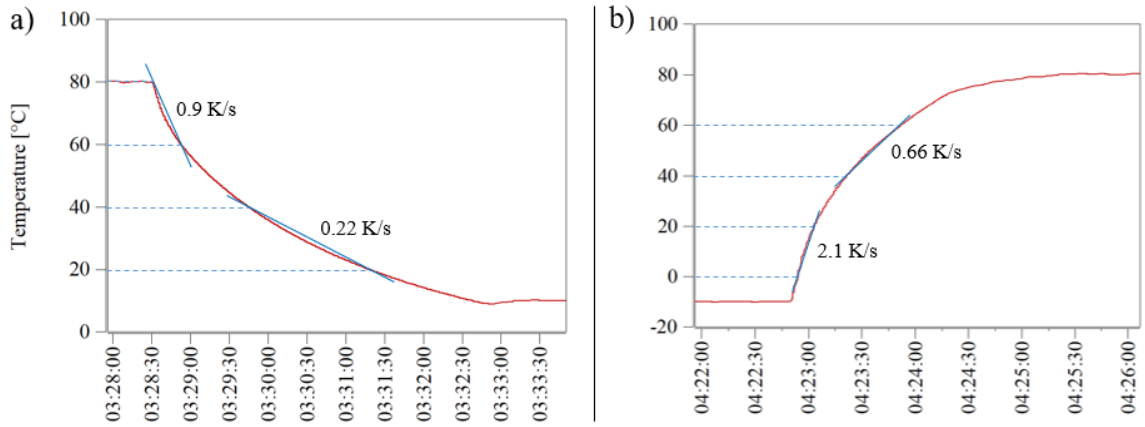


**Figure 28: (a)** Cooling behavior of the PET SC TP50 at a temperature jump from 80 °C to 10 °C, and **(b)** the heating behavior during start-up at a temperature of -10 °C.

## 4.2 PET TP285 single cell

### 4.2.1. State-of-the-art

The supreme challenge is the characterization of PEMFCs of an automotive size. Due to the significantly larger active surface area of 285 cm², a different flow and coolant flow field, and the fact that several hundred cells are stacked, which influence each other during operation, inhomogeneous operating parameters occur in the cells. A decisive inhomogeneous operating parameter is the non-uniform temperature distribution on the PEMFC surface. A well-known example is an operation at sub-zero temperatures. As a rule, the stacks are cooled down to the desired temperature in a climate chamber. At the start-up, an uneven temperature distribution then occurs during the heating process [41, 42]. This temperature distribution and the heating rate strongly depend on the output power and the thermal mass of the fuel cell stack. Here, the closer the number of cells is to that of a real automobile stack, the more realistic the experiment. The same applies to normal operation. Since a liquid coolant is usually used and the supply can vary from cell to cell, uneven temperature distribution can occur at higher current densities. This leads to a local reduction in performance and ultimately to degradation of the affected cells [31]. All conventional temperature control methods lack the ability to simulate temperature gradients or local hot spots at the surface of a PEMFC single cell. Furthermore, even with this cell size, cell temperatures outside the usual operating range and high rates of temperature change are complicated or require increased effort to achieve. All missing options require a further or new development of measurement technology for single cells in automotive size.

### 4.2.2. Characteristics

As with the small TP50 unit, the cell temperature of the TP285 unit is adjusted by means of the cooling water, which is tempered by the test bench. Therefore, the automotive size TP285 cell hardware has the same advantages and disadvantages as the TP50 cell hardware (listed in **Table 4**) and will not be enumerated again. Due to the identical points, it is obvious that further development of the tempering design would be beneficial for this size. Here, too, the last two disadvantages were decisive for further developing the cell hardware and partly determined the development of the new tempering units.

Therefore, the following boundary conditions had to be met in the final design of the PET TP285 single cell:

- A cell temperature between <**-20 °C**-**120 °C** should be possible.
- Heating and cooling rates of more than **1 K/s** and **0.5 K/s** should be possible.
- A temperature stability of <**±0.5 °C** (at all temperature points).
- Temperature gradients or local hot spots should be possible on the cell surface.
- Easy handling, i.e. easy set-up with a new PEMFC, should be given.

The fast dynamics, as well as the extended temperature range are also two decisive points for this PET cell hardware size, which can only be achieved by using Peltier elements. Nevertheless, due to the significantly larger cell size, a complete redesign of the tempering units must take place. On the one hand, there are no Peltier elements with an area of approx. 285 cm², and on the other hand, the newly added point (4) can only be achieved with several individually controllable Peltier elements per electrode. Like the small PET SC TP50 single cell, the PET SC TP285 single cell offers many advantages, but also some disadvantages. Although these are largely identical to those of the PET SC TP50, they are listed again below because of the associated technical data:

**Table 7:** All summarized advantages and disadvantages with the associated technical data of the newly developed single-cell PET SC TP285.

| **Advantages** | **Description** |
|---|---|
| Extended temperature range | Temperatures between -30 °C and 125 °C are possible in practice. The limitation at 125 °C is given by the used resistance-to-digital converters of the PT1000 temperature sensors (more information about this can be found in chapter 4.2.3). |
| Dynamics of temperature control | Due to the high cooling power of up to 2.368 W per electrode, heating rates of more than 1 K/s are possible. |

| Advantages | Description |
|---|---|
| Short controlled loop | Due to the smaller tempering areas and the short control loops, the temperature can be set within a control window of ±0.1 °C (in the controlled state). |
| Individually controllable tempering areas | Temperature gradients $\partial T_g$ of up to 70 °C over the temperature control surface can be achieved using the 64 controllable Peltier elements. |
| No further sources of contamination | Since glycol compounds are often added to the cooling water in the automotive sector in order to achieve low temperatures, this point was not listed in the boundary conditions. Nevertheless, the probability of contamination is also significantly lower here since no cooling water is used in the PET SC TP285. |
| Cost effective | With the all-in-one solution, temperature stress tests outside the usual working range of PEMFCs as well as standard long-term tests can be performed cost-effectively without the use of additional hardware (e.g. climate chamber). |

| Disadvantages | Description |
|---|---|
| Additional electrical hardware | For the control of the Peltier elements, an additional control cabinet is required, which regulates the power and the temperature of the 64 tempering areas. More information about this can be found in chapter 4.2.4. |

Since the PET SC TP285 is in operation for a significantly shorter time than the PET SC TP50, no clear statement can yet be made about its long-term stability. As with the PET SC TP50, it can be said that the only wear parts in the new automotive size cell design are the Peltier elements and the O-rings. Nevertheless, due to the similar operating principle, long-term stability similar to that of the PET SC TP50 can be assumed.

### 4.2.3. Design

As with the PET SC TP50 single cell, the “sandwich structure” has been retained for the automotive PET SC hardware. This means that, ideally, only one new MEA needs to be used to rebuild the PET cell hardware. Nevertheless, the development of the final PET SC hardware also took place in two development steps. At the beginning of the automotive PET SC hardware development, the MEA design level A2 was used. The MEAs of this design level could be characterized with a Tandem Technologies Ltd. TP288 cell hardware and had an active area of about 288 cm². During the development of the PET SC TP288 hardware, the MEA design level A3 was introduced, which can be characterized with a TP285 cell unit. Except for the dimensions of the components, the basic design and functionality of the TP288 components are identical to those of the TP285. Since the possibility of temperature control with Peltier elements was confirmed with the PET SC TP50 hardware, substantially different aspects had to be investigated for the PET SC TP prototype. In summary, the PET SC TP288 prototype served to verify whether

- the possibility exists to integrate several Peltier elements in parallel in one tempering unit;
- it is possible to create a temperature gradient or a local hot spot on the surface;
- such a large temperature control unit can be made of Ultem™ without warping;
- the electrical components, which are located close to the tempering components, can withstand temperature fluctuations.

**Figure 29** shows the CAD model of the PET SC TP288 prototype with the cathode tempering unit in exploded view. Most of the components of the tempering unit, such as the water-conducting plate **(a)**, waste heat transfer plate **(c)**, the 32 Peltier elements **(d),** base plate **(e)** and thermal transfer plate **(f)** of the prototype PET SC TP288 have almost the same design and function as those of the final PET SC version, namely the PET SC TP285. The exact function of the individual components is, therefore, described in detail later in the chapter. The main difference between the PET SC TP288 and the PET SC TP285 are the electrical components used for the power electronics **(b)** and the temperature sensor fingers **(g)**, as well as their arrangement and structure.

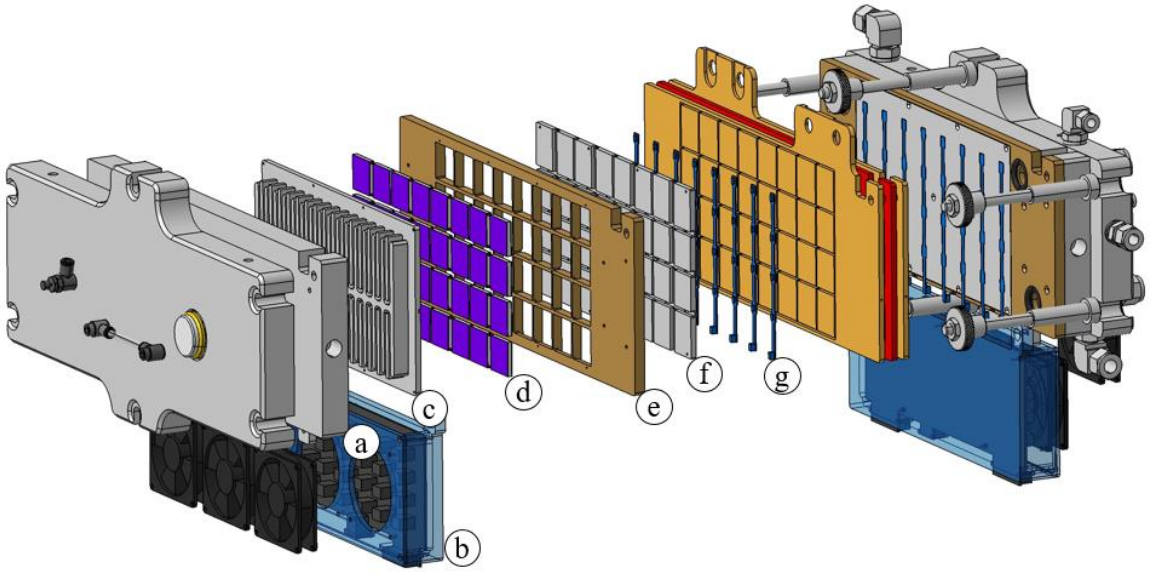


**Figure 29: (a)** The CAD model of the PET SC TP288 prototype with the cathode tempering unit in exploded view with the water-conducting plate, **(b)** the power electronics, **(c)** the waste heat transfer plate, **(d)** 32 Peltier elements**, (e)** the base plate, **(f)** the thermal transfer plate and **(g)** the temperature sensor fingers.

In contrast to the PET SC TP50, the PET SC TP288 is a redundant system that could theoretically also operate without a test bench. This means that the test bench communicates only with the PET cell hardware, or more precisely with the controller of the PET cell hardware, and transmits set point and actual values via the common Control Area Network (CAN) bus. Thus, the main task of the controller is to ensure the communication between the test bench and the PET cell hardware and to control the 64 tempering segments. As with the PET SC TP50, the respective PI controller increases or decreases the power of the individual Peltier elements via the cycle time of the PWM signal. To be able to process the data from the 64 PI controllers in quasi-real-time, a powerful microcontroller had to be selected. Therefore, the core of the controller is a Teensy 3.5 microcontroller from the company PJRC. The advantage of this microcontroller is the high clock rate of 120 MHz, the integrated buses, and the simple programming environment (more about this in chapter 4.2.4). **Figure 30** shows the CAD top view of the anode tempering unit and the simplified representation of the power supply and the controller.

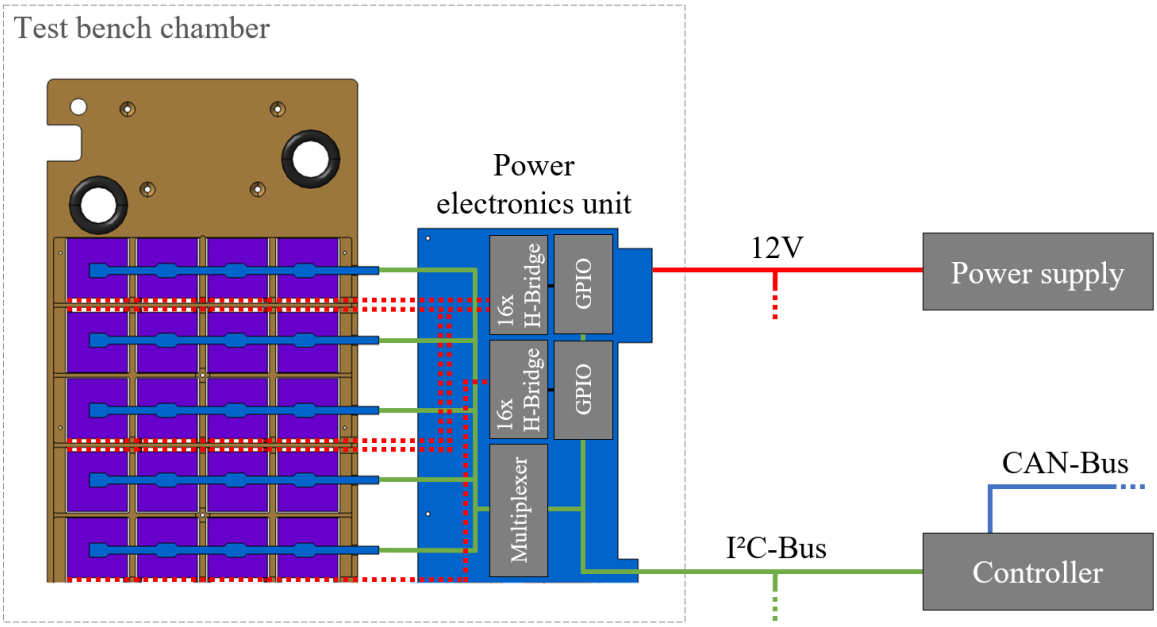


**Figure 30:** CAD top view of the cathode tempering unit with a simplified representation of the power electronics unit components and their arrangement. For better understanding, the current-carrying copper wires between the Peltier elements and the power electronics are shown in dashed red and the Inter-Integrated Circuit (I²C) bus wires in green.

Since the power electronics are virtually a part of the tempering unit, the communication between each power electronics and the controller takes place via two separate Inter-Integrated Circuit (I²C) buses (shown in green). Per tempering unit, the I²C bus is used to establish communication between two essential components of the power electronics: The central multiplexer, which switches the I²C bus for sensor evaluation between the eight identically addressed temperature sensor fingers with four I²C temperature sensors each, and the two General-Purpose I/O (GPIO) drivers with 16 outputs each for switching the H-bridge driver modules with which the electrical power for the respective Peltier elements is enabled. The Peltier elements are directly connected to the respective H-bridges of the power electronics by means of single-core sheathed copper wire (shown in dashed red). More precisely, two sheathed copper wires are required per Peltier element and thus a total of 64 wires per temperature control unit. Since each Peltier element can draw a maximum current of 4.2 A, wires with a diameter of 0.65 mm (0.332 mm²) were used. This was also the maximum possible wire diameter since the space for passing the cables between the individual layers of the tempering unit was limited. **Figure 31 (a)** shows a section of the anode power electronics and the wiring with the Peltier elements and the temperature sensor

fingers. The I²C temperature sensor fingers are screwed directly onto the temperature transfer plate (TTP) and contacted it via heat-conducting pads. The communication of the individual temperature sensor fingers with the power electronics is ensured via a Molex® pico flat connector and a ribbon cable. In this case, a pluggable connection was necessary since bus systems are very susceptible to interference and all temperature sensors communicate with the controller via the same I²C bus. **Figure 31 (b)** shows the commissioning of the PET SC TP 288 prototype. In the course of commissioning, the design, the electronics, and the software could be tested for their function, and thus the results could be incorporated into the further development of the PET cell hardware. In summary, the PET SC TP288 served as a proof of concept (POC) to verify whether the construction of such a segmented tempering unit was at all possible.

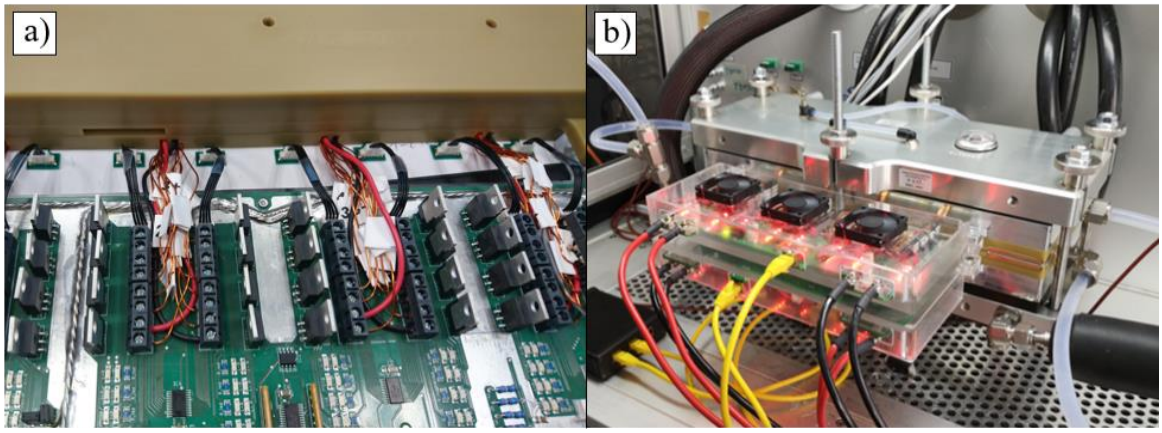


**Figure 31: (a)** Enlarged view of the tempering unit and the associated power electronics with the wiring of the Peltier elements and the temperature sensors, as well as **(b)** the commissioning of the PET SC TP288 prototype.

Although the first commissioning was successfully completed, stable and, above all, failure-free operation of the PET SC TP288 was only possible to a limited extent. Since the concept was not yet fully matured, some failures occurred during commissioning, which are described in detail in **Table 8**.

**Table 8:** The most essential failure cases detected during commissioning with the associated failure cause.

| Failure | Triggered by | Error cause |
|---|---|---|
| Uncontrolled heating or cooling | • GPIO communication error | • I²C bus overload<br>• I²C bus breakdown |
| Temperature detection failure | • Temperature sensor failure | • I²C bus overload<br>• I²C bus breakdown<br>• Short circuit of the I²C bus |
| Heating or cooling failure | • Burned out H-bridge<br>• Wire break<br>• GPIO communication error | • Short circuit of the copper wires<br>• Wiring ducts too narrow<br>• I²C bus overload<br>• I²C bus breakdown |
| Broken housing for power electronics | • Carelessness during assembly | • Unhandy cell components |
| Inhomogeneous tempering surface | • Temperature cycles | • Material tension (Ultem™) |

In addition to all the failures that occurred, there was also the safety aspect. This was not considered with the PET SC TP288, because, as already mentioned, the cell served as a POC. However, since the next version of the PET cell hardware will also be operated in 24/7 mode, the test bench must be able to shut down the PET cell hardware in the event of a fault. This made it all the more important to eliminate all the listed points of failure and enable the next generation of PET cell hardware for stable endurance-capable operation. If we now summarize all the listed error causes from **Table 8** and take into account the requirement of 24/7 operation, the following system-specific need for improved results for the next version:

- **A more stable and faster data bus.** Since many errors that occur can be traced back to the I²C bus, a data bus must be selected for the next PET cell concept that has both higher bandwidth and is less sensitive to EMC influences.

- **A new concept of temperature measurement.** In locations where the temperature fluctuates strongly (in this case -20 °C to 120 °C), the use of resistive temperature sensors is recommended. In contrast to digital sensors, these are much more robust, less sensitive to moisture, and have no logic of their own.

- **The more robust concept for the power supply of the Peltier elements.** The power lines must be robust and insensitive to environmental influences. Besides, the replacement of a Peltier element should be possible quickly and without complications.

- **Generation and provision of relevant data of individual components.** Important components, such as the H-bridges, must be able to transmit diagnostic information. This can reduce the overall probability of failure, improve transparency and shorten troubleshooting.

- **Customer-friendly and modular design.** First and foremost, the design should be modular and ensure easy handling during commissioning. A crucial point is the separation of the power electronics from the temperature control unit. But it should also be possible to replace wearing parts, such as the Peltier elements, without complications.

- **Safety functions must be guaranteed.** In the event of a malfunction, both the test bench must be able to shut down the PET cell hardware, and the PET cell hardware must be able to shut down the test stand safely. In addition, the internal control electronics must be fail-safe and shut down all hardware in the event of a fault.

All the points listed ultimately lead to a reduction in the probability of failure and must be taken into account in the next PET cell hardware design. In summary, the overriding goal in developing the next PET cell hardware concept was to create cell hardware that is stable over the long term, customer-friendly, and, above all, self-safe.

**Figure 32** shows the CAD model of the final PET SC TP285 with the exploded view of the anode tempering unit. Each tempering unit consists of 8 basic components, namely the temperature sensor printed circuit board (PCB) **(a)**, the thermal transfer plate **(b)**, the base plate **(c)**, the 32 Peltier elements **(d)**, the power-unit PCB **(e)**, the waste heat transfer plate **(f)**, the water-conducting plate **(g)** and the stabilization plate **(h)**. All components are screwed together and can be replaced very easily and quickly in the case of a failure. In contrast to the prototype PET SC TP288, the two temperature control units of the PET SC TP285 form a closed unit. The power electronics have been completely outsourced, and the two tempering units have the regular dimensions of the commercial TP285. This has significantly improved the handling and thus the customer-friendliness of the PET cell hardware. Furthermore, the tempering units can be installed in any TP285 cell hardware and are therefore not location-bound.

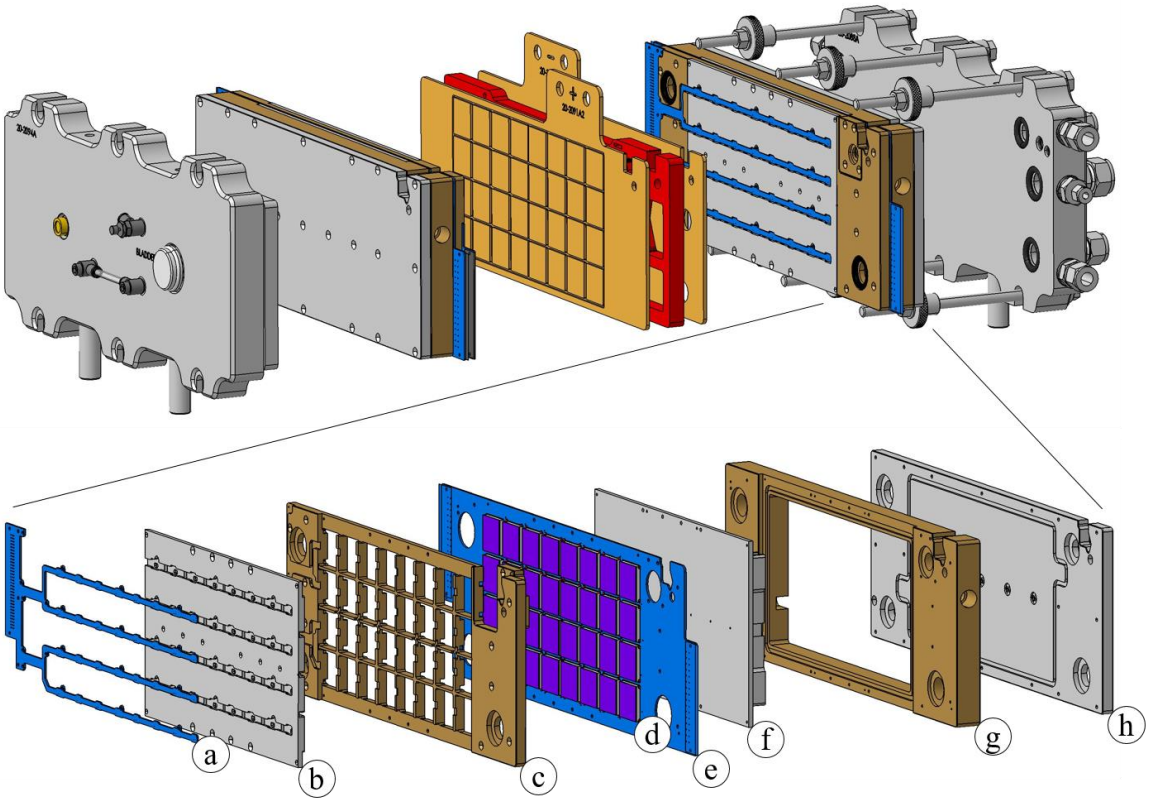


**Figure 32: (a)** The CAD model of the final PET SC TP285 and the exploded view of the anode tempering unit with the temperature sensor PCB, **(b)** the thermal transfer plate, **(c)** the base plate, **(d)** the 32 Peltier elements, **(e)** the power-unit PCB, **(f)** the waste heat transfer plate, **(g)** the water-conducting plate and **(h)** the stabilization plate.

**Figure 33 (a)** shows the fully assembled anode tempering unit and **(b)** the PET SC TP285 during initial commissioning at -20 °C.

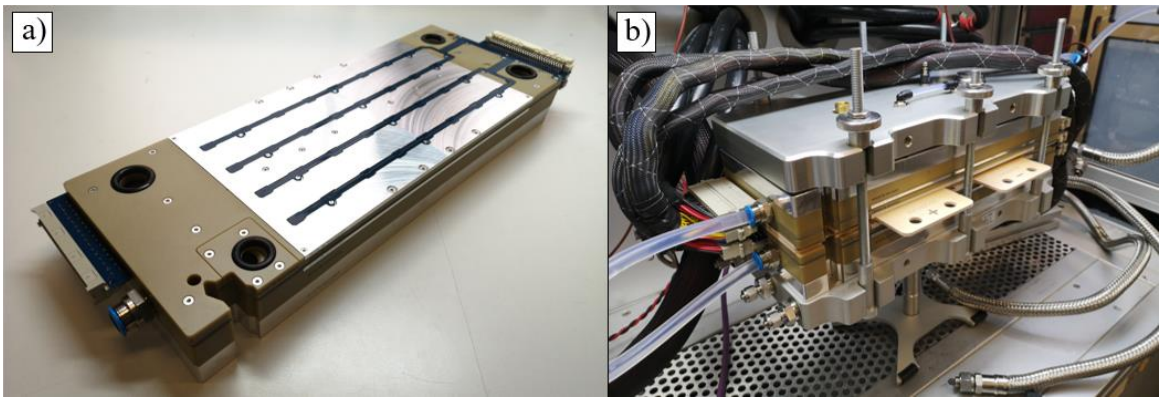


**Figure 33: (a)** The fully assembled anode tempering unit and **(b)** the PET SC TP285 during initial commissioning at -20 °C**.**

The components and their exact function of the anode tempering unit are described step by step below. It should be mentioned at this point that the cathode tempering unit is identical in construction but has no gas-carrying channels.

**Temperature sensor PCB**

One of the main differences to the PET prototype is the temperature measurement concept. While digital I²C temperature sensors with their own evaluation unit were used for the PET SC TP288 prototype, resistive Pt1000 sensors with a three-wire connection were used for the PET SC TP285. Pt1000 sensors belong to the family of resistance temperature detectors (RTD) with a positive temperature coefficient. These are based on the relationship between temperature and the associated lead resistance and have a resistance of 1000 **Ω** at a reference temperature of 0 °C [108]. The resistance of the respective Pt1000 sensor as a function of temperature can be calculated as follows:

$$R_{Pt1000} = R_{0,Pt1000} \cdot (1 + \alpha_{Pt} \cdot \partial T) \qquad (3.4.1)$$

With the resistance at the current temperature $R_{Pt1000}$, the reference resistance at 0 °C $R_{o,Pt1000}$, the temperature coefficient $\alpha_{Pt}$, and the deviation temperature between 0 °C and the current temperature $\partial T$. The advantages of the measuring concept with Pt1000 sensors are apparent. In addition to the simple measuring principle and the analog technology, the

RTD sensors are very robust, have a compact design and are cost-effective. Furthermore, due to the high resistance and the three-wire connection, overall measurement accuracy of less than 0.5 % can be achieved. All relevant properties of the Pt1000 temperature sensors used in the PET SC TP285 are listed in **Table 9**.

**Table 9:** Relevant properties of the Pt1000 temperature sensors used in the PET SC TP285.

| **Property** | **Value** |
|---|---|
| Standardization | DIN EN 60751 |
| Nominal resistance $R_{o,Pt1000}$ | 1000 **Ω** |
| Tolerance | Class B ($R_{o,Pt1000}$ ±0.12 %) |
| Temperature coefficient $\alpha_{Pt}$ | $3.85 \cdot 10^{-3}\ K^{-1}$ |
| Temperature range | -50 °C to +130 °C |
| Self-heating | 0.8 $Km^{-1}W^{-1}$ at 0 °C |

In the PET SC TP288 prototype, the temperature sensor fingers were arranged transversely with four digital temperature sensors each. The main disadvantage of this arrangement was the proximity to the thermal transfer plate. During temperature cycles, condensation formed on the Molex® pico flat connectors, which caused the I²C bus system to malfunction. In the PET SC TP285, the temperature sensor board consists of a longitudinally arranged unit with 32 temperature measuring points and a central plug connection. A significant advantage of this arrangement is the increased distance between the central connector and the heat transfer plate.

Furthermore, by merging the measuring lines, it was possible to select a significantly more robust connector from the company Harting®, which increases user-friendliness. The evaluation electronics for the individual temperature sensors are located in the additional control cabinet (more on this in chapter 4.2.4). The front and connector side of the temperature sensor PCB of the anode tempering unit is shown in **Figure 34 (a)** and **(b)**.

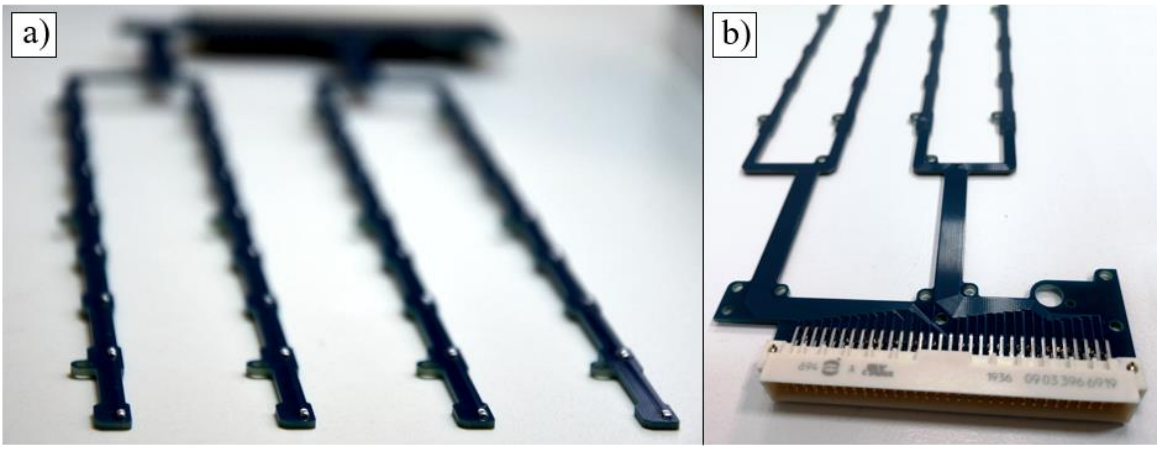


**Figure 34: (a)** The front and **(b)** the connector side with the Harting® connector of the anode temperature sensor PCB used in the PET SC TP285.

### Thermal transfer plate

As with the PET SC TP50, the essential task of the thermal transfer plate (TTP) is to transfer the amount of heat $\dot{Q}_T$. To achieve the previously defined heating and cooling rates, the mass of the TTPs was also not allowed to exceed a specific value. With the performance data of the Peltier elements (more under the Peltier element) and the formula 3.4.1, the maximum permissible mass of the TTP can be calculated. Since the monopolar plates are made of thin stainless steel and the exact mass is not known, they are neglected in this calculation. Due to the good thermal conductivity and stability, aluminum was again used for the calculation of the maximum permissible mass $m_{TTP}$, as well as for the production of the TTP. Using the direct relationship between the heat quantity for heating $\dot{Q}_{Th}$ and cooling $\dot{Q}_{Tc}$, the mass of the current collector $m_{CC}$, the specific heat quantity of copper $c_{Cu}$ and aluminum $c_{Al}$, and the temperature change rate $\dot{T}$, the permissible material mass of the TTP $m_{TTP}$ can be calculated:

$$m_{TTP} = \dot{Q}_{Tc,sum} | \dot{Q}_{Th,sum} \cdot -\dot{T}(m_{CC} * c_{Cu}) \cdot (\dot{T} \cdot c_{Al})^{-1} \qquad (3.4.1)$$

$$m_{TTP} = \frac{1184 | 1776\, Ws - 0.5 | 1\, K^{-1}s (1.879\, kg \cdot 385\, JKg^{-1}K^{-1})}{0.5 | 1\, K^{-1}s \cdot 896\, JKg^{-1}K^{-1}} \qquad (3.4.2)$$

$$m_{TTP-Cool} = 1.835\ Kg \qquad m_{TTP-Heat} = 1.175\ Kg \tag{3.4.3}$$

With a maximum permissible mass $m_{TTP}$ of 1.175 kg, there was sufficient scope for the design of the TTP. Two crucial points were decisive for the design: the reduction of the transverse influence of the neighboring Peltier elements and the flat contact surface to the current collector. Both points are indirectly related to each other, as intermediate webs had to be incorporated into the TTP to ensure a flat and at the same time stable surface. On the one hand, this design feature reduces the thermal mass and thus the transverse influences between the Peltier elements, and on the other hand, they provide sufficient contact surface to support the TTP with the help of the base plate. In the end, a mass of 0.53 kg was achieved by design, which is significantly below the calculation. **Figure 35 (a)** shows the bottom side of the TTP, which is in contact with the 32 Peltier elements via heat-conducting pads, and **(b)** the top side with the cutouts for the temperature sensor PCB. The temperature sensor PCB is screwed directly onto the TTP and the heat conduction between the Pt1000 temperature sensors and the TTP is ensured via heat conduction pads.

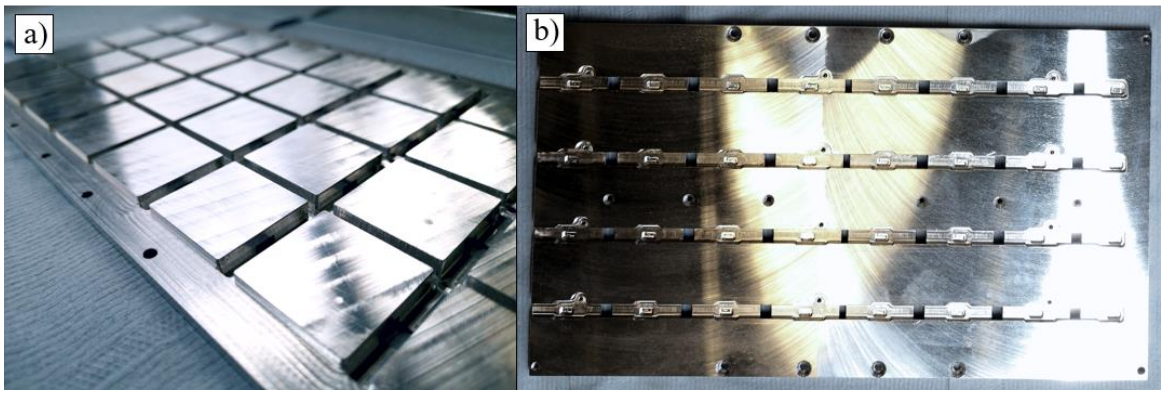


**Figure 35: (a)** The bottom side of the thermal transfer plate (TTP), which is in contact with the 32 Peltier elements via heat-conducting pads and **(b)** the top side with the cutouts for the temperature sensor PCB.

**Base plate**

As with the PET TP 50, the main task of the base plate (BP) is to isolate the individual components from each other and to support the TTP. **Figure 36 (a)** shows the BP placed on the waste heat transfer plate of the cathode tempering unit. In the standard configuration, the power-unit PCB is still screwed between the two components, while the Peltier elements are placed in the individual recesses. Due to the wide temperature range and the necessary hardness of the BP, Ultem™ was also used as the material here. This made it possible to manufacture the intermediate webs, which also support the TTP, narrow and still ensure sufficient stability. To ensure sufficient and, above all, even compression of all heat conduction pads, the TTP is screwed to the waste heat plate with 18 continuous screws. **Figure 36 (b)** shows the connector side of the tempering unit with the cut-out in the BP for the temperature sensor PCB. The temperature sensor PCB is screwed reinforced to the edge of the BP, which provides additional stability during the plugging process. **Figure 36 (c)** shows the gas guide adapter of the hydrogen channel. With the help of this adapter piece, other PEMFC single-cell formats can be installed in the PET SC TP285.

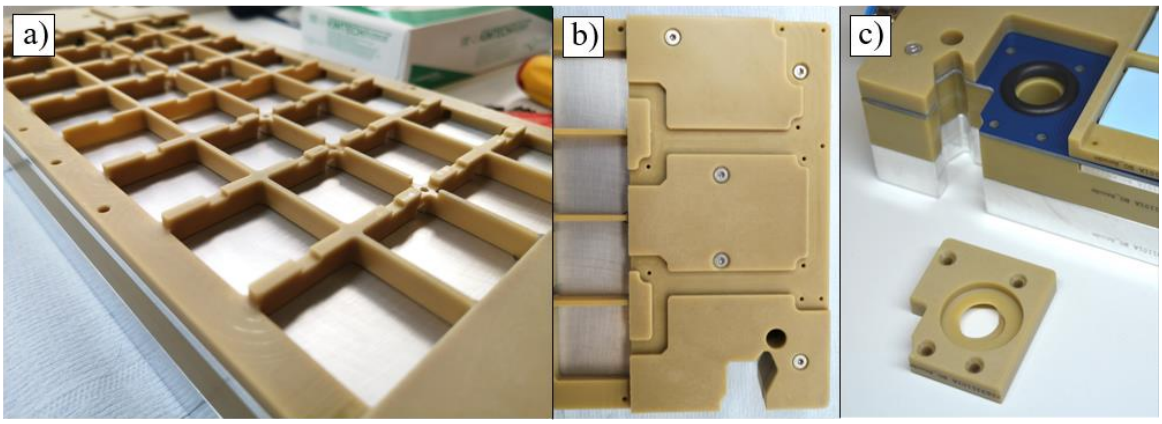


**Figure 36: (a)** The base plate placed on the waste heat transfer plate of the cathode temperature control unit without the power-unit PCB and **(b)** the connection side of the tempering unit with the cut-out in the base plate for the temperature sensor PCB.

**Peltier element**

Probably the most significant challenge in the development of the PET SC TP285 was the possibility of targeted temperature spreading over the active area of 285 cm². A crucial point was the selection of the suitable Peltier elements. Since most of the doped semiconductor bars in a Peltier element are connected in series, the smaller the Peltier element, the lower the operating voltage. In other words, the more individually controllable Peltier elements, the lower the operating voltage and the higher the total operating current at full load. This, in turn, increases the cross-section of the system's power supply lines and is reflected in the manufacturing costs of current-carrying components. Therefore, as with the PET SC TP288 prototype, Peltier elements with dimensions of 30 x 30 mm were selected, which in turn corresponds to 32 Peltier elements per tempering unit. The key data for the selected Peltier elements are shown in **Table 10**.

**Table 10:** The key physical properties of the selected Peltier element used with the PET SC TP285.

| **Property** | **Value**[vii] |
|---|---|
| Maximum voltage $U_{max}$ | 16.4 V |
| Maximum current $I_{max}$ | 4.2 A |
| Maximum cooling capacity $Q_{cmax}$ | 37 W |
| Maximum temperature difference $\partial T_{max}$ | 71 °C |
| Maximum working temperature $T_{wmax}$ | 200 °C |
| Dimensions | 30±0.3 mm x 30±0.3 mm x 3.6±0.2 mm |

[vii] With a tolerance of ±10 % for thermal and electrical parameters specified by the manufacturer.

With the known cooling capacity of a Peltier element, the total cooling, as well as the heating capacity of one tempering unit, can thus be calculated:

$$Q_{Tc,sum} = n_{Peltier} \cdot Q_{Tc} = 32 \cdot 37\ \text{W} = 1184\ \text{W}$$

$$Q_{Th,sum} = n_{Peltier} \cdot Q_{Tc} = 32 \cdot 55.5\ \text{W} = 1776\ \text{W}$$

**Power-unit PCB**

The power supply of the Peltier elements is one of the main differences to the PET SC TP288 prototype. While the Peltier elements of the PET SC TP288 were supplied with power via sheathed single-core copper wires, this is done via the power-unit PCB in the PET SC TP285. The power-unit PCB thus represents the interface between the Peltier elements and the Harting® connector and is therefore installed between the base plate and the waste heat transfer plate/water-conducting plate. Due to the stacked arrangement, the power supply board must have high planarity, withstand temperatures of up to 90 °C and contact pressure of 1.5 N/mm². **Figure 37** shows the layout of the anode power- unit PCB of the PET SC TP285. Due to the installation space, it was not possible to combine all power supply lines (shown in red) in one Harting® connector. For this reason, the power supply lines of 16 Peltier elements were combined on two Harting® connectors.

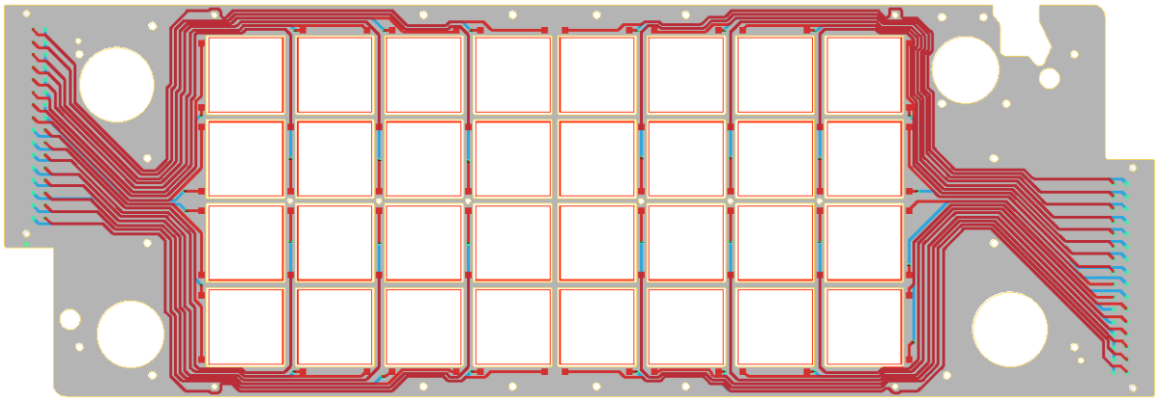

**Figure 37:** Layout of the PET SC TP285 anode power supply board with the power supply lines shown in red.

The power-unit PCB was manufactured in double layers with a copper layer thickness of 70 µm each. With an average power supply line length $l_{Psl}$ of 15 cm and 1 mm width, the line resistance $R_{Psl}$ and finally the waste heat of the power unit board can be calculated here:

$$R_{Psl} = 2 \cdot l_{Psl} \cdot \rho_{Co} \cdot {A_{Psl}}^{-1} = 2 \cdot 15\ cm \cdot 1.69 \cdot 10^{-8}\ \Omega m \cdot (1\ mm\ \cdot 70\ \mu m)^{-1} = 0.072\ \Omega$$

With the power supply line resistance per Peltier element, the total power dissipation of the power-unit PCB can be calculated:

$$P_{Co,loss} = 32 \cdot R_{Psl} \cdot I_{max} = 32 \cdot 0.072\ \Omega \cdot 4.2\ A = 40.6\ W$$

It is imperative that the power loss is dissipated in full-load operation to avoid unnecessary heating of the power-unit PCB and thus keep the line resistance as low as possible. For this reason, the waste heat transfer plate was designed to be as large as possible so that most of the power-unit PCB surface can rest on it. This prevents overheating, and the waste heat can be dissipated directly into the cooling water of the test bench. The power-unit PCB of the anode tempering unit, which is equipped with the Peltier elements and the Harting® connectors, is shown in **Figure 38 (a)**. Each Peltier element is only connected to the circuit board via the two release points. This allows easy replacement in case of a defect. The enlarged view of the power-unit PCB, in which the solder joints are clearly visible, as shown in **Figure 38 (b)**.

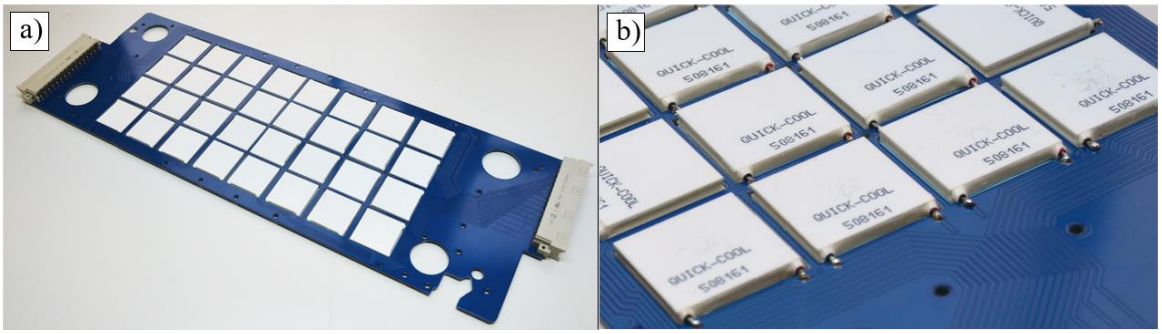


**Figure 38: (a)** the overall view of the assembled anode power-unit PCB, as well as **(b)** the magnified view, in which the solder joint of the respective grid and Peltier element can be seen in figure.

**Waste heat transfer plate & water-conducting plate**

The waste heat transfer plate forms the direct interface between the test bench coolant circuit and the thermal actuator. The main task of the waste heat transfer plate (WHTP) is therefore, to dissipate the generated waste heat via the Peltier elements and the power-unit PCB. To optimally dissipate the waste heat and ensure sufficient stability, the WHTP is made of aluminum. As with the PET SC TP50, a balance had to be found between stability and cooling performance. Therefore, the average cooling channel diameter of the WHTP is 54 mm², which corresponds to an active cooling surface $A_{CS}$ of $31.23 \cdot 10^4$ mm². Due to the large channel diameter, the limiting factor here is the maximum flow rate of the test rig's cooling water pump. At a maximum of 166.7 cm³/s, the water pressure of ~180 kPa is significantly lower than that of the small PET cell hardware. Nevertheless, the cooling surface was ultimately sufficient to dissipate the waste heat generated. More information on this topic can be found in chapter 4.2.5. Like the BP, the water-conducting plate (WCP) is made of Ultem™. The main functions of the WCP are to direct the cooling water to the WHTP and to enclose it. The test bench coolant hoses are connected directly to the two sides of the WCP using Festo quick couplings.

**Figure 39** shows the underside with the cooling channels of the WHTP in the assembled state with the WCP.

**Figure 39:** Underside of the aluminum heat transfer plate with the visible cooling channels in the assembled state with the water-conducting plate made of Ultem™.

### Stabilization plate

Due to the size and, in particular, the long format of the tempering unit, distortion and thus an uneven support surface would occur without the stabilizing plate (SP). Therefore, the tempering unit is built on an SP, which is milled from a precision aluminum plate. The main characteristics of the precision aluminum plate are high stability, high surface quality, and, above all, a uniform surface. In addition, the direct contact between the SP and the endplate also allows the Tandem Technologies Ltd. endplate to be tempered, which minimizes cold bridges and water condensation. Viton™ O-rings were used to seal the water- and gas-carrying spaces between the SP and WHTP. **Figure 40** shows the bottom view of the SP.

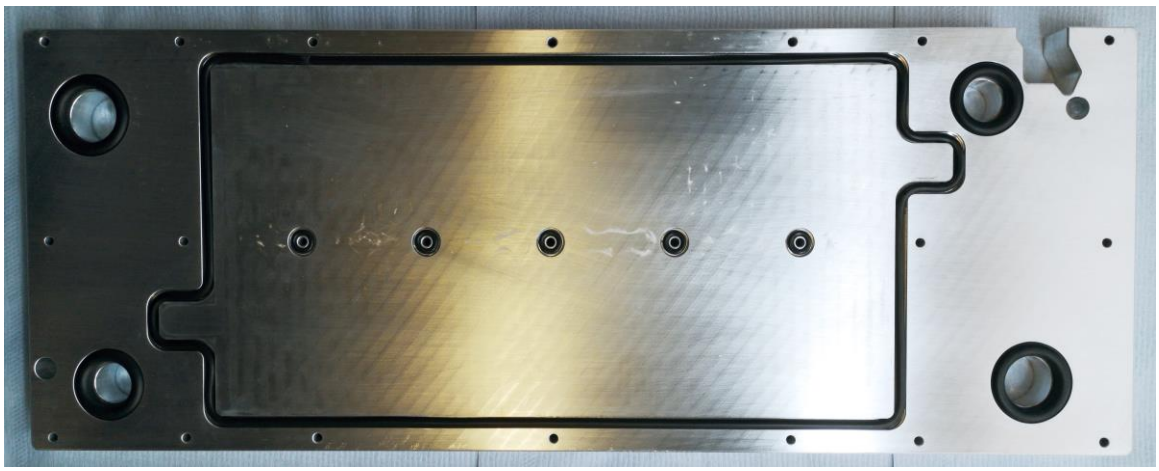

**Figure 40:** The stabilizing plate made of precision aluminum with the Viton™ sealing rings.

### Constructive properties

Similar to the PET TP50, a homogeneous contact surface to the current collector must be ensured at all operating temperatures. Therefore, it was also important to consider the thermal expansion of the materials at both high and low temperatures. **Figure 41 (a)** shows the side sectional view (longitudinal direction) of the tempering unit with the enlarged sectional view of one temperature control loop. Due to the very limited installation space and the short cable lengths between the Peltier element and the power unit PCB, heat conduction pads with a thermal conductivity value of 6 $Wm^{-1}K^{-1}$ and a thickness of 1 mm were used. With a Peltier element thickness of 3.6 mm and an installation height $l_{Pe}$ of 5.2 mm, the heat-conducting pads of the 32 Peltier elements can be compressed by approx.

20 %. **Figure 41 (b)** shows the front sectional view of the tempering unit. As with the PET TP50, the TPP partially rests on the BP. The most critical point here is step $\partial S$, where the TPP has the greatest material thickness (here $l_{TTP}$) of 4 mm and at the same time rests on the BP. Here, the greatest thermal expansion occurs at the possible edge temperatures (-20 °C and 120 °C) of the tempering unit. If it is also assumed that the TPP was manufactured at a temperature of 30 °C, the thickness change can be calculated with the following equation:

$$\partial l_{T140} = \alpha_{Al} \cdot l_{TTP} \cdot \partial T = 23.5 \cdot 10^{-6}\ \mathrm{K}^{-1} * 0.00520\ m \cdot 110\ K = +1.1 \cdot 10^{-5}\ m$$

$$\partial l_{T-20} = \alpha_{Al} \cdot l_{TTP} \cdot \partial T = 23.5 \cdot 10^{-6}\ \mathrm{K}^{-1} \cdot 0.00520\ m \cdot -50\ K = -6.1 \cdot 10^{-6}\ m$$

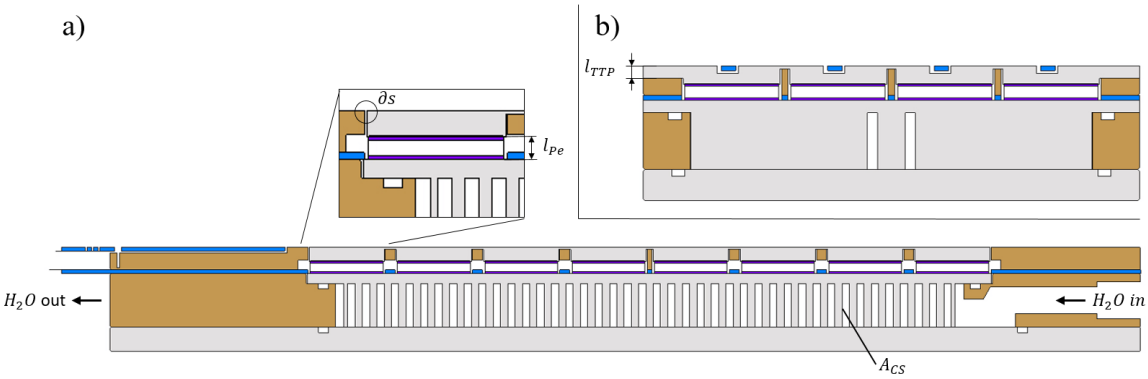


**Figure 41: (a )**The side sectional view (longitudinal direction), with **(b)** the front sectional view of the anode tempering unit.

### 4.2.4. Control cabinet

Decoupling the power electronics from the tempering unit was an important step to increase both the handling and the modularity of the system. In contrast to the PET SC TP288 prototypes, the tempering units of the PET SC TP285 consist of 32 analog sensors and actuators, which are completely controlled by the control cabinet. Thus, it can be summarized that the control cabinet has the following main tasks:

- Control of the 64 temperature control loops, including the power supply
- Communication with the test bench
- Ensure the safety of the system

**Hardware concept**

The internal structure of the control cabinet is shown in simplified form in **Figure 42**. Due to the high electrical power, the control cabinet is connected directly to the 400 V power supply of the house mains via a CEE plug. The other two connections are, on the one hand, for the CAN communication between the control cabinet and the test bench and, on the other hand, for enabling the load breaker, which is directly connected to the 24 V voltage supply of the test bench and is switched off in the event of a fault.

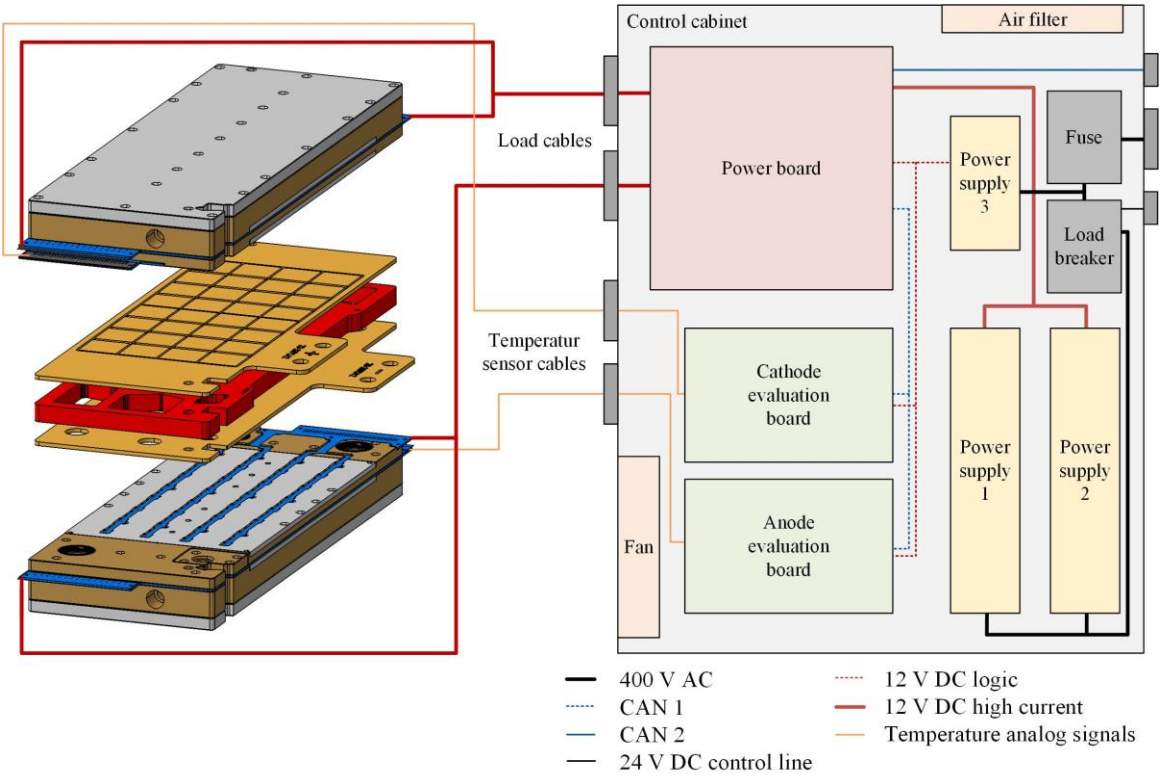


**Figure 42:** Simplified representation of the internal structure of the control cabinet for the PET SC TP285

The internal 12 V voltage supply for the electrical components of the control cabinet is provided by three power supply units. Two of these parallel-connected high-current power supplies connected to one phase of the 400 V mains, provide the electrical energy for the Peltier elements. The third power supply unit supplies the logical components of the boards, including the three microcontrollers, and is not switched off by the load breaker in the event of a fault. This arrangement is necessary to be able to continue communicating with the PET SC TP285 in the event of a fault. As with the other components of the PET SC TP285

cell hardware, attention was paid to the modularity of the control cabinet. For this reason, a strict separation was made between the electrical components that release the electrical power to the Peltier elements and those that evaluate the temperatures. The electrical power for the 64 Peltier elements is provided by the power board. Each channel consists of an IFX9201SG H-bridge from the company Infineon Technologies. The output stage of each H-bridge consists of four n-channel MOSFETs that allow the polarity on the Peltier element to be changed for heating or cooling. To reduce the probability of system failure, the H-bridges are controlled via digital pins, one for direction and one for on/off state, and via the serial peripheral interface (SPI). The advantage of the SPI is the possibility of communication with the respective H-bridge. Important information such as over-temperature, over-current or under voltage of the respective H-bridge can be queried here. A PJRC Teensy 3.6 microcontroller was used here as the central processing unit. The core of this microcontroller is an MK66FX1M0VMD18 chip from the company NXP Semiconductors, which has a clock frequency of 180 MHz. Another highlight of the microcontroller are the many available analog and digital interfaces, including the two CAN buses that can be used in parallel. The CAN 1 bus is used for internal communication with the anode and cathode evaluation boards, and the CAN 2 bus for communication with the test bench. The microcontroller cyclically receives the actual temperatures via the CAN 1 bus, evaluates them and controls the 64 temperature control loops. Each tempering unit has its own evaluation board, which sends the temperature messages cyclically to the CAN 1 bus system. As already mentioned, analog Pt1000 temperature sensors were used for the PET SC TP285. For the conversion of the analog signal, an analog-to-digital converter (ADC) of the type MAX31865 was used. Besides the SPI, the advantage of these devices is the high resolution of 15 bits and a measuring frequency of up to 47.6 Hz. Furthermore, the current status of the ADC can be queried via the SPI, which facilitates the detection of short circuits or open circuits. Data processing and transmission of the measurement data into the CAN 1 bus is performed by a Teensy 3.5 microcontroller from the company PJRC. To be able to detect a bus failure in time, a watchdog is implemented on the Teensy 3.6 of the power board. This receives cyclical feedback from the two evaluation boards. If no feedback is received within a defined time, the temperature control is stopped, and an error message is an output on the test bench. The interior of the control cabinet is shown in **Figure 43 (a),** and the exterior front and rear view with the Harting® connectors and the 400 V mains connection in **(b)**.

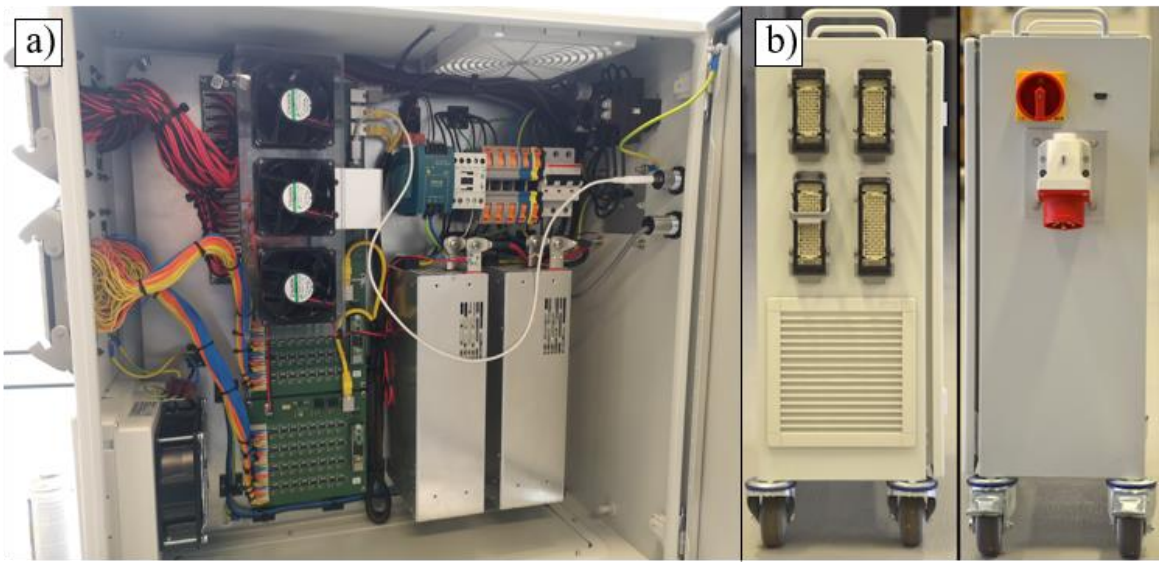


**Figure 43: (a)** The interior of the control cabinet of the PET SC TP285, as well as **(b)** the front and rear view with the Harting® connectors and the 400 V mains connection.

### Software

Due to the local separation of the microcontrollers and the internal and external communication via the two CAN buses, each bus participant has its own software algorithm. Therefore, it is all the more important that individual safety functions are implemented at the respective bus nodes and that no dangerous states can occur in the event of a complete or brief failure of communication. **Figure 44** shows the VBA software algorithm that must be run on the test bench to operate the PET SC TP285. The TAG variables that are displayed in the test work main view for the input or output of values are shown in orange. The most important input variables here would be the set temperature of the individual areas *Tat*, the activation or deactivation of the temperature control *Ca* and the setting of the ramp function *Rf*. With the latter, defined temperature ramps can be run that protect the system and reduce wear on electronic components. In addition to the 64 current range temperatures *Cat*, the current states of the H-bridges *Aps*, the watchdog timer alarms *Ewt*, and the temperatures alarms *Aat* are displayed in the test work main view. Since all necessary safety functions are executed on the power board's microcontroller, only the actual coolant flow *Acf* is monitored in the test bench software. If the coolant flow falls below the minimum permissible value *Mcf*, the temperature control is deactivated via the control variable *Ca*. Besides the active monitoring of the coolant flow *Acf*, alarm values are stored on all actual temperatures

TAGs, which switch off the test bench and thus the PET SC TP285 at temperatures above 125 °C.

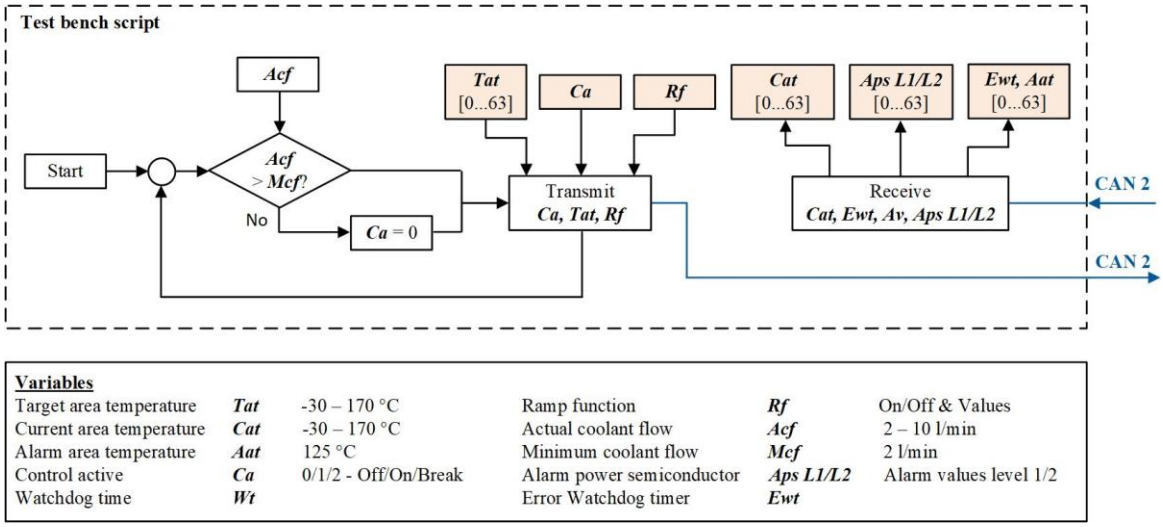


**Figure 44:** Algorithm of the test bench VBA software for the control of the PET SC TP285.

While the software algorithm on the test bench is written in the VBA language and executed on the Siemens SIMATIC controller, the Arduino programming environment with a C-like language is used to program the Teensy microcontrollers. When starting the microcontrollers, all data bus systems, as well as interfaces, are initialized once. Afterward, the programmed algorithm starts and is then in the endless data processing loop. **Figure 45** shows the simplified algorithm of the anode and cathode evaluation board. The 64 analog temperatures are read out via the ADC converter, digitized and written to the CAN 1 bus with an update rate of 10 ms.

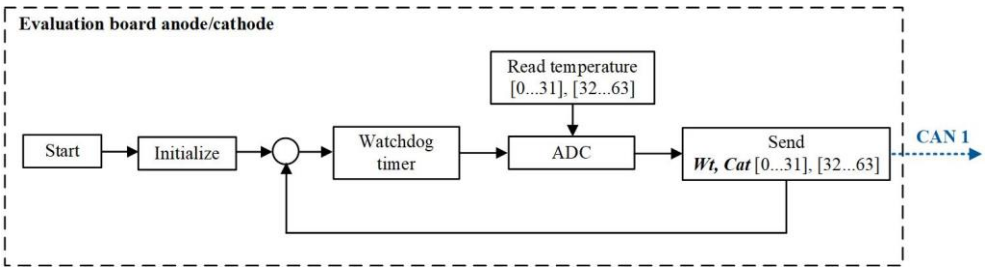


**Figure 45:** Simplified software algorithm of the anode and cathode evaluation board.

**Figure 46** shows the simplified algorithm which is performed on the power board. Due to the complexity of the algorithm, it becomes immediately clear that the actual master participant of the CAN 1 bus is the power board. The main loop shows the simplified main

program sequence with the respective subroutines, such as the transmission subroutine TS, the alarm subroutine AS, and the control subroutine CS. As with the evaluation board, all data bus systems and interfaces are initialized once at the beginning and then executed in the endless loop. The first subroutine TS is mainly responsible for receiving and sending data via the two CAN buses. In addition to the reception and forwarding of the temperatures and the communication with the test bench, the communication to the two evaluation cards is also monitored here. In the event of an error, the variable *Ewt* is written, which is then evaluated later in the alarm subroutine. When all values have been received and sent, the alarm subroutine AF is executed. In the first step, it is checked whether one of the 64 measured actual temperatures exceeds the maximum permissible working temperature *Aat* and in the next step whether one of the 64 power semiconductors reports a level 2 alarm or the variable *Ewt* was activated before. If an alarm activation AA occurs, the temperature control is deactivated, and the PET SC TP285 is transferred to the safe state. Leaving this state can only be done by restarting the control cabinet and thus the microcontroller. Before starting the control subroutine CS, a check of the control-active variable ***Ca*** is made whether the temperature control is to be activated or stopped. Besides the two states, the value transfer to the control subroutine CS can additionally be interrupted. In this way, the 64 temperature values, as well as the ramp functions, can be entered without the control subroutine immediately adopting the newly entered values. This allows easy parameterization and simultaneous approach of the desired temperatures. The core of the whole algorithm is the control subroutine CS, which controls the 64 temperature areas simultaneously. As with the PET SC TP50, PI controllers without a D component were used here. Each of the 64 control loops thus has its own PI controller, whereby the parameters of the PI controllers were also determined heuristically here using the Ziegler/Nichols oscillation method d [107]. A significant difference between the PET SC TP50 control is the choice between heating and cooling mode. While in the small cell hardware, the coolant temperature is taken into account; here the mode is selected according to the sign of the correction value P. This means that if the sign is negative, the cooling mode is used, and if the sign is positive, the heating mode is used. Another difference is the limitation of the controller. Each PI controller has a setting range for the output variable P between 0 and 100. With a cycle time of 1000 ms, an increase by 1 corresponds to an extension of the duty cycle by 10 ms. To avoid possible overshoots or undershoots, an anti-windup filter has been implemented. In contrast to the direct limitation of the I component, with the anti-windup filter

the P and I components are only limited when the maximum output variable Y is reached. When the set point is reached, there is then a decrease in the I component and thus in the output variable Y.

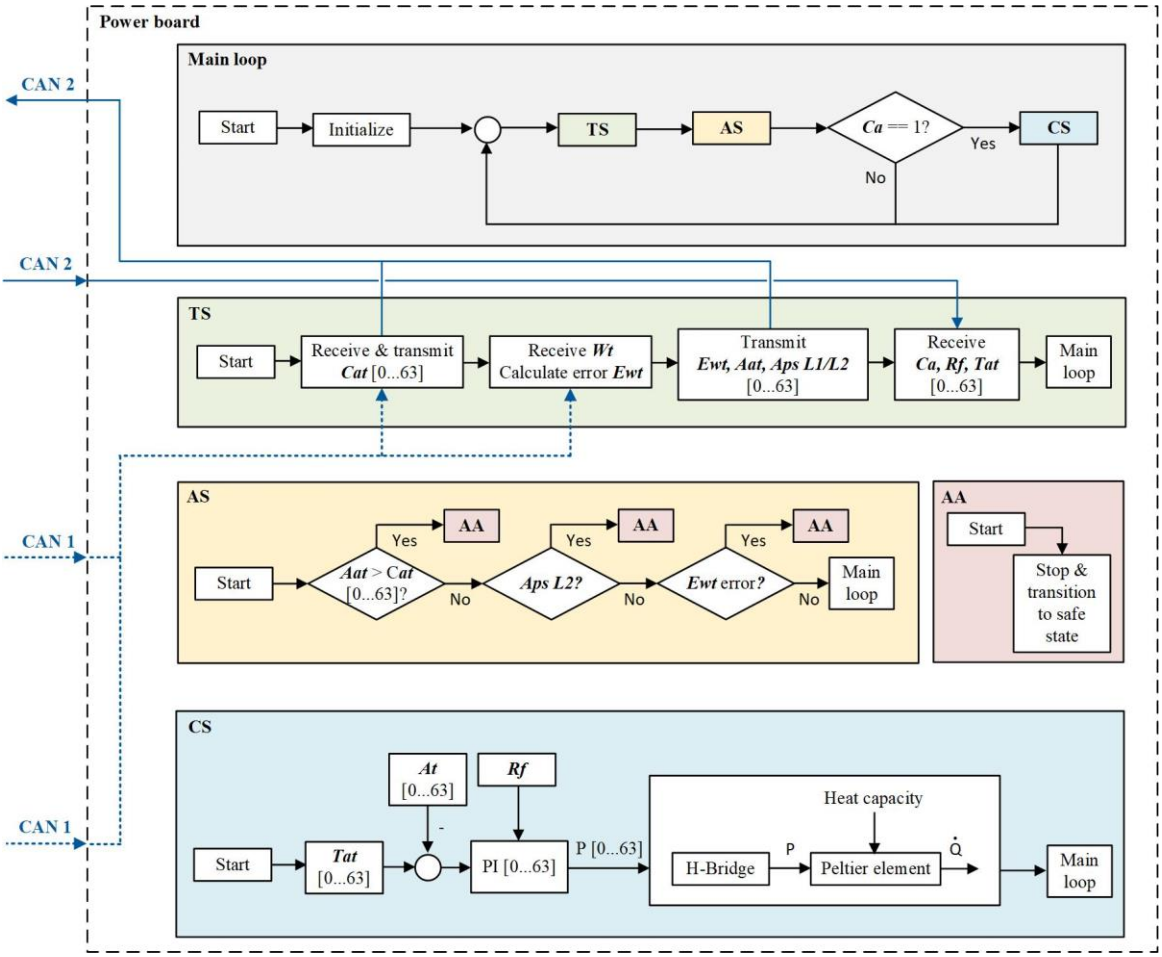


**Figure 46:** The simplified algorithm performed on the power board, which controls the tempering of the 64 surfaces of the PET SC TP285.

### 4.2.5. New opportunities with PET SC TP285

Besides the PET SC TP50, the PET SC TP285 also offers significant advantages over a commercial single cell tempered with test bench cooling water. The control stability of the temperature control of the 64 tempering areas is shown in **Figure 47 a)**. Here, the significantly more stable control compared to the PET SC TP50 is immediately apparent. Due to the faster calculation of the PID parameters and the significantly faster PWM modulation, an average control deviation of ±0.1 °C can be achieved. Short-term over- or undershoots do occur during stable operation or dynamic temperature jumps, but they are compensated quickly and specifically. **Figure 47 b)** shows a temperature jump from 120 °C to -20 °C. The different temperature dynamics can be attributed to the position of the individual tempering areas. While the inner areas cool down more quickly, the outer areas take significantly longer. In addition, the contact points to the solid power cables (300 mm²) influence the cooling dynamics of the outer areas. Nevertheless, cooling rates of up to 1.4 K/s (from 120 °C to 100 °C) can be achieved. **Figure 47 c)** shows a temperature jump in the opposite direction, from 0 °C to 120 °C. Due to the 50 % higher heating power, temperature rates of up to 2 K/s (Low-temperature start-up at -20 °C) can be achieved here.

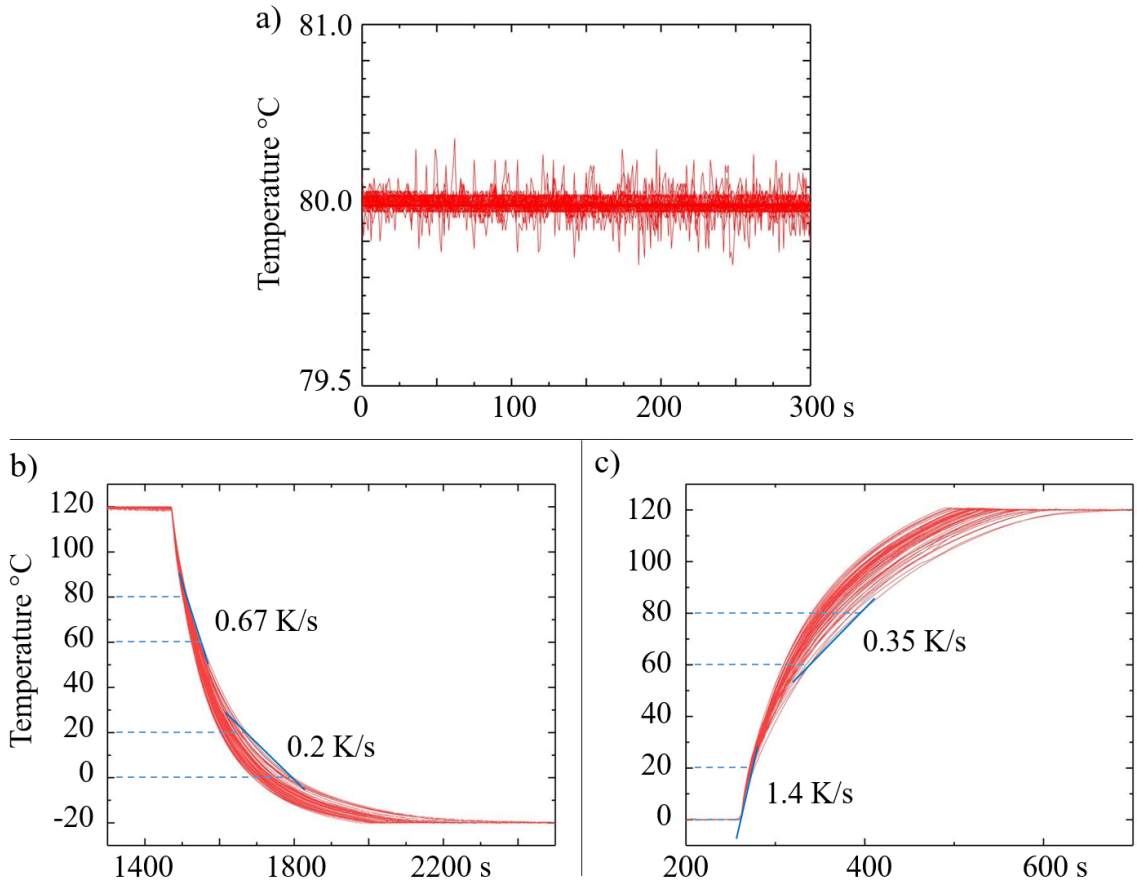


**Figure 47: (a)** Temperature profiles of all 64 temperature sensors with the visible control stability at 80 °C, a **(b)** temperature jump from 120 to -20 °C with the cooling rates, and **(c)** an opposite temperature jump from 0 to 120 °C with the heating rates.

With the mentioned tempering rates, a typical low-temperature cycle between 80 °C and -10 °C can be carried out in less than 10 min with the presented design. On the other hand, a low-temperature cycle between 120 °C and -20 °C can be performed in less than 30 minutes. The individually controllable tempering segments of the PET SC TP285 make it possible to simulate several scenarios of a fuel cell stack during operation. In addition to the possibility of running a temperature jump over a defined ramp function (see **Figure 48 (a)**), temperature gradients in the plane as well as across the cell between anode and cathode (see **Figure 48 (b)**) or even local hot spots (see **Figure 48 (c)**) can be simulated.

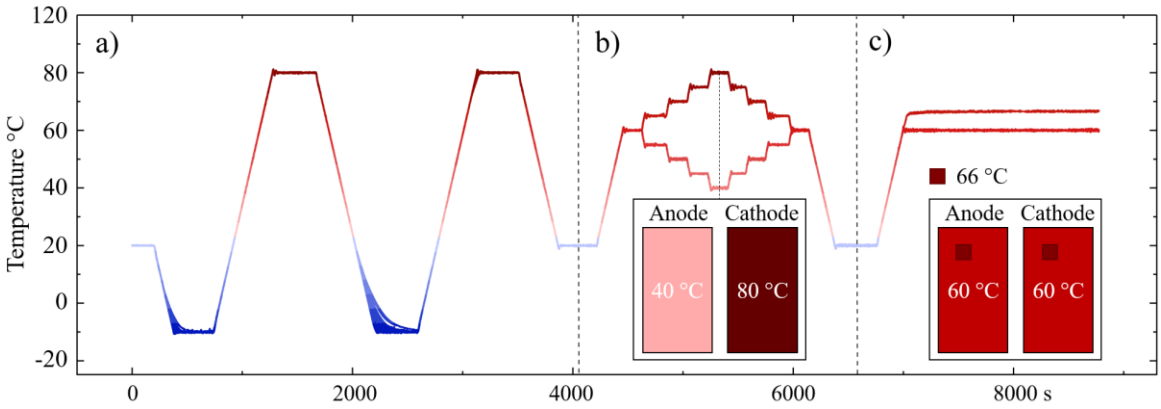


**Figure 48:** Temperature profiles of all 64 temperature sensors while performing cycles between **(a)** 80 °C and -10 °C with a defined ramp, **(b)** with the subsequent spreading of the anode and cathode temperatures to a final temperature of 40 °C/80 °C, and **(c)** finally setting a local hot spot of 66 °C vs. 60 °C cell temperature.

**Figure 49 (a)** shows a temperature gradient of 70 °C in the plane during operation, i.e. with an MEA and closed-cell unit. In the longitudinal direction, a temperature difference of up to 10 °C is therefore possible between adjacent segments. This temperature gradient can be used to demonstrate once again how small the overshoots are and how accurately the temperature is ultimately set. The set temperature gradient of 10 °C to 80 °C over the anodic current collector surface was also confirmed by a thermal infrared image (**Figure 49 (b)**).

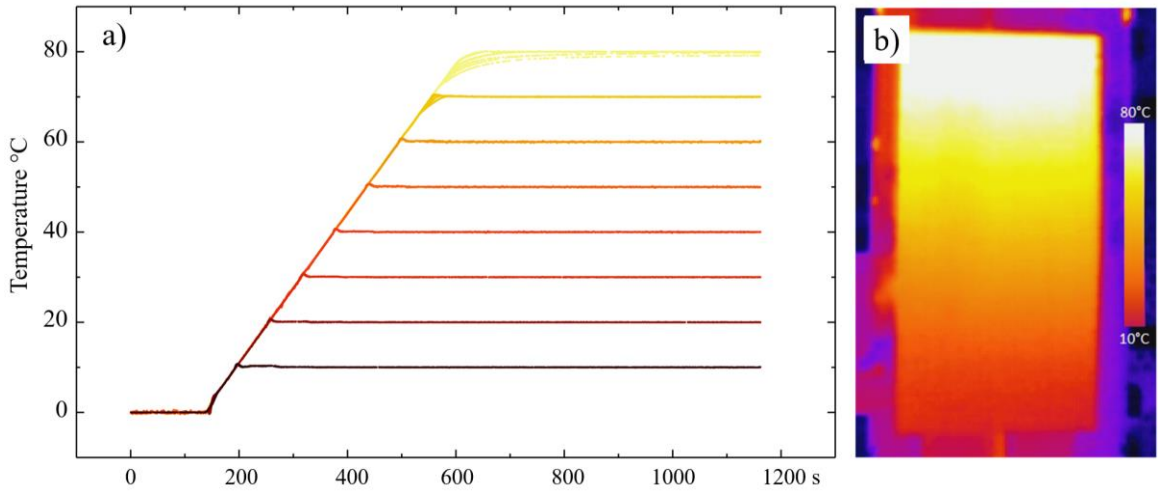


**Figure 49:** Temperature profiles of all 64 temperature sensors when a horizontal temperature gradient of **(a)** 10 °C to 80 °C is set in ramp mode, and **(b)** the corresponding thermal infrared image of the anodic current collector surface.

# 5 Results and discussion

This chapter deals with the experimental procedures and the associated measurement results. This chapter's main focus is the targeted degradation of PEMFC single cells caused by temperatures below the freezing point of water. Since temperature is a major factor in degradation, the ability to determine the local temperatures of a PEMFC single cell via impedance was also demonstrated. Since different cell sizes, as well as different versions of the PET SC TP were used to set the cell temperature, the individual test procedures and the associated measurement results are divided into separate sub-chapters.

## 5.1. Determination of the local temperature using the cell impedance

### 5.1.1. Introduction

As mentioned earlier, the cell temperature of a PEMFC is one of its most important operating parameters. Various degradation mechanisms and diverse electrochemical processes, such as the HOR, proton transport across the membrane or the ORR, are strongly dependent on the cell temperature. Therefore, the individual cell temperature determination after shutdown and prolonged downtime, especially at ambient temperatures below 0 °C, can be of immense importance. Due to their heat capacity, the inner cells of a stack can still be well above 0 °C, while the edge cells can already be below this value. This could lead to uneven degradation of the cells. To avoid this and keep the degradation as low as possible, the individual cell temperature can be used to adjust the start-up and thus the operating strategy [91, 109, 110]. Probably the simplest and at the same time cheapest way to determine the cell temperature would be to use a commercially available resistive temperature sensor placed close to the active surface. In a full-scale automotive stack (active area of ~285 cm²) with ~400 cells, where the space between the cells is very limited, measuring the temperature with a standard temperature sensor is hardly possible. An alternative is to measure the coolant temperature. However, the measured temperature does not correspond to the actual membrane or CL temperature. The cell impedance measurement is an attractive alternative to determine the cell temperature without using a resistive temperature sensor. With the impedance response and the corresponding EEC model, the model parameters can be used to accurately determine the cell temperature in a range between -5 °C and

60 °C. In this experiment, the cell temperature was adjusted with the PET SC TP50 prototype, and an MEA with an active area size of 43.56 cm² was used. The MEA has a 15 µm thick polymer electrolyte membrane with an anode/cathode platinum loading of 0.05/0.45 mg Pt/cm². A GDL with a total thickness of 235 µm was used on both coated CLs. More detailed data on the MEA are not known and may also not be published.

### 5.1.2. Test methodology

The entire test run was programmed in the test bench programming language VBA and fully automated. **Figure 50** shows the simplified sequence of a measurement procedure loop. To ensure reproducibility, the measurement procedure loop was repeated three times for each temperature step.

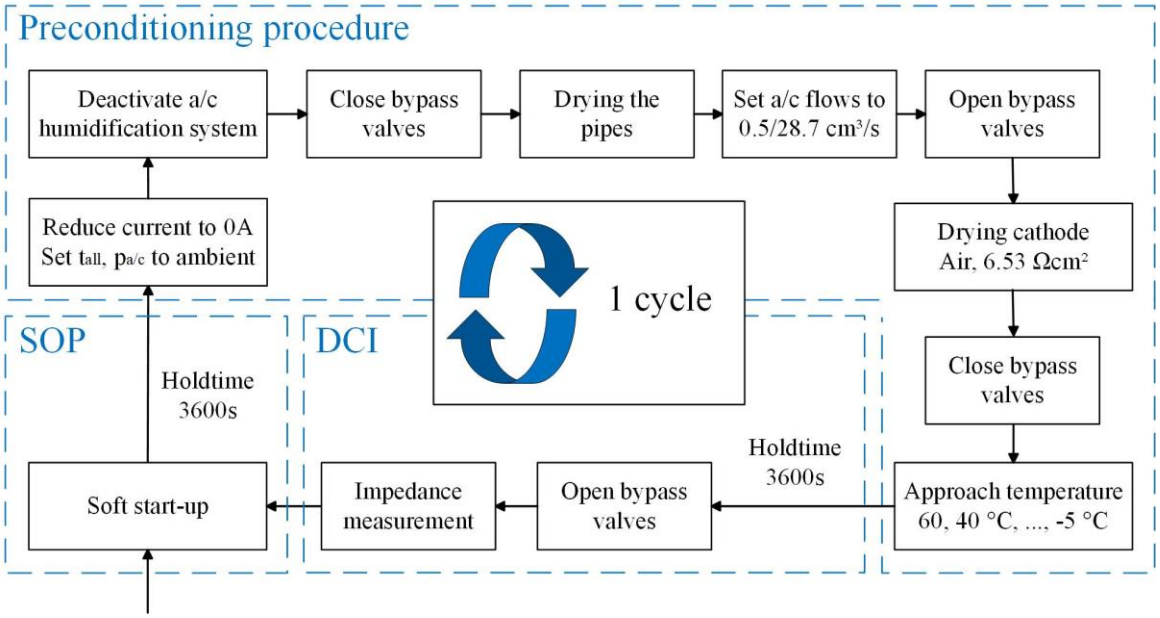


**Figure 50:** Simplified sequence of the measurement procedure loop, with the stable operating point (SOP), preconditioning to maintain the same measurement parameters, and determination of the cell impedance (DCI).

The measurement procedure loop, or more precisely one temperature measurement cycle, can be divided into the parts described below.

**Stable operation point (SOP)**

The main task of the SOP is to bring the cell carefully and in a defined way to the standard working parameters. In this process, the start-up has been programmed so that it is irrelevant whether the cell was previously at a temperature below 0 °C or at 60 °C. Therefore, in the first phase, the cell was bypassed and heated to a target temperature of 60 °C. Parallel to the heating of the cell, the reactants were heated to the desired temperatures of 80 °C. When a gas temperature of 60 °C was reached, the anode/cathode humidification was turned on and set to dew point temperatures of 46 °C (50 % RH). Once all target temperatures were reached, the bypasses were opened, and humidified $H_2$ and air were fed directly into the cell at flow rates of ~8.3 cm³/s and ~16.7 cm³/s, respectively. Upon reaching an OCV of ~0.9 V, the cell output pressure was set to 200 kPa with a defined ramp, and subsequently, the current was ramped up to the current density of 0.5 A/cm² at a ramp rate of 0.0023 A/cm² per s and held at this current density for 3600 s. In the final step, the target current density of 0.8 A/cm² was set and held for 4600 s until the preconditioning procedure was subsequently started.

**Preconditioning procedure**

Besides the cell temperature, the cell's residual water content is one of the most important influencing parameters in impedance measurements. Therefore, the preconditioning process is one of the key steps in temperature determination. Before starting the drying and the actual preconditioning, the cell must be prepared. Therefore, the first step is to set the load to 0 A (for OCV), turn off humidification, and set the output pressure and all heaters to ambient conditions. To dry the gas lines and remove residual liquid water, the cell was bypassed, and the lines were purged for 600 s with maximum flows of $H_2$ and air. Subsequently, the flow rates of $H_2$ and air were adjusted to 0.5 cm³/s and 28.7 cm³/s, respectively, and passed back into the cell. Since the humidity on the anode side remains constant, the water content of the membrane and the proton network is controlled only by the cathode airflow. During the drying process, the water content in the membrane and protonic network is determined from the measured impedance at a frequency of 2 kHz. After reaching the desired high-frequency resistance (HFR) of 6.53 Ωcm², the cell was bypassed and tempered to the target temperature.

**Determination of the cell impedance (DCI)**

To stabilize the entire system, the cell was kept in bypass for 3600 s at the desired temperature. After this waiting time, the anode and cathode bypasses were opened and reactants with flows of 0.5 cm³/s and 2 cm³/s were introduced into the cell. After a waiting time of 60 s at OCV, the impedance spectra were subsequently recorded in a frequency range between 10 kHz and 0.11 Hz and current amplitude of 20 mA. Since the gases were fed into the cell, both unpressurized and unheated at minimal flows, dehydration of the membrane and the proton-conducting network in the CL was avoided.

### 5.1.3. Measurement results

To fit the measured impedance data, an EEC model was used, which consists of 5 EEC elements (see **Figure 51 (a)**). These include the uncompensated (Nafion® -electrolyte) resistance $R_u$, the charge transfer resistance, $R_{ct}$, the double layer capacitance, $C_{dl}$ , the adsorption resistance, $R_{ads}$ and the adsorption capacitance, $C_{ads}$, which originate from the specific quasi-reversible adsorption of the sulfonate-groups of Nafion® on the surface of the Pt-electrocatalyst [76, 111, 112, 113, 114, 115]. The fitting and calculation of the numerical values of the model parameters were performed using the freely available software EIS Data Analysis 1.3 [116]. **Figure 51 (b)** shows two examples of fitting impedance data to the EEC model.

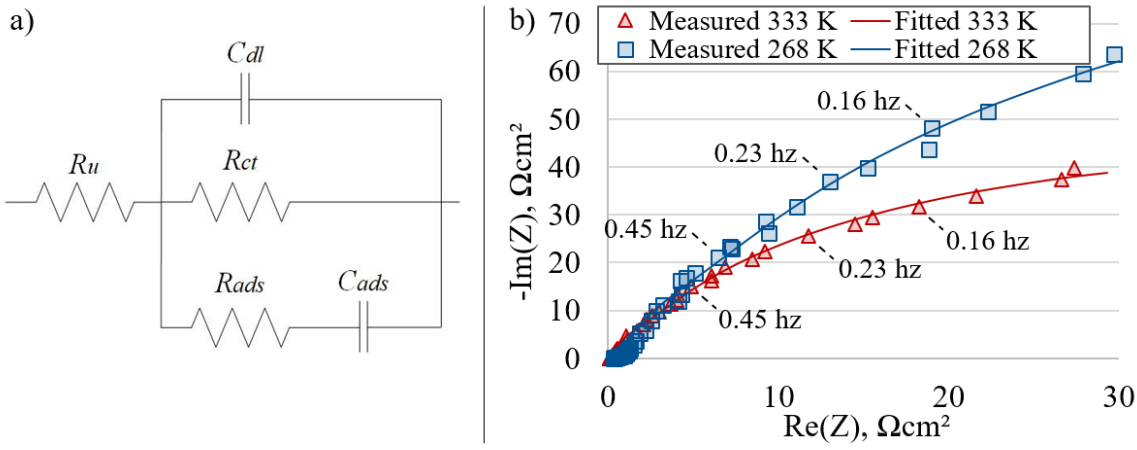


**Figure 51: (a)** Physical impedance model consisting of 5 equivalent circuit elements for fitting the impedance data measured with the PEM single cell at OCV, and **(b)** typical examples of the impedance spectra (open symbols) together with the fit to the equivalent circuit (solid lines).

It can be seen that both the visible quality of the spectra shown in **Figure 51 (b)** and the calculated individual parameter error values are sufficiently low for each fitted spectrum. A prerequisite for the accuracy and good reproducibility of the low-frequency points is the consistent preconditioning procedure and the stable operating parameters during the impedance measurements [117]. The temperature dependencies of the equivalent circuit parameters (except for the $C_{dl}$, which will be discussed later) are shown in **Figure 52**.

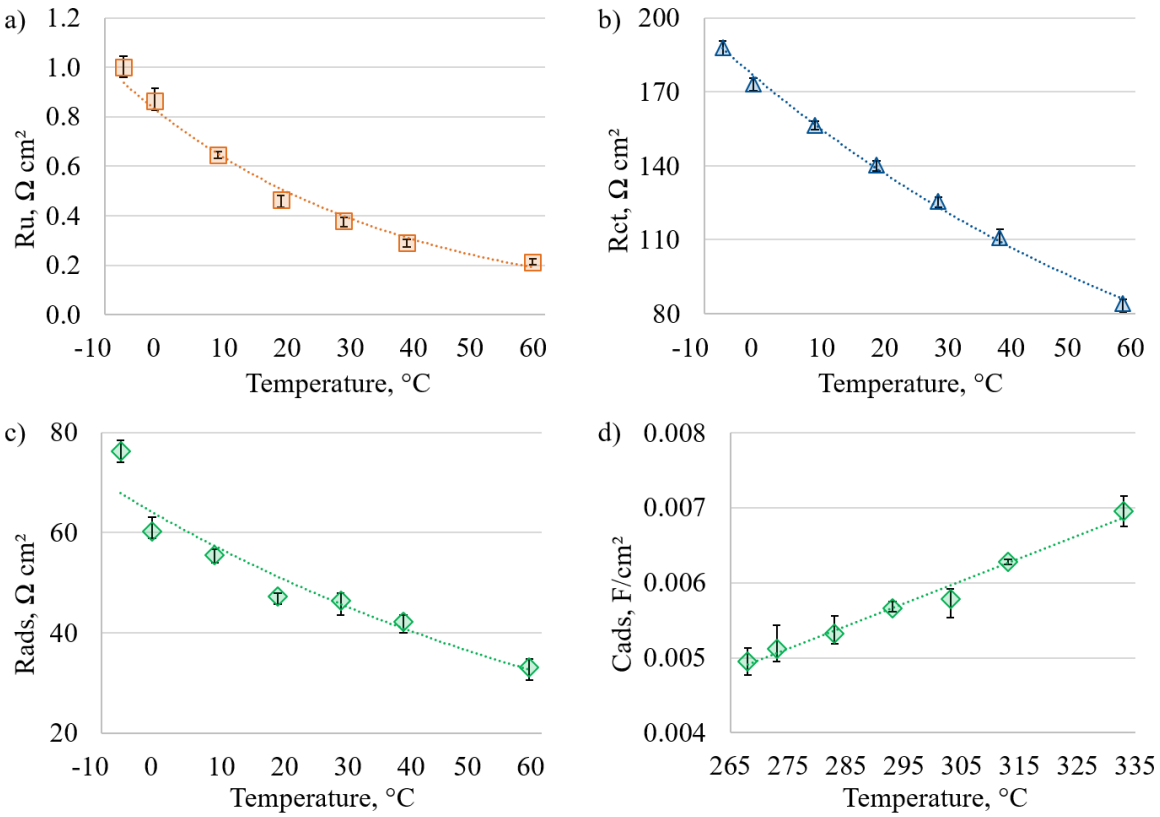


**Figure 52:** The temperature dependences of the equivalent circuit parameters (corresponding to **Figure 51 (a)**, without the double layer capacitance $C_{dl}$). The dashed lines are given as guides for the eye.

The uncompensated resistance $R_u$ (mainly related to the Nafion® electrolyte) shows a significant decrease with cell temperature (see **Figure 52 (a)**). One interpretation of this phenomenon discussed in the literature is that at cold Nafion® electrolyte, the repulsion energy between the hydrophobic and hydrophilic parts of the matrix domains is present and less water can be absorbed at the hydrophilic sulfonate groups. Conversely, at higher temperatures, more hydrophilic groups are dispersed into the hydrophobic matrix (entropy-driven), leading to an increase in the number of water molecules absorbed at the hydrophilic groups, thus improving proton conductivity [65, 118, 119]. However, the determination of the exact

individual high-frequency resistances, such as the membrane resistance and the exact proton path resistance in the CL, is not possible with the impedance model used in this work. A dependence of the R-C elements with respect to the cell temperature, which are related to the specific quasi-reversible adsorption of the sulfonate groups of the Nafion® electrolyte on the Pt electrocatalyst, can also be observed (see **Figure 52 (c)**, **(d)**) [120]. Since the $R_{ads}$ and $C_{ads}$ have a high sensitivity to the residual moisture in the system, the interpretation of the dependencies for both parameters in this series of measurements is difficult. In contrast, the temperature dependence of the $R_{ct}$, which is mainly related to the ORR and is shown in **Figure 52 (b)**, is more predictable. The $R_{ct}$ at a defined electrode potential ($E$) can be given as follows [77]:

$$R_{ct}(E) = \frac{RT}{n^2F^2\alpha k(E,T)C_s(E,T)A_{sc}(E)} \tag{5.2.1}$$

with the transfer coefficient, α, the active surface area of the Pt catalyst, $A_{SC}$, the surface oxygen concentration, $C_s$, the electron number, $n$, the Faraday constant, $F$ and the rate coefficient, $k$, whose temperature dependence can be described by the Arrhenius equation [121]. All parameters in equation (5.2.1) except temperature, $T$, oxygen concentration, $C_s$, which should have a small effect at OCV, and rate coefficient, $k$, should behave consistently at the measured temperature points. Due to the quantitative relationship between the local catalyst temperature and the activation energy, the rate coefficient $k$ changes significantly with temperature, which in turn leads to a corresponding change from the $R_{ct}$. However, if the $R_{ct}$ were to be used as an indicator of temperature in automotive applications, the temperature determination would only work if the constant amount of $O_2$ is available as a reactant. On the other hand, $R_{ct}$ is much more sensitive to certain degradation mechanisms of the CL compared to $C_{dl}$. More specifically, the $C_{dl}$ is formed between the carbon and ionomer interfaces. The reduction of the ECSA due to, for example, Ostwald ripening changes the $R_{ct}$ at the OCV, whereas the $C_{dl}$ should remain constant [122]. Therefore, it is more appropriate to use the $C_{dl}$ as an indicator for temperature determination.

**Figure 53** shows the temperature dependence of the $C_{dl}$. In contrast to various approximations (e.g. mean spherical approximation (MSA)), the calculated EEC values show a quasi-linear temperature profile [123].

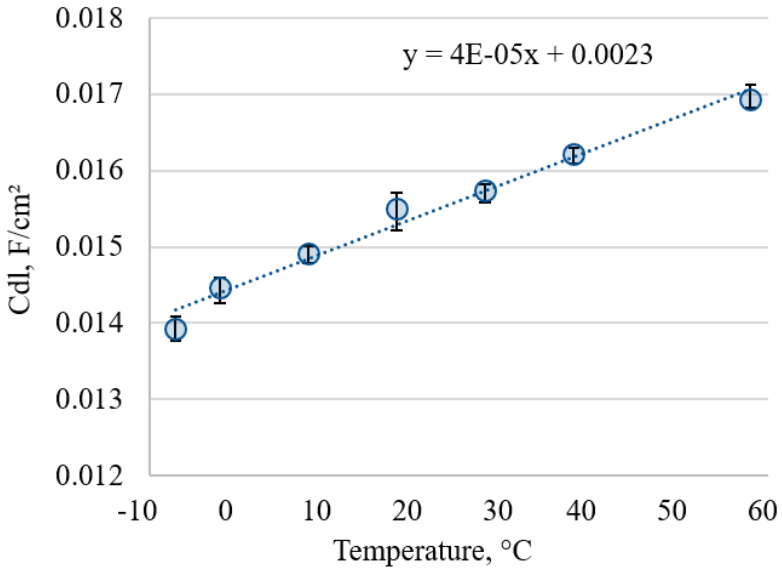


**Figure 53:** Temperature dependence of the double layer capacitance $C_{dl}$ in a temperature range from - 5 °C to 60 °C.

One can suspect that the observed experimental dependence in the case of the $C_{dl}$ is the consequence of several influencing factors. In this context, two main mechanisms could be responsible for the behavior of the measured $C_{dl}$. Firstly, the proportion of free ions decreases sharply at low temperatures, which leads to a decrease in capacitance. Secondly, the influence of the volume change triggered by the different temperatures cannot be neglected. This means that due to the volume reduction towards lower temperatures, a smaller amount of sulfonate groups comes into contact with the electrically conductive carbon surface, resulting in a reduction of the interface and thus the capacitance.

## 5.2. Investigation of degradation mechanisms caused by freeze-cycles

### 5.2.1. Introduction

As described earlier, temperatures below the freezing point of water, as well as the wrong operating strategy at such temperatures, have a negative impact on the long-term stability of the PEMFC. This chapter presents the first low-temperature stress test that was not performed using a conventional cooling device such as a climatic chamber. The cell temperature was set here using the newly developed PET SC TP50 prototype (for further details, see chapter 4.1). Ultimately, the aim of the first low-temperature stress test (LTST) was to verify whether

- the low-temperature stress test can be performed with the new PET SC TP50 prototype without an additional cooling device;
- the test procedure can be derived from a real automotive application and applied to a single cell;
- the measurement results are in agreement with the *in-situ* and *ex-situ* measurements of other publications.

In addition, the first LTST was a POC for the entire new tempering design and was decisive in determining whether development should continue or the whole idea should be discarded.

For this stress test, an identical MEA with an active area size of 43.56 cm² was used, as already described in chapter 5.1. Also, here, more precise data on the MEA are not known and, moreover, may not be disclosed.

### 5.2.2. Test methodology

The entire accelerated LTST was programmed in the test bench programming language VBA and fully automated. **Figure 54** shows the simplified sequence of the entire LTST, in which the procedure loop was executed 100 times.

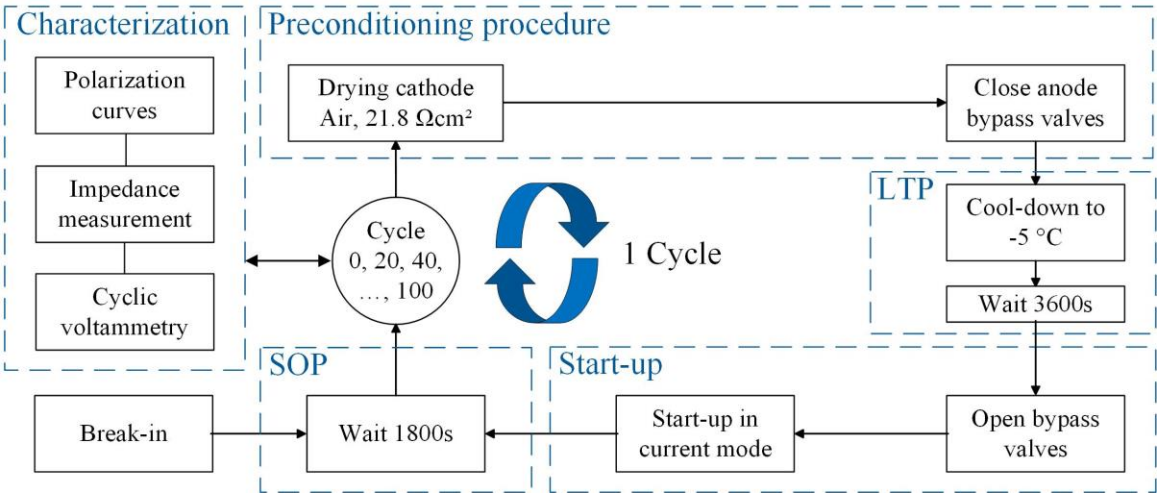


**Figure 54:** Simplified description of the low temperature stress test sequence, with the procedure loop (break-in, stable operation point, pre-conditioning, low-temperature part and start-up) and the characterization part (polarization curves, EIS and cyclic voltammetry).

Before the first procedure loop, the break-in was performed with a mixed load profile. For this purpose, the MEA was ramped up fully automatically to a constant operating point and then run with a load profile at current densities of 0 A/cm² to 2 A/cm². The operating parameters of the stable operating point were used for the break-in procedure. After the break-in procedure, the BOL (begin of life) characterization with polarization curves, cyclic voltammetry and electrochemical impedance spectroscopy was performed for the first time. If the BOL performance of the characterized MEA differed significantly from the reference data, the MEA was discarded, and a new MEA was subsequently used. When the desired output performance was obtained, the procedure loop was started, which can be divided into the subroutines described below.

**Stable operation point (SOP)**

On the one hand, the SOP ensures identical operating conditions before each preconditioning procedure, and on the other hand, it serves as a recovery phase for the MEA. Therefore, this point was performed with a hold time of 1800 s in the potentiostatic mode at 0.7 V and a cell temperature of 60 °C. In this process, the reactants $H_2$ and air are fed into the cell at a flow rate of 8.33 $cm^3/s$ and 16.67 $cm^3/s$, with a gas temperature and dew point of 85 °C and 46 °C (50 % RH), respectively. In this phase, the cell runs under an initial pressure of 200 kPa.

**Preconditioning procedure**

Since preconditioning before the low temperature phase indirectly affects the degradation rate, this is one of the most critical parts of the whole procedure. Before starting the preconditioning process, the MEA was unloaded, and the load was set to 0 A. After reaching the OCV, the outlet pressure was reduced to ambient pressure with a defined ramp of 5 kPa/min, and then the humidification and heating of the anode and cathode lines were switched off. To keep the residual water content in the lines as low as possible, the cell was bypassed for a short time, and the lines were blown through with maximum $H_2$ and air flows. After the short purge phase, the reactants $H_2$ and air were again passed through the cell with flow rates of 0.5 $cm^3/s$ and 28.67 $cm^3/s$, respectively. As a result, the moisture on the anode side is maintained, and the water content in the membrane and in the cathode CL is reduced only via the cathode airflow. During drying, the moisture content of the membrane and the protonic network is determined from the measured HFR at a frequency of 2 kHz. After reaching the target HFR of 21.8 $\Omega cm^2$, the cell was bypassed again, and the low-temperature part was started.

**Low-temperature part (LTP)**

After preconditioning, the cell was cooled down to -5 °C and held at this temperature for 3600 s. During the entire low-temperature part, the cell was separated by the bypasses and thus isolated from the environment.

**Start-up**

Like preconditioning, the start-up from temperatures below 0 °C is one of the most important procedures in the accelerated stress test since the start-up procedure directly affects the degradation rate. In the first step, the bypasses are opened, allowing dry $H_2$ and air to enter the cell at flow rates of 8.33 cm³/s and 16.67 cm³/s, respectively. After reaching OCV, the cell was galvanostatically ramped up to a lower voltage limit of 0.6 V with current steps of 0.05 A/cm² and a hold time of 2 s/step. The heating process of the cell was started 4 s after setting the first current stage. During the first heating phase, heating rates of 0.37 K/s were achieved. After exceeding a cell temperature of 50 °C, both humidification and heating of the gas lines were switched on. The start-up process was considered successful when the cell reached the target temperature of 60 °C, and no performance anomalies were visible.

**Characterization**

The characterization part determines the performance loss of the MEA during the accelerated stress test. This part of the script takes significantly longer compared to a low-temperature cycle, so the characterization was performed only every 20 cycles, i.e. after 0, 20, 40, 60, 80 and 100 cycles. The characterization part consists of 3 *in-situ* diagnostic methods: The direct performance loss was determined from polarization curves. The polarization curves were run in galvanostatic mode with a reversal point at 0.3 V. During the procedure, the $H_2$ and air flows were kept constant at 20.67 cm³/s and 65.17 cm³/s, respectively. All other operating parameters, such as the cell temperature, gas temperature, dew points and outlet pressures, correspond to those of the SOP. The change in ECSA was determined by CV measurement using the CO-stripping method. The measurement was performed in a potential range of 0.1-1.0 V (RHE) and a cell temperature of 60 °C. The reactants $H_2$ and 0.1 % CO in $N_2$ were heated to a gas temperature of 60 °C and humidified to a dew point of 60 °C (100 % RH) throughout the measurement. Before starting the ECSA measurement, three purification cycles were performed with $H_2$ and $N_2$ in a potential range of 0.05-1.2 V (RHE). For the ECSA measurement, as for the cleaning cycles, flow rates of 8.33 cm³/s and 8.33 cm³/s were used. The cell impedance was recorded within a frequency range from 10 kHz down to 0.3 Hz at current density of 0.8 A/cm² and an AC amplitude of 1.0 A.

The distribution of the 91 measurement points was determined experimentally before the experiment. For the impedance measurement, the flow rates of $H_2$ and air were set to 16.67 $cm^3/s$ and 33.33 $cm^3/s$, respectively. The other operating parameters such as cell temperature, gas temperature, dew points and outlet pressures were the same as for the previously described SOP.

### 5.2.3. In-situ measurement results

**Preconditioning procedure**

**Figure 55** shows the HFR curves during cathode drying for the repetitive preconditioning procedures. It is immediately apparent that achieving the target HFR of 21.8 $\Omega cm^2$ never occurs at the same drying time. This is because the drying time strongly depends on the water content in the membrane and the protonic network and thus ultimately on the mode of operation prior to the preconditioning process. If the MEA was previously operated at higher current densities, drying and thus reaching the target HFR takes much longer than if the MEA was previously operated near OCV.

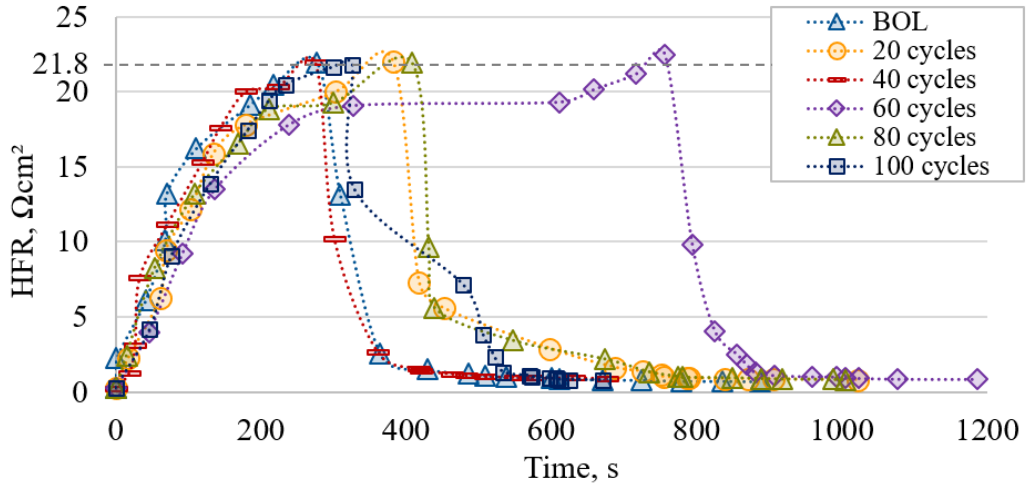


**Figure 55:** High frequency resistance (HFR) measured during several preconditioning procedures with the target resistance of 21.8 $\Omega cm^2$ and a visible relaxation of the HFR.

**Table 11** shows a summary of the HFR values obtained during the different preconditioning procedures, including drying time and resistance after HFR relaxation. The relaxation of the HFR is due to the residual water present on the anode side flowing back through the

ionomer network into the membrane, and the cathode proton network after the drying process is completed. This is particularly evident in the relaxation of the HFR value during the low-temperature part. The HFR relaxation after drying depends strongly on the achieved drying resistance and the moisture content on the anode side. Even with different drying times, the HFR value settled at a resistance between ca 0.81 Ωcm² and ca 0.88 Ωcm² after the preconditioning process, i.e. during the low-temperature part. Reproducible drying is therefore only possible by measuring the HFR value during the drying process.

**Table 11:** Summary of the measured HFR values obtained in the different preconditioning processes, including drying time and resistance after HFR relaxation.

| **Cycles** | **0** | **20** | **40** | **60** | **80** | **100** |
|---|---|---|---|---|---|---|
| Target HFR, Ωcm² | 21.8 | 21.8 | 21.8 | 21.8 | 21.8 | 21.8 |
| Reached HFR, Ωcm² | 22.0 | 22.1 | 21.9 | 22.5 | 21.9 | 21.8 |
| Reached HFR after, s | 277 | 382 | 275 | 756 | 408 | 326 |
| Relaxed HFR, Ωcm² | 0.83 | 0.87 | 0.88 | 0.86 | 0.81 | 0.82 |

### Polarization curve

The polarization curves and the current density points derived from the polarization curves vs. the number of cycles are shown in **Figure 56 (a)** and **(b)**. The performance loss is much more pronounced at current densities above 0.5 A/cm², indicating an increase in cell resistance. After 100 cycles performed, a performance loss of 118 mV occurred at a current density of 1.5 A/cm².

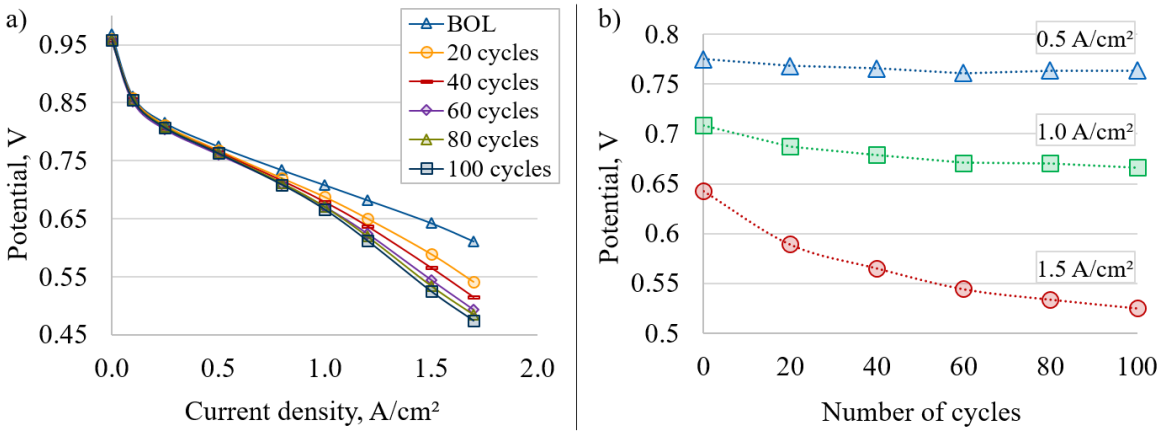


**Figure 56: (a)** Polarization curves recorded after different stress cycles, and **(b)** the current density points extracted from the polarization curves to visualize the degradation characteristics.

### Cyclic voltammetry (CV)

Using the CV measurement, the degradation of the catalytically active surface could be assessed during the LTST. **Figure 57** shows the ECSA curve, which had a BOL value of 46.2 m²/g and decreased by 20.6 % during the LTST. The reduction in ECSA per cycle can be attributed to many reasons. One of the main reasons is the start-up from temperatures below 0 °C. The product water floods the pore structures of the MPL and GDL, changes the aggregate state and freezes [109]. This leads to deformation of the pore structure, blockage of the reaction pathways and possible starvation during start-up [124, 125]. Another reason for the high degradation of the ECSA could be the high water content on the anode side. In this experiment, the anode was not preconditioned before the low-temperature phase, i.e. the cell was shut down with high residual anode moisture. As a result of the temperature change, the condensed water, which was not adsorbed by the ionomer network, could freeze. This ultimately led to blockage of the gas pathways, followed by starvation and shift of the cathode potential to higher potentials [126, 127]. Both effects lead to the oxidation of carbon, which is driven by the carbon oxidation reaction (COR). This, in turn, leads to a redistribution of the Pt catalyst particles and finally to a reduction of the ECSA [128, 129]. A smaller, non-negligible influence is also likely to be the potential changes during commissioning and CV measurement, where the potential was in the range between 0.05 V-1.2 V (CV measurement) and 0 V-OCV (during commissioning). These potential changes also lead to a reduction in ECSA, but not to the same extent as the previously

described effects. However, the literature indicates that the dominant degradation mechanism must be the COR [130].

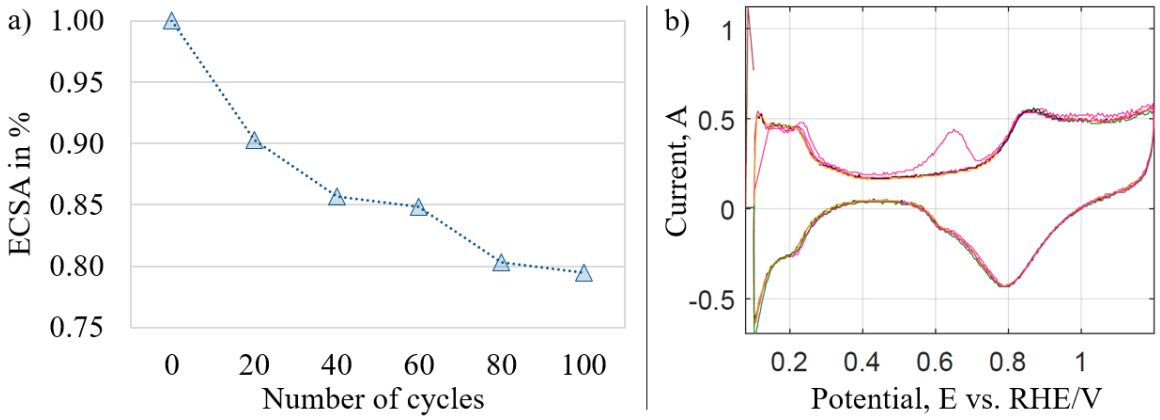


**Figure 57: (a)** Decrease of the electrochemical surface area ECSA (in %) during the accelerated low-temperature stress test, and **(b)** the cleaning cycle before ECSA measurement with a small desorption current peak at ~0.65 V.

**Electrochemical impedance spectroscopy (EIS)**

The impedance measurements were performed at current densities from 0.2 A/cm² up to 0.8 A/cm². For current densities above 0.8 A/cm², impedance measurements were also performed, but the voltage response at lower frequencies was too noisy and could not be evaluated. Analogous to the polarization curves, a significant change in the impedance during LTST was observed at current densities above 0.5 A/cm². Therefore, the impedance response at a current density of 0.8 A/cm² was evaluated using a physical impedance model consisting of 6 EEC (shown in **Figure 58 (a)**). Because of the second time constant representing the diffusion, the only difference from the EEC model used in chapter 5.1 is the additional Warburg short element ($W_S$) with a finite-length diffusion and reflective boundaries. The impedance of the $W_S$ element is given by formula (5.1.1).

$$Z_{Ws}(\omega) = \frac{Aw}{\sqrt{\omega}}(1-j)\tanh(Av\sqrt{j\omega}) \tag{5.1.1}$$

The $W_S$ element has two parameters, the Warburg coefficient $A_w$ and the parameter $A_v$, which can be described by formula (5.1.2) with the Nernst diffusion layer thickness $d$ and the diffusion coefficient $D$ of the electroactive species [131, 132].

$$Av = d/D^{0.5} \tag{5.1.2}$$

In both LTST experiments (see chapter 5.3), the fitting and calculation of the numerical values of the model parameters were performed using the EIS Data Analysis 1.3 software [116]. With the EEC model, a good fit was achieved. The recorded and fitted impedance spectra after different cycles are shown in **Figure 58 (b)**. It can be clearly seen that the spectra and, in particular, the low frequency intercept of the spectrum with the real axis (Total R) change due to the low-temperature cycles. As with various potential cycling durability tests, the low frequency intercept shows the most significant change and can also be used as an indicator of CL degradation [130, 133].

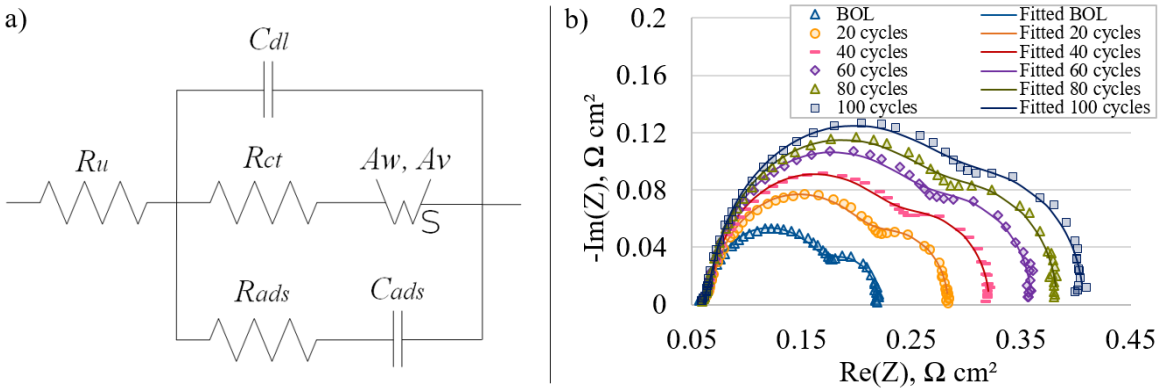


**Figure 58: (a)** Physical impedance model, which was used to fit **(b)** the measured impedance data during the low temperature stress test at a current density of 0.8 A/cm².

The dependencies of the resistors used in the EEC model on the cycle number during the stress test are shown in **Figure 59 (a)**. The uncompensated (Nafion®-electrolyte) resistance, $R_u$ shows a constant behavior during the 100 cycles. This suggests that no significant degradation of the proton network occurred. A correlation between the performance loss and the number of cycles is clearly visible in the dependence of the charge transfer resistance, $R_{ct}$. In this case, the $R_{ct}$ is directly related to the loss of ECSA, indicating a structural change in the cathode CL [130]. In other words, with a reduced cathode ECSA, the charge transfer can only occur with more resistance at the same current density. The $R_{ct}$ at a defined electrode potential (E) can be given by equation (5.1.3) [77]:

$$R_{ct}(E) = \frac{RT}{n^2F^2\alpha k_{app}(E)C_s(E)A_{sc}(E)} \tag{5.1.3}$$

with the transfer coefficient, $\alpha$, the active surface area of the Pt catalyst, $A_{sc}$, the surface concentration of oxygen, $C_s$, the electron number, $n$, the Faraday constant, $F$, and the cumulative apparent rate coefficient, $k_{app}$, which describes the relative contribution of the local rate coefficients at different active sites. The slight increase in adsorption resistance $R_{ads}$ can also be attributed to the decrease in ECSA. Due to the reduction of Pt active surface area, there is less specific adsorption of ionomer and *OH/*O-groups, which leads to an increase in resistance. The behavior of the two capacity parameters, $C_{dl}$ and $C_{ads,}$ during LTST is shown in **Figure 59 (b)**. The significant increase of the double layer capacity $C_{dl}$ during the performed cycles is closely related to the reduction of the cathode CL thickness. The reduction increases the contact area between carbon and ionomer, which ultimately leads to an increase in the $C_{dl}$. In contrast to the $C_{dl}$, the adsorption capacity $C_{ads}$ decreases during LTST and is directly related to the degradation of the cathode ECSA. Due to the reduction of the active surface area, a smaller amount of sulfonate groups, *OH, *O, and other species can be adsorbed on the Pt surface, leading to a reduction of the interface to a decrease of the capacity.

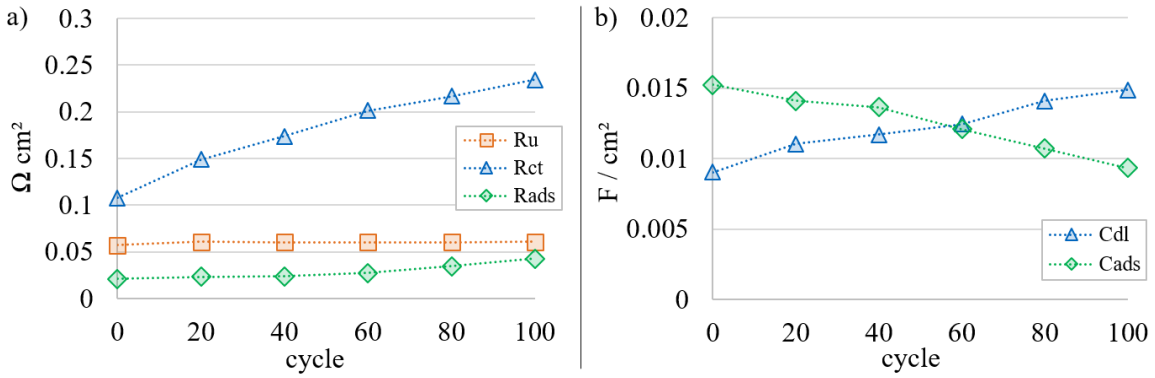


**Figure 59: (a)** Summary related to the ohmic parameters with the uncompensated (Nafion® -electrolyte) resistance, $R_u$, charge transfer resistance, $R_{ct}$, and adsorption resistance, $R_{ads}$, and **(b)** the summary related to the capacitance parameters with the double layer capacitance $C_{dl}$ and adsorption capacitance $C_{ads}$.

Besides the charge transfer resistance, the Warburg coefficient $A_w$ also shows the largest correlation between the cycles performed and the resulting performance loss (shown in

**Figure 60 (a)**). This could be strongly related to the decrease of the CL thickness and thus to the dissolution of Pt. Ultimately, the reduction in CL thickness leads to a decrease in ECSA, higher mass transport resistances, and thus a change in the oxygen concentration at the catalyst surface. Since mass transfer limitation basically occurs at higher current densities and diffusion of the electroactive species plays a decisive role here, the Warburg coefficient can also be used as an indicator for the degradation state of the cathode CL. The $A_w$ can be given by equation (5.1.4) with the diffusion coefficient $D$ [132]:

$$Aw(E) = \frac{RT}{n^2F^2\alpha\sqrt{2D}C_s(E)A_{sc}(E)} \tag{5.1.4}$$

The slight increase in the parameter $A_v$ during the 100 temperature cycles performed (shown in **Figure 60 (b)**) suggests that the relationship between the Nernst diffusion layer thickness $d$ and the diffusion coefficient $D$ has changed. This could be related to the change in cathode CL thickness and thus a slight increase in Nernst diffusion layer thickness $d$ with constant diffusion coefficient $D$.

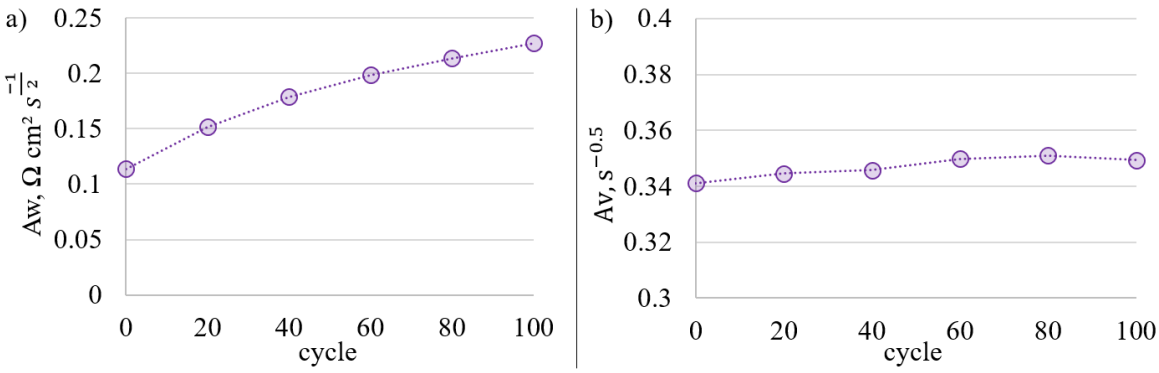


**Figure 60: (a)** Trend of the calculated Warburg coefficient, $A_w$, and **(b)** the calculated parameter $A_v$ during the performed temperature cycles.

The cumulative apparent reaction rate coefficient, $k_{app}$ (a simplified representation is shown in **Figure 61**), can be used to provide important information about the relationship between the performance loss and the change in structure as well as crystal faces of the Pt catalyst particles. More specifically, if the main mechanism for degradation is the so-called Ostwald ripening during the stress test, the Pt particles grow, and as a result, the structure and crystal faces of the Pt change [122]. Furthermore, a structural change in the Pt crystal faces leads

to a change in the turnover frequency and directly affects the performance [134]. The coefficient $k_{app}$ can be calculated from the ratio of $A_w/R_{ct}$ and the diffusion coefficient $D$ as shown in equation (5.1.5).

$$\sqrt{2D}\frac{Aw(E)}{R_{ct}(E)} = k_{app}(E) \tag{5.1.5}$$

Since the diffusion coefficient is not known in this case, the exact determination of the $k_{app}$ is not possible. Nevertheless, based on the calculated values of $A_w$, $R_{ct}$ and their ratio, a statement can be made about the change in the surface structure during the stress test. **Figure 61 (b)** shows the constant trend of the $A_w/R_{ct}$ ratio during the performed stress test. If the diffusion coefficient $D$ is considered stable, it can be assumed that there were no changes in the structure and crystal faces of the Pt particles. Thus most likely, no Ostwald ripening occurred during the 100 performed cycles. When the diffusion coefficient is assumed according to the values reported in [135], the calculated $k_{app}$ values agree well with the turnover frequencies for small Pt nanoparticles that were reported for 0.8 V and 80 °C in [134].

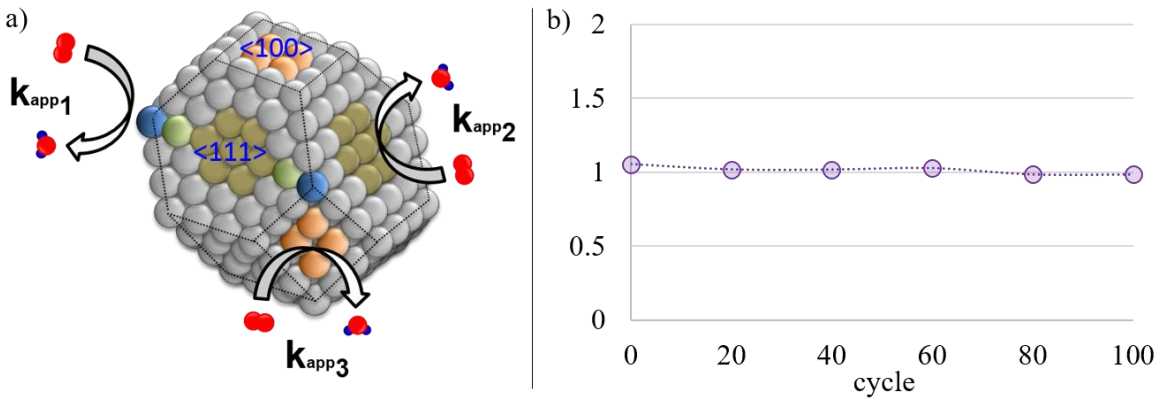


**Figure 61: (a)** Simplified representation of the oxygen reduction reaction (ORR) on a Pt particle with the reaction rate coefficient $k_{app(n)}$ of different active sites, and **(b)** the trend of the ratio $A_w/R_{ct}$ during the performed stress cycles.

**CNLS vs. DIA**

As described in chapter 3.2.3, EEC model parameters such as $R_u$, $R_{ct}$ and $C_{dl}$ can also be estimated by differential impedance analysis (DIA). For the determination of the EEC model parameters using the DIA method, 20 measuring points per characterization cycle were used here in a frequency range between 1 kHz and 40 Hz. **Figure 62 (a)** shows the ohmic resistances $R_u$, and $R_{ct}$ obtained by the classical CNLS and the DIA methods. The curves of the $R_u$ and $R_{ct}$ for both methods are almost superimposed and show the same evolution during the performed cycles. This confirms that the ohmic EEC parameters can be determined with the DIA with nearly the same quality as with the CNLS, but the fitting process is much easier and faster. **Figure 62 (b)** shows the dependence of the two double layer capacities $C_{dl}$ obtained with the CNLS and DIA. A clear difference can be seen here in the individual points calculated but also in the overall trend of the two capacities. This could be explained by the fact that a more complex model was used in the CNLS fitting, which takes into account the $C_{ads}$ in addition to the $C_{dl}$. Thus, with the CNLS method, there is a clear separation between the individual capacities, which is not the case with the DIA.

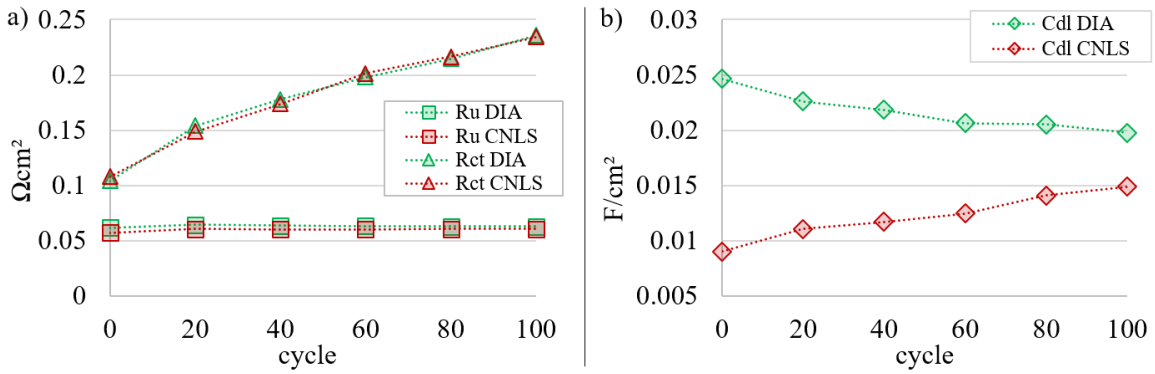


**Figure 62: (a)** Curves of the ohmic model parameters $R_u$ and $R_{ct}$ calculated by the CNLS and DIA methods, and **(b)** the curves of the two double-layer capacitances $C_{dl}$.

### 5.2.4. Ex-situ measurement results

To understand the degradation mechanisms deeper, *ex-situ* cross-sectional microscopy was used, and SEM images were obtained after the low-temperature stress tests. Based on the cross-sectional images shown in **Figure 63 (a)** and **(b)**, the cathode CL thickness of the MEAs used could be determined. As previously indicated, there was a significant reduction in the cathode CL thickness, which decreased by ca 21.6 % to ~7.7 µm during the stress test (reference cathode CL ~ 9.8 µm). This could be due to a potential shift on the cathode side, which favored the COR and ultimately led to a redistribution of platinum [136]. The dissolved platinum can be seen in the cross-sectional image as a Pt band in the membrane. This, in turn, substantiates the previously described mechanism and clearly shows the relationship between the change in the cathode CL thickness, the redistribution of Pt, and ultimately the decrease in ECSA. Based on the cross-sectional SEM image (**Figure 63 (b)**), it can be assumed that no delamination occurred between the membrane and the two CLs during the performed stress test. Both the membrane and the ionic network connecting the membrane to the CLs appear to be completely intact. It should be mentioned here that delamination could occur at even lower temperatures [91].

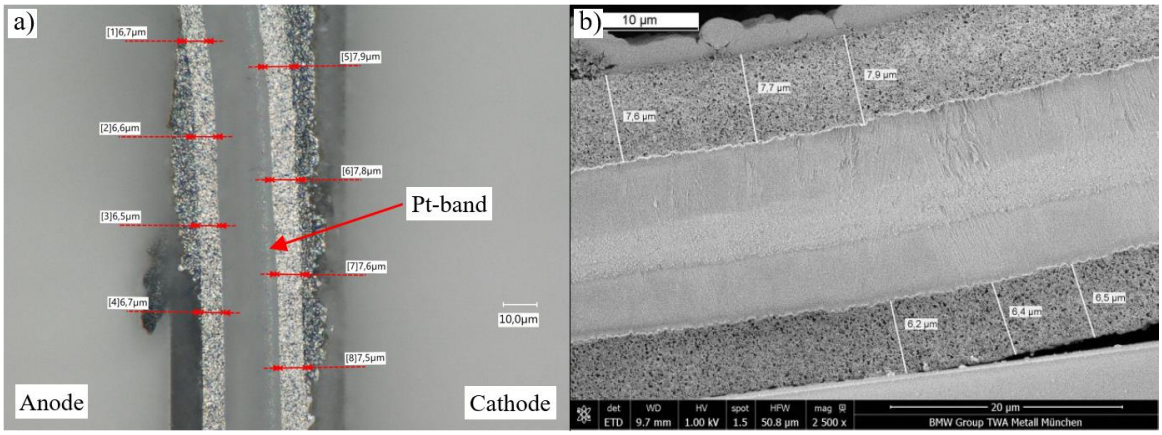


**Figure 63: (a)** Cross-sectional micrograph showing the reduced thickness (~7.7 µm vs. ~9.8 µm) of the cathode catalyst layer and visible Pt band in the polymer electrolyte membrane, and **(b)** cross-sectional SEM image of the used MEA [137].

SEM analysis in material contrast mode (BSE mode) and energy dispersive X-ray spectroscopy (EDXS) were performed to characterize the visible Pt band within the PEM further. EDX analysis shows that, in addition to the standard elements contained in the PEM, Pt is also present as a catalyst (bright spots in **Figure 64 (a)** and **(b)**). Thus, it is again clear that

due to the oxidation of carbon, the released platinum migrated into the membrane during the LTST.

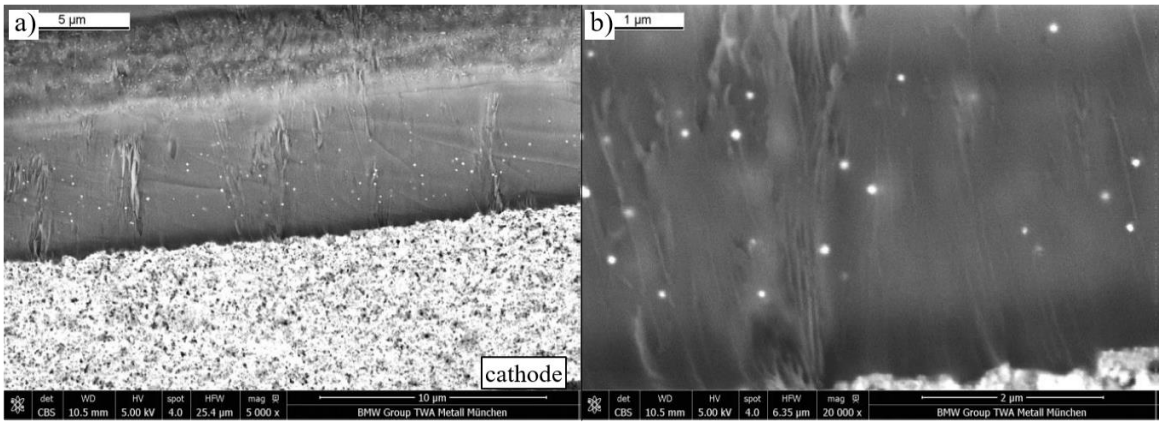


**Figure 64: (a)** Cross-sectional SEM image of the transition region in material contrast mode (BSE mode) of the cathode catalyst layer and membrane, and **(b)** more detailed SEM image of the polymer electrolyte membrane [137].

## 5.3. Effect of different ionomer to carbon weight ratios on the degradation

### 5.3.1. Introduction

Based on the measurement results from chapter 5.2, the low-temperature stress test was further developed. While the previously performed stress test was more like a POC and was carried out with the PET SC TP50 prototype, further points were developed in this test as described below.

- The final version of the PET SC TP50 was used for the test series.
- Parts of the test procedure were brought even closer to the procedures in real automotive applications.
- In this series of tests, three different MEAs with different cathode ionomer-carbon (I/C) weight ratios were characterized.

Furthermore, the temperature of the low-temperature part was lowered to -10 °C, and the number of cycles per test item was increased to 120. All MEAs used in this test series have an active area of 43.56 cm² and were equipped with SGL 29BC type GDLs for the anode and cathode. All other parameters, except for the composition of the cathode CL, were identical for all MEAs. The key data of the MEAs used in this chapter are listed in **Table 12**.

**Table 12:** Summarized key data of the MEAs used in the test series.

| | **Anode** | | **Cathode** | | **Membrane** | |
|---|---|---|---|---|---|---|
| | Pt-loading mgPt/cm² | I/C-ratio | Pt-loading mgPt/cm² | I/C-ratio | Type | Thickness µm |
| **MEA 1** | 0.08 | X | 0.29 | 0.5 | Gore M815 | 18 |
| **MEA 2** | 0.08 | X | 0.34 | 1.0 | Gore M815 | 18 |
| **MEA 3** | 0.08 | X | 0.3 | 1.5 | Gore M815 | 18 |

### 5.3.2. Test methodology

By further approximating the test sequence to the real automotive application, performing the test with the PET SC TP50 and varying the cathode composition, a conclusion can be drawn cost-effectively as to which MEA has the lowest degradation in such an application. As with the previous chapters, the entire test sequence was programmed in the test bench programming language VBA and fully automated. **Figure 65** shows a simplified description of a whole test procedure loop, i.e., a low-temperature cycle. All significantly changed or newly added sequences (compared to the procedure in chapter 5.2) are shown in blue.

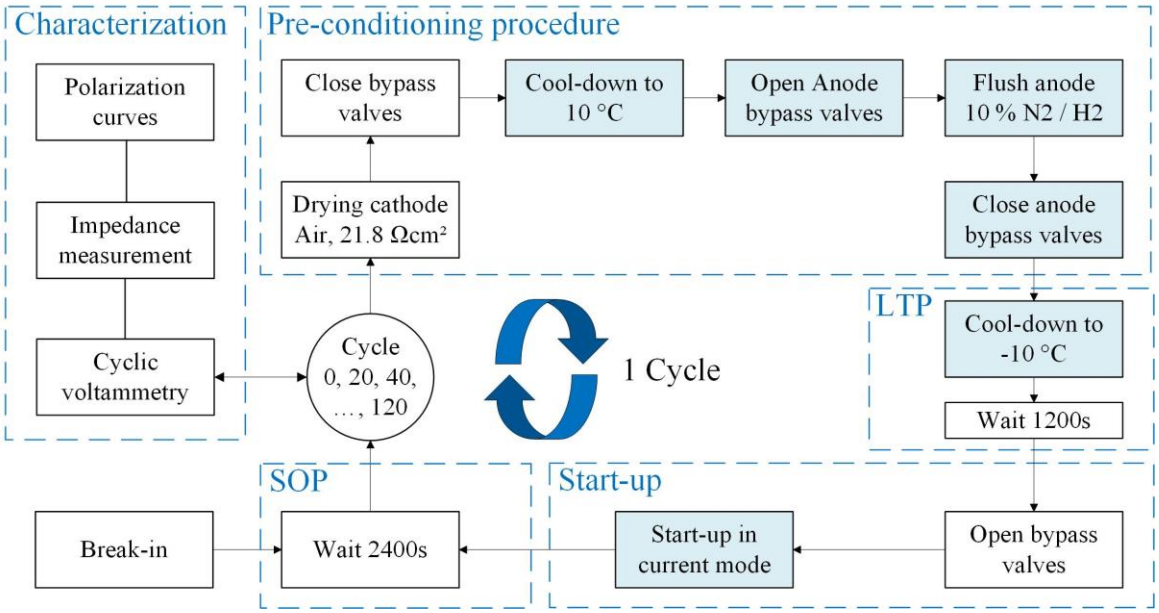


**Figure 65:** Simplified representation of an entire test procedure loop, i.e., a low-temperature cycle. The newly added or significantly changed sequences (compared to the procedure in chapter 5.2) are shown in blue.

Since the initial performance of the MEAs was not known, the break-in had to be adjusted. A mixed load profile was used, where at low current densities up to 0.15 A/cm², the cell was operated in galvanostatic mode and at higher current densities in the potentiostatic mode at a cell voltage of 0.55 V. The hold times for the galvanostatic and potentiostatic modes were 900 s and 2700 s, respectively. After ten repetitions, the break-in procedure was completed, and the first BOL characterization was performed.

With successful BOL characterization, the first procedure loop was started, which can be divided into the parts, as described below.

**Stable operating point (SOP)**

As with the first LTST (see chapter 5.2), the SOP should provide identical baseline conditions before the preconditioning procedure and should serve as a recovery period for the system. The main difference from the SOP in the first LTST is the extended waiting time of 2400 s, the cell temperature of 80 °C and the higher dew points of 63.8 °C (50 % RH). The reactant flows were 8.3 $cm^3/s$ and 16.7 $cm^3/s$, respectively. All other parameters are the same as in the previously presented SOP.

**Preconditioning procedure**

While in the first LTST, only the cathode was preconditioned, in this test series, the anode is also prepared for the low temperatures. Since the preconditioning of the cathode has remained the same, only that of the anode will be described in more detail. After drying the cathode and reaching the desired HFR of 21.8 $\Omega cm^2$, the cell is bypassed and sealed from the environment. At this point, the preconditioning of the anode begins. As liquid water condenses out at the anode due to the cooling of the cell, this phase aims to remove the remaining liquid water. For this purpose, the cell was cooled down to a temperature of 10 °C, and then the anode bypass was opened. The gas mixture ($H_2$ with 10% $N_2$) with a dew point of 10 °C and a flow rate of 28.7 $cm^3/s$ is passed through the anode for 60 s. In the last step, the bypass is closed again, and the low-temperature part begins.

**Low-temperature part (LTP)**

In this test series, the cell was cooled to a temperature of -10 °C and held for 1200 s.

**Start-up**

In the first step of the start-up, the bypasses are opened and reactants with flow rates of 8.3 $cm^3/s$ and 16.7 $cm^3/s$ were fed into the cell. Two seconds after reaching OCV, a current density of 0.05 $A/cm^2$ was set for 20 s. During this time, the cell was kept at a temperature of -10 °C. After this holding time, the heating phase of the system begins. In this phase, all transition heaters and the cell temperature were set to the target temperatures of 85 °C and 80 °C, respectively. During the heating phase, the current was increased in the galvanostatic

mode in steps of 0.05 A/cm² with a hold time of 2 s/step until a lower voltage limit of 0.6 V was reached. When all working parameters have been reached, and no alarm criterion has been violated, the load is switched to the potentiostatic mode, and a voltage of 0.7 V is set.

**Characterization**

The measurement methods used in the characterization section are mainly identical to those presented in the first LTST. The main difference is in the parameterization. The polarization curve was measured at flow rates of 22.9 cm³/s and 73.3 cm³/s, cell temperature of 80 °C, dew points of 52.8 °C (30 % RH), and outlet pressure of 200 kPa. The CV measurement using the CO stripping method was performed with $H_2$ and 0.1 % CO in $N_2$ at flow rates of 8.3 cm³/s and 41.7 cm³/s, respectively. In this series of experiments, the ECSA measurement was also performed twice, at a cell temperature and a dew point of 60 °C each. The impedance measurement was also repeated three times at a current density of 0.8 A/cm² and a frequency range from 10 kHz to 0.3 Hz. All other operating parameters correspond to those in the previously described SOP.

### 5.3.3. In-situ measurement results

**Polarization curves**

The summarized current density points during the 120 low-temperature cycles are shown in **Figure 66** (1.0 A/cm² **(a)** and 2.0 A/cm² **(b)**).

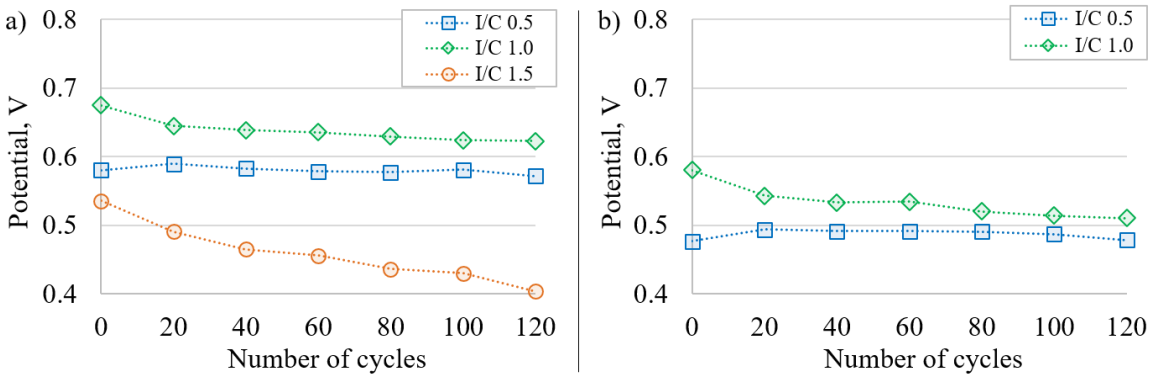


**Figure 66:** Current density points derived from polarization curves (**(a)** 1.0 A/cm² and **(b)** 2.0 A/cm²) to visualize the degradation behavior of the MEAs used during the low-temperature stress test.

The course of the individual MEAs and the possible mechanisms are explained below. Since the MEA with the cathode ionomer to carbon weight ratio (I/C-ratio) of 1.5 never reached the current density of 2.0 A/cm², only the current density points at 1.0 A/cm² could be shown. The MEA $_{I/C-\ 0.5}$ with the lowest cathode I/C-ratio of 0.5 shows the most stable behavior during LTST. Due to the low ionomer content at the cathode and better gas permeability than the other MEAs (cathode I/C-ratio of 1.0, 1.5), there is smaller decrease in oxygen concentration in deeper layers of the CL. As a result, the core reaction area is more uniformly distributed over the cathode CL [138]. Therefore, the performance shows a "break-in" behavior during the first 20 cycles and improves by ca +1.47 % (ca +8.5 mV). As with the first LTST, it can be assumed that the oxidation of carbon, driven by the COR, led to a decrease in the cathode CL thickness and thus to an accumulation of ionomer. This leads to better platinum utilization and more efficient proton conductivity, which improved the performance of MEA$_{I/C-\ 0.5}$ [139, 140, 141]. Between cycles 20 and 100, the MEA$_{I/C-0.5}$ shows stable behavior, and no significant degradation is visible. During the last 20 cycles, there is a slight drop in the performance with an average degradation rate of about -0.47 mV/cycle. Despite the slight degradation, the MEA$_{I/C-0.5}$ reaches ~571 mV at the last characterization point (end of life (EOL)), which is close to the BOL performance of ~580 mV (BOL vs. EOL ca -1.49 %).

The MEA with the balanced cathode I/C-ratio of 1.0 shows significantly better performance compared to the MEA$_{I/C-0.5}$. This can be attributed to the higher amount of ionomer in the cathode CL, which leads to more efficient proton conductivity at higher current densities [142]. In contrast to the MEA$_{I/C-0.5}$, the initial voltage here was ~675 mV and decreased by ~52 mV during the stress test (BOL vs. EOL ca -7.75 %). The degradation behavior is very similar to the MEA used in the first LTST (see chapter 5.2) and can be directly attributed to the COR and the reduction in the thickness of the cathode CL.

With an initial voltage of ~535 mV, the third characterized MEA showed the worst BOL performance. The high ionomer loading causes the poor performance. Consequently, this leads to reduced pore sizes, high oxygen transport resistances, and thus a larger drop in oxygen concentration in deeper layers [143, 144, 145, 146]. During the first 40 cycles (**Figure 66 (a)**), a performance loss of ~-1.7 mV/cycle is visible. One of the main reasons for this is the shifted core reaction area. The COR triggered enrichment of ionomer near the interface between the cathode CL and GDL leads to a much faster blocking of the outer

reactant pathways [128]. In the mid-life, between cycle 40 and 100, the degradation behavior stabilizes and levels off at a degradation rate of ~-0.6 mV/cycle. From cycle 100 until the end of the stress tests, the degradation rate increases again to a rate of ~-1.32 mV/cycle. Here it can be assumed that another degradation mechanism is responsible for the accelerated drop (more on this in chapter 5.3.4). During the entire stress test run, the voltage drops by ~132 mV (BOL vs. EOL ca -24.7 %).

**Cyclic voltammetry**

The change in ECSA of each MEA during the stress test is shown in **Figure 67**.

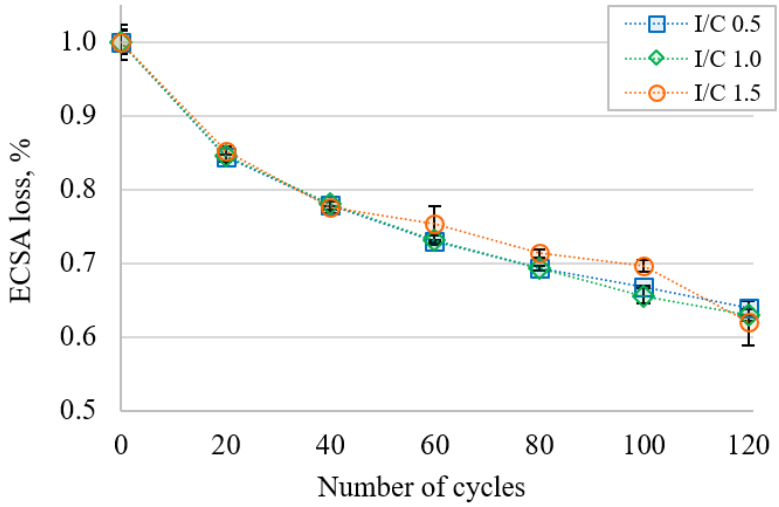


**Figure 67:** The decrease in electrochemical surface area ECSA (in %) of the MEAs used during the low-temperature stress test.

It is immediately apparent that the three characterized MEAs exhibit an almost identical loss of Pt active surface area of ~35±2 % after the 120 low temperature cycles. This illustrates that the mechanism responsible for the decrease in ECSA appears to be independent of the cathode I/C-ratio and is more or less identical for all MEAs. In this case, it can also be assumed that the decrease in ECSA was driven by the COR, leading to a decrease in cathode CL thickness and thus redistribution of Pt [128, 129, 147, 148, 149].

**Electrochemical impedance spectroscopy (EIS)**

As in Section 5.2, the same EEC model was used to fit the impedance response (see **Figure 68 (a)**). The fitting results for the $MEA_{I/C-0.5}$ and $MEA_{I/C-1.0}$ during the BOL characterization are shown in **Figure 68 (b)**. The color of the fitted data (solid line) corresponds to the color-framed equivalent circuit elements of **Figure 68 (a)**. For example, the blue-framed Warburg short element $W_S$ in **Figure 68 (a)** corresponds to the measured response of the second blue warped semicircle in the Nyquist plot in **Figure 68 (b)** [77]. Considering now the impedance response of the $MEA_{I/C-1.0}$ (shown as x in **Figure 68 (b)**), it is immediately noticeable that the first semicircle, which usually refers to the Faradaic impedance $R_{ct}$, the double layer capacitance $C_{dl}$, and the quasi-reversible adsorption $R_{ads}$ and $C_{ads}$, shows a clear difference from the impedance profile of the $MEA_{I/C-0.5}$ (shown as + in **Figure 68 (b)**). This can be attributed to an additional time constant, which thereby warps the high-frequency semicircle of the impedance response of the $MEA_{I/C-0.5}$. As a result, the impedance response cannot be completely matched with the previously presented EEC model (solid red line). It can be surmised here that due to the low ionomer content in the cathode CL and the associated low mass transport limitation, the gas permeability of the cathode CL is close to or equal to that of the anode CL. This results in an additional time constant, which becomes visible in the medium frequency range (~8 kHz-0.35 kHz) of the measured impedance response [133].

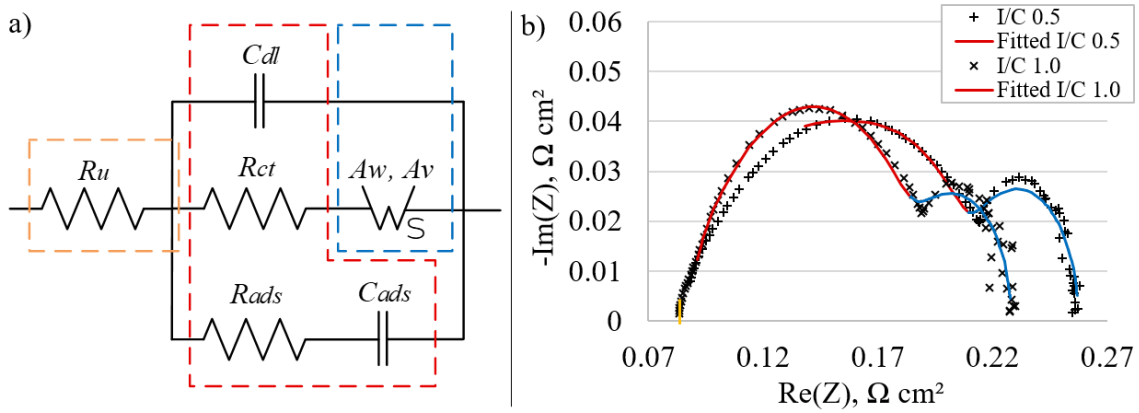


**Figure 68:** (a) Physical impedance model showing the color-framed EC elements, each corresponding to sections of the impedance response, and (b) the impedance response at the beginning of the lifetime (BOL) for the MEAs with a cathode ionomer carbon weight ratio (I/C) of 0.5/1.0 (open symbols) along with the fit to the equivalent circuit (solid lines).

**Figure 69** shows the summarized behavior of the uncompensated resistance $R_u$. To determine the resistance $R_u$, the HFR at 10 kHz was evaluated for all MEAs.

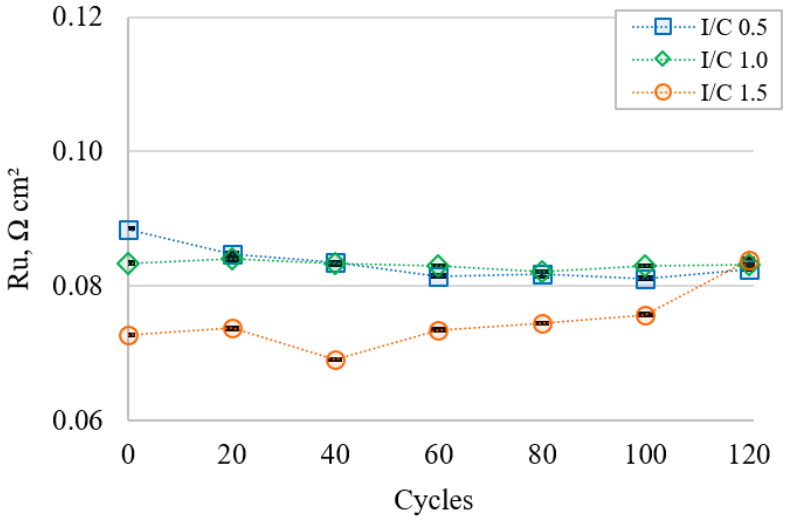


**Figure 69:** Summary and trends of the calculated ohmic resistances $R_u$ of the tested MEAs measured at a current density of 0.8 A/cm² during the low temperature stress test.

The resistance $R_{u\ I/C\text{-}0.5}$ shows a significant decrease during the first 60 cycles and then stabilizes near the resistance $R_{u\ I/C\text{-}1.0}$. As described earlier, the enrichment of the ionomer and the enhancement of the ionomer network in the CL results in improved proton conductivity, which ultimately affects the resistance $R_{u\ I/C\text{-}0.5}$. In contrast to the $R_{u\ I/C\text{-}0.5}$, the $R_{u\ I/C\text{-}1.0}$ resistance shows stable behavior during the 120 stress cycles. The $R_{u\ I/C\text{-}1.5}$ behaves almost stably until cycle number 100 and shows an interesting behavior towards the test's end. As can be seen from the current density points, there was a significant drop in the performance over the last 20 cycles. Since the resistance $R_u$ generally describes the proton conductivity in the MEA, it can be assumed that in this case, there was a deterioration or decrease in the protonic pathways. This means that the increase in $R_{u\ I/C\text{-}1.5}$ was most likely induced by the rupture and delamination of the anode CL, resulting in a disruption of the protonic pathways (see chapter 5.3.4 for more details) [150].

**Figure 70 (a)** shows the trend for the summarized charge transfer resistances $R_{ct}$ during the LTST. As seen previously in the current density points of the polarization curves, the performance of the $MEA_{I/C\text{-}0.5}$ with the lowest cathode I/C-ratio increased during the first cycles. This trend is also visible in the $R_{ct\ I/C\text{-}0.5}$. It can be partially attributed to the morphological change of the CL and the more efficient platinum utilization. In contrast to the $R_{ct\ I/C\text{-}1.0}$, which is almost stable during the 120 temperature cycles, the $R_{ct\ I/C\text{-}1.5}$ shows the biggest change. The visible gap compared to the other charge transfer resistances is due to the

higher flow resistance through the CL. This leads to a shift in the core reaction area and decreased surface oxygen concentration $C_s$ [140].

For the double layer capacitances $C_{dl}$ (summarized in **Figure 70 (b)**), it is worth noting that the capacitance is to some extent related to the ionomer to carbon weight ratio in the cathode CL [151]. This is particularly evident in the gap between the $C_{dl\ I/C\text{-}0.5}$ and the other two capacitances ($C_{dl\ I/C\text{-}1.0}$ and $C_{dl\ I/C\text{-}1.5}$). Due to the low ionomer content, the reduction of the cathode CL thickness causes a morphological change. This, in turn, increases the contact area between ionomer/carbon and thus the capacitance $C_{dl\ I/C\text{-}0.5}$ during the first 20 cycles. After 20 cycles, quasi-saturation was reached, and the trend stabilized until the end of the stress test. In contrast to the $C_{dl\ I/C\text{-}0.5}$, the $C_{dl\ I/C\ 1.0}$ and $C_{dl\ I/C\ 1.5}$ show a stable behavior during the first 40 cycles, followed by a significant decrease until the end of the test. In this case, maximum saturation was reached after only 40 test cycles. The continuous reduction in capacity can be directly attributed to the enrichment of the ionomer and the shift in the core reaction area described earlier.

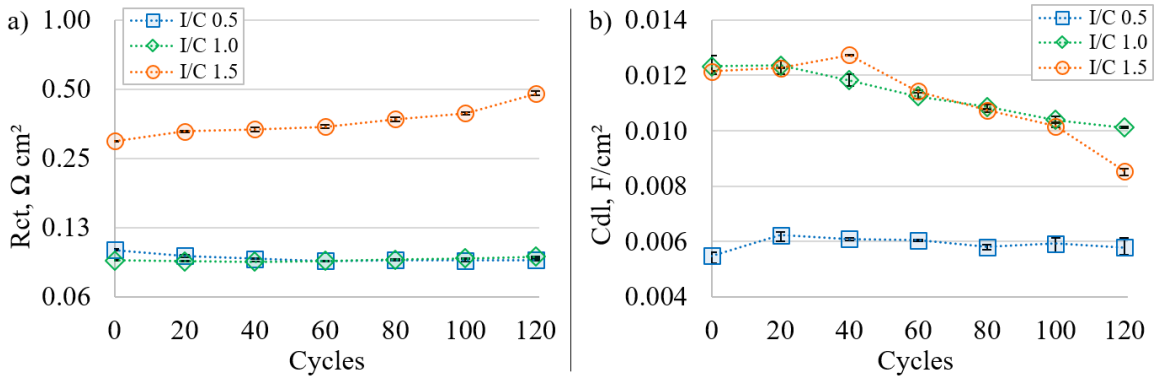


**Figure 70: (a)** Summary and trend of the calculated charge transfer resistances $R_{ct}$ and **(b)** the calculated double layer capacitances $C_{dl}$ of the tested MEAs at a current density of 0.8 A/cm² during the stress test.

The changes in the R-C elements related to the specific quasi-reversible adsorption of the sulfonate groups of Nafion® on the Pt catalysts are summarized in **Figure 71** [115, 120]. In addition to the $R_{ct\ I/C\text{-}0.5}$, the $R_{ads\ I/C\text{-}0.5}$ also decreases during the first 60 cycles. This again indicates enrichment of the ionomer and increased adsorption of sulfonate groups on the surface of the Pt catalyst in the core reaction area of the cathode. However, the development of the adsorption capacity $C_{ads\ I/C\text{-}0.5}$, which is not visible at first glance, is interesting. Here it can be assumed that the decrease from the 20th cycle onwards is related to the loss of the

active Pt surface. The $R_{ads\ I/C\text{-}1.0}$ and $C_{ads\ I/C\text{-}1.0}$ exhibit expected behavior and are very similar to the results presented in chapter 5.2. Oxidation of carbon and loss of ECSA results in lower specific adsorption of sulfonate groups, leading to an increase in $R_{ads\ I/C\text{-}1.0}$ and a decrease in $C_{ad\ I/C\text{-}1.0}$. The course of the adsorption resistance $R_{ad\ I/C\text{-}1.5}$ can be divided into two main sections (the same applies to the capacitance $C_{ads\ I/C\text{-}1.5}$, but here the behavior is mirror-inverted): In the first section, the resistance increases, which is related to the decrease of the cathode CL thickness. In the second section, the resistance changes direction and starts to decrease, indicating a morphological change in or around the core reaction area (see chapter 5.3.4 for more details).

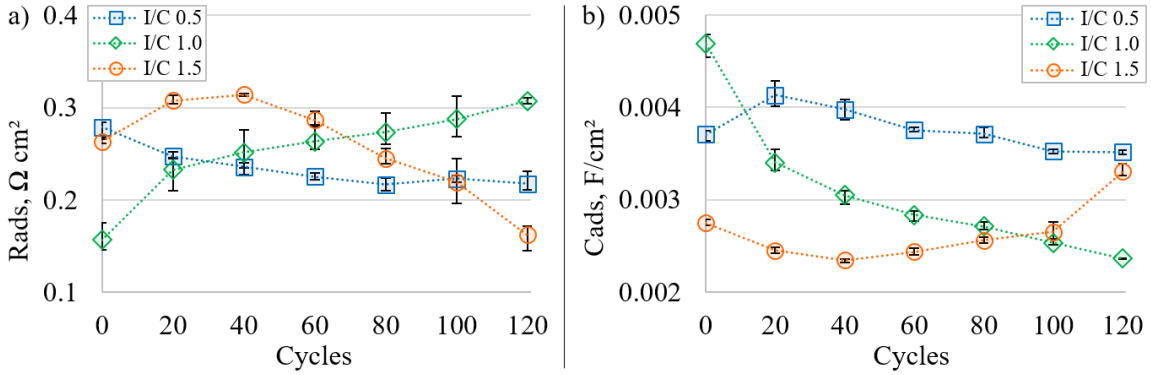


**Figure 71:** Summary of the trends of estimated R-C elements with **(a)** the adsorption resistance $R_{ads}$ and **(b)** adsorption capacitance $C_{ads}$ of the studied MEAs measured at a current density of 0.8 A/cm² during the low temperature stress test.

The behavior of the calculated Warburg "short" elements $W_S$ with the coefficients $A_w$ and $A_v$ are shown in **Figure 72**. As expected, the Warburg coefficients $A_w$ (**Figure 72 (a)**) behave identically to the individual charge transport resistances $R_{ct}$ and can also be used here as an indicator of the degradation state. As also expected here, the individual associated coefficients $A_v$ remain nearly stable during LTST (see **Figure 72 (b)**).

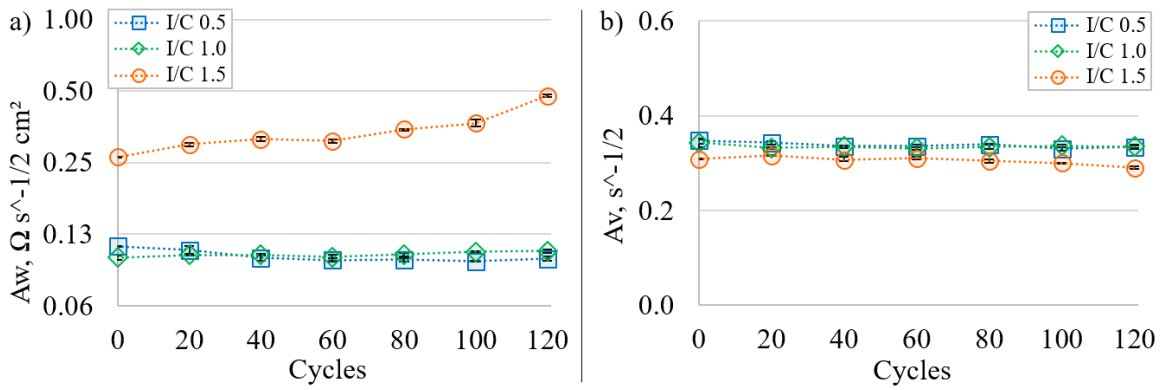


**Figure 72:** Summary and trend of the calculated **(a)** Warburg coefficients $A_w$ and **(b)** the associated parameter $A_v$ of the studied MEAs measured at a current density of 0.8 A/cm² during the low-temperature stress test.

**Figure 73** shows the $A_w/R_{ct}$ ratio of the characterized MEAs during the performed stress test. As in chapter 5.2, the diffusion coefficient $D$ is assumed to be constant during the test. Here it is immediately noticeable that the $k_{app}$ depends strongly on the cathode I/C-ratio, which in turn means that the ionomer/Pt ratio must ultimately influence the $k_{app}$. Nevertheless, all calculated coefficients $k_{app}$ show a relatively stable behavior during the stress test. Again, it can be assumed that, assuming a constant diffusion coefficient $D$, no changes occurred in the structure and crystal faces of the Pt particles, and thus most likely, no Ostwald ripening happened at the individual MEAs.

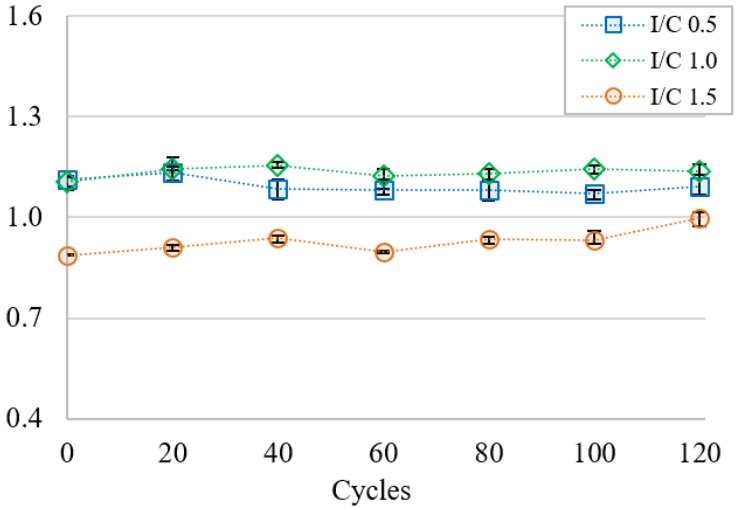


**Figure 73:** Summary of the trends for the calculated $A_w/R_{ct}$ ratios of the investigated MEAs.

### 5.3.4. Ex-situ measurement results

Since the behavior of each MEA toward the stress test was individual, the MEAs were evaluated after the stress test using scanning electron microscope (SEM) images, microscope images, and energy dispersive X-ray spectroscopy (EDXS). These analyses were imperative because some individual behaviors were difficult to attribute to the respective degradation mechanisms. **Table 13** shows a summary of the physical damage revealed by the *ex-situ* analyses.

**Table 13:** Summary of defect patterns for the anode and cathode catalyst layers of the MEAs used, with different weight ratios of cathode ionomer to carbon (I/C).

| | **Error indication** | **MEA 1 I/C - 0.5** | **MEA 2 I/C - 1.0** | **MEA 3 I/C - 1.5** |
|---|---|---|---|---|
| **Anode** | Adhesive break and lift off of the CL | | | x |
| | Crack formation | x | x | x |
| | CL thickness BOL / EOL (µm) | 7.2 / 6.9 | 7.2 / 7.1 | 7.2 / 6.4 |
| | Worms deformation | | | x |
| **Cathode** | Worms / Buckling deformation | | x | x |
| | Crack formation | x | x | x |
| | CL thickness BOL / EOL (µm) | 9.3 / 7.7 | 7.5 / 6.9 | 5.3 / 4.8 |
| | Bonding of CL and MPL | | | x |

The destructive mechanisms can be divided into two main categories: One is driven by rapid enthalpy changes that lead to mechanical failure of MEA components. The others are driven by rapid potential changes or potential shifts (overpotentials), which are directly related to the test sequence.

In order to determine the CL thicknesses of the individual MEAs, cross-sections were made at different positions of the active surface area using a computer-controlled ion milling system. All MEAs show a significant decrease in cathode CL thickness (see **Table 13**) and redistribution of Pt (visible as a Pt band in the membrane). Considering the fact that all three MEAs showed almost identical loss of ECSA, it can be assumed that the mechanism responsible for the decrease in cathode CL thickness must be the same in all cases. Since

the same anode CL was used for all three MEAs, two main mechanisms seem to be responsible for the loss of ECSA. First, the condensed water on the anode side could not be adsorbed by the ionomer network, which most likely froze during the low-temperature step. This blocked the gas pathways during low-temperature start-up, resulting in $H_2$ starvation and a shift of the cathode potential toward higher values. Second, the slight overpressure on the anode side during the low-temperature phase causes an $H_2$ crossover from the anode to the cathode, which leads to a gradual local reaction of $H_2$ and air in the cathode CL. Due to the continuous local exothermic reaction, the OCV decreased to 0 V after about 1800 s (duration of the low-temperature phase about 3200 s). This, in turn, means that the oxygen on the cathode side was used up after 1800 s and both $N_2$ and $H_2$ had to be present at the end of the low-temperature part. During start-up, the air was directed back into the cathode (opening the test item bypasses), forming an $H_2$/air front with the accumulated $H_2$. Both mechanisms resulted in high overvoltages and higher local temperatures in the cathode, which promoted carbon oxidation as well as dissolution and redistribution of Pt [139, 140].

The next degradation mechanism that became visible in all MEAs was the formation of cracks (with a length of up to 500 µm) over the entire active anode and cathode area (see **Figure 74**). There is much evidence to suggest that the main cause of cracking is the interaction between the rapid temperature change and the residual water stored in the anode CL and cathode CL during the low-temperature phase and start-up. In other words, the rapidly changing parameters (in water content and temperature) caused contraction and expansion longitudinally (thermally driven) of the MEA, leading to material failure and cracking in both CLs [152].

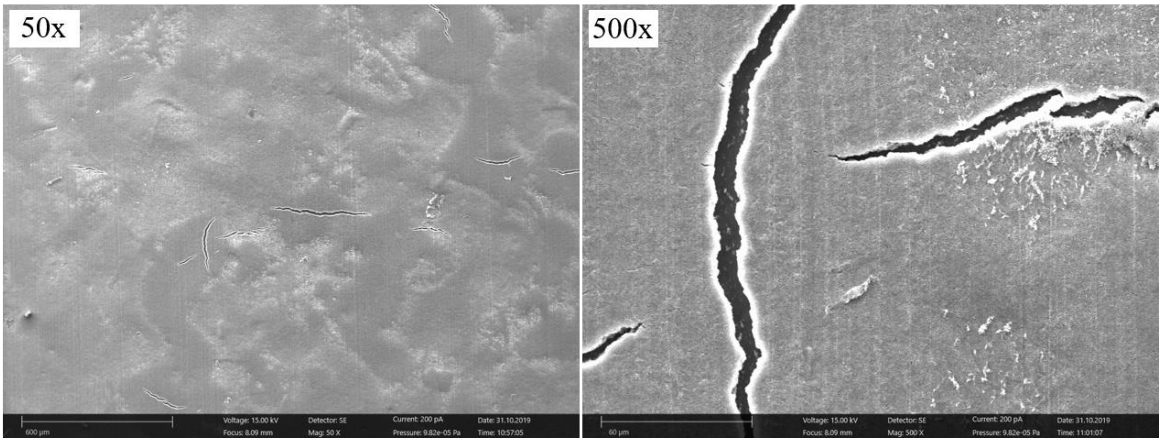


**Figure 74:** Scanning electron microscope (SEM) images (15 kV, 200 pA) at different scales showing the visible cracks on the surface of the anode catalyst layer [153].

Another mechanism, also driven by the rapid enthalpy and moisture changes, caused worm and buckling deformations over the entire active area of the cathode (see **Figure 75 (a)** and **(b)**). In contrast to the cracking, the worm and buckling deformations protruded out of a plane or formed dents and bulges with diameters predominantly between ca 100 µm and ca 150 µm. However, this degradation mechanism occurred only in the two MEAs with the higher ionomer loading ($MEA_{I/C-1.0}$ and $MEA_{I/C-1.5}$). The $MEA_{I/C-0.5}$ did not show any visible deformation in this direction. Therefore, one can suspect that this destruction mechanism is related to the ionomer loading of the cathode CL and the difference in water movement from anode to cathode [154].

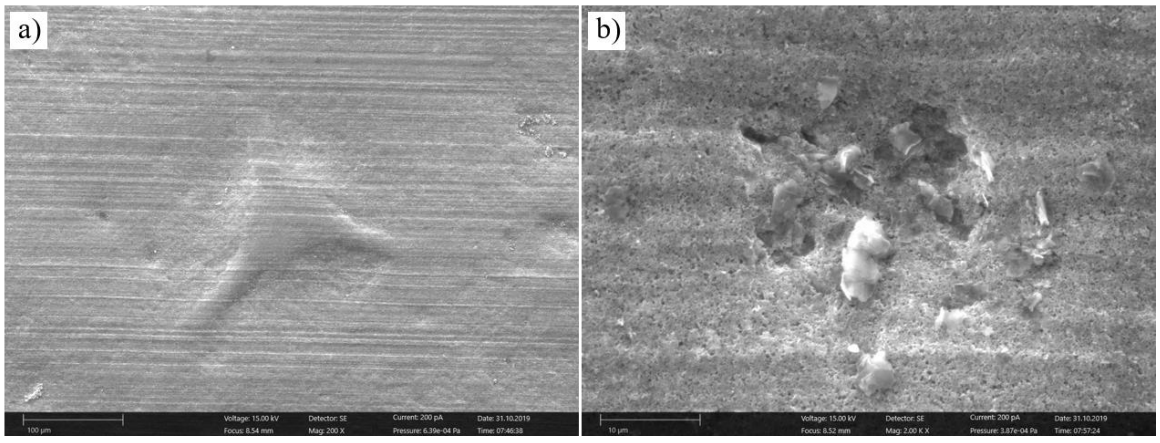


**Figure 75:** Scanning electron microscope (SEM) images (15 kV, 200 pA) of the surface of the anode catalyst layer showing **(a)** the visible worms and **(b)** buckling deformations [153].

As mentioned previously, the MEA with the highest I/C-ratio of 1.5 showed an increased performance loss and an accelerated increase in the measured resistance $R_{u\ I/C\text{-}1.5}$ during the last 20 cycles. One can hypothesize that this increase is related to the rupture and detachment of the anodic CL (**Figure 76 (a)** and **(b)**) and a disruption of the proton pathways [150]. The *ex-situ* results indicate that a locally higher amount of water was stored in the anode CL due to the high ionomer loading and pronounced water movement. During the low-temperature phase, the stored water changed the aggregate state, led to volume expansion and gradual fracture and breakage of the anode CL.

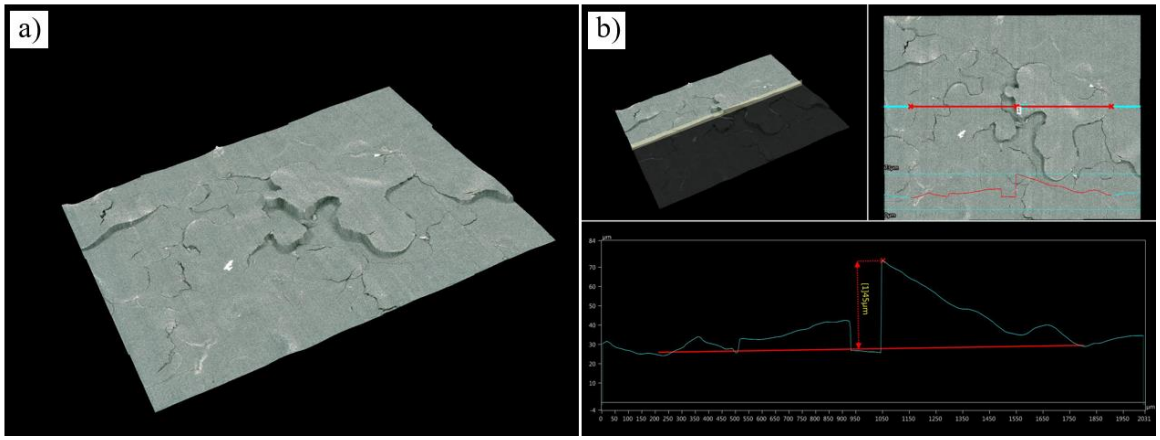


**Figure 76:** 3D microscopy images and generated height profile sections showing the visible extensive fracture and detachment of the anode catalyst layer of the MEA with a cathode ionomer carbon weight ratio (I/C) of 1.5 [153].

All these mechanisms damage the CLs in the long term but are probably not the main origin of the significant performance loss. However, a critical issue is a decrease in cathode CL thickness, which leads to excessive ionomer loading towards the GDL. The following SEM images of the $MEA_{I/C\text{-}1.5}$ cathode catalyst structure (see **Figure 77 (a)** reference, **(b)** used - after 120 freeze cycles) clearly show that the porosity of the cathode CL has changed significantly due to the LTST. This change in porosity and the resulting increased mass transport limitation was particularly visible at the current density points and for almost all calculated EEC parameters described in Section 5.3.3. This hypothesis is also supported by the EDXS and the peak ratio between Pt and F (ionomer) (see **Figure 77** reference **(c)**, used **(d)**). The peak ratio between Pt and F decreased during the stress test (reference/used - 2.1/1.8), indicating that more ionomer must be present at the surface of the cathode CL. Another indication of ionomer accumulation at the interface was the binding between the cathode CL and the GDL. During the preparation for the SE micrographs, the GDL was

practically glued to the CL, which made the separation of the two layers extremely difficult. In this context, two main mechanisms could be responsible for the bonding of the two layers. First, as mentioned above, the reduction of the cathode CL thickness and thus the accumulation of ionomer at the interface with the GDL. Second, the cold and hot cycles favored the contraction and expansion of the materials and, thus, the two layers' interlinking.

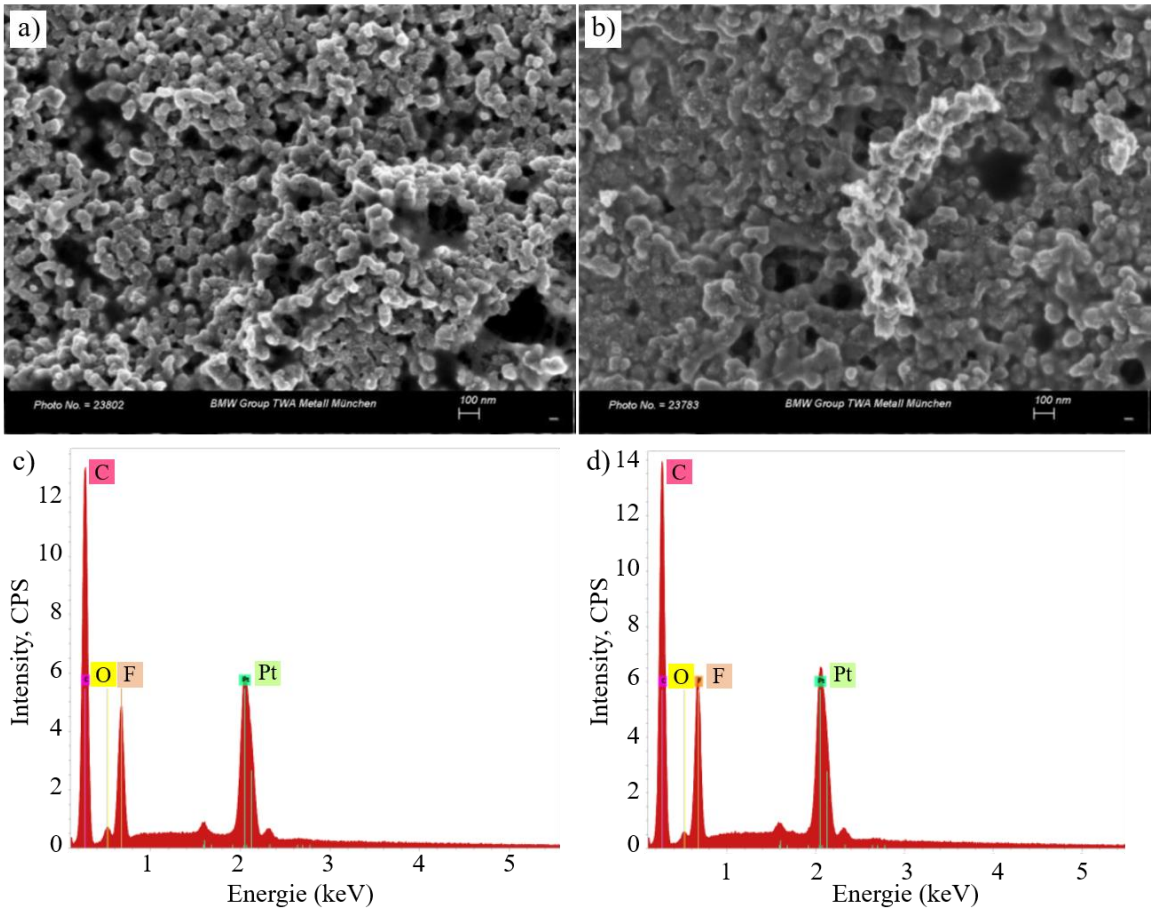


**Figure 77:** Scanning electron microscope (SEM) and energy dispersive X-ray spectroscopy results of the cathode catalyst structure of the MEA with a cathode ionomer carbon weight ratio of 1.5. The analysis was performed before and after the stress test. **(a)** Reference SEM, **(b)** SEM of the used sample , **(c)** reference EDX, **(d)** EDX of the used sample [155].

## 5.4. Investigation of local degradation caused by temperature gradients

### 5.4.1. Introduction

Based on the two low-temperature stress tests performed previously, a novel test was performed using the automotive-size PET SC TP285. Besides the other quantity, the main difference is the low-temperature part (LTP), which was modified by a temperature gradient. In other words, whereas in the two previous tests a negative cell temperature of -5 °C and -10 °C was set, here a gradient from -8 °C to +2 °C was set above the active surface. The background of this gradient is the simulation of a stationary vehicle where the stack is not completely cooled down. In other words, the stack in the vehicle cools from the outside inwards so that after a certain time, there is a homogeneous negative temperature over the active area. However, suppose the vehicle is started in the middle of the cooling process. In that case, the central area of some cells may be in the positive temperature range and the outer areas in the negative temperature range. The aim of this temperature gradient during the LTP phase is to stimulate the degradation mechanisms on the active surface to different degrees, depending on the temperature. This should ideally result in differential degradation on the active surface, which could be represented by measuring the local impedance and current density. In summary, the following points were changed compared to the last stress test:

- The PET SC TP285 was used for the stress test.
- In the LTP, no uniform negative temperature is set over the active surface, but a temperature gradient from -8 °C to +2 °C.
- In addition to standard *in-situ* measurement methods, local impedance and current density were measured over 46 and 612 measurement points, respectively.

Since an automotive-sized MEA with an active surface area of 285 cm² was used in this stress test, no further details on the composition of the MEA can be provided for confidentiality reasons.

### 5.4.2. Test methodology

Similar to the stress test presented in chapter 5.3, the entire test sequence was programmed in the test bench programming language VBA and fully automated. The main difference in the test bench setup is in the measurement technique. While the test bench load was used, all *in-situ* measurements, with the exception of the polarization curves, were performed with additional measurement hardware from ZAHNER-elektrik GmbH & Co. KG and S++® (for more details, see chapter 3.1.2). The entire test sequence, with the exception of the LTP, was taken from Chapter 5.3.2 and adapted to the automotive-sized cell hardware. More precisely, the complete sequence remained, but some operating parameters were adapted to the cell size. The changed operating parameters are shown in detail below:

Due to the cell size, only the reactant flows were adjusted during the break-in procedure. The anode and cathode flows were increased to 133 $cm^3/s$ and 400 $cm^3/s$, respectively. All other parameters corresponded to those of the SOP described in chapter 5.3.2.

**Stable operating point (SOP)**

At the SOP, the anode and cathode reactant flows were increased to 33.3 $cm^3/s$ and 78.83 $cm^3/s$, respectively. During this phase, the load is switched in galvanostatic mode at 0.8 $A/cm^2$ and held for 1800 s. The long waiting time is necessary because the local impedance and current density measurements were subsequently performed. In contrast to the last stress test, the impedance measurements were performed at each cycle and are therefore not a part of the characterization section. The impedance of each measuring point is measured in a frequency range between 0.3 Hz to 10 kHz. To exclude hysteresis effects, the impedance measurement starts at a frequency of 1 kHz and initially goes up to 10 kHz. After that, the measuring direction is reversed and goes back to a frequency of 0.3 Hz. In total, 47 frequencies are recorded, which are evenly distributed on a logarithmic scale. A current amplitude of 10 A was selected for the impedance measurements. The current density distribution was recorded simultaneously at a frequency of 0.1 Hz. Faster recording frequencies would have been possible but hardly manageable due to the enormous amount of data.

### Preconditioning procedure

During preconditioning of the cathode side, an HFR resistance of ca 8.55 Ωcm² was approached with a drying flow of 333.3 cm³/s. The preconditioning of the anode side was also performed at a cell temperature of 10 °C. As before, a gas mixture ($H_2$ with 10 % $N_2$) with a dew point of 10 °C and a flow rate of 150 cm³/s was used. The gas mixture was directed to the anode side for 120 s.

### Low-temperature part (LTP)

As mentioned before, the main difference to the previous stress tests is the LTP. **Figure 78** shows a simplified representation of the MEA with the monopolar plate and the temperature gradient from -8 °C to +2 °C on the active surface. Once the temperature gradient was reached, the temperatures were held for 600 s.

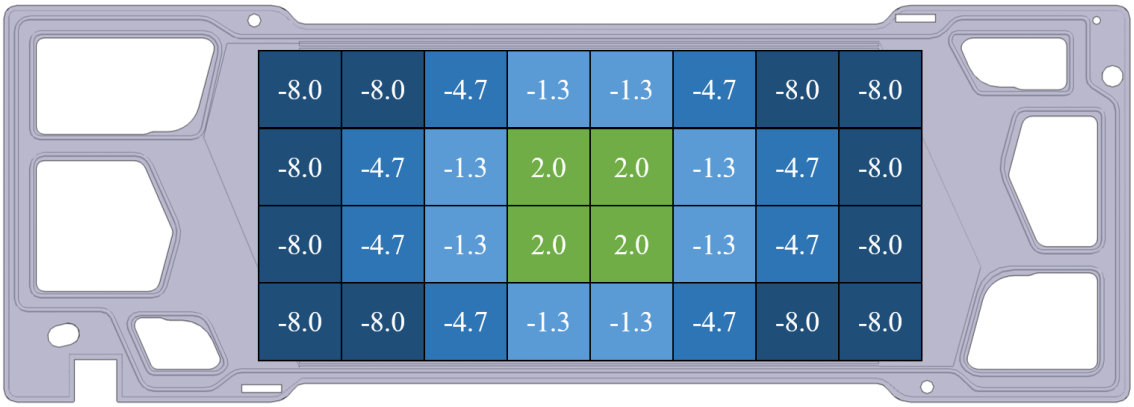


**Figure 78:** A simplified representation of the MEA with the monopolar plate and the temperature gradient from -8 °C to +2 °C on the active surface.

### Start-up

In the first part of the start-up procedure, the reactants were fed into the cell at anode and cathode flow rates of 33.3 cm³/s and 78.83 cm³/s, respectively. After reaching OCV, a current density of 0.1 A/cm² was set for 20 s, and the current was then ramped up to a lower voltage limit of 0.6 V with current steps of 0.05 A/cm² and a hold time of 2 s/step. When all working parameters have been reached and no alarm criterion has been violated, the load is switched to the potentiostatic mode, and a voltage of 0.7 V is set.

**Characterization**

In contrast to the previous stress tests, only a polarization curve and a classic $H_2/N_2$ cyclic voltammetry measurement are performed in the characterization part after the break-in and every 20 cycles. The polarization curves were measured at flow rates of 166.7 cm³/s and 400 cm³/s and dew points of ca 63.8 °C (50 % RH). The cyclic voltammetry measurement was performed with anode and cathode flow rates of 33.3 cm³/s and 66.7 cm³/s, respectively. For better reproducibility, the ECSA measurement was performed twice, each time at a cell temperature of 80 °C and a dew point of ca 63.8 °C.

### 5.4.3. In-situ measurement results

**Preconditioning procedure**

**Figure 79** shows the drying times for cathode preconditioning with the target HFR of ca 8.55 Ωcm² during the stress test. As with the stress test presented in Chapter 5.2, the target HFR is never reached at the same drying time. This can be due to a variety of causes, including random water deposits in the flow field or cells that are detached by the increased air flow. However, the quasi-exponential decrease in average drying time over the course of the stress test is very interesting. Now, assuming that similar degradation mechanisms occurred as in the first two stress tests, the decrease in drying time can be directly related to the decrease in cathode CL thickness.

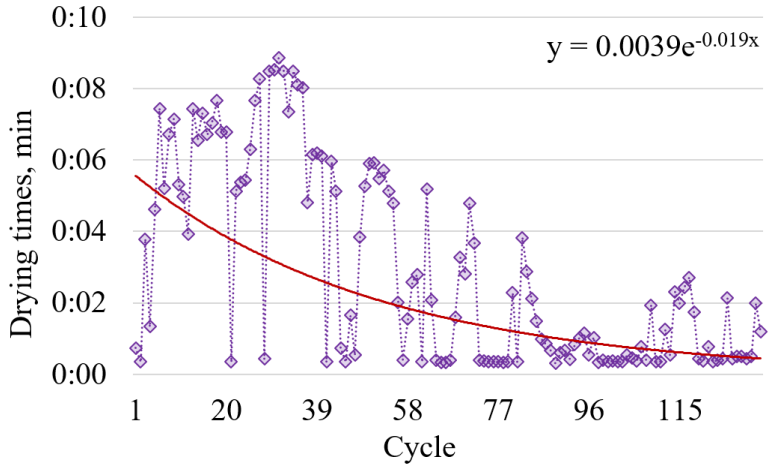


**Figure 79:** Drying times for cathode preconditioning with the target HFR of 8.55 Ωcm² during the stress test.

### Polarization curve

The current density points vs. the number of cycles derived from the polarization curve are shown in **Figure 80**. The change in the performance is more pronounced at higher current densities, indicating a change in cell resistance. If one now looks at the current density at 1.5 A/cm², one can see a pronounced dip during the first 20 cycles, where the performance increased by +6.84 % (ca +32 mV). Between cycles 20 and 80, the performance continues to grow slightly, resulting in an overall increase of +2.4 % (+12 mV). As described in section 5.3, the growth can be attributed to an improvement of the protonic network due to the reduction of the cathode CL thickness, which is also shown later in the higher frequency impedance response (uncompensated resistance, $R_u$). A slight decrease with subsequent increase in the performance is seen from cycle 80. If the measuring point at cycle 100 (498 mV) is left out, stabilization occurs between cycles 80 and 120 (512 mV and 509 mV). Similar behavior was seen in **Figure 79**, where the exponential drop gradually stabilized from cycle ~80.

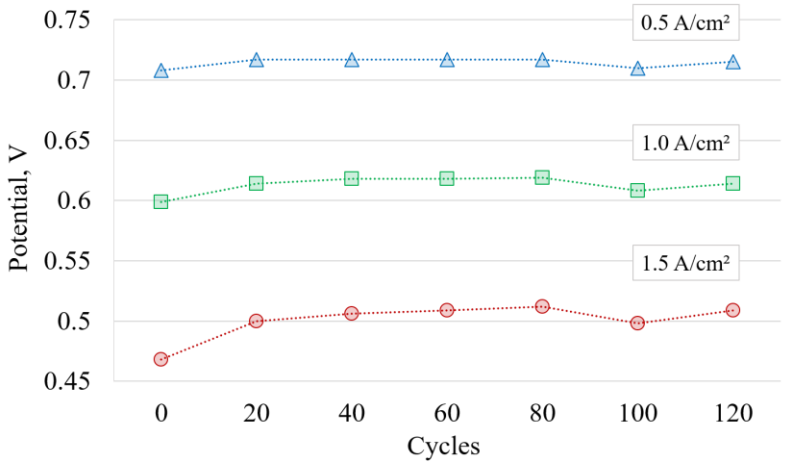


**Figure 80:** Current density points vs. number of cycles derived from polarization curve.

### Cyclic voltammetry

The percent decrease in ECSA during the low-temperature test is shown in **Figure 81**. Similar behavior was observed in the two low-temperature stress tests conducted previously. Overall, there was an ECSA decrease of 27 % during the 120 cycles performed. The reduction in ECSA can be attributed to many causes. As in the experiments before, it is suspected that a change in ECSA was also induced by the COR in this case, leading to a decrease in cathode CL thickness and dissolution and redistribution of Pt [128, 129, 147, 148, 149].

Although no uniform subzero temperature was set on the active surface in the LTP, the entire area at the flow field inlet and most of the active surface were well below the freezing point of the water. Therefore, hydrogen starvation and thus a potential shift could still occur. As in the experiments before, the potential changes during commissioning and CV measurement are likely to have a small, non-negligible influence. But again, it should be mentioned that the literature indicates that the dominant degradation mechanism is COR [130].

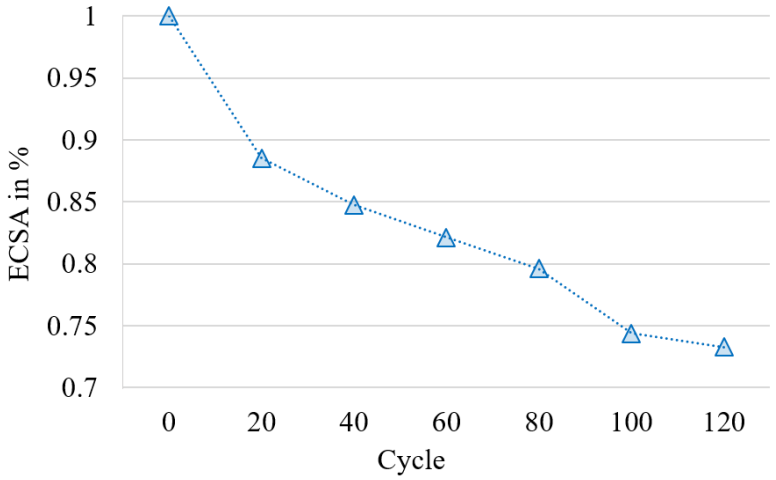


**Figure 81:** The decrease in electrochemical active surface area (ECSA) in % during the low-temperature stress test (LTST).

### Current density distribution

In addition to the locally resolved impedance measurements, the current density distribution in the SOP was measured. The current density distribution measurement can be used to measure a PEMFC single cell's local performance, which depends mainly on the conductivity of the electrolyte, the diffusion or activation overvoltage, or the design of the system. This makes this measurement principle particularly convinient for optimizing operating strategies or fuel cell components, such as the flow field. In the case of this stress test, where a temperature gradient was set in the LTP, the current density distribution can provide important information about the local change or degradation of the active surface. **Figure 82** shows the current density distribution of the active surface during the LTST. The red or blue arrow indicates the flow direction of the respective reactant. More precisely, the air flows from right to left on the x-axis, and the hydrogen flows in the opposite direction

due to the cross-flow arrangement (more on this in chapter 3.1.4). It can be seen immediately that there was no homogeneous current density distribution in the BOL measurement either. Nevertheless, a change in current density can be observed during the LTST.

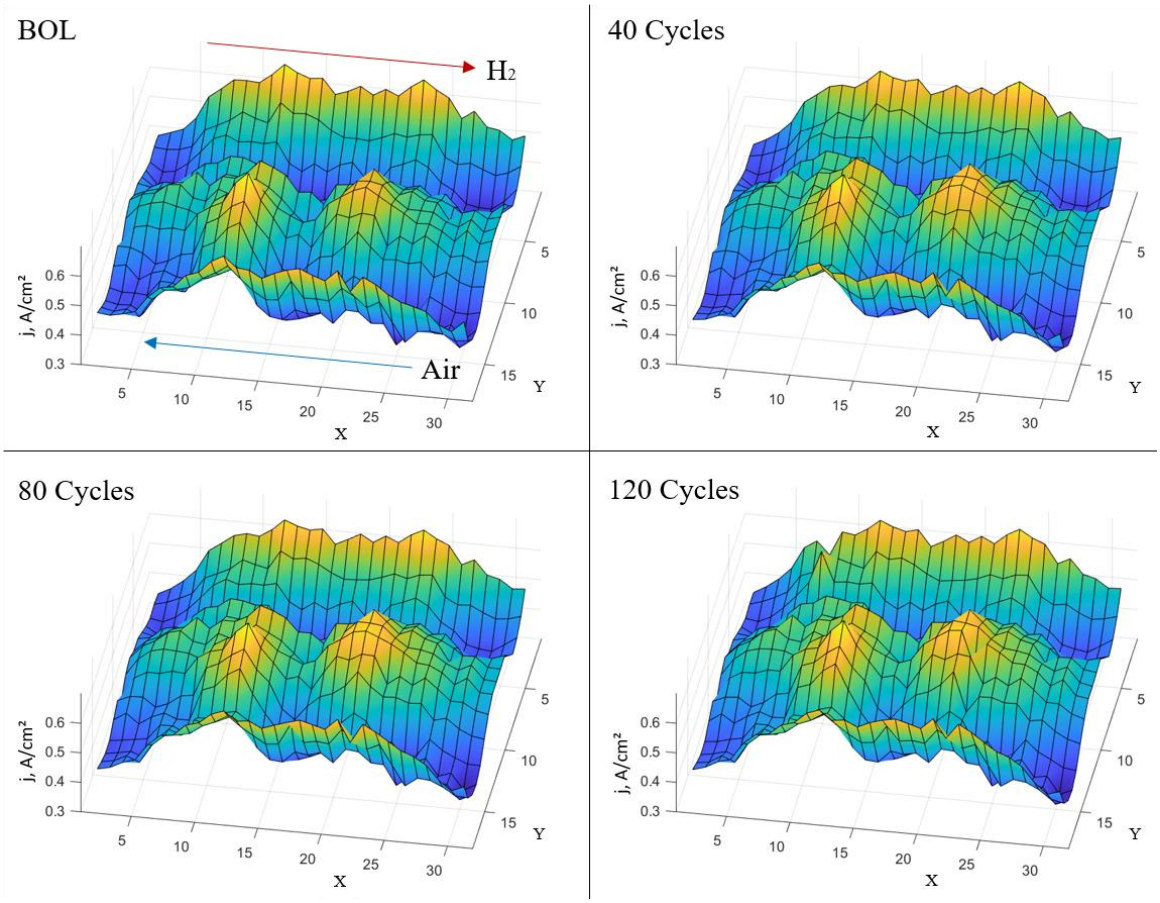


**Figure 82:** Current density distribution of the active surface measured in the stable operation point (SOP) during low-temperature stress test (LTST).

For a better overview, **Figure 83** shows the absolute difference of the measured current density between BOL and after 120 temperature cycles. In this case, an apparent decrease in current density of up to -0.05 A/cm² can be seen directly at the sides (flow field inlet and outlet) that were exposed to a temperature of -8 °C. Here it can be assumed that the trigger for the increased degradation was the significantly lower temperature. The lower performance at the sides is compensated by the rest of the active area, resulting in a measurable increase in the current density. However, regions that already had significantly higher current densities at the beginning (e.g., the two mound-like formations in the middle) appear to contribute less to compensation than areas where current densities were lower. To be able to make a more precise statement, post-mortem *ex-situ* analyses would

be necessary in this case. Since these are very time-consuming, they could no longer be carried out within the scope of this thesis.

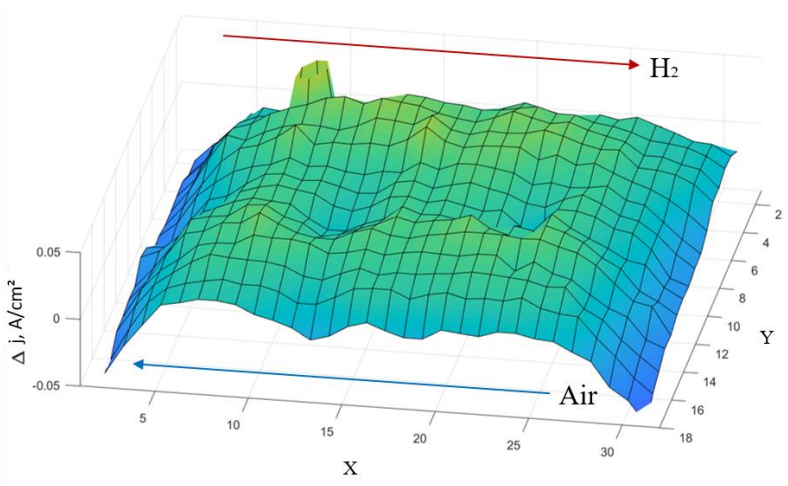


**Figure 83:** The absolute difference between the measured current density between BOL and after cycle 120.

### Electrochemical impedance spectroscopy (EIS)

As in the experiments before, the cell impedance can provide valuable information about the state of the PEMFC. In contrast to the previously conducted experiments, an attempt was made here to measure the locally resolved impedance. The measurement setup for recording the local impedances is explained in more detail in chapter 3.1.2. As described before, the total current is modulated similarly to the usual impedance measurement, but the voltage response is tapped at 46 measurement points distributed on the active surface. At this point, it should be mentioned that due to the velocity of the potential change, the cross-influence by opposing surfaces is probably very high. Thus the individual impedance responses could be distorted.

**Figure 84 (a)** shows the EEC model used to fit the locally measured impedance responses. Like the previously used EEC models, this one is also based on the modified Randles model, but a good approximation could be obtained even without the R-C part describing the quasi-reversible adsorption. Therefore, the meaning of the individual elements will not be discussed in detail in this chapter. Due to the enormous amount of measurement data, the measured raw data were automatically processed using a Matlab script based on the Zfit function [156]. Despite the best possible shielding, inductive effects occurred probably due

to the high number of measurement data lines between the measuring device and the cell hardware. To avoid these artifacts, the fitting was performed only for the frequency range from 1 kHz to 0.3 Hz. **Figure 84 (b)** shows the measured impedance response of the 46 measurement points at BOL.

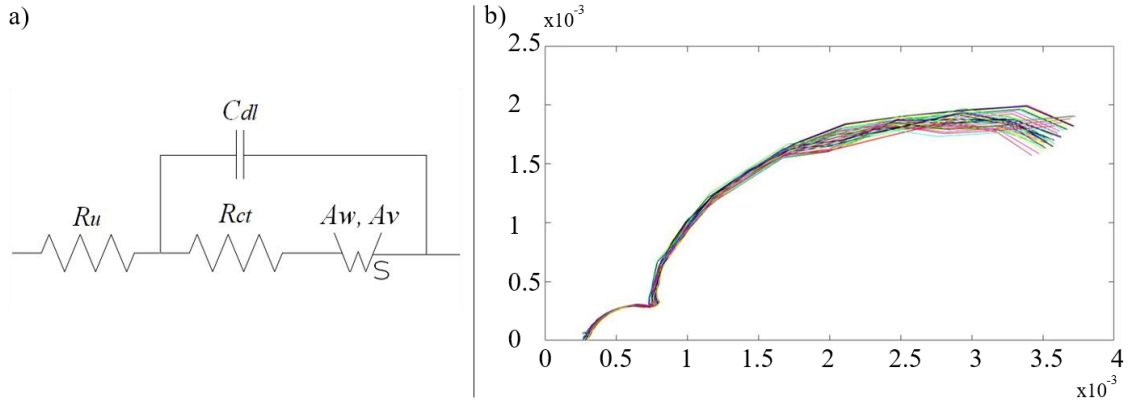


**Figure 84:** The EC model used to fit the locally measured impedance responses **(a)**, and the impedance responses of the 46 measurement points at BOL **(b)**.

During the stress test, three measuring points showed open-circuit characteristics, indicating a wire break. Unfortunately, the source of the fault could not be identified. Therefore, the three faulty measurement points were deleted from all subsequently presented plots. Furthermore, a prolonged impedance measurement failure occurred between cycles 83 and 97. The evolution of the calculated model parameters of the uncompensated (Nafion® electrolyte) resistance $R_u$ and the charge transfer resistance $R_{ct}$ of the total cell impedance is shown in **Figure 85**. Similar to the drying time (**Figure 79**), the ohmic resistance $R_u$ shows an exponential decrease. A similar trend was already observed in section 5.3 ($MEA_{I/C-0.5}$), where temperature changes led to an enrichment of the ionomer. The increase of the ionomer network in the CL leads to an improved proton conductivity. The $R_{ct}$ again shows a significant decrease during the first cycles and stabilizes by the end of the stress test. Since the $R_{ct}$ is directly related to the performance and thus to the degradation state, a similar behavior could be observed for the current density points shown in **Figure 80**.

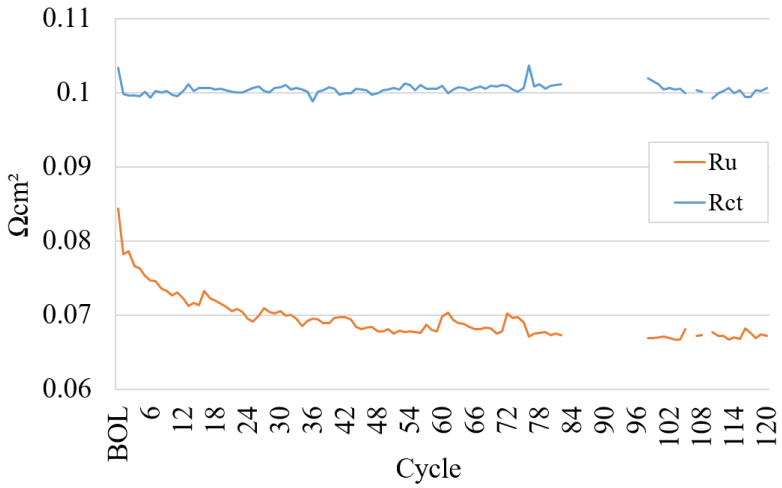


**Figure 85:** The evolution of the calculated model parameters $R_u$ and $R_{ct}$ of the total cell impedance during LTST.

**Figure 86 (a)** shows the locally resolved model parameters of the ohmic resistance $R_u$. The two centered mound-like formations, which were clearly visible in the current density distribution, are again visible here as two regional depressions. It can be assumed that the higher current density at these locations improves the degree of wetting of the protonic network, and thus the calculated $R_u$ is significantly lower here. **Figure 86 (b)** shows the absolute difference of the locally calculated resistance $R_u$ between BOL and the 120 cycles. An approximately uniform decrease in $R_u$ can be seen here, indicating a uniform improvement in proton conductivity.

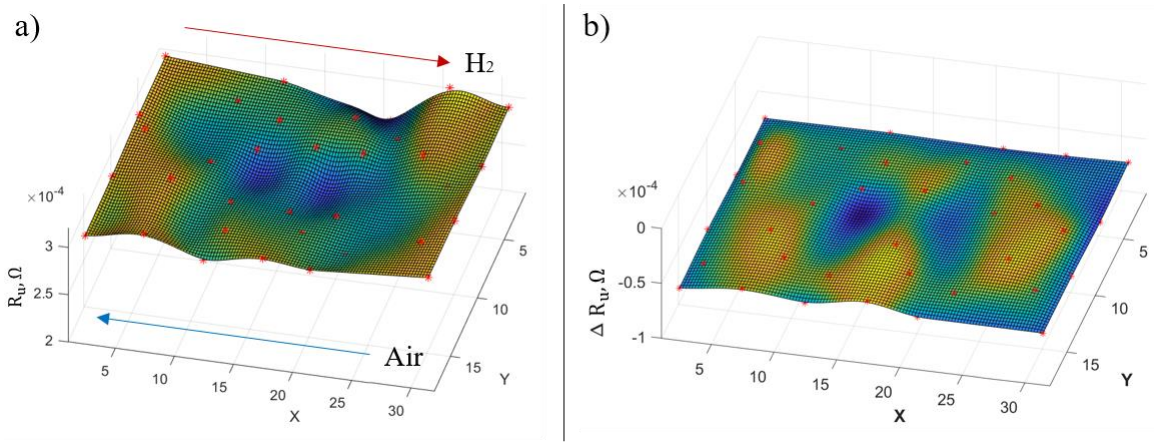


**Figure 86:** Locally resolved model parameters of **(a)** the ohmic resistance $R_u$ and **(b)** the absolute difference in resistance $R_u$ between BOL and the 120 cycles.

**Figure 87 (a)** shows the locally calculated $R_{ct}$ at BOL. In this case, the two mound-like formations that were visible in the current density distribution are not directly identifiable as depressions. In the area of the mound-like formations, the $R_{ct}$ seems to be higher than in the areas where a lower current density was present. **Figure 87 (b)** shows the absolute difference of the locally calculated $R_{ct}$ between BOL and after 120 cycles. All the depressions visible in **Figure 87 (a)**, indicating a lower $R_{ct}$, decrease less during the stress test (visible in the areas shown in yellow). It appears that a harmonization of the surface has taken place.

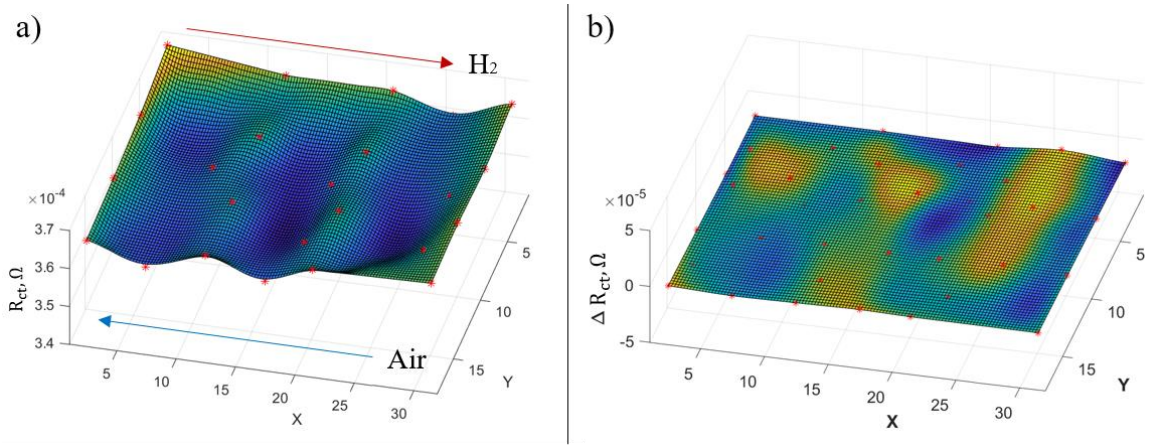


**Figure 87:** Locally resolved calculated charge transfer resistances $R_{ct}$ at **(a)** BOL and **(b)** the absolute difference of the charge transfer resistances $R_{ct}$ between BOL and after 120 cycles.

Very interesting, however, is the course of the double layer capacitance $C_{dl}$ of the total cell impedance, which is shown in **Figure 88**. Similar to the current density points (**Figure 80**), an increase in $C_{dl}$ occurs during the first cycles. This increase could be related to the reduction of the cathode CL thickness and the accumulation of ionomer. In other words, the contact area between carbon and ionomer increases in the core reaction area, which ultimately leads to an increase in capacitance. Similar behavior could be observed in chapter 5.3 with the $MEA_{I/C0.5}$, where first an increase in $C_{dl}$ could be observed and subsequently a stabilization. In this case, however, no stabilization occurs, but again an exponential decrease of the $C_{dl}$, which is directly related to the reduction of the cathode CL thickness and thus also of the ECSA.

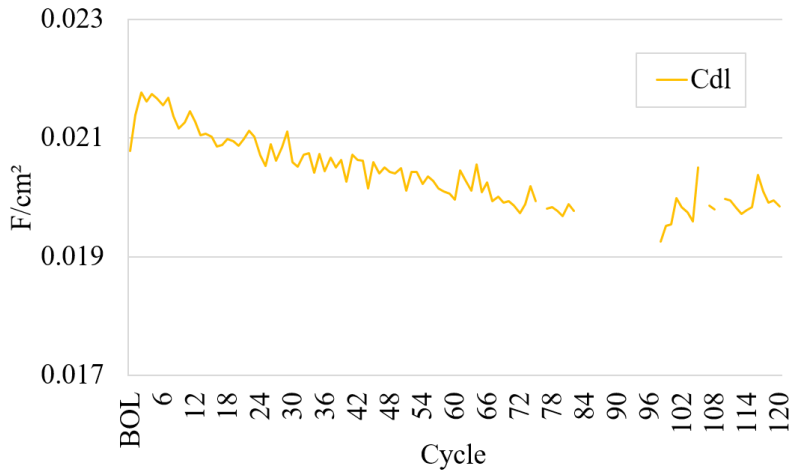


**Figure 88:** Course of the calculated double layer capacitance $C_{dl}$ of the total cell impedance during LTST.

The calculated local $C_{dl}$ values at BOL are shown in **Figure 89 (a)**. It can be clearly seen that the area of the mound-like formations loses capacity during the LTST (see **Figure 89 (b)**). Those areas that had lower capacitance at the BOL time point degraded significantly less than those areas that had increased capacitance and higher current density. At this point, it can only be speculated how the degradation behavior comes about. An inhomogeneous CL or enhanced degradation mechanisms directly related to the test procedure are conceivable. Ultimately, the behavior would have to be investigated in more detail in further studies.

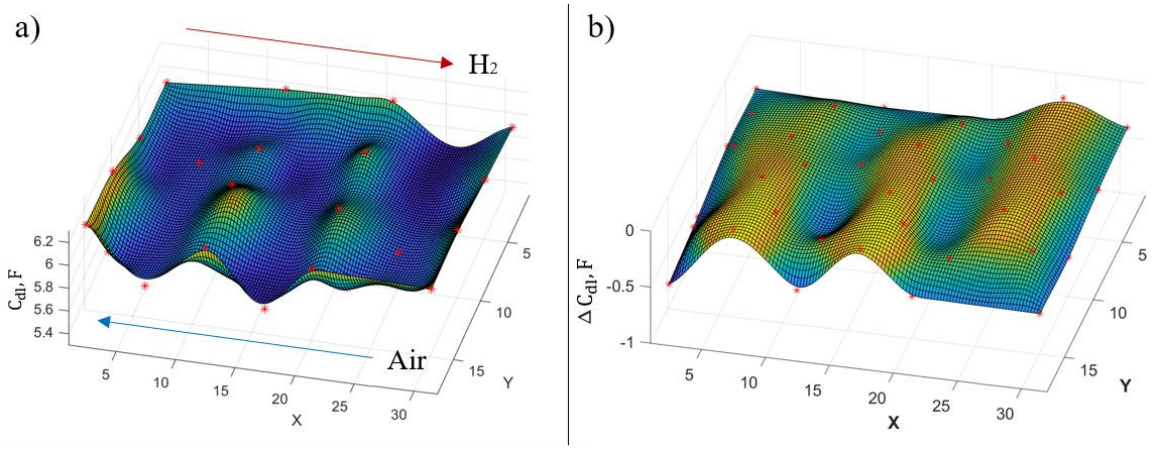


**Figure 89:** Locally resolved calculated $C_{dl}$ at **(a)** BOL and **(b)** the absolute difference of the double layer capacities $C_{dl}$ between BOL and after 120 cycles.

The behavior of the calculated Warburg short element $W_S$ parameters with the coefficients $A_w$ and $A_v$ of the total cell impedance is shown in **Figure 90**. As expected, the Warburg coefficient $A_w$ (**Figure 90 (a)**) behaves identically to the $R_{ct}$. The parameter $A_v$ (**Figure 90 (b)**) shows a clear decrease during the first cycles followed by an increase until the end of the LTST. Here it can be assumed that the relationship between the Nernst diffusion layer thickness $d$ and the diffusion coefficient $D$ has changed.

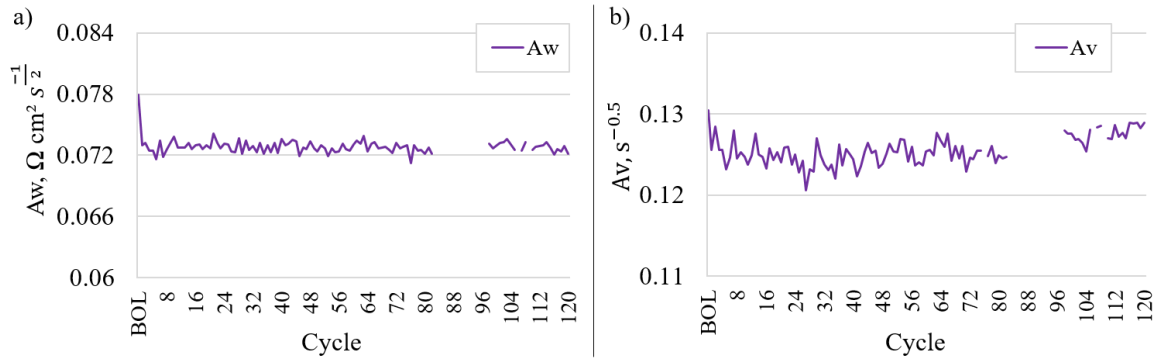


**Figure 90:** Trend of the calculated **(a)** Warburg coefficients $A_w$ and **(b)** the associated coefficient $A_v$ of the total cell impedance during the LTST.

The calculated local coefficients $A_w$ at BOL are shown in **Figure 91 (a)**. A clear increase of the calculated coefficient along the x-axis can be seen. This increase can be directly coupled with the diffusion resistance along the air flow field. Very interesting is the clearly visible peak where a locally increased flow resistance occurs. This could be caused by a different catalyst morphology leading to an increased drop in oxygen concentration in this region. **Figure 91 (b)** shows the absolute difference of the local coefficients $A_w$ between BOL and after 120 cycles. Assuming the progression shown in **Figure 90 (a)**, the overall decrease occurs during the first cycles. The regions where the capacitance $C_{dl}$ hardly decreased during the LTST (see **Figure 89 (b)**) also show a smaller decrease in the diffusion coefficient $A_w$ here. In summary, the areas that have a higher current density have a more significant decrease in the diffusion resistance. By reducing the cathode CL thickness during the LTST, the increased current density, which is simultaneously accompanied by increased production of product water, presumably leads to the removal of excess ionomer. This may prevent the accumulation of ionomer in these areas. Furthermore, the COR leads to a reduction in carbon content and thus to a change in morphology. The question here is whether COR occurs only at the surface of the cathode CL or throughout the entire layer. In the

latter case, the CL structure and probably the pore size could change, leading to a change in the core reaction area and ultimately the coefficient $A_w$.

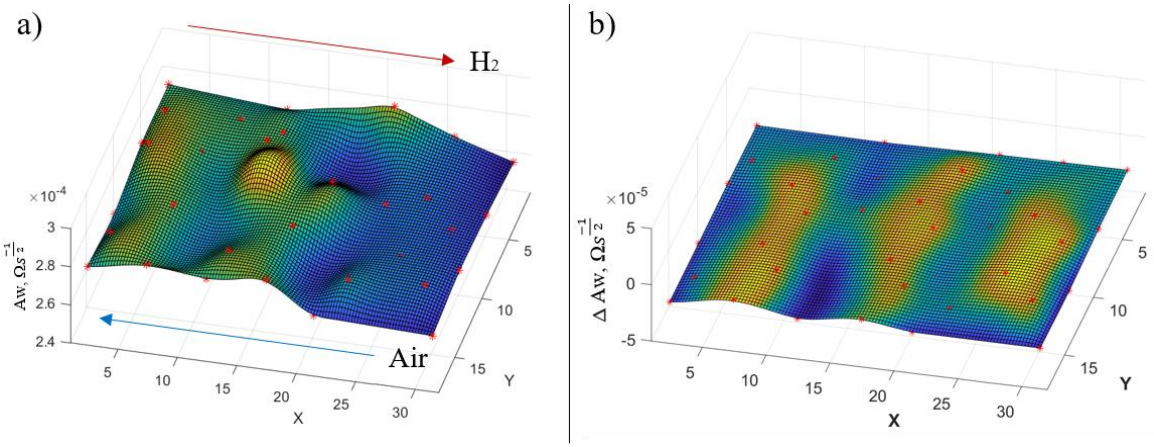


**Figure 91:** Locally resolved calculated Warburg short element $W_S$ parameters with the coefficient $A_w$ at **(a)** BOL and **(b)** the absolute difference of the coefficient $A_w$ between BOL and after 120 cycles.

The calculated local coefficients $A_v$ at BOL are shown in **Figure 92 (a),** and the absolute difference of the coefficient $A_v$ between BOL and after 120 cycles is shown in **(b)**. It can be clearly seen that similar regions as for the locally calculated capacities $C_{dl}$ (**Figure 89 (b)**) change. This similar behavior can again be attributed to the different decrease in cathode CL thickness.

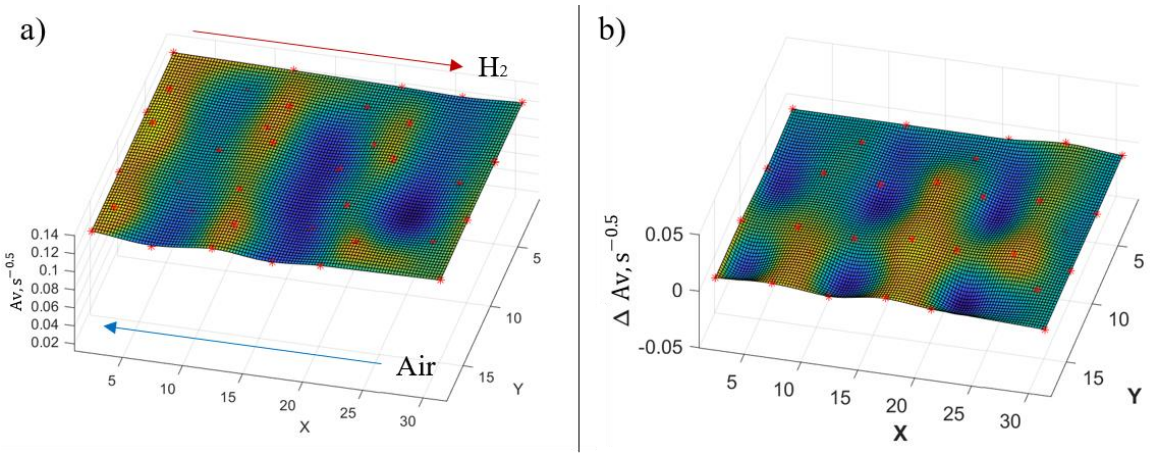


**Figure 92:** Locally resolved calculated coefficient *Av* at **(a)** BOL, and **(b)** the absolute difference of the coefficient *Av* between BOL and after 120 cycles.

# 6 Conclusion and Outlook

The topics covered in this thesis range from completely new methodology development to its use to generate meaningful measurement results.

In the first part of the work, a new method for temperature control of PEMFC single cells was presented. With these two novel tempering units, which can be used to temper single cells with a size of 50 cm² and of 285 cm², the scope of single-cell testing can be significantly extended compared to the conventional measurement setups. The core of the tempering units is powerful Peltier elements, which directly control the temperature of the PEMFC single cell surface. As a result, the new designs achieve temperatures from -30 °C to over 125 °C, temperature change rates of up to 80 $Kmin^{-1}$ and, due to the short control loop, a temperature control accuracy of less than ±0.3 °C. In addition, the automotive-sized design provides individual control of the 64 Peltier elements, enabling local hot spots, different anode and cathode temperatures, and longitudinal temperature gradients of up to 70 °C. This makes the temperature control method clearly superior to all conventional methods and offers an all-in-one solution for the temperature control of single cells.

For the second part of the work, the newly developed cell designs were used, and two main questions were addressed. First, is it possible to quantitatively determine temperature using cell impedance, and second, can qualitative degradation experiments be performed using the newly developed cell designs? The latter question can be divided into several stress tests, each with a different focus. A novel method for determining the PEMFC cathode temperature after shutdown was developed here. In this method, impedance spectra are recorded and evaluated at temperatures between -5 °C and 60 °C. All evaluated EEC elements are sensitive to temperature changes. However, the dependence of the double layer capacitance $C_{dl}$ on temperature appeared to be interesting. In contrast to various approximations (e.g., Mean Spherical Approximation), a quasi-linear dependence was observed for the PEMFC cathodes. Based on this finding, a novel method for estimating the temperature at the cathode using the double layer capacitance values is proposed. For the second question, a total of three low-temperature stress tests were performed. The first low-temperature stress test was a concept test for the new temperature control design and was therefore conducted with the new PET SC TP50 prototype. It was shown that with the new temperature control method, a complete low-temperature stress test on a PEMFC single

cell with a size of 43.56 cm² could be carried out quickly and cost-effectively without the aid of a climatic chamber. Furthermore, it was shown that electrochemical impedance spectroscopy can be used to determine the degradation state and that the degradation mechanisms are directly related to the test procedure used. This includes preconditioning, which is an essential part of the test procedure. Here it has been shown that reproducible drying of the cathode cannot be carried out with the drying time but only with the aid of the high-frequency resistor. Building on the first low-temperature stress test, the second run investigated the effect of different cathode ionomer-carbon weight ratios (0.5/1.0/1.5) on long-term stability during 120 low-temperature cycles. The test procedure for the low-temperature stress test was largely derived from the automotive application and performed with the advanced PET SC TP50. The generated *in-situ* measurement data clearly show that the performance of each PEMFC single cell changes individually depending on the cathode ionomer-carbon weight ratios. In addition, post-mortem *ex-situ* analysis was able to determine the exact damage pattern of each individual cell, allowing conclusions to be drawn about the exact degradation mechanisms. In summary, the destruction mechanisms responsible for the damage can be divided into two categories. One part was driven by the rapid enthalpy change leading to mechanical failure. The other part was driven by rapid potential changes and potential shifts (overpotentials). In the last stress test performed, the automotive size design PET SC TP285 was used, which in addition to low temperatures, can also map temperature gradients on the PEMFC surface. With this additional feature, as well as the ability to perform local impedance spectroscopy over 64 measurement points, a novel experiment was conducted where the shutdown temperature exhibited a gradient on the PEMFC surface from -8 °C to +2 °C. The aim of this experiment was to simulate a parked vehicle where the fuel cell stack had not completely cooled to a homogeneous temperature. Ultimately, 132 temperature cycles could be performed until the PEMFC single-cell finally suffered irreparable damage. The locally resolved measurement methods, such as the current density distribution and impedance measurements, as well as the other results of the *in-situ* methods, indicate a significant change in the cathode catalyst layer. It could be clearly shown that the changes in the catalyst layer are directly related to the test procedure and the set surface temperature gradient during the shutdown phase. Furthermore, a clear correlation between the two cell sizes can be seen, further confirming that with the right measurement hardware, meaningful degradation experiments can be performed even at the small single-cell level.

# Symbols and abbreviations

| | |
|---|---|
| $\alpha$ | transfer coefficient |
| $\alpha_{Al}$ | thermal conductivity aluminum |
| $\alpha_t$ | material-dependent thermal force |
| $A_{CS}$ | active cooling surface |
| *ADC* | analog to digital converter |
| $A_{sc}$ | Pt active surface area |
| $A_w$ | Warburg short coefficient |
| $A_v$ | Warburg short parameter defined by formula 5.1.2 |
| *BP* | base plate |
| *BEV* | battery electric vehicle |
| *BSE* | backscattered electrons |
| *BOL* | begin of life |
| *C* | specific heat capacity |
| *CAD* | computer-aided design |
| $c_{Al}$ | heat quantity of aluminum |
| *CAN* | control area network |
| $C_{Ads}$ | adsorption capacitance |
| $c_{Cu}$ | heat quantity of copper |
| $C_{dl}$ | double layer capacitance |
| *CE* | counter electrode |
| $c_{Gr}$ | heat quantity of graphite |
| *CL* | catalyst layer |
| *CNLS* | complex nonlinear least square |
| *COR* | carbon oxidation reaction |
| $C_s$ | concentration of oxygen |
| *CV* | cyclic voltammetry |
| *CVM* | cell voltage monitoring |
| *d* | Nernst diffusion layer thickness |
| *D* | diffusion coefficient |
| *DCI* | determination cell impedance |
| *DIA* | differential impedance analysis |
| $d_{Leff}$ | effective inductance |
| *E* | potential |
| *EC* | equivalent circuit |
| *ECSA* | electrochemical catalyst surface area |
| *EDLC* | electric double-layer capacitor |
| *EDX* | X-ray surface analysis |
| *EIS* | electrochemical impedance spectroscopy |
| *FCEV* | fuel cell electric vehicle |
| *F* | Faraday's constant |
| *GDL* | gas diffusion layer |
| *GPIO* | general-Purpose I/O |
| *H* | Enthalpy |
| *HFR* | high frequency resistance |
| *HOR* | hydrogen oxidation reaction |
| *i* | current |
| $i_0$ | exchange current density |
| $I^2C$ | inter-integrated Circuit |
| *I/C-ratio* | ionomer to carbon weight ratio |
| *Im(Z)* | imaginary part impedance |
| *ISA* | impedance spectrum analyzer |
| $l_{Pe}$ | thickness of the Peltier element |
| $l_{TTP}$ | thickness of the thermal transfer plate |
| $k_0$ | standard rate constants |
| $k_{app}$ | apparent reaction rate coefficient |
| $K_d$ | differential component |
| $k_f$ | forward oxidation reaction rates |
| $k_b$ | reverse oxidation reaction rates |
| $K_i$ | integral component |
| $K_p$ | proportional component |
| *LOM* | local operation model |
| *LSM* | laser scanning microscope |

| | |
|---|---|
| *LTP* | low-temperature part |
| *LTST* | low temperature stress test |
| $m_{CC}$ | material mass current collector |
| *MEA* | membrane electrode assembly |
| *MFC* | mass flow controller |
| $m_{MP}$ | material mass monopolar plate |
| *MPL* | microporous layer |
| *MSA* | mean spherical approximation |
| $m_{TTP}$ | material mass thermal transfer plate |
| *n* | number of electrons |
| *OCV* | open circuit voltage |
| *P&ID* | piping and instrumentation diagram |
| *PCB* | printed circuit board |
| *PEMFC* | polymer electrolyte membrane fuel cell |
| $P_{El}$ | total electrical power |
| *PET* | Peltier element tempered |
| *PHEV* | plug-in-hybrid electric vehicle |
| *PID* | proportional–integral–derivative |
| *POC* | proof of concept |
| *POM* | polyoxymethylene plastic |
| *PWM* | pulse width modulation |
| $Q_f$ | monolayer adsorption |
| *ORR* | oxygen reduction reaction |
| $O_x$ | oxidized form |
| $Q_{cmax}$ | maximum cooling capacity |
| $Q_{hmax}$ | total heating power |
| $Q_J$ | Joule heating |
| $Q_{Peltier}$ | heat transfer caused by the Peltier effect |
| *QTC* | maximum cooling power |
| *R* | resistance |
| $R_{Ads}$ | adsorption resistance |
| $R_{ct}$ | charge transfer resistance |
| $R_d$ | reduced form |
| *RDE* | rotating disk electrode |
| *RE* | reference electrode |
| *Re(Z)* | real part impedance |
| *RTD* | resistance temperature detectors |
| $R_u$ | uncompensated resistance |
| *S* | Gibbs' free energy |
| *SC* | single cell |
| *SE* | secondary electrons |
| *SEM* | scanning electron microscope |
| *SOP* | stable operating point |
| *SPI* | serial peripheral interface |
| $\tau$ | time constant |
| *T* | Temperature |
| *TTP* | thermal transfer plate |
| *WCP* | water-conducting plate |
| *WE* | working electrode |
| *WHTP* | waste heat transfer plate |
| $W_s$ | Warburg short |
| *VBA* | visual basic for applications |
| *Z* | impedance |

# Figures and Tables

**Figure 1:** Break down of the total costs of a PEM fuel cell system depending on the production figure [24]. ..... 10

**Figure 2:** PEM fuel cell system with the simplified representation of the cells connected in series to achieve the required operating voltage. ..... 17

**Figure 3:** A simplified cross-section through an MEA showing the individual layers, as well as the reactants $H_2$ and air, the protons $H^+$ and the output product water $H_2O$..... 18

**Figure 4: (a)** High-performance Peltier element used in the PET single cell, and **(b)** its basic operating principle with a simplified representation of the internal structure..... 25

**Figure 5:** Two Horiba FuelCon test benches of the type Evaluator C1000-LT..... 28

**Figure 6:** Simplified technical drawing of test bench type C1000-LT. ..... 29

**Figure 7: (a)** Simplified technical representation of the electrical measurement setup used on the TP50 cell with the load cables, **(b)** the sense cables, **(c)** the TrueData-EIS impedance spectrum analyzer and **(d)** the potentiostat..... 33

**Figure 8: (a)** Simplified CAD (Computer-Aided Design) representation of the current scan shunt board from the company S++® with the detailed magnification of one measuring point: **(b)** The separately tapped input voltage of each measuring point $U_1$, which also corresponds to the local impedance behavior, **(c)** the shunt resistor and **(d)** the resistive temperature sensor, with which the current and temperature can be read out in digital form via **(e)** the USB interface..... 35

**Figure 9:** The top view of the current scan shunt board from the company S++® with the red-framed active surface of the MEA. The measuring points used in this thesis are colored and divided into 4 measuring groups (red, violet, green and blue), which are individually switched through the multiplexer to the impedance evaluation unit. ..... 36

**Figure 10:** Simplified representation of the complete electrical measurement setup with commercial TP285 cell hardware and the built-in current scan shunt board, which can be used to measure the local impedance, current density distribution and temperature distribution over the active area of the MEA.... 37

**Figure 11:** Testwork main window for the manual control of the test item's operating parameters, divided into color-coordinated areas. .....40
**Figure 12: (a)** Additional Testwork views with the TAG manager, **(b)** the trend-viewer for quick analysis of current and historical measurement data, **(c)** the script manager for starting and stopping automated testing procedures and **(d)** the script monitor. .....41
**Figure 13: (a)** Commercially available TP units from the company Tandem Technologies Ltd, including the TP50, which can accommodate MEAs with a maximum active surface area of 50 cm², and **(b)** the TP285, which can accommodate automotive-size MEAs with a size of 285 cm². .....42
**Figure 14:** Detailed view of the CAD (Computer-Aided Design) model of the TP285 cell hardware. The numbers for the individual cell components are explained in detail in **Table 3**. .....43
**Figure 15: (a)** Detailed view of the CAD (Computer-Aided Design) model of the "sandwich structure" with the graphite monopolar plates with integrated cooling channels, **(b)** the monopolar graphite plates with integrated gas channels, **(c)** the glass fiber gaskets ensuring a correct compression of the GDLs and **(d)** the membrane electrode assembly (MEA). .....45
**Figure 16: (a)** Exploded view of the CAD (Computer-Aided Design) model of the "sandwich structure" with the automotive-sized metallic cathode monopole plate, **(b)** the membrane electrode assembly (MEA) with 285 cm² active area and **(c)** the automobile-size metallic anode monopole plate. .....46
**Figure 17:** Typical course of a polarization curve (U-I curve) of a hydrogen PEMFC, divided into 3 main sections: Blue area describes the activation range; red area describes the ohmic range; green describes the diffusion limiting range. .....48
**Figure 18:** Cyclic voltammetry (CV) measurement with the CO-stripping method. Blue hatched area corresponds to the monolayer adsorption of hydrogen, red hatched area corresponds to the carbon monoxide (CO) monolayer oxidation. By integrating the corresponding areas between $E_1$ and $E_2$ (blue or red hatched) the electrochemical catalyst surface area (ECSA) can be calculated. .....49

**Figure 19: (a)** Exemplary EIS-data (open symbols), and fitting of these data to **(b)** the equivalent electric circuit (EEC). ..... 52
**Figure 20: (a)** Simplified technical description of a scanning electron microscope (SEM) and **(b)** a typical SEM image, which is discussed in detail in chapter 5.3. ..... 56
**Figure 21: (a)** The PET SC TP50 prototype during initial commissioning with the CAD model. The anode side is shown in exploded view with the thermal transfer plate (TTP), **(b)** the Peltier element, **(c)** the waste heat transfer plate (WHTP) and **(d)** the polyoxymethylene plastic (POM) base plate (BP). ..... 63
**Figure 22: (a)** The final version of the PET SC TP50 with the CAD model. The anode side is shown in exploded view with the significantly reduced thermal transfer plate (TTP), **(b)** the Peltier element with the 0.5 mm thick heat-conducting pads, **(c)** the waste heat transfer plate (WHTP), **(d)** the base plate (BP) and **(e)** the water-conducting plate (WCP). ..... 65
**Figure 23:** Simplified technical representation of the entire PET SC TP50 structure. For better understanding, both the reactant channels ($H_2$ and air) and the water channels ($H_2O$) were shown on a cross-sectional axis. The letters **(a)-(e)** correspond to those used in **Figure 22**. ..... 66
**Figure 24: (a)** The CAD model of a tempering unit from different perspectives with a partial cross-section, **(b)** the bottom sectional view of the BP and the WHTP and **(c)** the top view without the TPP and faded-in hidden edges. ..... 70
**Figure 25:** Simplified interconnection of the PET SC TP50 with the H-bridge-based control unit, which amplifies the +24 V signal of the test bench interface and the test bench. For a better understanding of the operation of the H-bridges, the switching states of the MOSFETs of the anode side during the heating and cooling modes have been magnified. ..... 71
**Figure 26:** Simplified flow of the programmed software for anode and cathode cell temperature control. From the main procedure, the control algorithm is called, and in it, the algorithms A1 and A2 are arranged hierarchically further below. ..... 72
**Figure 27: (a)** The anode temperature control behavior of the PET SC TP50, and **(b)** a temperature cycle between 80 °C and -10 °C as performed in chapter 5.3. ... 75
**Figure 28: (a)** Cooling behavior of the PET SC TP50 at a temperature jump from 80 °C to 10 °C, and **(b)** the heating behavior during start-up at a temperature of -10 °C. ..... 75

**Figure 29: (a)** The CAD model of the PET SC TP288 prototype with the cathode tempering unit in exploded view with the water-conducting plate, **(b)** the power electronics, **(c)** the waste heat transfer plate, **(d)** 32 Peltier elements**, (e)** the base plate, **(f)** the thermal transfer plate and **(g)** the temperature sensor fingers.....80

**Figure 30:** CAD top view of the cathode tempering unit with a simplified representation of the power electronics unit components and their arrangement. For better understanding, the current-carrying copper wires between the Peltier elements and the power electronics are shown in dashed red and the Inter-Integrated Circuit (I²C) bus wires in green. .....81

**Figure 31: (a)** Enlarged view of the tempering unit and the associated power electronics with the wiring of the Peltier elements and the temperature sensors, as well as **(b)** the commissioning of the PET SC TP288 prototype. .....82

**Figure 32: (a)** The CAD model of the final PET SC TP285 and the exploded view of the anode tempering unit with the temperature sensor PCB, **(b)** the thermal transfer plate, **(c)** the base plate, **(d)** the 32 Peltier elements, **(e)** the power-unit PCB, **(f)** the waste heat transfer plate, **(g)** the water-conducting plate and **(h)** the stabilization plate. .....85

**Figure 33: (a)** The fully assembled anode tempering unit and **(b)** the PET SC TP285 during initial commissioning at -20 °C**.**.....86

**Figure 34: (a)** The front and **(b)** the connector side with the Harting® connector of the anode temperature sensor PCB used in the PET SC TP285. .....88

**Figure 35: (a)** The bottom side of the thermal transfer plate (TTP), which is in contact with the 32 Peltier elements via heat-conducting pads and **(b)** the top side with the cutouts for the temperature sensor PCB.....89

**Figure 36: (a)** The base plate placed on the waste heat transfer plate of the cathode temperature control unit without the power-unit PCB and **(b)** the connection side of the tempering unit with the cut-out in the base plate for the temperature sensor PCB.....90

**Figure 37:** Layout of the PET SC TP285 anode power supply board with the power supply lines shown in red.....92

**Figure 38: (a)** the overall view of the assembled anode power-unit PCB, as well as **(b)** the magnified view, in which the solder joint of the respective grid and Peltier element can be seen in figure. ..... 93
**Figure 39:** Underside of the aluminum heat transfer plate with the visible cooling channels in the assembled state with the water-conducting plate made of Ultem™. ..... 94
**Figure 40:** The stabilizing plate made of precision aluminum with the Viton™ sealing rings. ..... 95
**Figure 41: (a )**The side sectional view (longitudinal direction), with **(b)** the front sectional view of the anode tempering unit. ..... 96
**Figure 42:** Simplified representation of the internal structure of the control cabinet for the PET SC TP285 ..... 97
**Figure 43: (a)** The interior of the control cabinet of the PET SC TP285, as well as **(b)** the front and rear view with the Harting® connectors and the 400 V mains connection. ..... 99
**Figure 44:** Algorithm of the test bench VBA software for the control of the PET SC TP285. ..... 100
**Figure 45:** Simplified software algorithm of the anode and cathode evaluation board. . 100
**Figure 46:** The simplified algorithm performed on the power board, which controls the tempering of the 64 surfaces of the PET SC TP285. ..... 102
**Figure 47: (a)** Temperature profiles of all 64 temperature sensors with the visible control stability at 80 °C, a **(b)** temperature jump from 120 to -20 °C with the cooling rates, and **(c)** an opposite temperature jump from 0 to 120 °C with the heating rates. ..... 104
**Figure 48:** Temperature profiles of all 64 temperature sensors while performing cycles between **(a)** 80 °C and -10 °C with a defined ramp, **(b)** with the subsequent spreading of the anode and cathode temperatures to a final temperature of 40 °C/80 °C, and **(c)** finally setting a local hot spot of 66 °C vs. 60 °C cell temperature. ..... 105
**Figure 49:** Temperature profiles of all 64 temperature sensors when a horizontal temperature gradient of **(a)** 10 °C to 80 °C is set in ramp mode, and **(b)** the corresponding thermal infrared image of the anodic current collector surface. ..... 105

**Figure 50:** Simplified sequence of the measurement procedure loop, with the stable operating point (SOP), preconditioning to maintain the same measurement parameters, and determination of the cell impedance (DCI). .....107
**Figure 51: (a)** Physical impedance model consisting of 5 equivalent circuit elements for fitting the impedance data measured with the PEM single cell at OCV, and **(b)** typical examples of the impedance spectra (open symbols) together with the fit to the equivalent circuit (solid lines). .....109
**Figure 52:** The temperature dependences of the equivalent circuit parameters (corresponding to **Figure 51 (a)**, without the double layer capacitance $C_{dl}$). The dashed lines are given as guides for the eye. .....110
**Figure 53:** Temperature dependence of the double layer capacitance $C_{dl}$ in a temperature range from - 5 °C to 60 °C. .....112
**Figure 54:** Simplified description of the low temperature stress test sequence, with the procedure loop (break-in, stable operation point, pre-conditioning, low-temperature part and start-up) and the characterization part (polarization curves, EIS and cyclic voltammetry). .....114
**Figure 55:** High frequency resistance (HFR) measured during several preconditioning procedures with the target resistance of 21.8 Ωcm² and a visible relaxation of the HFR. .....117
**Figure 56: (a)** Polarization curves recorded after different stress cycles, and **(b)** the current density points extracted from the polarization curves to visualize the degradation characteristics. .....119
**Figure 57: (a)** Decrease of the electrochemical surface area ECSA (in %) during the accelerated low-temperature stress test, and **(b)** the cleaning cycle before ECSA measurement with a small desorption current peak at ~0.65 V. .....120
**Figure 58: (a)** Physical impedance model, which was used to fit **(b)** the measured impedance data during the low temperature stress test at a current density of 0.8 A/cm² .....121
**Figure 59: (a)** Summary related to the ohmic parameters with the uncompensated (Nafion® -electrolyte) resistance, $R_u$, charge transfer resistance, $R_{ct}$, and adsorption resistance, $R_{ads}$, and **(b)** the summary related to the capacitance parameters with the double layer capacitance $C_{dl}$ and adsorption capacitance $C_{ads}$. .....122

**Figure 60: (a)** Trend of the calculated Warburg coefficient, $A_w$, and **(b)** the calculated parameter $A_v$ during the performed temperature cycles. ..... 123
**Figure 61: (a)** Simplified representation of the oxygen reduction reaction (ORR) on a Pt particle with the reaction rate coefficient $k_{app(n)}$ of different active sites, and **(b)** the trend of the ratio $A_w/R_{ct}$ during the performed stress cycles. ..... 124
**Figure 62: (a)** Curves of the ohmic model parameters $R_u$ and $R_{ct}$ calculated by the CNLS and DIA methods, and **(b)** the curves of the two double-layer capacitances $C_{dl}$. ..... 125
**Figure 63: (a)** Cross-sectional micrograph showing the reduced thickness (~7.7 µm vs. ~9.8 µm) of the cathode catalyst layer and visible Pt band in the polymer electrolyte membrane, and **(b)** cross-sectional SEM image of the used MEA [137]. ..... 126
**Figure 64: (a)** Cross-sectional SEM image of the transition region in material contrast mode (BSE mode) of the cathode catalyst layer and membrane, and **(b)** more detailed SEM image of the polymer electrolyte membrane [137]. ..... 127
**Figure 65:** Simplified representation of an entire test procedure loop, i.e., a low-temperature cycle. The newly added or significantly changed sequences (compared to the procedure in chapter 5.2) are shown in blue. ..... 129
**Figure 66:** Current density points derived from polarization curves (**(a)** 1.0 A/cm² and **(b)** 2.0 A/cm²) to visualize the degradation behavior of the MEAs used during the low-temperature stress test. ..... 131
**Figure 67:** The decrease in electrochemical surface area ECSA (in %) of the MEAs used during the low-temperature stress test. ..... 133
**Figure 68:** (a) Physical impedance model showing the color-framed EC elements, each corresponding to sections of the impedance response, and (b) the impedance response at the beginning of the lifetime (BOL) for the MEAs with a cathode ionomer carbon weight ratio (I/C) of 0.5/1.0 (open symbols) along with the fit to the equivalent circuit (solid lines). ..... 134
**Figure 69:** Summary and trends of the calculated ohmic resistances $R_u$ of the tested MEAs measured at a current density of 0.8 A/cm² during the low temperature stress test. ..... 135
**Figure 70: (a)** Summary and trend of the calculated charge transfer resistances $R_{ct}$ and **(b)** the calculated double layer capacitances $C_{dl}$ of the tested MEAs at a current density of 0.8 A/cm² during the stress test. ..... 136

**Figure 71:** Summary of the trends of estimated R-C elements with **(a)** the adsorption resistance $R_{ads}$ and **(b)** adsorption capacitance $C_{ads}$ of the studied MEAs measured at a current density of 0.8 A/cm² during the low temperature stress test. ..... 137

**Figure 72:** Summary and trend of the calculated **(a)** Warburg coefficients $A_w$ and **(b)** the associated parameter $A_v$ of the studied MEAs measured at a current density of 0.8 A/cm² during the low-temperature stress test. ..... 138

**Figure 73:** Summary of the trends for the calculated $A_w/R_{ct}$ ratios of the investigated MEAs. ..... 138

**Figure 74:** Scanning electron microscope (SEM) images (15 kV, 200 pA) at different scales showing the visible cracks on the surface of the anode catalyst layer [153]. ..... 141

**Figure 75:** Scanning electron microscope (SEM) images (15 kV, 200 pA) of the surface of the anode catalyst layer showing **(a)** the visible worms and **(b)** buckling deformations [153]. ..... 141

**Figure 76:** 3D microscopy images and generated height profile sections showing the visible extensive fracture and detachment of the anode catalyst layer of the MEA with a cathode ionomer carbon weight ratio (I/C) of 1.5 [153]. ..... 142

**Figure 77:** Scanning electron microscope (SEM) and energy dispersive X-ray spectroscopy results of the cathode catalyst structure of the MEA with a cathode ionomer carbon weight ratio of 1.5. The analysis was performed before and after the stress test. **(a)** Reference SEM, **(b)** SEM of the used sample , **(c)** reference EDX, **(d)** EDX of the used sample [155]. ..... 143

**Figure 78:** A simplified representation of the MEA with the monopolar plate and the temperature gradient from -8 °C to +2 °C on the active surface. ..... 146

**Figure 79:** Drying times for cathode preconditioning with the target HFR of 8.55 Ωcm² during the stress test. ..... 147

**Figure 80:** Current density points vs. number of cycles derived from polarization curve. ..... 148

**Figure 81:** The decrease in electrochemical active surface area (ECSA) in % during the low-temperature stress test (LTST). ..... 149

**Figure 82:** Current density distribution of the active surface measured in the stable operation point (SOP) during low-temperature stress test (LTST). ..... 150

**Figure 83:** The absolute difference between the measured current density between BOL and after cycle 120. ..... 151
**Figure 84:** The EC model used to fit the locally measured impedance responses **(a)**, and the impedance responses of the 46 measurement points at BOL **(b)**. ..... 152
**Figure 85:** The evolution of the calculated model parameters $R_u$ and $R_{ct}$ of the total cell impedance during LTST. ..... 153
**Figure 86:** Locally resolved model parameters of **(a)** the ohmic resistance $R_u$ and **(b)** the absolute difference in resistance $R_u$ between BOL and the 120 cycles. ..... 153
**Figure 87:** Locally resolved calculated charge transfer resistances $R_{ct}$ at **(a)** BOL and **(b)** the absolute difference of the charge transfer resistances $R_{ct}$ between BOL and after 120 cycles. ..... 154
**Figure 88:** Course of the calculated double layer capacitance $C_{dl}$ of the total cell impedance during LTST. ..... 155
**Figure 89:** Locally resolved calculated $C_{dl}$ at **(a)** BOL and **(b)** the absolute difference of the double layer capacities $C_{dl}$ between BOL and after 120 cycles. ..... 155
**Figure 90:** Trend of the calculated **(a)** Warburg coefficients $A_w$ and **(b)** the associated coefficient $A_v$ of the total cell impedance during the LTST. ..... 156
**Figure 91:** Locally resolved calculated Warburg short element $W_S$ parameters with the coefficient $A_w$ at **(a)** BOL and **(b)** the absolute difference of the coefficient $A_w$ between BOL and after 120 cycles. ..... 157
**Figure 92:** Locally resolved calculated coefficient *Av* at **(a)** BOL, and **(b)** the absolute difference of the coefficient *Av* between BOL and after 120 cycles. ..... 157

**Table 1:** Detailed description of the numbered components in **Figure 6**. Please note that the working ranges of the individual components, as well as the tolerance specifications, are provided by the test bench manufacturer. .....29
**Table 2:** Detailed description of the numbered components in **Figure 10**. Please note that the specified measuring tolerances of the individual electrical components were provided by the respective manufacturers.....38
**Table 3:** Detailed description of the numbered cell components in **Figure 14**. .....43
**Table 4:** All summarized advantages and disadvantages of the commercial TP50 cell hardware, which is used on a test bench with common water cooling circuit. .....58
**Table 5:** All summarized advantages and disadvantages with the associated technical data of the newly developed single-cell PET SC TP50.....60
**Table 6:** The main physical properties of the selected Peltier element used with the PET SC TP50.....67
**Table 7:** All summarized advantages and disadvantages with the associated technical data of the newly developed single-cell PET SC TP285.....77
**Table 8:** The most essential failure cases detected during commissioning with the associated failure cause.....83
**Table 9:** Relevant properties of the Pt1000 temperature sensors used in the PET SC TP285.....87
**Table 10:** The key physical properties of the selected Peltier element used with the PET SC TP285.....91
**Table 11:** Summary of the measured HFR values obtained in the different preconditioning processes, including drying time and resistance after HFR relaxation.....118
**Table 12:** Summarized key data of the MEAs used in the test series. .....128
**Table 13:** Summary of defect patterns for the anode and cathode catalyst layers of the MEAs used, with different weight ratios of cathode ionomer to carbon (I/C). .....139

# References


[1] J. Wang, L. Feng, X. Tang, Y. Bentley and M. Höök, "The implications of fossil fuel supply constraints on climate change projections: A supply-side analysis," *Futures,* vol. 86, pp. 58-72, 2000.

[2] J. Szulejko, P. Kumar, A. Deep and K.-H. Kim, "Global warming projections to 2100 using simple CO2 greenhouse gas modeling and comments on CO2 climate sensitivity factor," *Atmospheric Pollution Research,* vol. 8, pp. 136-140, 2017.

[3] "Statistika.com," [Online]. Available: https://www.statista.com/statistics/281134/number-of-vehicles-in-use-worldwide/. [Accessed 17 January 2020].

[4] "European Parliament," [Online]. Available: https://www.europarl.europa.eu/news/de/headlines/society/20180920STO14027/neue-co2-ziele-fur-autos. [Accessed 14 February 2020].

[5] X. Feng, M. Ouyang, X. Liu, L. Lu, Y. Xia and X. He, "Thermal runaway mechanism of lithium ion battery for electric vehicles: A review," *Energy Storage Materials,* vol. 10, pp. 246-267, 2018.

[6] L. YAO, B. Yang, H. CUI, J. ZHUANG, J. YE and J. XUE, "Challenges and progresses of energy storage technology and its application in power systems," *J. Mod. Power Syst. Clean Energy 4,* pp. 519-528, 2016.

[7] K. E. Aifantis, S. A. Hackney and R. V. Kumar, High Energy Density Lithium Batteries: Materials, Engineering, Applications, John Wiley & Sons, 2010.

[8] A. V. Mclean, M. S. Halper and J. C. Ellenbogen, "Supercapacitors: A Brief Overview," *Materials Science,* 2006.

[9] B. E. Conway, Electrochemical Supercapacitors, Springer US, 1999.

[10] "Elton super capacitors," [Online]. Available: http://www.elton-cap.com/products/capacitor-cells/. [Accessed 5 August 2020].

[11] P. L. Fèvre, "elektroniknet.de," [Online]. Available: https://www.elektroniknet.de/elektronik/power/die-stille-kraft-der-superkondensatoren-161449.html. [Accessed 5 August 2020].

[12] P. Boyd, "NASA Archieved," 12 November 1996. [Online]. Available: https://imagine.gsfc.nasa.gov/ask_astro/stars.html#961112a. [Accessed 5 August 2020].

[13] R. Chaubey, S. Sahu, O. O. James and S. Maity, "A review on development of industrial processes and emerging techniques for production of hydrogen from renewable and sustainable sources," *Renewable and Sustainable Energy Reviews,* vol. 23, pp. 443-462, 2013.

[14] K. Grote and J. Feldhusen, Taschenbuch für den Maschinenbau, Springer, 2014.

[15] J. Abe, A. Popoola and O. P. E. Ajenifuja, "Hydrogen energy, economy and storage: Review and recommendation," *International Journal of Hydrogen Energy,* vol. 44, pp. 15072-15086, 2019.

[16] N. Zhevago, "Other methods for the physical storage of hydrogen," *Compendium of Hydrogen Energy,* vol. 2, pp. 189-218, 2016.

[17] "Europäische Kommision," 8 July 2020. [Online]. Available: https://ec.europa.eu/germany/news/20200708-wasserstoffstrategie_de. [Accessed 6 August 2020].

[18] C. Acar and I. Dincer, "The potential role of hydrogen as a sustainable transportation fuel to combat global warming," *International Journal of Hydrogen Energy,* vol. 45, pp. 3396-3406, 2020.

[19] O. Z. Sharaf and M. F. Orhan, "An overview of fuel cell technology: Fundamentals and applications," *Renewable and Sustainable Energy Reviews,* vol. 32, pp. 810-853, 2014.

[20] Y. Wang, D. F. R. Diaz, K. S. Chen, Z. Wang and X. C. Adroher, "Materials, technological status, and fundamentals of PEM fuel cells – A review," *Materialstoday,* vol. 32, pp. 178-203, 2020.

[21] "Bundesregierung," [Online]. Available: https://www.bundesregierung.de/breg-de/themen/energiewende/fragen-und-antworten/verkehr/verkehr-456434. [Accessed 6 August 2020].

[22] J. Wang, "Barriers of scaling-up fuel cells: Cost, durability and reliability," *Energy,* vol. 80, pp. 509-521, 2015.

[23] J. Marcinkoski, B. D. James, J. A. Kalinoski, W. Podolski, T. Benjamin and J. Kopasz, "Manufacturing process assumptions used in fuel cell system cost analyses," *Journal of Power Sources,* vol. 196, pp. 5282-5292, 2011.

[24] A. Wilson, G. Kleen and D. Papageorgopoulos, "DOE Hydrogen and Fuel Cells Program Record," Department of Energy, 2017.

[25] M. Ramezanizadeh, M. A. Nazari, M. H. Ahmadi and L. Chen, "A review on the approaches applied for cooling fuel cells," *Internattional Journal of Heat and Mass Transfer,* vol. 139, pp. 517-525, 2019.

[26] R. O. Stroman, M. W. Schuette and G. S. Page, "Cooling System Design for PEM Fuel Cell Powered Air Vehicles," Naval Research Laboratory, Washington, 2010.

[27] H.-S. Lee, C.-W. Cho, J.-H. Seo and M.-Y. Lee, "Cooling Performance Characteristics of the Stack Thermal Management System for Fuel Cell Electric Vehicles under Actual Driving Conditions," *Energies,* vol. 9, p. 320, 2016.

[28] Z. Rao and S. Wang, "A review of power battery thermal energy management," *Renewable and Sustainable Energy Reviews,* pp. 4554-4571, 2011.

[29] W. Bi and T. F. Fuller, "Temperature Effects on PEM Fuel Cells Pt/C Catalyst Degradation," *Journal of The Electrochemical Society,* vol. 155, no. 2, p. B215, 2007.

[30] J. P. Sabawa and A. S. Bandarenka, "Degradation Mechanisms in Polymer Electrolyte Membrane Fuel Cells Caused by Freeze-Cycles: Investigation Using Electrochemical Impedance Spectroscopy," *Electrochimica Acta,* vol. 311, pp. 21-29, 2019.

[31] T. Lochner, R. M. Kluge, J. Fichtner, D. H. A. El-Sayed, D. B. Garlyyev and P. D. A. S. Bandarenka, "Temperature Effects in Polymer Electrolyte Membrane Fuel Cells," *ChemElectroChem,* vol. 7, no. 17, pp. 3545-3568, 2020.

[32] A. Kusoglu and A. Z. Weber, "New Insights into Perfluorinated Sulfonic-Acid Ionomers," *Chemical reviews,* vol. 3, pp. 987-1104, 2017.

[33] S. S. Kocha, Polymer Electrolyte Membrane (PEM) Fuel Cells: Automotive Applications, SpringerLink, 2018.

[34] L. Vichard, F. Harel, A. Ravey, P. Venet and D. Hissel, "Degradation prediction of PEM fuel cell based on artificial intelligence," *International Journal of Hydrogen Energy,* vol. 45, no. 29, pp. 14953-14963, 2020.

[35] J. Han, J. Han and S. Yu, "Experimental analysis of performance degradation of 3-cell PEMFC stack under dynamic load cycle," *International Journal of Hydrogen Energy,* vol. 45, no. 23, pp. 13045-13054, 2020.

[36] H. A. El-Sayed, A. Weiß, L. F. Olbrich, G. P. Putro and H. A. Gasteiger, "OER Catalyst Stability Investigation Using RDE Technique: A Stability Measure or an Artifact?," *Journal of The Electrochemical Society,* vol. 166, no. 8, p. F458, 2019.

[37] S. Asghari, A. Mokmeli and M. Samavati, "Study of PEM fuel cell performance by electrochemical impedance spectroscopy," *International Journal of Hydrogen Energy,* vol. 35, no. 17, pp. 9283-9290, 2010.

[38] X. Yuan, J. C. Sun, M. Blanco, H. Wang, J. Zhang and D. P. Wilkinson, "AC impedance diagnosis of a 500 W PEM fuel cell stack Part I: Stack impedance," *ScienceDirect,* vol. 161, pp. 920-928, 2006.

[39] J. Park and X. Li, "Effect of flow and temperature distribution on the performance of a PEM fuel cell stack," *Journal of Power Sources,* vol. 162, no. 1, pp. 444-459, 2006.

[40] M. Kandidayenia, A. Macias, L. Boulon and S. Kelouwani, "Investigating the impact of ageing and thermal management of a fuel cell system on energy management strategies," *Applied Energy,* vol. 279, p. 115813, 2020.

[41] R. Lin, Y. Ren, X. Lin, Z. Jiang, Z. Yang and Y. Chang, "Investigation of the internal behavior in segmented PEMFCs of different flow fields during cold start process," *Energy,* vol. 123, pp. 367-377, 2017.

[42] K. Jiao, I. E. Alaefour, G. Karimi and X. Li, "Simultaneous measurement of current and temperature distributions in a proton exchange membrane fuel cell

during cold start processes," *Electrochimica Acta,* vol. 56, no. 8, pp. 2967-2982, 2011.

[43] J. Wisniak, "The History of Catalysis. From the Beginning to Nobel Prizes," *Educación Química,* vol. 21, no. 1, pp. 60-69, 2010.

[44] J. J. Berzelius, "Quelques Idées sur une nouvelle Force agissant dans les Combinaisons des Corps Organiques," *Annales de chimie et de physique,* vol. 61, pp. 146-151, 1836.

[45] A. J. B. Robertson, "The early history of catalysis," *Platinum Metals Review,* vol. 19, no. 2, pp. 64-69, 1975.

[46] "Wilhelm Ostwald - Facts," Nobel Media AB 2014, [Online]. Available: https://www.nobelprize.org/prizes/chemistry/1909/ostwald/facts/. [Accessed 23 September 2020].

[47] G. Ertl and H.-J. Freund, "Catalysis and Surface Science," *Physics Today,* vol. 52, p. 32, 1999.

[48] A. S. Bommarius, J. K. Blum and M. J. Abrahamson, "Status of protein engineering for biocatalysts: how to design an industrially useful biocatalyst," *Current Opinion in Chemical Biology,* vol. 15, no. 2, pp. 194-200, 2011.

[49] P. R. Schlögl, "Heterogeneous Catalysis," *Angewandte Chemie,* vol. 54, no. 11, pp. 3465-3520, 2015.

[50] E. Sher, Handbook of Air Pollution From Internal Combustion Engines, Elsevier Inc., 1998.

[51] P. Sabatier, "New synthesis of methane," *Comptes rendus,* vol. 134, pp. 514-516, 1902.

[52] G. Rothenberg, Catalysis: Concepts and Green Applications, Wiley-VCH, 2008.

[53] A. J. Medford, A. Vojvodic, J. S. Hummelshøj, J. Voss, F. Abild-Pedersen, F. Studt, T. Bligaard, A. Nilsson and J. K. Nørskov, "From the Sabatier principle to a predictive theory of transition-metal heterogeneous catalysis," *Journal of Catalysis,* vol. 328, pp. 36-42, 2015.

[54] H. S. Taylor, "A Theory o f the Catalytic Surface," *Proceedings of the Royal Society,* vol. 108, no. 745, pp. 105-111, 1925.

[55] O. Deutschmann, H. Knözinger, K. Kochloefl and T. Turek, Heterogeneous Catalysis and Solid Catalysts, Ullmann's Encyclopedia of Industrial Chemistry, 2009.

[56] A. A. Balandin, "Modern State of the Multiplet Theor of Heterogeneous Catalysis," *Advances in Catalysis,* vol. 19, pp. 1-210, 1969.

[57] T. Bligaard, J. Nørskov, S. Dahl, J. Matthiesen, C. Christensen and J. Sehested, "The Brønsted–Evans–Polanyi relation and the volcano curve in heterogeneous catalysis," *Journal of Catalysis,* vol. 224, no. 1, pp. 206-217, 2004.

[58] S. Trasatti, "Work function, electronegativity, and electrochemical behaviour of metals: III. Electrolytic hydrogen evolution in acid solutions," *Journal of Electroanalytical Chemistry and Interfacial Electrochemistry,* vol. 39, no. 1, pp. 163-184, 1972.

[59] F. Barbir, PEM fuel cells: Theory and Practice, New York: Elsevier Academic Press, 2005.

[60] J. T. Gostick, M. A. Ioannidis, M. W.Fowler and M. D. Pritzker, "On the role of the microporous layer in PEMFC operation," *Electrochemistry Communications,* vol. 11, no. 3, pp. 576-579, 2009.

[61] R. Wang, H. Wang, F. Luo and S. Liao, "Core–Shell-Structured Low-Platinum Electrocatalysts for Fuel Cell Applications," *Electrochemical Energy Reviews,* vol. 1, pp. 324-387, 2018.

[62] K. W. H. Ekström, A. E. C. Palmqvist, A. Lundblad, K. Holmberg and G. Lindbergh, "Alternative Catalysts and Carbon Support Material for PEMFC," *Fuel Cells,* vol. 6, no. 1, pp. 21-25, 2006.

[63] J. Shui, C. Chen, L. Grabstanowicz, D. Zhao and D.-J. Liu, "Highly efficient nonprecious metal catalyst prepared with metal–organic framework in a continuous carbon nanofibrous network," *PNAS,* vol. 112, no. 34, pp. 10629-10634, 2015.

[64] R. Liua, W. Zhou, L. Wan, P. Zhang, S. Li, Y. Gao, D. Xu, C. Zheng and M. Shang, "Electrostatic spraying of membrane electrode for proton exchange membrane fuel cell," *Current Applied Physics,* vol. 30, pp. 11-17, 2020.

[65] W. Y. Hsu and T. D. Gierke, "Ion transport and clustering in Nafion perfluorinated membranes," *Journal of Membrane Science,* vol. 13, no. 3, pp. 307-326, 1983.

[66] M. Ulbricht, "Advanced functional polymer membranes," *Polymer,* vol. 47, no. 7, pp. 2217-2262, 2006.

[67] F. Meier, Stofftransport in Polymerelektrolyt-Membranen für Brennstoffzellen - experimentelle Untersuchung, Modellierung und Simulation, Berlin: Logos Verlag Berlin GmbH, 2005.

[68] Y. Wanga, K. S. Chen, J. Mishler, S. C. Cho and X. C. Adrohera, "A review of polymer electrolyte membrane fuel cells: Technology, applications, and needs on fundamental research," *Applied Energy,* vol. 88, no. 4, pp. 981-1007, 2011.

[69] F. Barbir, Fuel Cell Basic Chemistry, Electrochemistry and Thermodynamics, Springer Netherlands, 2008.

[70] C. H. Hamann, A. Hamnett and W. Vielstich, Electrochemistry, Weinheim: Wiley-VCH, 2007.

[71] J. C. A. Peltier, "Nouvelles Experiences sur la Caloricite des Courans Electriques," *Annales de physique et chimie,* vol. 56, pp. 371-386, 1834.

[72] D. Champier, "Thermoelectric Generators: A Review of Present and Future Applications," in *3rd International Congress on Energy Efficiency and Energy Related Materials (ENEFM2015)*, 2017.

[73] S. Schaad, "Peltier-Element kurz erklärt," Deltron AG, Kirchberg, Switzerland.

[74] M. Charlwood, S. Turner and N. Worsell, A methodology for the assignment of safety integrity levels (SILs) to safety-related control functions implemented by safety-related electrical, electronic and programmable electronic control systems of machines, HSE - Health & Safety Executive, 2004.

[75] P. Kurzweil, Brennstoffzellentechnik - Grundlagen, Komponenten, Systeme, Anwendungen, Wiesbaden: Springer, 2013.

[76] M. Obermaier, A. S. Bandarenka and C. Lohri-Tymozhynsky, "A Comprehensive Physical Impedance Model of Polymer Electrolyte Fuel Cell Cathodes in Oxygen-free Atmosphere," *Scientific Reports*, vol. 8, p. 4933, 2018.

[77] D. Vladikova, "THE TECHNIQUE OF THE DIFFERENTIAL IMPEDANCE ANALYSIS: Part I: BASICS OF THE IMPEDANCE SPECTROSCOPY," Sofia, Bulgaria, 2004.

[78] Kanika, M. Duhan and S. Khasa, "Impedance Spectroscopy Analysis using CNLS fitting for lithium bismuth borate glass containing 10 mol% d-Block Nickel & Vanadium Ions," *International Advanced Research Journal in Science, Engineering and Technology*, vol. 4, no. 6, 2017.

[79] D. Vladikova, "THE TECHNIQUE OF THE DIFFERENTIAL IMPEDANCE ANALYSIS. Part II. DIFFERENTIAL IMPEDANCE ANALYSIS," Sofia, Bulgaria, 2004.

[80] T. Lochner, D. M. Perchthaler, J. T. Binder, J. P. Sabawa, T. A. Dao and P. A. S. Bandarenka, "Real-Time Impedance Analysis for the On-Road Monitoring of Automotive Fuel Cells," *ChemElectroChem*, vol. 7, no. 13, 2020.

[81] J. E. B. Randles, "Kinetics of rapid electrode reactions," *Discussions of the Faraday Society*, vol. 1, pp. 11-19, 1947.

[82] L. Reimer and G. Pfefferkorn, Raster-Elektronenmikroskopie, Springer, 1977.

[83] Flegler, Heckmann and Klomparens, Elektronenmikroskopie: Grundlagen. Methoden. Anwendungen, Spektrum Akademischer Verlag, 1995.

[84] F. Eggert, Standardfreie Elektronenstrahl-Mikroanalyse (mit dem EDX im Rasterelektronenmikroskop), Rheinberg-Buch, 2005.

[85] J. Goldstein, D. Newbury, D. Joy, C. Lyman, P. Echlin, E. Lifshin, L. Sawyer and J. Michael, Scanning Electron Microscopy and X-Ray Microanalysis, Spinger, 2003.

[86] KEYENCE CORPORATION, [Online]. Available: https://www.keyence.de/products/microscope/laser-microscope/vk-x100_x200/models/vk-x1100/. [Accessed 19 November 2020].

[87] J. B. Pawley, Handbook Of Biological Confocal Microscopy, Springer, 2006.

[88] D. Papageorgopoulos, "Fuel Cell R&D Subprogram Overview," in *DOE Hydrogen and Fuel Cells Program*, 2019.

[89] Z. Zhan, C. Yuan, Z. Hu, H. Wang, P. Sui, N. Djilali and M. Pan, "Experimental study on different preheating methods for the cold-start of PEMFC stacks," *Energy*, vol. 162, pp. 1029-1040, 2018.

[90] J. Hou, H. Yu, S. Zhang, S. Sun, H. Wang, B. Yi and P. Ming, "Analysis of PEMFC freeze degradation at −20 °C after gas purging," *Journal of Power Sources*, vol. 162, no. 1, pp. 513-520, 2006.

[91] Q. Yan, H. Toghiani, Y.-W. Lee, K. Liang and H. Causey, "Effect of sub-freezing temperatures on a PEM fuel cell performance, startup and fuel cell components," *Journal of Power Sources*, vol. 160, no. 2, pp. 1242-1250, 2006.

[92] J. Zhang, Z. Xie, J. Zhang, Y. Tang, C. Song, T. Navessin, Z. Shi, D. Song, H. Wang, D. P. Wilkinson, Z.-S. Liu and S. Holdcroft, "High temperature PEM fuel cells," *Journal of Power Sources*, vol. 160, no. 2, pp. 872-891, 2006.

[93] E. Quartarone, S. Angioni and P. Mustarelli, "Polymer and Composite Membranes for Proton-Conducting, High-Temperature Fuel Cells: A Critical Review," *Materials*, vol. 10, no. 7, p. 687, 2017.

[94] A. Berger, "Glycole," Thieme RÖMPP, [Online]. Available: https://roempp.thieme.de/lexicon/RD-07-01538. [Accessed 23 November 2020].

[95] G. Zhang and S. G. Kandlikar, "A critical review of cooling techniques in proton exchange membrane fuel cell stacks," *International Journal of Hydrogen Energy*, vol. 37, no. 3, pp. 2412-2429, 2012.

[96] X. Xie, R. Wang, K. Jiao, G. Zhang, J. Zhou and Q. Du, "Investigation of the effect of micro-porous layer on PEM fuel cell cold start operation," *Renewable Energy*, vol. 117, pp. 125-134, 2018.

[97] S. Huo, N. J. Cooper, T. L. Smith, J. W. Park and K. Jiao, "Experimental investigation on PEM fuel cell cold start behavior containing porous metal foam as cathode flow distributor," *Applied Energy*, vol. 203, pp. 101-114, 2017.

[98] M. Zhu, X. Xie, K. Wu, A.-U.-H. Najmi and K. Jiao, "Experimental investigation of the effect of membrane water content on PEM fuel cell cold start," *Energy Procedia*, no. 158, pp. 1724-1729, 2019.

[99] Y. Ishikawa, T. Morita and M. Shiozawa, "Behavior of Water below the Freezing Point in PEFCs," *ECS Transactions*, vol. 1, no. 3, pp. 708-712, 2006.

[100] L. Rasha, J. Cho, T. Neville, A. Corredera, P. Shearing and D. Brett, "Water distribution mapping in polymer electrolyte fuel cells using lock-in thermography," *Journal of Power Sources,* no. 440, p. 227160, 2019.

[101] J. P. Sabawa and A. S. Bandarenka, "Applicability of double layer capacitance measurements to monitor local temperature changes at polymer electrolyte membrane fuel cell cathodes," *Results in Chemistry,* vol. 2, p. 100078, 2020.

[102] C.V.Pious and S. Thomas, "2 - Polymeric Materials—Structure, Properties, and Applications," *Printing on Polymers - Fundamentals and Applications,* pp. 21-39, 2016.

[103] P. Hidnert and H. S. Krider, "Thermal Expansion of Aluminum and Some Aluminum Alloys," *Journal of Resea rch of the Nationa l Bureau of Standards,* vol. 48, no. 3, p. 209, 1952.

[104] LEHIGH VALLEY PLASTICS, INC., "Data sheet Ultem 2300," [Online]. Available: http://www.lehighvalleyplastics.com/wp-content/uploads/2013/09/Ultem_2300-PEI.pdf. [Accessed 14 09 2020].

[105] K. S. Lau, "High-Performance Polyimides and High Temperature Resistant Polymers," in *Handbook of Thermoset Plastics (Third Edition),* William Andrew, 2014, pp. 297-424.

[106] I. T. AG, "https://www.infineon.com/," 17 05 2013. [Online]. Available: https://www.infineon.com/dgdl/Infineon-BTN8982TA-DS-v01_00-EN.pdf?fileId=db3a30433fa9412f013fbe32289b7c17. [Accessed 22 12 2020].

[107] J. G. Ziegler and N. B. Nichols, "Optimum Settings for Automatic Controllers," *Journal of Dynamic Systems Measurement and Control-transactions of The Asme,* vol. 115, pp. 220-222, 1942.

[108] S. Messlinger, "Universität Bayreuth," 2013. [Online]. Available: https://epub.uni-bayreuth.de/43/. [Accessed 17 01 2021].

[109] W. Schmittinger and A. Vahidi, "A review of the main parameters influencing long-term performance and durability of PEM fuel cells," *Journal of Power Sources,* vol. 180, no. 1, pp. 1-14, 2008.

[110] Z. Wan, H. Chang, S. Shu, Y. Wang and H. Tang, "A Review on Cold Start of Proton Exchange Membrane Fuel Cells," *Energies,* vol. 7, no. 5, pp. 3179-3203, 2014.

[111] M. A. Danzer and E. P. Hofer, "Analysis of the electrochemical behaviour of polymer electrolyte fuel cells using simple impedance models," *Journal of Power Sources,* vol. 190, no. 1, pp. 25-33, 2009.

[112] S. M. R. Niya and M. Hoorfar, "Study of proton exchange membrane fuel cells using electrochemical impedance spectroscopy technique – A review," *Journal of Power Sources,* vol. 240, pp. 281-293, 2013.

[113] J. Tymoczko, W. Schuhmann and A. S. Bandarenka, "The constant phase element reveals 2D phase transitions in adsorbate layers at the

electrode/electrolyte interfaces," *Electrochemistry Communications,* vol. 27, pp. 42-45, 2013.

[114] B. B. Berkes, G. Inzelt, W. Schuhmann and A. S. Bondarenko, "Influence of Cs+ and Na+ on Specific Adsorption of *OH, *O, and *H at Platinum in Acidic Sulfuric Media," *The Journal of Physical Chemistry C,* vol. 116, no. 20, pp. 10995-11003, 2012.

[115] B. Braunschweig and W. Daum, "Superstructures and Order−Disorder Transition of Sulfate Adlayers on Pt(111) in Sulfuric Acid Solution," *Langmuir,* vol. 25, no. 18, p. 11112–11120, 2009.

[116] A. Bandarenka, "Development of hybrid algorithms for EIS data fitting, a book chapter in: Lecture Notes on Impedance Spectroscopy, Measurement, Modeling and Applications," *O.-CRC Press, Tailor and Francis Group,* vol. 4, pp. 29-36, 2013.

[117] D. Aaron, S. Yiacoumi and C. Tsouris, "Effects of Proton-Exchange Membrane Fuel-Cell Operating Conditions On Charge Transfer Resistances Measured by Electrochemical Impedance Spectroscopy," *Separation Science and Technology,* vol. 43, no. 9-10, pp. 2307-2320, 2008.

[118] T. D. Gierke, G. E. Munn and F. C. Wilson, "The morphology in Nafion perfluorinated membrane products, as determined by wide- and small-angle x-ray studies," *Polymer Physics,* vol. 19, no. 11, pp. 1687-1704, 1981.

[119] S. Cui, J. Liu, M. E. Selvan, D. J. Keffer, B. J. Edwards and W. V. Steele, "A Molecular Dynamics Study of a Nafion Polyelectrolyte Membrane and the Aqueous Phase Structure for Proton Transport," *The Journal of Physical Chemistry B,* vol. 111, no. 9, p. 2208–2218, 2007.

[120] J. Tymoczko, F. Calle-Vallejo, V. Colic, M. T. M. Koper, W. Schuhmann and A. S. Bandarenka, "Oxygen Reduction at a Cu-Modified Pt(111) Model Electrocatalyst in Contact with Nafion Polymer," *ACS Catalysis,* vol. 4, no. 10, pp. 3772-3778, 2014.

[121] K. J. Laidler, "The development of the Arrhenius equation," *Journal of Chemical Education,* vol. 61, no. 6, p. 494, 1984.

[122] B. B. Berkes, J. B. Henry, M. Huang and A. S. Bondarenko, "Electrochemical Characterisation of Copper Thin-Film Formation on Polycrystalline Platinum," *ChemPhysChem,* vol. 13, no. 13, pp. 3210-3217, 2012.

[123] M. Holovko, V. Kapko, D. Henderson and D. Boda, "On the influence of ionic association on the capacitance of an electrical double layer," *Chemical Physics Letters,* vol. 341, no. 3-4, pp. 363-368, 2001.

[124] E. Cho, J.-J. Ko, H. Y. Ha, S.-A. Hong, w.-Y. Lee, e.-W. Lim and H. Oh, "Characteristics of the PEMFC Repetitively Brought to Temperatures below 0°C," *Journal of the Electrochemical Society,* vol. 150, p. A1667, 2003.

[125] Y. Wang, "Analysis of the Key Parameters in the Cold Start of Polymer Electrolyte Fuel Cells," *Journal of the Electrochemical Society,* vol. 154, p. B1041, 2007.

[126] J. P. Meyers and R. M. Darling, "Model of Carbon Corrosion in PEM Fuel Cells," *Journal of the Electrochemical Society,* vol. 153, no. 8, p. A1432, 2006.

[127] C. A. Reiser, L. Bregoli, T. W. Patterson, J. S. Yi, J. D. Yang, M. L. Perry and T. D. Jarvi, "A Reverse-Current Decay Mechanism for Fuel Cells," *Electrochemical and Solid-State Letters,* vol. 8, p. A273, 2005.

[128] Y. Li, Z. Zheng, X. Chen, Y. Liu, M. Liu, J. Li, D. Xiong and J. Xu, "Carbon corrosion behaviors and the mechanical properties of proton exchange membrane fuel cell cathode catalyst layer," *International Journal of Hydrogen Energy,* vol. 45, no. 43, pp. 23519-23525, 2020.

[129] J. Shan, R. Lin, S. Xia, D. Liu and Q. Zhang, "Local resolved investigation of PEMFC performance degradation mechanism during dynamic driving cycle," *International Journal of Hydrogen Energy,* vol. 41, no. 7, pp. 4239-4250, 2016.

[130] I. Pivac, D. Bezmalinović and F. Barbir, "Catalyst degradation diagnostics of proton exchange membrane fuel cells using electrochemical impedance spectroscopy," *International Journal of Hydrogen Energy,* vol. 43, no. 29, pp. 13512-13520, 2018.

[131] N. Fouquet, C. Doulet, C. Nouillant, G. Dauphin-Tanguy and B. Ould-Bouamama, "Model based PEM fuel cell state-of-health monitoring via ac impedance measurements," *Journal of Power Sources,* vol. 159, no. 2, pp. 905-913, 2006.

[132] A. S. Bondarenko and G. A. Ragoisha, "abc.chemistry," 2008. [Online]. Available: http://www.abc.chemistry.bsu.by/vi/analyser/parameters.html. [Accessed 13 02 2021].

[133] I. Pivac, B. Šimić and F. Barbir, "Experimental diagnostics and modeling of inductive phenomena at low frequencies in impedance spectra of proton exchange membrane fuel cells," *Journal of Power Sources,* vol. 365, pp. 240-248, 2017.

[134] H. A. Gasteiger and N. M. Marković, "Just a Dream—or Future Reality?," *Science,* vol. 324, no. 5923, pp. 48-49, 2009.

[135] N. Zamela, N. G. Astrath, X. Li, J. Shen, J. Zhou, F. B. Astrath, H. Wang and Z.-S. Liu, "Experimental measurements of effective diffusion coefficient of oxygen–nitrogen mixture in PEM fuel cell diffusion media," *Chemical Engineering Science,* vol. 65, no. 2, pp. 931-937, 2010.

[136] W. Bi, G. E. Gray and T. F. Fuller, "PEM Fuel Cell Pt/C Dissolution and Deposition in Nafion Electrolyte," *Electrochemical and Solid-State Letters,* vol. 10, no. 5, p. B101, 2007.

[137] "Investigation Report No. 180114525, Reproduced with permission from BMW Group," BMW Group, Technology Material a Process Analysis (TWA), München, Germany, 2019.

[138] X. Xie, G. Zhang, J. Zhou and K. Jiao, "Experimental and theoretical analysis of ionomer/carbon ratio effect on PEM fuel cell cold start operation," *International Journal of Hydrogen Energy,* vol. 42, no. 17, pp. 12521-12530, 2017.

[139] A. Taniguchia, T. Akita, K. Yasuda and Y. Miyazaki, "Analysis of electrocatalyst degradation in PEMFC caused by cell reversal during fuel starvation," *Journal of Power Sources,* vol. 130, no. 1-2, pp. 42-49, 2004.

[140] S. Maass, F. Finsterwalder, G. Frank, R. Hartmanna and C. Merten, "Carbon support oxidation in PEM fuel cell cathodes," *Journal of Power Sources,* vol. 176, no. 2, pp. 444-451, 2008.

[141] D. Malko, T. Lopes, E. A. Ticianelli and A. Kucernak, "A catalyst layer optimisation approach using electrochemical impedance spectroscopy for PEM fuel cells operated with pyrolysed transition metal-N-C catalysts," *Journal of Power Sources,* vol. 323, pp. 189-200, 2016.

[142] A. Suzuki, U. Sen, T. Hattori, R. Miura, R. Nagumo, H. Tsuboi, N. Hatakeyama, A. Endou, H. Takaba, M. C. Williams and A. Miyamoto, "Ionomer content in the catalyst layer of polymer electrolyte membrane fuel cell (PEMFC): Effects on diffusion and performance," *International Journal of Hydrogen Energy,* vol. 36, no. 3, pp. 2221-2229, 2011.

[143] A. Orfanidi, P. J. Rheinländer, N. Schulte and H. A. Gasteiger, "Ink Solvent Dependence of the Ionomer Distribution in the Catalyst Layer of a PEMFC," *Journal of The Electrochemical Society,* vol. 165, p. F1254, 2018.

[144] Z. Yu, R. N. Carter and J. Zhang, "Measurements of Pore Size Distribution, Porosity, Effective Oxygen Diffusivity, and Tortuosity of PEM Fuel Cell Electrodes," *Fuel Cells,* vol. 12, no. 4, pp. 557-565, 2012.

[145] H. Yu, J. M. Roller, W. E. Mustain and R. Maric, "Influence of the ionomer/carbon ratio for low-Pt loading catalyst layer prepared by reactive spray deposition technology," *Journal of Power Sources,* vol. 283, pp. 84-94, 2015.

[146] M. Eguchi, K. Baba, T. Onuma, K. Yoshida, K. Iwasawa, Y. Kobayashi, K. Uno, K. Komatsu, M. Kobori, M. Nishitani-Gamo and T. Ando, "Influence of Ionomer/Carbon Ratio on the Performance of a Polymer Electrolyte Fuel Cell," *Polymers,* vol. 4, no. 4, pp. 1645-1656, 2012.

[147] E. F. Holby, W. Sheng, Y. Shao-Horn and D. Morgan, "Ptnanoparticle stability in PEMfuelcells: influence of particle size distribution and crossover hydrogen," *Energy & Environmental Science,* vol. 2, pp. 865-871, 2009.

[148] W. Bi and T. F.Fuller, "Modeling of PEM fuel cell Pt/C catalyst degradation," *Journal of Power Sources,* vol. 178, no. 1, pp. 188-196, 2008.

[149] K. J. J. Mayrhofer, J. C. Meier, S. J. Ashton, G. K. H. Wiberg, F. Kraus, M. Hanzlik and M. Arenz, "Fuel cell catalyst degradation on the nanoscale," *Electrochemistry Communications,* vol. 10, no. 8, pp. 1144-1147, 2008.

[150] S. Park, Y. Shao, H. Wan, V. V. Viswanathan, S. A. Towne, P. C. Rieke, J. Liu and Y. Wang, "Degradation of the Ionic Pathway in a PEM Fuel Cell

Cathode," *The Journal of Physical Chemistry C,* vol. 115, no. 45, p. 22633–22639, 2011.

[151] Y. Liu, M. W. Murphy, D. R. Baker, W. Gu, C. Ji, J. Jorne and H. A. Gasteiger, "Proton Conduction and Oxygen Reduction Kinetics in PEM Fuel Cell Cathodes: Effects of Ionomer-to-Carbon Ratio and Relative Humidity," *Journal of The Electrochemical Society,* vol. 156, p. B970, 2009.

[152] T. Uchiyama, H. Kumei and T. Yoshida, "Catalyst layer cracks by buckling deformation of membrane electrode assemblies under humidity cycles and mitigation methods," *Journal of Power Sources,* vol. 238, pp. 403-412, 2013.

[153] "Investigation Report No. 190115143, Reproduced with permission from BMW Group," BMW Group, Technology Material a Process Analysis (TWA), München, Germany, 2020.

[154] T. Uchiyama, M. Kato and T. Yoshida, "Buckling deformation of polymer electrolyte membrane and membrane electrode assembly under humidity cycles," *Journal of Power Sources,* vol. 206, pp. 37-46, 2012.

[155] "Investigation Report No. 200100884, Reproduced with permission from BMW Group," BMW Group, Technology Material a Process Analysis (TWA), München, Germany, 2020.

[156] J.-L. Dellis, Laboratoire de la Physique de la Matière Condensée, UFR des Sciences, Amiens, France.